Predicting and Identifying Signs of Criticality near Neuronal Phase Transition

A thesis

submitted in fulfilment

of the requirements for the degree

of

Doctor of Philosophy in Physics

at

The University of Waikato

by

Malithi Eranga Chandrasiri

THE UNIVERSITY OF
WAIKATO
Te Whare Wānanga o Waikato

2020

Abstract

This thesis examines the critical transitions between distinct neural states associated with the transition to neuron spiking and with the induction of anaesthesia. First, mathematical and electronic models of a single spiking neuron are investigated, focusing on stochastic subthreshold dynamics on close approach to spiking and to depolarisation-blocked quiescence (spiking death) transition points. Theoretical analysis of subthreshold neural behaviour then shifts to the anaesthetic-induced phase transition into unconsciousness using a mean-field model for interacting populations of excitatory and inhibitory neurons. The anaesthetic-induced changes are validated experimentally using published electrophysiological data recorded in anaesthetised rats. The criticality hypothesis associated with brain state change is examined using neuronal avalanches for experimentally recorded rat local field potential (LFP) data and mean-field pseudoLFP simulation data.

We compare three different implementations of the FitzHugh–Nagumo single spiking neuron model: a mathematical model by H. R. Wilson, an alternative due to Keener and Sneyd, and an op-amp based nonlinear oscillator circuit. Although all three models can produce nonlinear "spiking" oscillations, our focus is on the altering characteristics of noise-induced fluctuations near spiking onset and death via Hopf bifurcation. We introduce small-amplitude white noise to enable a linearised stochastic analyses using Ornstein–Uhlenbeck theory to predict variance, power spectrum and correlation of voltage fluctuations during close approach to the critical point, identified as the point at which the real part of the dominant eigenvalue becomes zero. We validate the theoretical predictions with numerical simulations and show that the fluctuations exhibit critical slowing down divergences when approaching the critical point: power-law increases in the variance of the fluctuations simultaneous with prolongation of the system response.

We expand the study of stochastic behaviour to two spatial dimensions using the

Waikato mean-field model operating near phase transition points controlled by the infusion or elimination of anaesthetic inhibition. Specifically, we investigate close approach to the critical point (CP), and to the points of loss of consciousness (LOC) and recovery of consciousness (ROC). We select the equilibrium states using λ anaesthetic inhibition and ΔV_e^{rest} cortical excitation as control parameters, then analyse the voltage fluctuations evoked by small-amplitude spatiotemporal white noise. We predict the variance and power spectrum of voltage fluctuations near the marginally stable LOC and ROC transition points, then validate via numerical simulation. The results demonstrate a marked increase in voltage fluctuations and spectral power near transition points. This increased susceptibility to low-intensity white noise stimulation provides an early warning of impending phase transition.

Effects of anaesthetic agents on cortical activity are reflected in local field potentials (LFPs) by the variation of amplitude and frequency in voltage fluctuations. To explore these changes, we investigate LFPs acquired from published electrophysiological experiments of anaesthetised rats to extract amplitude distribution, variance and time-correlation statistics. The analysis is broadened by applying detrended fluctuation analysis (DFA) to detect long-range dependencies in the time-series, and we compare DFA results with power spectral density (PSD). We find that the DFA exponent increases with anaesthetic concentration, but is always close to 1.

The penultimate chapter investigates the evidence of criticality in anaesthetic induced phase-transitions using avalanche analysis. Rat LFP data reveal an avalanche power-law exponent close to $\alpha = 1.5$, but this value depends on both the time-bin width chosen to separate the events and the z-score threshold used to detect these events. Power-law behaviour is only evident at lower anaesthetic concentrations; at higher concentrations the avalanche size distribution fails to align with a power-law nature. Criticality behaviour is also indicated in the Waikato mean-field model for anaesthetic-induced phase-transition using avalanches detected from the pseudoLFP time-series, but only at the critical point (CP) and at the secondary phase-transition points of LOC and ROC.

In summary, this thesis unveils evidence of characteristic changes near phase transition points using computer-based mathematical modelling and electrophysiological data analysis. We find that noise-driven fluctuations become larger and persist for longer as the critical point is closely approached, with similar properties being seen not only in

single-neuron and neural population models, but also in biological LFP signals. These results consistent with an increase of susceptibility to noise perturbations near phase transition point. Identification of neuronal avalanches in rat LFP data for low anaesthetic concentrations provides further support for the criticality hypothesis.

Dedication

To my parents Mr. O. G. Chandrasiri and Ms. Yamuna Wadasinghe

To my husband Prasad

To my two sisters Chethana and Ardithya

Thank you for your endless love and support

Acknowledgements

I would like to render my warmest thanks to my supervisor, Associate Professor Alistair Steyn-Ross, who made this work possible. His friendly guidance and expert advice have been invaluable throughout all stages of the work. I would also wish to express my gratitude to Professor Moira Steyn-Ross for valuable suggestions and advice which have contributed greatly to the improvement of the thesis. The thesis has also benefited from comments and suggestions made by Dr Logan Voss and Professor Jamie Sleigh who advise me throughout my experimental data analysis. I take this opportunity to thank them.

Moreover I would like to express my heartful gratitude to all my family members for the support has given to me throughout my journey. Also, my special thanks go to my beloved husband, Prasad Wickramasinghe, for his endless encouragement and understanding.

Finally, I would like to thank Fisher & Paykel Healthcare, for providing the funding which allowed me to undertake this research.

Contents

List of Figures

List of Tables

Acronyms and Abbreviations

1D, 2D	one-dimensional, two-dimensional
AMPA	α-amino-3-hydroxy-5-methyl-4 isoxazole propionic acid (a fast excitatory neurotransmitter)
BVP	Bonhoeffer Van der Pol model
CP	critical point
DFA	detrended fluctuation analysis
ECoG	electrocorticogram (brain activity recorded via electrodes attached directly to the cerebral cortex)
EEG	electroencephalogram (brain activity recorded via scalp electrodes)
EPSP	excitatory postsynaptic potential
FHN	FitzHugh–Nagumo (spiking point neuron model)
GABA	γ-aminobutyric acid (an inhibitory neurotransmitter)
HH	Hodgkin–Huxley (spiking point neuron model)
IEI	inter-event interval
IPSP	inhibitory postsynaptic potential
LFP	local field potential
LOC	loss of consciousness
MAC	minimum anaesthetic concentration (a standard measure of anaesthetic potency)
NMDA	N-methyl-D-aspartate (a slow excitatory neurotransmitter)
OU	Ornstein–Uhlenbeck (random process describing the velocity of a Brownian particle)
PED	paroxysmal epileptiform discharge
PDF	probability density function
PSD	power spectral density
ROC	recovery of consciousness
SOC	self-organised criticality
WMF	Waikato mean-field cortical model

Preface

This thesis reports our investigations of neuronal phase transitions, attempting to identify signs of criticality using computer-based mathematical modelling and by analysing electrophysiological data. Specifically, this thesis analyses the state changes associated with onset of spiking in a single neuron and induction of anaesthesia in neuronal populations. The thesis proceeds as follows:

Chapter 1 provides an overview of basic neurophysiology, describing formation of action potentials and the neurochemical basis of anaesthetic induction. We consider that these neuronal behavioural changes can be treated as phase transitions that can be investigated using a range of mathematical modelling approaches, briefly described in this chapter. We summarise the literature on critical dynamics associated with phase transitions, highlighting the role of scaling laws.

In **Chapter 2**, we analyse the simplest mathematical description of a single spiking neuron, the FitzHugh–Nagumo model, comparing three implementations: Wilson, Keener & Sneyd, and an op-amp equivalent circuit. The steady states and their linear stability are analysed to identify the spiking phase transition boundaries. The subthreshold stochastic dynamics for close approach to spiking threshold is analysed using variance, power spectra and autocorrelation, and we find strong evidence supporting the notion of "critical slowing down".

The anaesthetic-induced phase transition is investigated theoretically and numerically in **Chapter 3**, using the Waikato mean-field cortical model stimulated by low-intensity white-noise. Our analysis unveils critical dynamics using theoretical predictions and numerical simulation validation for close approach to the three transition points: loss of consciousness, recovery of consciousness, and the critical point.

In **Chapter 4**, we apply our criticality analysis to biological measurements: local field potential data recorded from anaesthetised rats. Brain activity under different anaesthetic

concentrations is examined, engaging both traditional and modern analysis methodologies. The behavioural changes linked with the anaesthetic phase transition are disclosed.

Chapter 5 reports neuronal avalanche behaviours with anaesthesia. The existence of avalanche distribution scaling laws illustrates criticality dynamics for experimental local field potential (LFP) data of anaesthetised rats. We find that power-law behaviour is only evident at low anaesthetic concentrations. Then we examine numerical pseudo-LFP data recorded using Waikato mean-field cortical model, and we observe power-law alignment only at the loss of consciousness, recovery of consciousness, and critical transition points.

The thesis is concluded in **Chapter 6** with a brief summary of the major findings, and suggestions for future work.

In **Appendices**, I present the derivation of differential equations for op-amp equivalent circuit for FHN model, LTSpice netlist and schematic diagram, a code for locating FHN steady states, elements of Jacobian matrix for Waikato mean-field model and proof of the DFA and PSD relationship.

Original contributions

The theoretical and numerical analysis and related MATLAB codes, the codes for experimental data analysis and interpretation, and most of the graphic presentations are my own work, except:

- MATLAB codes for numerical simulation, and codes for locating steady-states and eigenvalues of Waikato mean-field cortical model written by D. A. Steyn-Ross
- Local field potential data provided by Jamie Sleigh, Waikato Clinical School (recorded by Anthony G. Hudetz, Medical College of Wisconsin)

Conference presentations

- M.E. Chandrasiri, D.A. Steyn-Ross and M.L. Steyn-Ross. Examining critical fluctuation of the Waikato mean-field cortical model near phase transition, *New Zealand Institute of Physics Conference*, Dunedin, New Zealand, July 2017
- M.E. Chandrasiri, D.A. Steyn-Ross and M.L. Steyn-Ross. Exploring the dynamics of the FitzHugh-Nagumo spiking neuron model, *New Zealand Institute of Physics Conference*, Hamilton, New Zealand, July 2015

Chapter 1

Introduction

1.1 Basic neurophysiology

1.1.1 Neurons and synapses

A healthy human brain contains approximately 10^{11} neurons and $\sim 10^{15}$ synaptic connections for communication between neurons. The three major components of a neuron are the soma or cell body containing the nucleus of the cell; dendrites, tree-like structures, that acquire input from the other neurons; and an axon to transmit signals away from the soma to other neurons. Long rang axons are covered with a myelin sheath which helps to speed up the transmission of electrical signals via the axon. Figure 1.1 shows the structure.

Axon terminals release neurotransmitter chemicals into synapses to complete the transfer of information to other neurons. These synaptic connections transmit signals from the presynaptic neuron to the target neuron (the postsynaptic neuron) via either chemical or electrical synapses. Chemical synapses convert the electrical signal into a neurotransmitter which is released from the presynaptic neuron and attaches to a receptor of the postsynaptic neuron which may excite or inhibit the receiving neuron. Chemical synapses are classified into different types according to the released neurotransmitter which activates specific ion channels. The major inhibitory neurotransmitter is GABA (γ-aminobutyric acid) which activates $\mathrm{GABA_A}$ (fast) and $\mathrm{GABA_B}$ (slow) receptors. The primary excitatory neurotransmitters are NMDA (N-methyl-D-aspartate acid) (slow) and AMPA (α-amino-3-hydroxy-5-methyle-4-isoxazolepropionic acid) (fast). Figure 1.2 illustrates the chemical basis of synaptic communication.

In electrical synapses, the signal is communicated directly via so-called gap junctions, which allow transfer of electric currents, thus inducing voltage changes in the postsynaptic

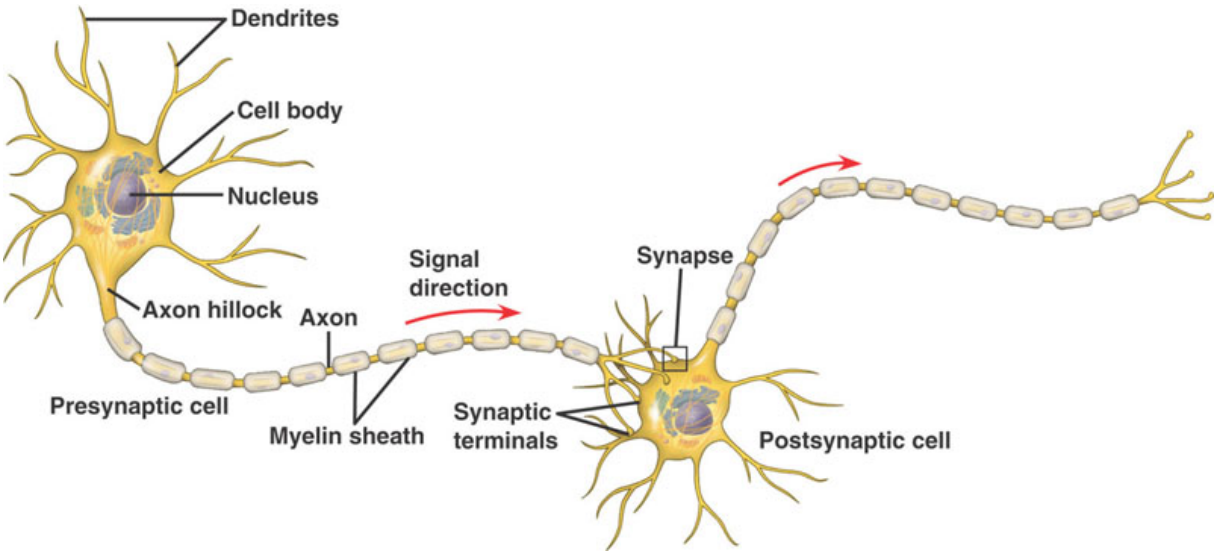

Figure 1.1: Basic structure of a neuron [30]

neuron.

A neuron collects input other neurons via synapses located throughout its dendrites. These synapses produce transmembrane electric currents, which propagate to the soma and induce postsynaptic potentials. If this potential exceeds a particular threshold, the neuron is likely to generate one or more action potentials or "spikes" which will be transmitted via its axon to downstream neurons.

1.1.2 Action potentials

The cell body of the neuron is covered by a membrane plasma, which acts as a thin boundary between the extracellular (outside of the neuron) and intracellular (inside of the neuron) fluids. The membrane plasma contains ion channels that allow electrically charged ions such as sodium (Na^+), potassium (K^+), chloride (Cl^-), and calcium (Ca^{2+}) ions to diffuse across the membrane. Some are voltage-gated channels, controlled by the voltage difference across the membrane, and some are chemically-gated channels which open or close as a result of interactions with chemicals in the extracellular fluid. The differential ion flows between channels produce a voltage difference across the membrane called the membrane potential. When the cell is at its resting state, the membrane voltage maintains a negative potential relative to the extracellular fluid. The is called resting membrane potential, and falls within the range of -40 to -90 mV.

Action potentials are electrical impulses that occur due to a sudden change of membrane potential caused by the influx of Na^+ ions through the membrane. This influx is

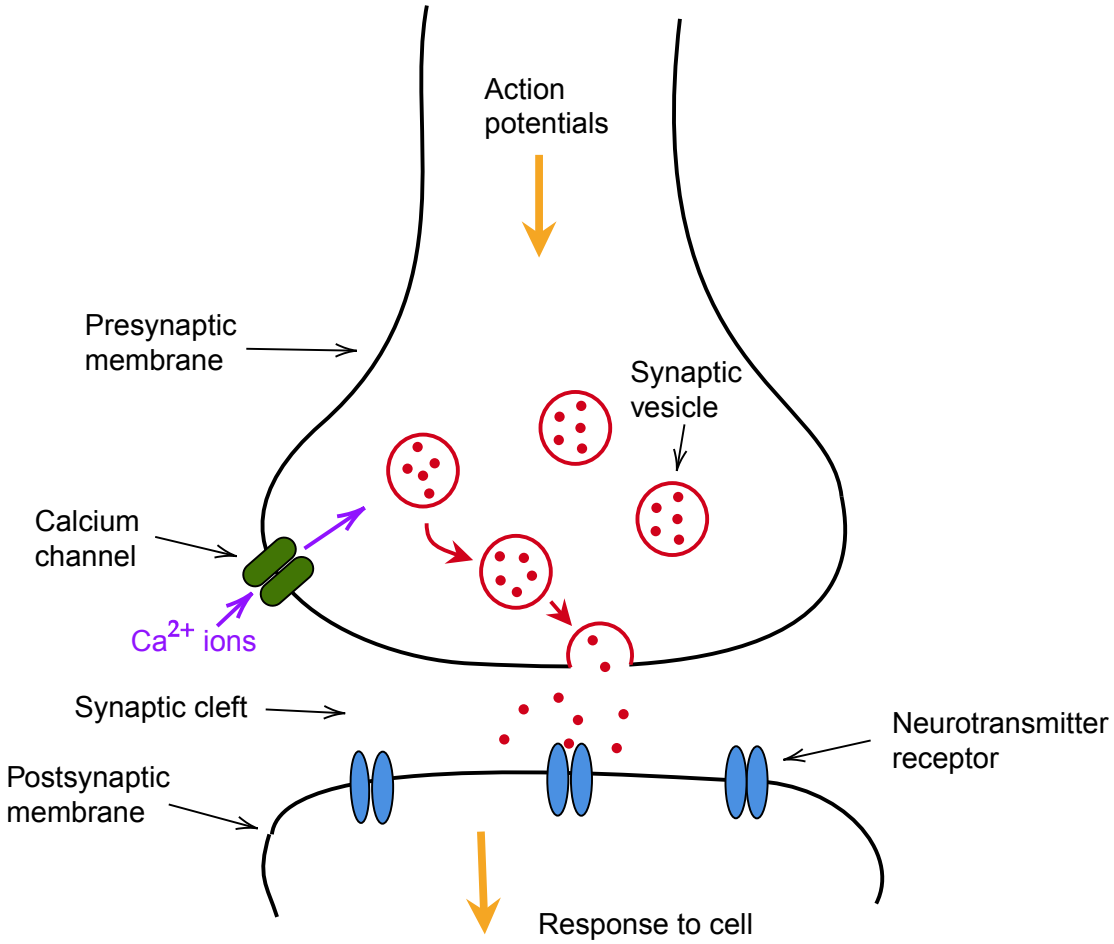

Figure 1.2: Neuronal communication via chemical synapses [51]

triggered by an external stimulus that allows an initial flow of ions into the cell resulting in *depolarization*. If the cell body becomes sufficiently depolarized, so that the membrane voltage reaches threshold, the voltage-sensitive Na^+ channels will open, allowing an influx of Na^+ ions, resulting in further depolarisation and a sudden jump of membrane potential to about +30 mV, generating an action potential. The membrane voltage then starts *repolarizing* as voltage-gated K^+ channels open and efflux of K^+ ions commences. At the same time Na^+ channels close and stop the influx of Na^+ ions. Eventually, the K^+ channels close, bringing the cell back to its resting state. Figure 1.3 shows the action potential process.

1.1.3 General anaesthesia

General anaesthetic drugs are an essential component of modern medicine due to their ability to block the unpleasant stimulus from surgery. General anaesthesia is a controlled

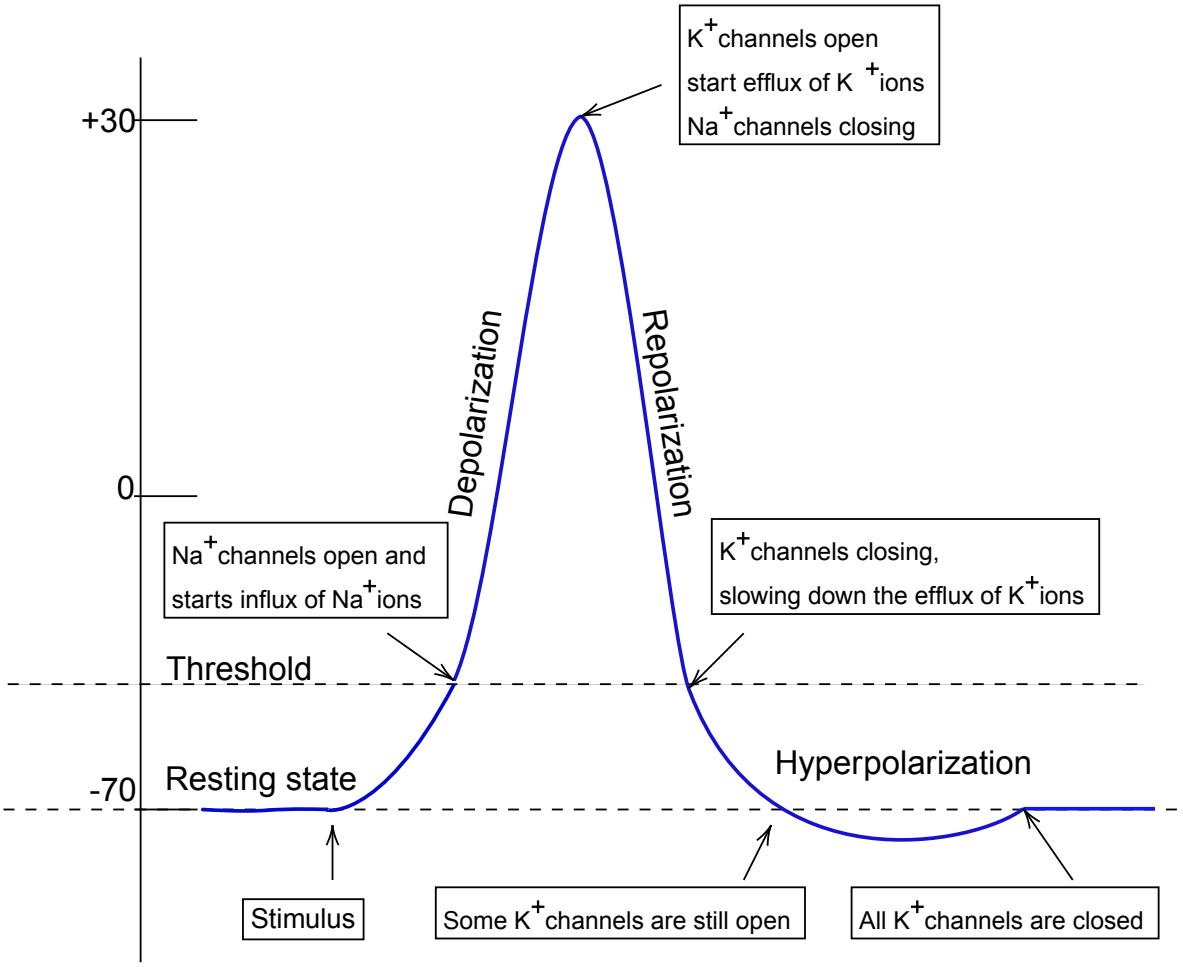

Figure 1.3: Formation of action potential [42]

and reversible state of consciousness, which can be classified into five stages [12, 13]:

- Unconsciousness: loss of sensitivity to stimulus
- Analgesia: loss of sensitivity to pain
- Akinesia: loss of movement
- Amnesia: lack of memory
- Physiological stability: maintenance of regular breathing, heart rate, blood pressure and other physiological functions

There has been much research activity attempting to identify the mechanisms of general anaesthesia. Anaesthetic drugs act to decrease cortical activity by acting on neurotransmitter-gated ion channels by either decreasing excitation, or increasing inhibition, or both [24, 97]. GABAergic drugs, such as propofol and sevoflurane, act by increasing the activity of inhibitory $GABA_A$ receptors (Fig. 1.4), while non-GABAergic

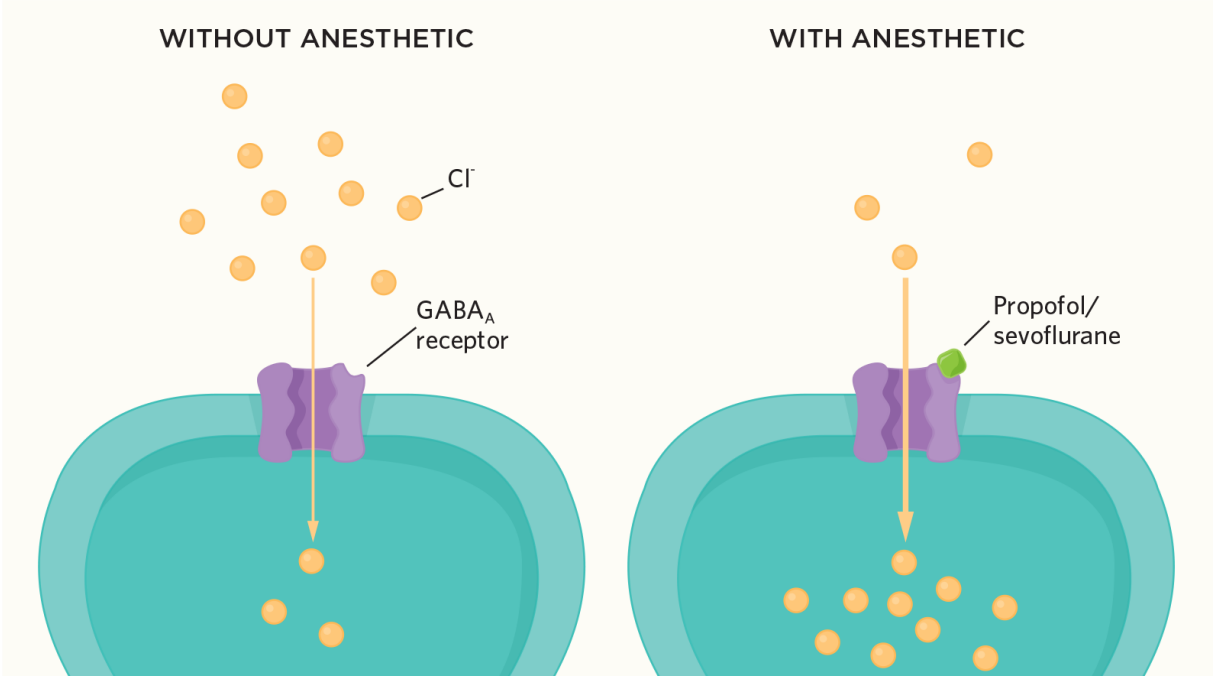

Figure 1.4: Propofol and sevoflurane effect on $GABA_A$ receptors. Propofol and sevoflurane promote activity in the $GABA_A$ receptors resulting in neuronal inhibition [12]

drugs such as ketamine block excitatory NMDA receptors (Fig. 1.5). The $GABA_A$ receptor permits Cl^- ions to flow into the neuron, resulting in a decrease of intracellular voltage and consequent reduction in the probability of neuronal firing [28, 38]. On the other hand, ketamine blocks the NMDA receptor, so decreases excitability. It does this by choking off inflows of Na^+ and Ca^2+, and outflow of K^+ (Fig. 1.5) [38].

The net inhibitory effect of anaesthetic drugs is to alter the behaviour of the brain, producing synchronised neuronal activities that can be detected in electroencephalogram (EEG) recordings [78]. GABAergic anaesthetic drugs change the frequency of cortical oscillations: at lower anaesthetic concentration, oscillations are dominant in the beta frequency range (1–30 Hz); as the concentration increases the oscillations slow down to theta (4–8 Hz) and delta (1–4 Hz) bands [97]. At higher concentrations, anaesthetic drugs produce high-amplitude episodic sharp wave patterns (usually lasting < 70 ms) among background normal EEG patterns, which is called burst–suppressions [82, 97]. However, these spectral alterations differ from one agent to another.

Analysis by Kuizenga *et al.* [49] demonstrates the "biphasic" nature of propofol, being excitatory at lower concentration and inhibitory at higher concentration with two "biphasic" peaks per induction–emergence cycle between loss of consciousness (LOC) and

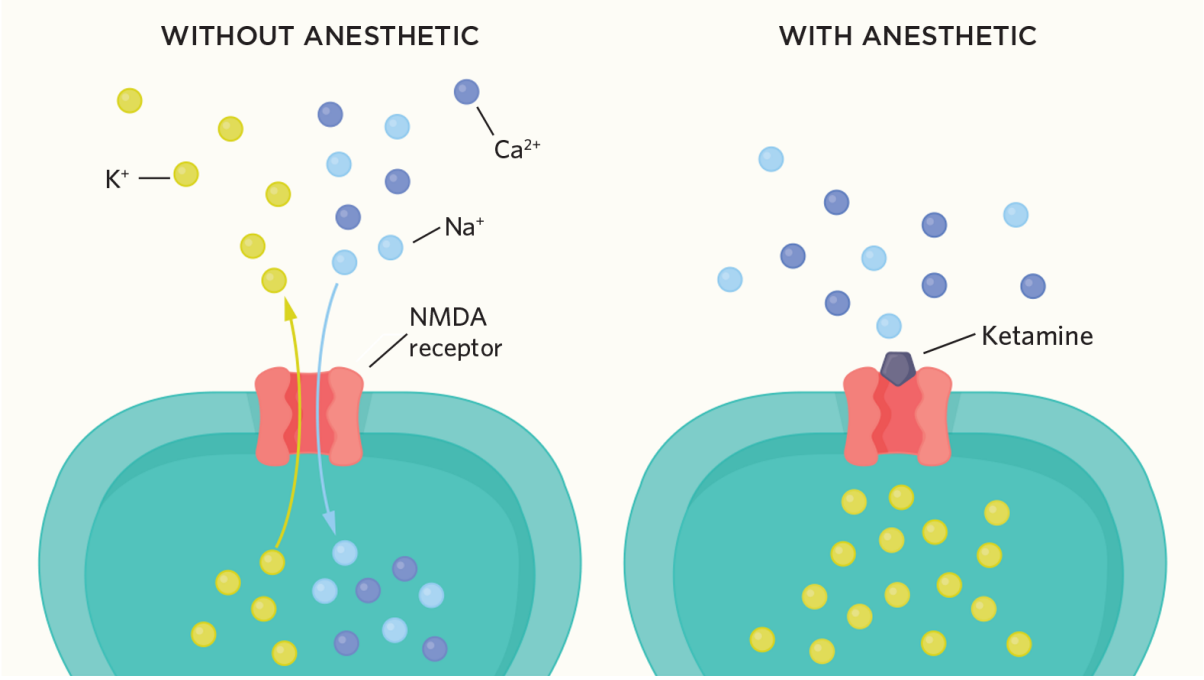

Figure 1.5: Effect of ketamine on NMDA receptors. Ketamine blocks the NMDA receptor which decreases excitation [12]

recovery of consciousness (ROC). There is a hysteretic separation between these two transitions as ROC occurs at a lower concentration than LOC, meaning subjects awaken at lower anaesthetic concentration than that required to induce unconsciousness.

1.2 Neuronal modelling

Neuronal models describe the biological neuron using a mathematical formalism that may contain biophysical and geometrical characteristics. These models attempt to explain the quantifiable and measurable behaviours of both single neurons and neuronal networks, and are typically validated by comparing experimental findings with model predictions. Their mathematical structure consists of sets of differential equations that can be analysed analytically and via numerical integration methods. Such models have been used to describe the behaviours of the nervous system, predicting, for example, changes in state of vigilance due to seizure, anaesthesia, and sleep.

1.2.1 Models of single spiking neuron

A single spiking neuron model is a mathematical description of a single cell that focuses on the mechanism by which action potentials are generated.

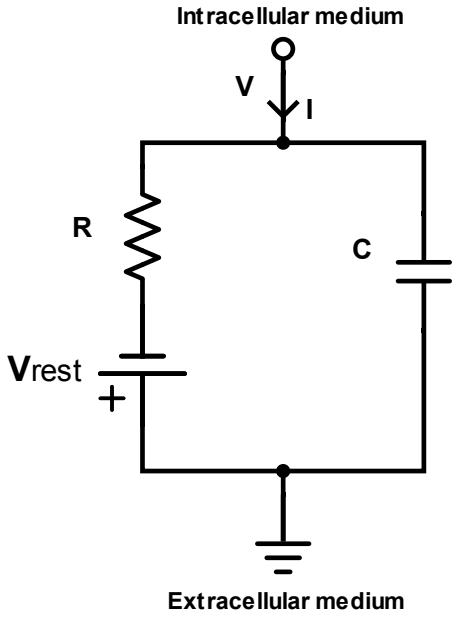

Figure 1.6: Equivalent circuit of an integrate-and-fire neuron model. The capacitor represents the charged membrane, V is the membrane voltage, I is the stimulus current and V_{rest} is the resting voltage

Introduced in 1907 by Lapicque, the integrate-and-fire model is one of the earliest and simplest descriptions of a neuron, explaining the spiking behaviour using a linear differential equation [1]. The basic electrical circuit equivalent to an integrate-and-fire model is shown in Figure 1.6: a capacitor C in parallel with a resistor R driven by a current $I(t)$.

The most biologically consistent model was introduced by Hodgkin and Huxley on the basis of a series of painstaking laboratory measurements. This is described next.

1.2.2 Hodgkin–Huxley equations

In the late 1940s and early 1950s, Alan Hodgkin and Andrew Huxley developed the core mathematical framework for modern biophysically-based neuron modelling based on a series of electrophysiological experiments on the giant squid axon [37]. This bio-realistic but complex conductance-based model is formed with four state variables which describe membrane potential, Na^+ channel activation and subsequent inactivation, paired with K^+ channel activation [37]. Their model is expressed as four coupled nonlinear differential equations,

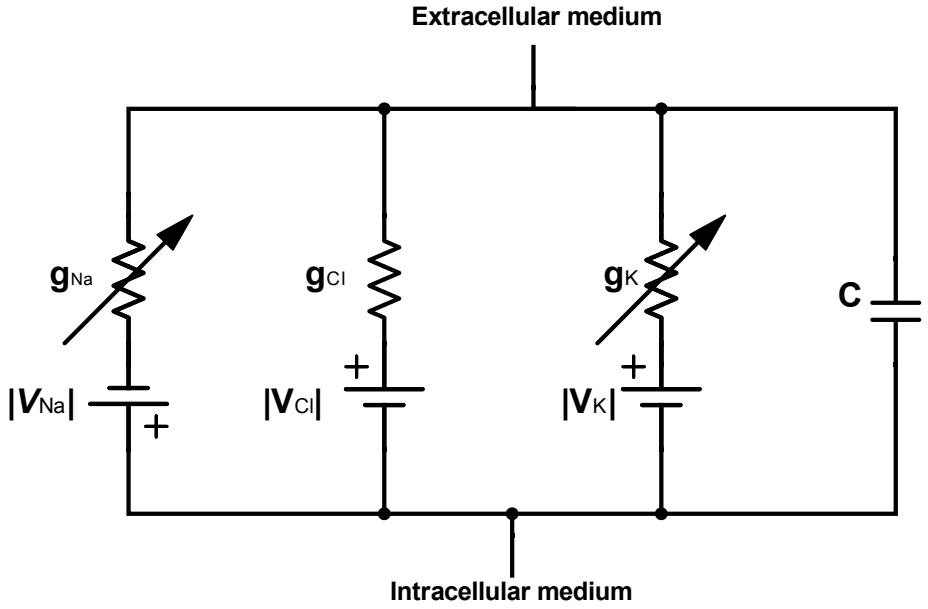

Figure 1.7: Equivalent circuit of Hodgkin–Huxley neuron model. Capacitor C represents the membrane, g_{Na}, g_{K} are nonlinear conductances of voltage-gated channels, and g_{Cl} is the linear conductance of the leakage channel. $|V_{\mathrm{Na}}|$, $|V_{\mathrm{K}}|$, $|V_{\mathrm{Cl}}|$ are resting voltages [37]

$$C\frac{dV}{dt} = -g_{\mathrm{Na}}m^3h(V - E_{\mathrm{Na}}) - g_{\mathrm{K}}n^4(V - E_{\mathrm{K}}) - g_{\mathrm{leak}}(V - E_{\mathrm{leak}}) + I_{\mathrm{input}} \tag{1.1a}$$

$$\frac{dm}{dt} = \frac{1}{\tau_m(V)}(-m + M(V)) \tag{1.1b}$$

$$\frac{dh}{dt} = \frac{1}{\tau_h(V)}(-h + H(V)) \tag{1.1c}$$

$$\frac{dn}{dt} = \frac{1}{\tau_n(V)}(-n + N(V)) \tag{1.1d}$$

where, as shown in Fig. 1.7, V is the voltage across membrane, $g_{\mathrm{Na}}, g_{\mathrm{K}}, g_{\mathrm{leak}}$ are electrical conductances, and $E_{\mathrm{Na}}, E_{\mathrm{K}}, E_{\mathrm{leak}}$ are equilibrium potentials of sodium, potassium and leakage channels respectively.

FitzHugh–Nagumo model (FHN)

Although the Hodgkin–Huxley (HH) equations provide biophysically realistic descriptions of neuron spiking dynamics, they are hard to analyse due to their complexity. This motivated FitzHugh [26] and Nagumo [61] to introduce a highly simplified model that contains only the essential nonlinear mathematical elements required for spike generation. Their model describes neuron dynamics in terms of membrane voltage V and a recovery

variable R [102],

$$\frac{dV}{dt} = 10(V - \frac{V^3}{3} - R + I_{\text{dc}}) \tag{1.2a}$$

$$\frac{dR}{dt} = V - 0.8R + 1.2 \tag{1.2b}$$

The FHN model will be examined in detail in Chapter 2.

Wilson spiking-neuron model

While the FHN equations capture the qualitative characteristics of neuron spiking dynamics, they discard most of the physiological detail. H. R. Wilson developed an alternate simplified description of the HH equations that retains reversal potentials and which is capable of simulating action potential formation in both squid axon and cortical neuron [102]. Like FHN, the Wilson neuron is described in terms of voltage and recovery variables [102],

$$C\frac{dV}{dt} = -g_{\text{Na}}(V - E_{\text{Na}}) - g_{\text{K}}R(V - E_{\text{K}}) + I_{\text{dc}} \tag{1.3a}$$

$$\tau_R\frac{dR}{dt} = -R + G(V) \tag{1.3b}$$

where $g_{\text{Na}}, g_{\text{K}}$ are the respective ion-channel conductances, $E_{\text{Na}}, E_{\text{K}}$ are the Na^+, K^+ reversal potentials, $G(V)$ is the steady state for recovery, C is membrane capacitance, and τ_R is time-constant for recovery. (The subthreshold properties of the Wilson neuron will be revisited in Section 1.3.1 of this chapter.)

1.2.3 Mean-field models

Mean-field models describe *populations* of inhibitory and excitatory neurons. The foundation mean-field model is that due to Wilson and Cowan [20]. More recently, a population model was developed at Waikato University to describe anaesthesia and cycles of natural sleep [89] [90].

Wilson–Cowan model

First proposed in 1972, the Wilson–Cowan model describes the collective behaviour of the interacting excitatory E and inhibitory I cortical neural populations. Rather than

following details of spike formation, the equations relate to the average spiking frequencies $E(t)$, $I(t)$ in the two populations [103],

$$\tau_E \frac{\partial E(x,t)}{\partial t} = -E(x,t) + S_E[w_{EE}(x) \otimes E(x,t) - w_{IE}(x) \otimes I(x,t) + P]$$
$$\tau_I \frac{\partial I(x,t)}{\partial t} = -I(x,t) + S_I[w_{EI}(x) \otimes E(x,t) - w_{II}(x) \otimes I(x,t) + Q]$$

where $E(x,t)$, $I(x,t)$ = mean firing rate of excitatory and inhibitory neurons at position x

τ_E, τ_I = time-constant of each population

w_{jk} = density of the synaptic coupling between and within populations

$S_{E,I}$ = sigmoidal response function mapping voltage to firing rate

P, Q = external voltage inputs

$\otimes \Rightarrow$ spatial convolution between synaptic coupling density and firing rate

Four types of interconnections are included: excitatory–excitatory, excitatory–inhibitory, inhibitory–excitatory and inhibitory–inhibitory.

The Wilson–Cowan model has provided the foundation for most modern mean-field neural populations. For example, the treatment of neural tissue as a 1D or 2D spatial continuum (rather than a discrete collection of spiking neurons), and the use of a sigmoidal mapping from voltage to firing rate, are both elements that are found in the Waikato mean-field model.

Waikato mean-field cortical model

The Waikato mean-field (WMF) cortical model represents the cortex as a two dimensional continuum of excitatory and inhibitory neural populations. These neurons communicate locally through electrical synapses (resistive gap junctions) and neurotransmitter-mediated chemical synapses as well as distant connections via long-range myelinated axons. The equations are defined for excitatory and inhibitory soma potentials, V_e and V_i, that have been spatially averaged across the $\sim$1 mm^2 area of a cortical macrocolumn [90],

$$\tau_b \frac{\partial V_b}{\partial t} = V_b^{\text{rest}} - V_b + \Delta V_b^{\text{syn}} + D_{bb} \nabla^2 V_b$$

where τ_b = soma time constants for the neuron population b ($b = e$ or i)

V_b^{rest} = resting voltage

ΔV_b^{syn} = voltage perturbation from chemical synapses

$D_{bb}\nabla^2 V_b$ = voltage perturbation due to gap-junction current diffusing between adjacent neurons

The WMF model and its phase transition characteristics will be discussed in considerable detail in Chapter 3.

1.3 Phase transition

In dynamical systems, the change of state of matter (e.g., solid $\rightleftarrows$ liquid, liquid $\rightleftarrows$ gas) is called a phase transition, and is categorised as either first-order or second-order. First-order transitions exhibit an abrupt change of state when a control variable (e.g., temperature) is varied smoothly across the transition point; further, the current state depends on the history of the control variable, a phenomena known as *hysteresis*. In contrast, second-order transitions do not show hysteresis, and the state changes are smooth, so are described as continuous phase transitions [35, 86].

Mathematicians refer to the qualitative change in system dynamics produced by varying a control parameter as a *bifurcation*. A bifurcation occurs when a small smooth change made to the stability properties of a steady point of a system causes a sudden qualitative or topological change in its behaviour.

The steady state analysis and linear stability analysis of the Jacobian matrix of partial derivatives evaluated at equilibrium provides insights as to the nature the bifurcation, allowing classification into different bifurcation types [42, 50, 98]:

1. Saddle–node bifurcation: occurs when two steady states collide and annihilate, and the dominant eigenvalue goes to zero; the system then evolves to some other state
2. Andronov–Hopf bifurcation occurs when the steady state owns a pair of complex conjugate eigenvalues with non-zero purely imaginary eigenvalues. A supercritical Hopf bifurcation leads to the appearance of small amplitude periodic oscillations about the steady state; in contrast a subcritical or “hard” Hopf bifurcation evolves directly to full-amplitude limit cycles

3. Turing bifurcation: occurs with non-zero wave number which describes the spatial frequency. In a Turing bifurcation, the system is temporally stable but spatially unstable
4. Wave instability: spatial inhomogeneity emerges at a nonzero wavenumber with nonzero frequency, resulting in wave propagation.

The equilibrium state located precisely at the transition between two qualitatively different phases is called the *critical state*, and fluctuations about this state exhibit statistical properties that are described as critical. In this thesis, we examine signs of criticality associated with phase transitions in single spiking neurons and in neural populations, looking for insights about changes of dynamical behaviour on close approach to the critical state.

Critical dynamics in single spiking neuron is discussed in Chapter 2. The anaesthetic-induced phase transition for neuronal populations will be investigated using the Waikato mean-field cortical model and local field potential data recorded from anaesthetised rats in Chapters 3, 4 and 5.

1.3.1 Phase transition in a single spiking neuron

The transition from resting state to spiking in a single spiking neuron can be considered to be a change of phase. The type of bifurcation determines the excitable properties of the neuron, which is influenced by the neuron's electrophysiology. Hodgkin [36] and Izhikevich [41] emphasised the clear difference in the dynamical behaviours between the two types, and introduced the terms *integrator* for type-I and *resonator* for type-II.

For an individual spiking neuron, two bifurcation types have been identified: saddle–node and Hopf. These distinct bifurcation behaviours at spiking threshold form the basis of the type-I and type-II classifications. Threshold dynamics of type-II neurons show an Andronov–Hopf bifurcation with the emergence of finite-frequency oscillations at spiking transition. In contrast, type-I neurons exhibit a saddle–node bifurcation with very sparse ("zero-frequency") spiking at onset [41, 87, 95].

With minor changes to parameter settings, Wilson's spiking neuron model (Eqs. (1.3)) [102] is capable of generating both type-I and type-II spiking behaviour. Figure 1.8 shows subthreshold stochastic simulations for both type-I (panel (b)) and type-II (panel (a)) Wilson spiking neuron models. The squid giant axon model of Fig. 1.8(a) shows an increasing tendency to oscillate at a characteristic frequency with larger amplitude

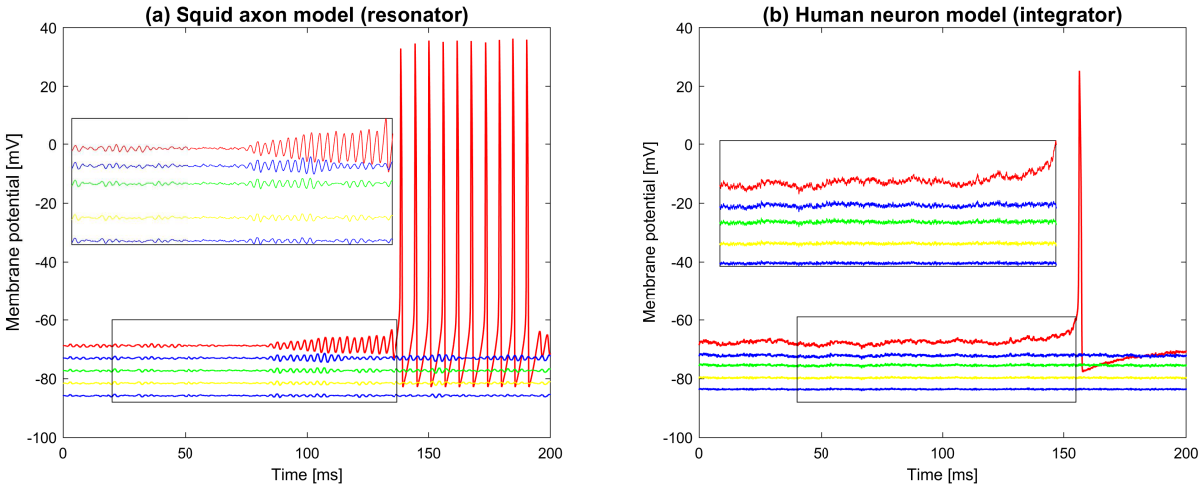

Figure 1.8: Stochastic simulations for Wilson spiking neuron models (a) squid-axon, type-II and (b) human neuron, type-I. The zoom-box illustrates subthreshold dynamics. Simulations are run for five different I_{DC} stimulation levels: (a) $I_{\mathrm{DC}} = 0,\ 2,\ 4,\ 6,\ 7.7\ \mu\mathrm{A/cm}^2$; (b) $I_{\mathrm{DC}} = -100, -40, 0, 16, 21.4752\ \mu\mathrm{A/cm}^2$. Figure modelled on Fig. 1 of [87]

and less damping on close approach to threshold current. When the random stimulus causes the membrane voltage to cross threshold, the neuron rapidly transitions from small amplitude linear oscillations to huge amplitude nonlinear spike trains. In contrast, the human neuron (type-I) shows noise-induced voltage fluctuations that become ever larger and slower, eventually evolving into an isolated single spike rather than a spike train.

The difference in subtheshold behaviours was investigated by Rinzel and Ermentrout using linear stability theory [74]. As the stimulus current increases towards threshold, the real part of the dominant eigenvalue approaches zero from below. For type-I neurons, the eigenvalues are real with a zero imaginary part, indicating zero frequency; for type-II neurons the eigenvalues are complex with the imaginary part of the eigenvalue implying a non-zero frequency pattern.

Figure 1.9 illustrates the steady states and eigenvalues of Wilson spiking neuron model for the squid axon (type-II) and human neuron (type-I) models examined in Fig. 1.8. These are two-variable systems, therefore the Jacobian matrix generates two eigenvalues. The eigenvalue which has the largest real part is called the dominant eigenvalue. The eigenvalues of squid axon (left panels) form a complex-conjugate pair: the real part gives the damping with $\alpha = 0$ marking the critical point: the non-zero imaginary part sets the oscillation frequency, $f_0 = \omega/2\pi$. For the human neuron model (right panels) the approach to the saddle–node turning point (panel (b)) is associated with the dominant eigenvalue

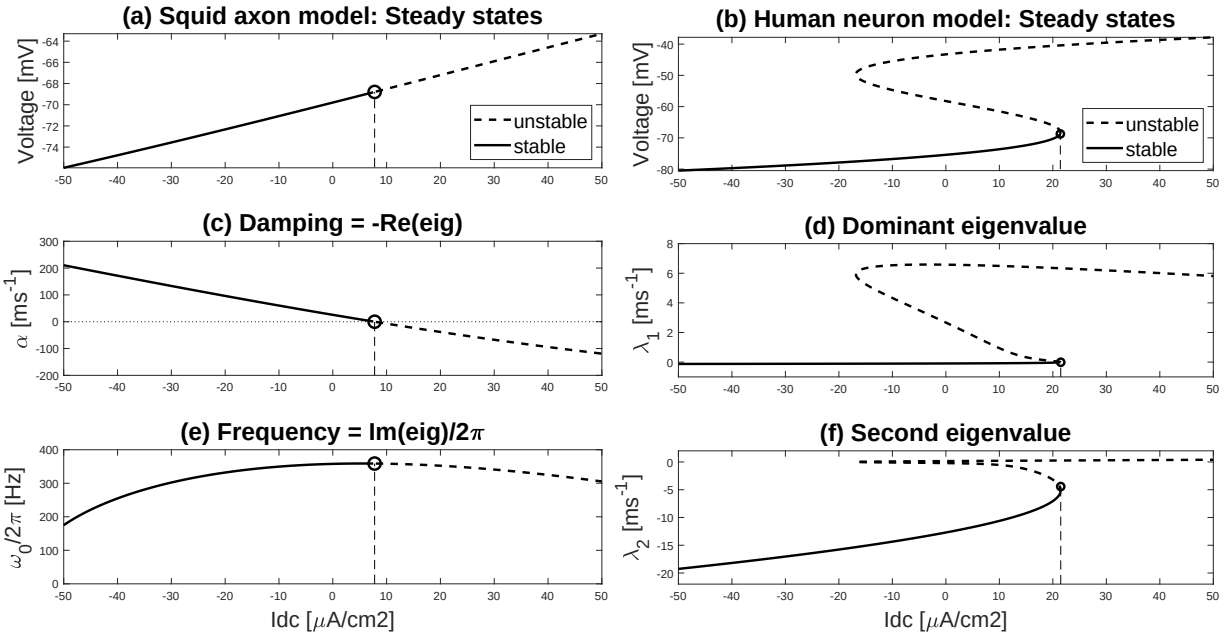

Figure 1.9: Steady state and eigenvalues for Wilson type-II (left panels) and type-I (right panels) spiking neuron models. Figures are modelled from [87]

approaching zero from below (panel (d)), thus fluctuations will become increasingly long-lived, eventually causing the neuron to make a jump transition towards the unstable upper branch at "zero" frequency.

1.4 Critical point

In a continuous phase transition, the critical point is defined as that coordinate in phase space at which the two phases are indistinguishable. In thermodynamics, the critical state marks the end point of the pressure–temperature curve, where vapour and liquid coexist (see Figure 1.10).

At the (P_c, v_c, T_c) critical point, the slope of the critical isotherm (constant temperature line) on the pressure–volume (P-v) diagram goes to zero [46, 56],

$$\left(\frac{\partial P}{\partial v}\right)_T\Big|_{(P_c,v_c,T_c)} = 0$$

consequently the inverse ratio diverges,

$$\left(\frac{\partial v}{\partial P}\right)_T\Big|_{(P_c,v_c,T_c)} \to \infty$$

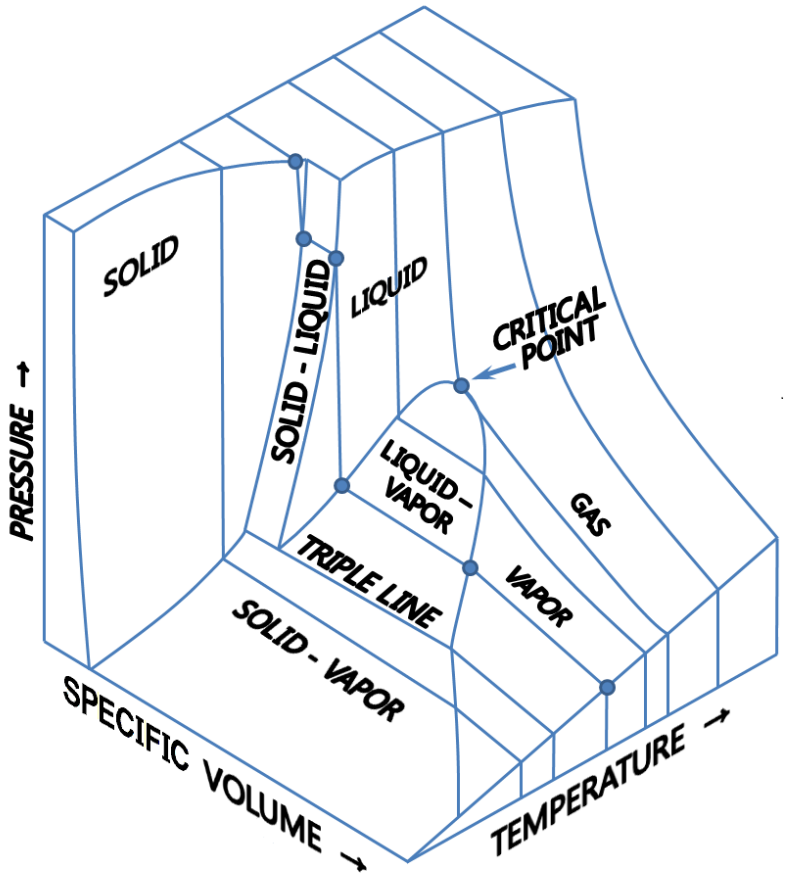

Figure 1.10: Thermodynamics P-v-T phase diagram [en.wikipedia.org/wiki/Phase_diagram]

meaning that the specific volume (inverse density) becomes extremely sensitive to small fluctuations of pressure. Molecular fluctuations grow sufficiently to cause scattering of visible light so the coexisting liquid–vapour mixture appears cloudy, a phenomenon known as "critical opalescence".

We can identify an analogous "opalescent point" for the anaesthetic-induced phase transition in the Waikato mean-field model (see Fig. 3.2). At the critical point, three firing rate equilibrium states merge to a single value, and the two phases, conscious (high-firing) and unconscious (low-firing), become indistinguishable.

The general properties of critical point fluctuations will be studied further in the next section.

1.5 Previous investigations of critical dynamics

Critical phenomena are of particular interest in many complex systems as a small change in system inputs can dramatically affect system behaviour. In some cases the critical transition is biologically useful, for example, allowing a neuron to rapidly switch from quiescence to spiking to enable transmission of information via action potentials. On the other hand, some critical transitions can be undesirable and pathological, as happens in an epileptic seizure [58, 87].

Criticality is a specific type of behaviour, exhibited by a system when it approaches a transition marking the boundary between two qualitatively different types of behaviour. To locate the critical state of a system, the relevant control parameter needs to be tuned precisely to the appropriate value.

Branching parameter

One approach to identifying criticality in brain tissue is to make use of the theory of branching processes, in which branching parameter σ can describe activity propagation in cortical culture [33]. The branching parameter is defined as the average number of descendants produced by one ancestor. In the subcritical state $\sigma < 1$, and $\sigma > 1$ in the supercritical state, and it is assumed the critical value for the branching parameter is $\sigma = 1$ [7, 35].

Critical slowing down

The system response to external stimuli can provide evidence of criticality. For example the system takes progressively longer to recover from small perturbations as it approaches bifurcation; this phenomenon is called *critical slowing down*. Signs of critical slowing can be elicited from the system by extracting the recovery rate after small perturbation, and by detecting increased fluctuation amplitudes [58, 62, 87]. To quantify critical slowing, we can monitor changes in the variance, autocorrelation and spectral content of the fluctuations.

Critical slowing down in a noise-stimulated spiking neuron has been demonstrated by Steyn-Ross *et al.* (2006) [87] for Wilson type-I and type-II neuron models (see Section 1.3.1), and by Bukoski *et al.* (2015) [14] for the Hodgkin–Huxley model. Meisal *et*

al. (2015) [58] introduced scaling-laws for critical slowing down phenomena, deriving exponents for saddle–node and Hopf–bifurcation transitions, which confirmed the 2006 results reported by Steyn-Ross *et al.*

Criticality investigations have been extended to mean-field cortical models. Negahbani *et al.* (2015) [62] analysed one-dimensional stochastic Wilson–Cowan model for saddle–node, Hopf and Turing–Hopf instabilities. Cortical dynamics of Waikato mean-field model in two-dimensions during natural sleep has been examined by Wilson *et al.* (2005) [104].

Power laws

Many recent studies have sought to identify power-law behaviour as potential evidence of criticality in experimental and simulation data. If the distribution $p(x)$ of a parameter x follows a straight line on a log-log scale, then it follows that,

$$p(x) \sim 1/x^{\alpha}$$

where α is the power-law exponent or scaling parameter. Realistically this relationship cannot hold for arbitrarily small x-values, therefore a lower bound must be imposed [19, 96].

The standard way of calculating the power-law exponent α is to plot the frequency distribution on a log-log scale; however this method is not particularly robust since the slope is dependent on the choice of the binning process used to construct the frequency distribution [19].

The slowing down phenomena can be related to the $1/f$ spectral noise characteristic of critical systems. If a low-intensity noise induces system fluctuations, then at the critical point, the power spectrum of fluctuations follows the power-law $P \sim 1/f^{\alpha}$ where α is a constant. However, the converse is not necessarily true: detection of power-law noise is not unique to critical systems since it also observed in many non-critical systems [17, 35].

The power-law distribution is described as being scale-free since the form of the distribution is, in principle, independent of the scale. This behaviour is characteristic of critical systems with observations exhibiting the same patterns over different spatial or temporal scales [35, 63].

Note that all of these criticality concepts are expected to be applicable to both individual neurons and neuronal systems.

Avalanches

Scale-free properties can also be identified in so-called *self-organised* critical systems. The mechanism by which a system continuously tunes itself to the critical state is called "self-organised criticality" (SOC). This concept was first introduced by Bak *et al.* in 1987 [4, 5] using the sandpile model. Self-organised critical models show avalanche behaviour: cascades of activity that spread through the network, producing avalanche statistics that are predicted to follow a scale-free power-law distribution at the critical state.

Power-law avalanche distributions have been observed for neuronal networks [6, 32, 68–70, 81]. There is a ongoing debate as to whether neuronal systems can be considered as being self-organised since the cortex is exposed to a continuous wash of external stimuli and does not lie exactly at the critical point [10, 35].

1.6 Identifying critical behaviour in single neurons and in neuronal populations

If the transition between quiescent rest and active spiking in a neuron can be regarded as a phase transition, then we should be able to observe characteristic precursor signals such as critical slowing of responsiveness and increased sensitivity to perturbations as the threshold point is approached. Similar critical behaviour should be evident in the case of populations of neurons as they approach the induction and recovery tipping points during an anaesthetic cycle. Emergence of power laws would provide evidence of increasingly correlated fluctuations linking the neurons within the population.

In this thesis we will be looking for evidence for criticality in three distinct neuron systems:

- the FitzHugh-Nagumo single-neuron model
- the Waikato mean-field population-based cortical model, and
- Local field potential (LFP) data for rats undergoing enflurane anaesthesia

Our general hypothesis is all three neural systems should exhibit critical slowing-down characteristics on approach to the transition point, with scale-free power-law behaviour at criticality.

Although the nonlinear "spiking" dynamics of the FHN neuron has been analysed in previous studies [18, 42, 43, 102], there has been no investigation of its subthreshold

stochastic dynamics. We will examine both the onset of spiking, and the death of spiking, and will show that these events represent distinct Hopf bifurcations with critically prolonged subthreshold oscillations emerging at the two critical points, and with emergence of an associated power-law for fluctuation variance, var $\sim 1/\epsilon$, where ϵ is the distance to the relevant bifurcation point.

Although the Waikato mean-field model has been in continuous development since 1999, examining the dynamics of a variety of phase transitions, there has been no exploration of possible power-law behaviour of noise-induced fluctuations, nor any examination of cooperative avalanche behaviour. We will investigate three distinct anaesthetic induced transitions:

- Loss of consciousness (LOC)
- Recovery of consciousness (ROC)
- Critical point (CP).

Voltage fluctuations will be analysed on close approach to these transition points, looking for evidence of scaling-laws. Moreover, we will quantify the avalanche statistics for each transition point, extracting power-law exponents for the size distributions.

Rat LFP changes under anaesthesia have been investigated in previous studies, but have not been analysed for criticality. We will quantify LFP changes during anaesthetic transition, analysing amplitude distribution, fluctuation variance and time-correlation, and determine scaling-laws for power spectral density and long-range correlation using detrended fluctuation analysis (DFA). Furthermore, criticality investigations will be extended to avalanche analysis.

In summary, we are aiming to unveil evidence of criticality in different types of neural phase transitions by quantifying behavioural changes and mapping these to scaling-laws. We seek to identify signs of criticality that are common to model of a single spiking neuron, a mean-field neuronal population model, and electrophysiological measurements in rat cortex.

The thesis is structured as follows: In Chapter 2 we will analyse the FitzHugh–Nagumo mathematical model looking for evidence of critical prolongation characteristics. We extend our analysis to the spatiotemporal domain using the Waikato mean-field cortical model for anaesthesia in Chapter 3.

Anaesthetic-induced changes in local field potential in anaesthetised rats will be examined in Chapter 4. Scale invariance properties at criticality are studied using rat local field-potential data, and also in the Waikato cortical model. The power-law studies of neuronal avalanches (in Chapter 5), power-spectrum and detrended fluctuation analysis (DFA) will also be applied for these data (Chapter 4).

Chapter 2

Nonlinear oscillations and subthreshold fluctuations in a spiking neuron

Dynamical systems typically exhibit a rapid transition between different states near a threshold or tipping point. Critical phenomena are of particular interest as a small change in system inputs can dramatically affect system behaviour [62, 79], and this has been observed in many complex systems with examples reported in biology, ecology, climate and economics [22, 99]. In some cases this transition is biologically useful, for example, allowing a neuron to rapidly switch from quiescence to spiking to enable transmission of information via the firing of action potentials. On the other hand, some critical transitions can be undesirable and pathological, as happens in the onset of epileptic seizure.

One of the early warning signs of proximity to a tipping point is the increased susceptibility or sensitivity to both external and internal perturbations, with the system taking progressively longer to recover from small disturbances, as it approaches the bifurcation point. This phenomenon is known as critical slowing down [58, 62, 87].

Changes in the characteristics of noise-induced fluctuation near the tipping-point transition from quiescence to spiking regimes have analysed in spiking neuron models. Steyn-Ross *et al.* [87] reported growth of fluctuations and time prolongation using variance, autocorrelation and spectral power in simplified point neuron models of the resonator and integrator type. Bukoski *et al.* [14] extended this work to the full Hodgkin–Huxley neuron near spiking onset, using fluctuation amplitudes, temporal autocorrelation and power spectral densities demonstrating critically slowed voltage fluctuations and prolonged correlation decay times.

In this chapter, we focus on the simplest mathematical description of a spiking neuron,

the FitzHugh–Nagumo (FHN) model. FitzHugh introduced this model in 1961 as a simplification of the four-variable Hodgkin–Huxley model, and referred to it as the Bonhoeffer Van der Pol (BVP) model [26]. Nagumo constructed an electronic circuit equivalent to this model [61]. This two-variable FHN model approximates the electrochemical ion flows of sodium (activation) and potassium (inactivation and recovery) to give a qualitative description for action potential generation.

After investigating the nonlinear limit-cycle oscillations generated by three variants of the FHN spiking neuron, we investigate their stochastic behaviour as each approaches its bifurcation point. We perturb the model neuron with low-intensity white noise and analyse the properties of the resulting voltage fluctuations [29]. Proceeding via an eigenvalue stability analysis of the subthreshold steady state, we show that the linear predictions for noise-induced fluctuation variance, autocorrelation and spectral power provide accurate predictions for stochastic subthreshold behaviour. However, once the neuron crosses the threshold into its spiking regime, the strongly nonlinear dynamics become dominant, completely swamping the stochastic component of the dynamics.

2.1 Model equations

The dynamics of an active cell in the nervous system is well-described using a spiking "point" neuron (meaning that the neuron has no spatial extent). The point neuron model consists of a set of state variables and differential equations which define the time-course of the state variables [42]. In the late 1940s and early 1950s, Hodgkin and Huxley developed the core mathematical framework to describe single-neuron dynamics based on a series of electro-physiological experiments on the squid giant axon [37]. This biorealistic conductance-based model is formed with four state variables which describe membrane potential, Na^+ channel activation and subsequent inactivation, paired with K^+ channel activation. Although the Hodgkin–Huxley equations provide biophysically sensible equations for neuron behaviour, they are hard to analyse due to their complexity. This motivated FitzHugh and Nagumo independently to introduce a reduced neuron model that contains only the essential nonlinear mathematical elements required for spike generation.

This chapter illustrates the emergence of deterministic nonlinear oscillations ("spikes") in three variants of the FHN point neuron. This is followed by an analysis of noise-induced

fluctuations during the approach to the birth of oscillations via stochastic theory and simulation.

2.1.1 Wilson and Keener & Sneyd FHN models

The FitzHugh–Nagumo equations have a "fast" excitation voltage variable and a "slow" recovery variable. A cubic nonlinearity in the voltage provides fast positive feedback; the recovery variable has linear dynamics giving slow negative feedback. This model consists of two coupled differential equations,

$$\frac{dv}{dt} = \frac{1}{\tau_v}(-f(v) - b_1 v - b_2 r + S) \tag{2.1a}$$

$$\frac{dr}{dt} = \frac{1}{\tau_r}(b_3 v - b_4 r + b_5 - b_6 S) \tag{2.1b}$$

where v represents the membrane voltage and r is the recovery variable, combining sodium channel inactivation and potassium channel activation. Their respective time constants are τ_v and τ_r, where the recovery variable has a much slower time scale than membrane voltage, typically $\tau_r \sim 20\tau_v$. Here, $f(v)$ is a cubic polynomial function of membrane voltage as listed in Table 2.1. S represents the external stimulus.

Table 2.1: Definitions and values for the FHN models defined by the Wilson [102] and Keener & Sneyd [45]. S_1^{HB} and S_1^{HB} are the experimentally determined Hopf bifurcation points for birth and death of nonlinear oscillations.

Symbol	Wilson FHN	K & S FHN	Electronic FHN (values)	Electronic FHN (symbols)
τ_v	0.1	0.01	0.1 ms	$C_1 R_5$
τ_r	1.25	2	5 ms	$C_2 R_5$
$f(v)^*$	$\frac{v^3}{3}$	$v^3 - 1.1v^2$	$2.56\left(v - 9\tanh\left(\frac{v}{3.6}\right)\right)$	$\frac{R_5}{R_3}\left(v - V_r \tanh\left(\frac{v}{V_r/2.5}\right)\right)$
b_1	-1	0.1	1	1
b_2	1	1	9	$(R_5 - R_4)$
b_3	1.25	2	1	$\frac{1}{R_4}$
b_4	1	1	1	1
b_5	1.5	0	0	0
b_6	0	0	1	$\frac{1}{R_4}$
S_1^{HB}	~ 0.9660641	~ 0.1050071	~ -2.0857867 V	
S_2^{HB}	~ 2.0339359	~ 1.2378076	~ 2.0857867 V	

* In the electronic FHN circuit Keener & Sneyd used a piecewise-linear function $f(v)$ which we replaced with tanh (Figure 2.4).

Table 2.2: Values of the electronic FHN circuit components

Symbol	value	units
R_1	100	kΩ
R_2	100	kΩ
R_3*	3.9	kΩ
R_4	1	kΩ
R_5	10	kΩ
C_1	0.01	μF
C_2	0.5	μF
V_r*	9	V

* Fig 5.20 of [45] sets $R_3 = 2.4$ Ω, but 2.4 kΩ was intended. We altered R_3 from 2.4 kΩ to 3.9 kΩ to allow us to replace the dual supply rails of ±12 V and ±15 V in the original circuit with a single supply of $V_r = \pm 9$ V.

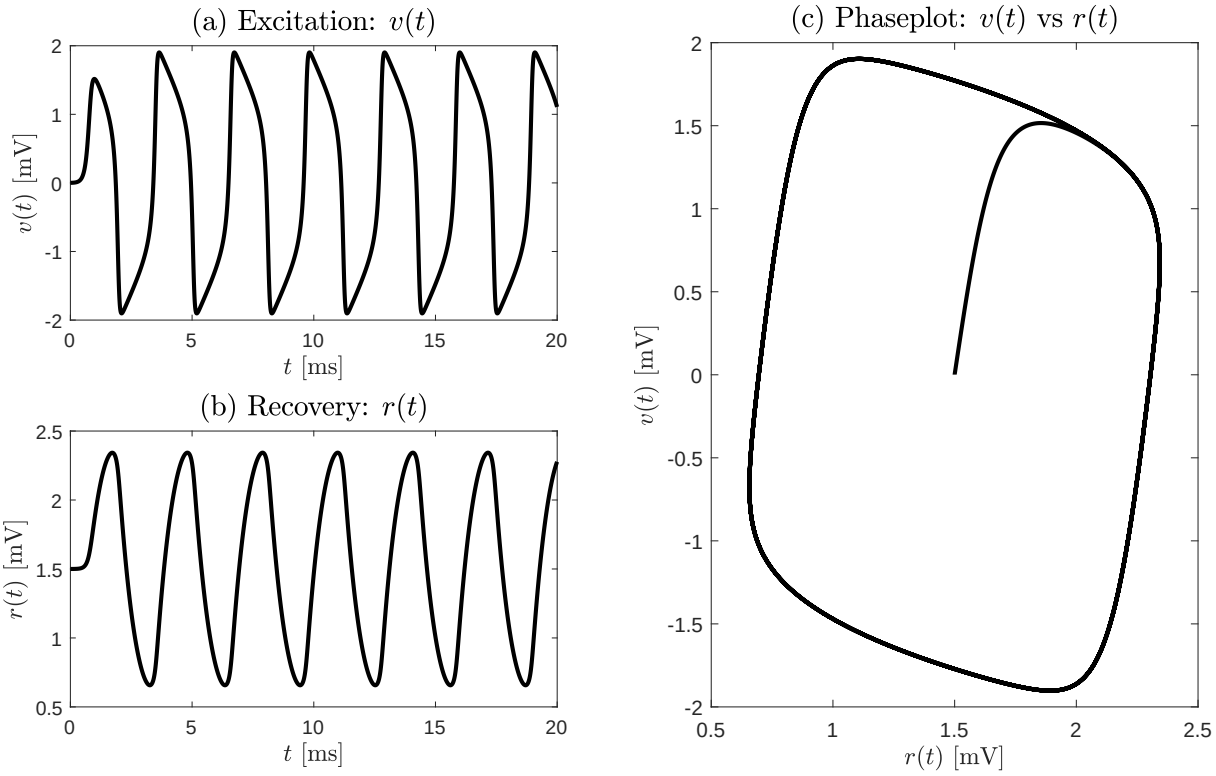

Figure 2.1: Simulations for Wilson FHN model at S = 1.5: (a) excitation variable $v(t)$, (b) recovery $r(t)$, (c) phaseplot of $v(t)$ vs $r(t)$. The model equations produce nonlinear limit-cycle oscillations at frequency ∼300 Hz. The FHN equations were solved numerically using Euler integration with time step of $\Delta t = 5$ ms

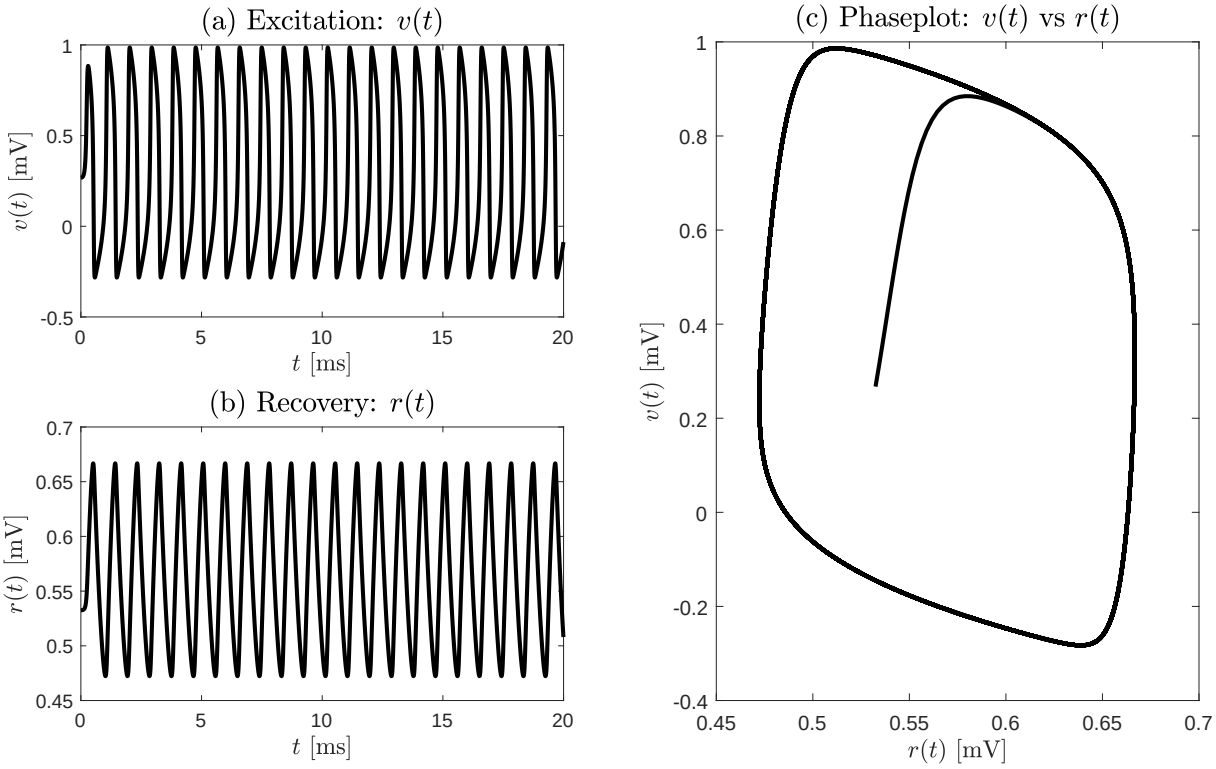

Figure 2.2: Simulations for Keener & Sneyd model at $S = 0.5$: (a) Excitation voltage $v(t)$, (b) recovery $r(t)$, (c) phase plot showing nonlinear oscillations of frequency ∼1100 Hz

Figures 2.1, 2.2 and 2.5 compare the nonlinear oscillation behaviour of the Wilson [102], Keener & Sneyd [45], and op-amp (described below) variants of the FitzHugh–Nagumo model. The Wilson and op-amp implementation show slower oscillations than the Keener & Sneyd FHN model as the latter has a smaller τ_v time constant. All three simulations exhibit nonlinear limit-cycle oscillations whose shape roughly approximates the highly non-sinusoidal form of an action potential spike.

2.1.2 Op-amp nonlinear oscillator

For many years there has been considerable interest in representing a biological neuron as an electronic circuit. In 1907, Lapicque introduced the integrate-and-fire model which modelled the neuron as a capacitor (cell membrane) in parallel with a resistor (providing a path for leakage current) with the product of resistance R and capacitance C defining the membrane time constant $\tau = RC$ [1]. Although this model does not produce the shape or form of an action potential the RC element forms the basis of almost all neuron equivalent circuits, and there have been many modifications and implementations using this concept [39]. Many researchers have used multiple RC compartments to implement

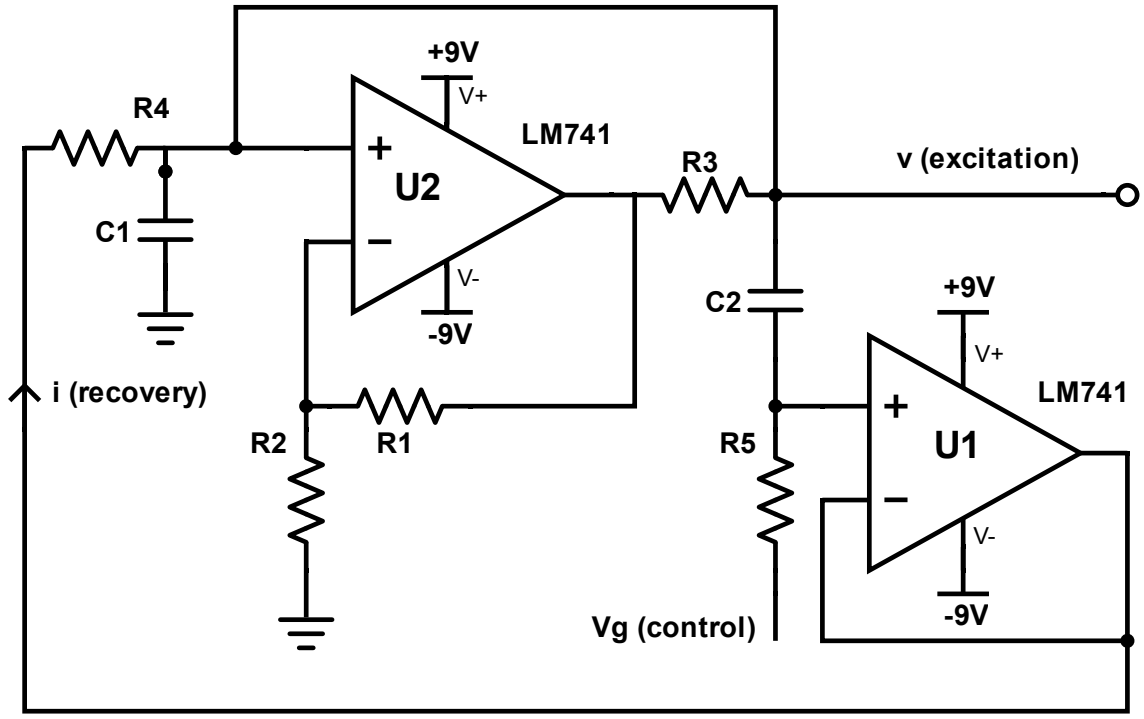

Figure 2.3: Keener & Sneyd electronic circuit equivalent to FitzHugh–Nagumo model [45]. Op-amp based electronic circuit works as a nonlinear oscillator whose behaviour is set by control voltage v_g. Component values are listed in Table 2.2

a single neuron structure, and also for neuronal networks [25, 107]. Later studies have implemented more modern electronic circuits to extend the variety of spiking patterns [39, 54, 101].

Hodgkin and Huxley modelled the cell membrane of the squid giant axon as a capacitor connected in parallel with three resistive current paths to represent Na^+, K^+ and Cl^+ ion channels. Each ion channel consists of a conductance driven by a battery that sets the ionic equilibrium potential [37,85]. While FitzHugh crafted a mathematical simplification of the Hodgkin–Huxley model, working independently Nagumo published an equivalent electronic circuit for a spiking neuron in which a diode provides the cubic nonlinearity.

Keener and Sneyd [45] designed an op-amp implementation of the FitzHugh–Nagumo equations. Their circuit, shown in Figure 2.3, couples two op-amps to act as a nonlinear oscillator. We made minor modifications to the circuit to allow both op-amps to share a common ±9 V supply (see caption of Table 2.2 for details).

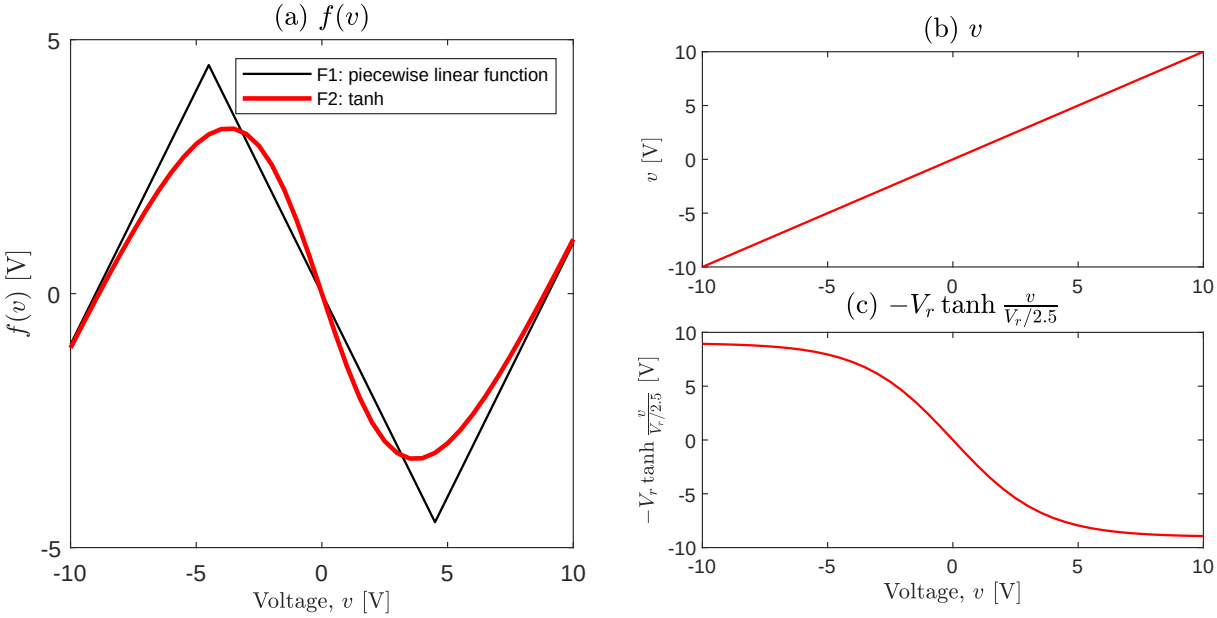

Figure 2.4: (a) Comparison between piecewise-linear function F1 (Eq. (2.3)) and hyperbolic tangent function F2 (Eq. (2.4)). The tanh function provides a smooth approximation to the piecewise description of an op-amp transfer characteristic

The excitation and recovery variables v and i obey a pair of coupled differential equations,

$$\frac{dv}{dt} = \frac{1}{C_1 R_5}\left(-f(v) - v - (R_5 - R_4)i + V_g \right) \tag{2.2a}$$

$$\frac{di}{dt} = \frac{1}{C_2 R_5}\left(\frac{v}{R_4} - i - \frac{V_g}{R_4} \right) \tag{2.2b}$$

(See Appendix A for derivation)

Excitation is expressed as the voltage across capacitor C_1, and recovery as the current through resistor R_4. This circuit can be mapped to the general form of the FHN equations; see Table 2.1. The $f(v)$ function provides the essential nonlinearity in the model. In the original Keener & Sneyd circuit, $f(v)$ is defined to be a piecewise-linear fit to the approximately cubic input-output transfer function of an op-amp,

$$F(v) = \begin{cases} v - V_{r+}, & \text{for} \quad v > aV_{r+} \\ -\frac{R_1}{R_2} v, & \text{for} \quad aV_{r-} \le v < aV_{r+} \\ v - V_{r-}, & \text{for} \quad v < aV_{r-} \end{cases} \tag{2.3}$$

where $a = 1/2$.

We chose to replace this sharp-edged function with a smooth continuous definition

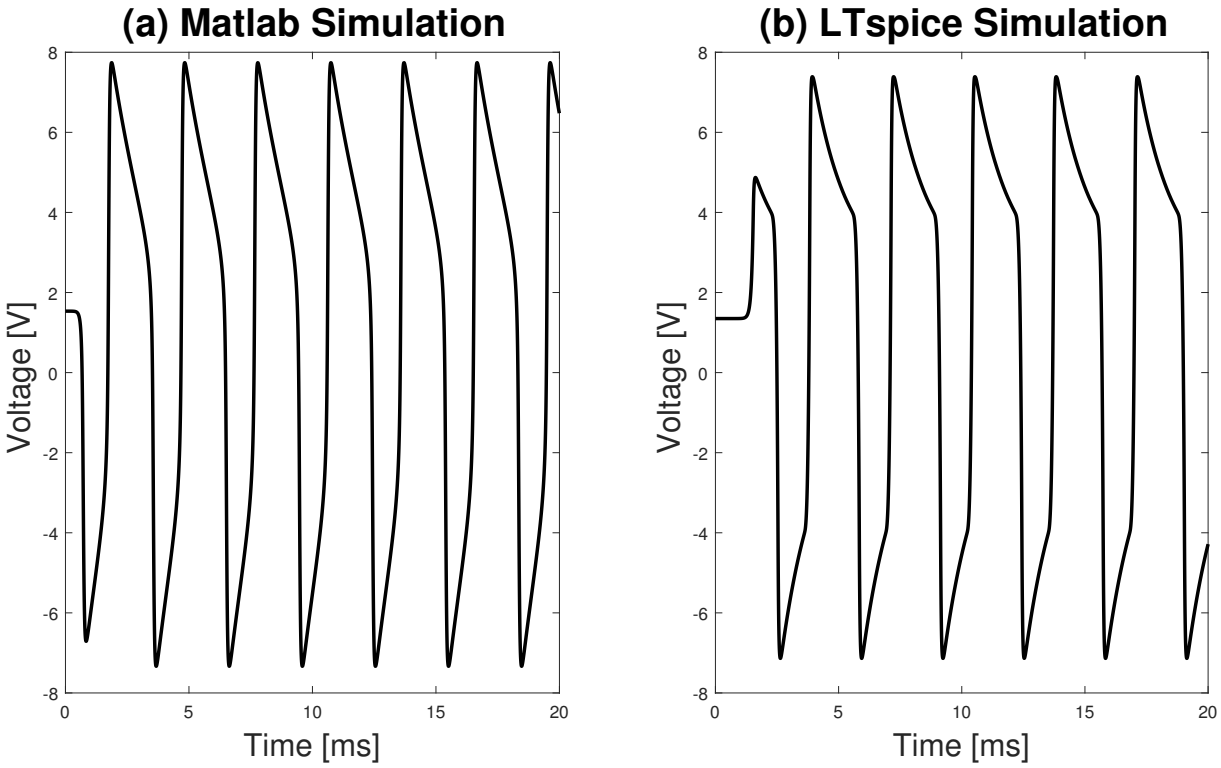

Figure 2.5: The MATLAB simulations in (a) uses the tanh() function of Eq. (2.4) while the LTspice simulation relies on internal library definitions of LM741 op-amp characteristics. While wave shapes differ somewhat, frequencies and amplitudes of the two simulations are pleasingly similar

that combines the known tanh() characteristic of a differential amplifier with a linear voltage term to give a reasonable fit to the Keener & Sneyd piecewise function as shown in Fig. 2.4,

$$f(v) = \frac{R_5}{R_3}\left(v - V_r \tanh\left(\frac{v}{V_r/2.5}\right)\right) \tag{2.4}$$

Equations (2.2) were simulated in MATLAB using the $f(v)$ definition of Eq. (2.4). Equations were integrated using an Euler algorithm with time step of 5 μs. Figure 2.5(a) shows the excitation output when the control voltage is set to $v_g = 1.0$ V. The nonlinear oscillations have frequency $\sim$375 Hz. The MATLAB simulation was checked against the LTSpice circuit simulator (See Appendix A for details) which uses "exact" library definitions for the LM741 op-amp characteristics. The agreement between the MATLAB and LTSpice output is very satisfactory. We bench-tested the circuit of Fig 2.3 and, using an oscilloscope, observed voltage waveforms that were indistinguishable from the LTSpice results (not shown). Note that we did not attempt subthreshold stochastic analysis of the bench circuit implementation due to the challenges associated with constructing a reliable white noise stimulus and measuring the expected sub-microvolt voltage fluctuations.

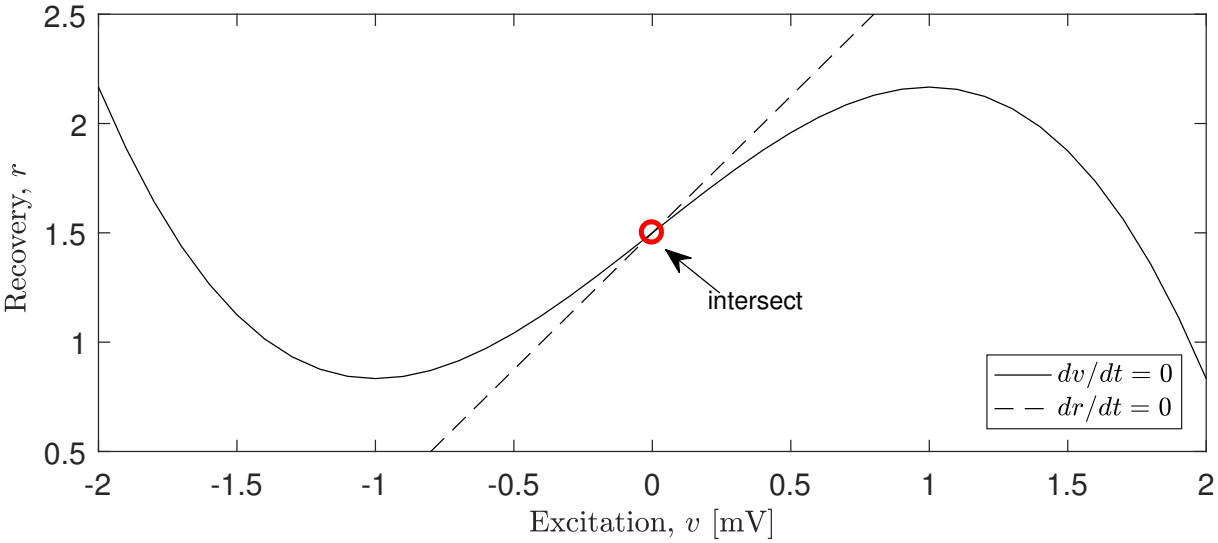

Figure 2.6: Nullclines for the Wilson FHN model at $S = 1.5$. Solid line is the cubic nullcline for dv/dt and dashed line is the dr/dt linear nullcline. The intersection of two nullclines locates the steady state

2.2 Steady states

Equations (2.1) can be written as nonlinear functions, F_1 and F_2,

$$F_1(v, r) \equiv \frac{dv}{dt} = \frac{1}{\tau_v}(-f(v) - b_1 v - b_2 r + S) \tag{2.5a}$$

$$F_2(v, r) \equiv \frac{dr}{dt} = \frac{1}{\tau_r}(b_3 v - b_4 r + b_5 - b_6 S) \tag{2.5b}$$

To investigate the dynamics of this system of equations, we locate the equilibrium states as a function of stimulus S, then probe their stability with respect to small perturbations about equilibrium. At steady state, the time derivatives dv/dt and dr/dt are simultaneously zero,

$$F_1(v, r) = 0 \qquad (dv/dt \text{ nullcline})$$

$$F_2(v, r) = 0 \qquad (dr/dt \text{ nullcline})$$

defining a pair of curves in (v, r)-space known as nullclines. Their intersection locates the steady state coordinate (v^0, r^0) for the membrane voltage and the recovery variable. Figure 2.6 illustrates the nullclines for the Wilson FHN equations at $S = 1.5$; these curves intersect at the point $(v^0, r^0) = (0, 1.5)$.

2.3 Linear stability analysis

We define a two-variable state vector,

$$\vec{X} = \begin{bmatrix} v \\ r \end{bmatrix}$$

The stability of a given equilibrium state $X^0 = [v^0, r^0]^{\mathrm{T}}$ is determined by a Taylor expansion to first order that is valid close to the X^0,

$$\frac{d}{dt}\,\delta\vec{X} = \mathbf{J}|_{[v^0,r^0]}\,\delta\vec{X} \tag{2.6}$$

where $\mathbf{J}$ is the Jacobian matrix of partial derivatives evaluated at $\vec{X^0}$,

$$J = \begin{bmatrix} \left.\dfrac{\partial F_1}{\partial v}\right|_{[v^0,r^0]} & \left.\dfrac{\partial F_1}{\partial r}\right|_{[v^0,r^0]} \\ \left.\dfrac{\partial F_2}{\partial v}\right|_{[v^0,r^0]} & \left.\dfrac{\partial F_2}{\partial r}\right|_{[v^0,r^0]} \end{bmatrix} \tag{2.7}$$

and $\delta\vec{X} = [v - v^0, r - r^0]^{\mathrm{T}}$ is a small deviation from the equilibrium point $\vec{X^0}$. Evaluating the four partial derivatives of the FHN equations (2.5) gives,

$$J = \begin{bmatrix} \frac{1}{\tau_v}\left(-\left.\dfrac{\partial f(v)}{\partial v}\right|_{[v^0,r^0]} - b_1 \right) & -\frac{1}{\tau_v}b_2 \\ \frac{1}{\tau_r}b_3 & -\frac{1}{\tau_r}b_4 \end{bmatrix} \tag{2.8}$$

The linear stability of the steady state can be quantified by extracting its eigenvalues since these predict the exponential decay or growth of small perturbations. If the dominant eigenvalue $\lambda = \alpha \pm i\omega$ has a real part α that is negative ($\alpha < 0$), then the perturbation will decay, indicating a stable equilibrium point. If $\alpha > 0$, then the perturbation will grow, so the equilibrium point is unstable. If $\alpha = 0$, with a nonzero imaginary part ω, then a Hopf bifurcation of characteristic frequency $\omega/2\pi$ is predicted. This point of delicate balance between exponential decay ($\alpha < 0$) and exponential growth ($\alpha > 0$) is known as the "critical point" since it marks the transition from quiescence to firing [42, 98].

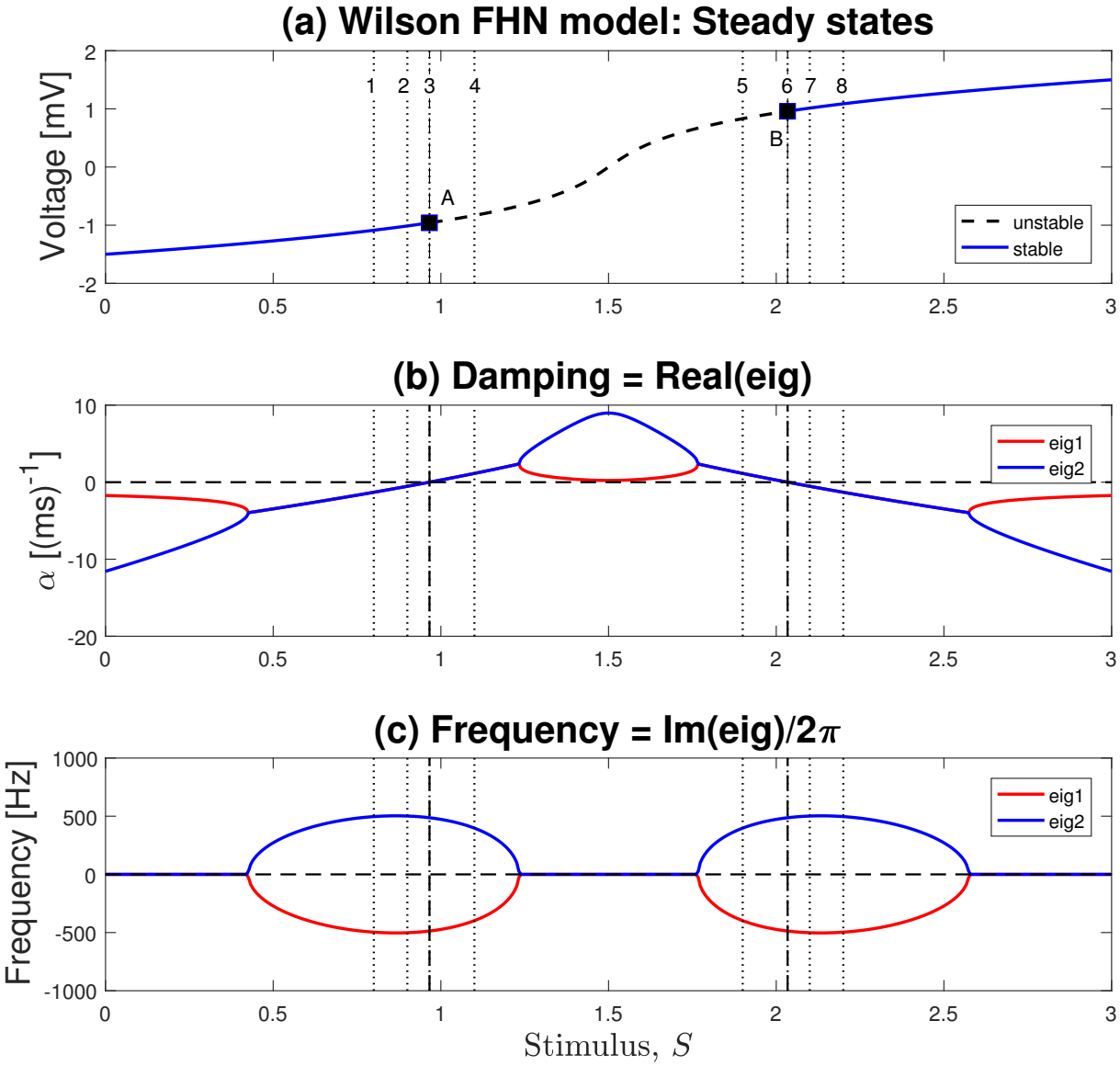

Figure 2.7: Steady-states and eigenvalues for the Wilson FHN equations. (a) Steady states: Two critical points are identified, lower critical point is at drive stimulus $S = S_1^{\mathrm{HB}} \simeq 0.9660$ (point A), higher critical point is at drive $S = S_2^{\mathrm{HB}} \simeq 2.0339$ (B). (b), (c) The eigenvalues near threshold form a complex conjugate pair, $\lambda = \alpha \pm i\omega$, imaginary part ω predicts the oscillatory frequency, the real part α is the damping rate. The steady-state is unstable when $\alpha > 0$ (dashed curve in (a)), leading to nonlinear oscillations. The zero crossings at $\alpha = 0$ mark Hopf bifurcation points. The numbered vertical dashed lines mark the stimulus values selected for simulation and displayed in Fig. 2.10

By injecting low-intensity white noise into FHN "neuron", we can quantify how close the neuron is to its "spiking" transition by examining the altering characteristics of the noise-induced fluctuations as a function of drive stimulus S. This motivates the FHN stochastic analysis to follow in Section 2.4.

Figures 2.7, 2.8, 2.9 show respectively the steady states and eigenvalue distributions for the Wilson, Keener & Sneyd and op-amp FHN models. All three FHN models have

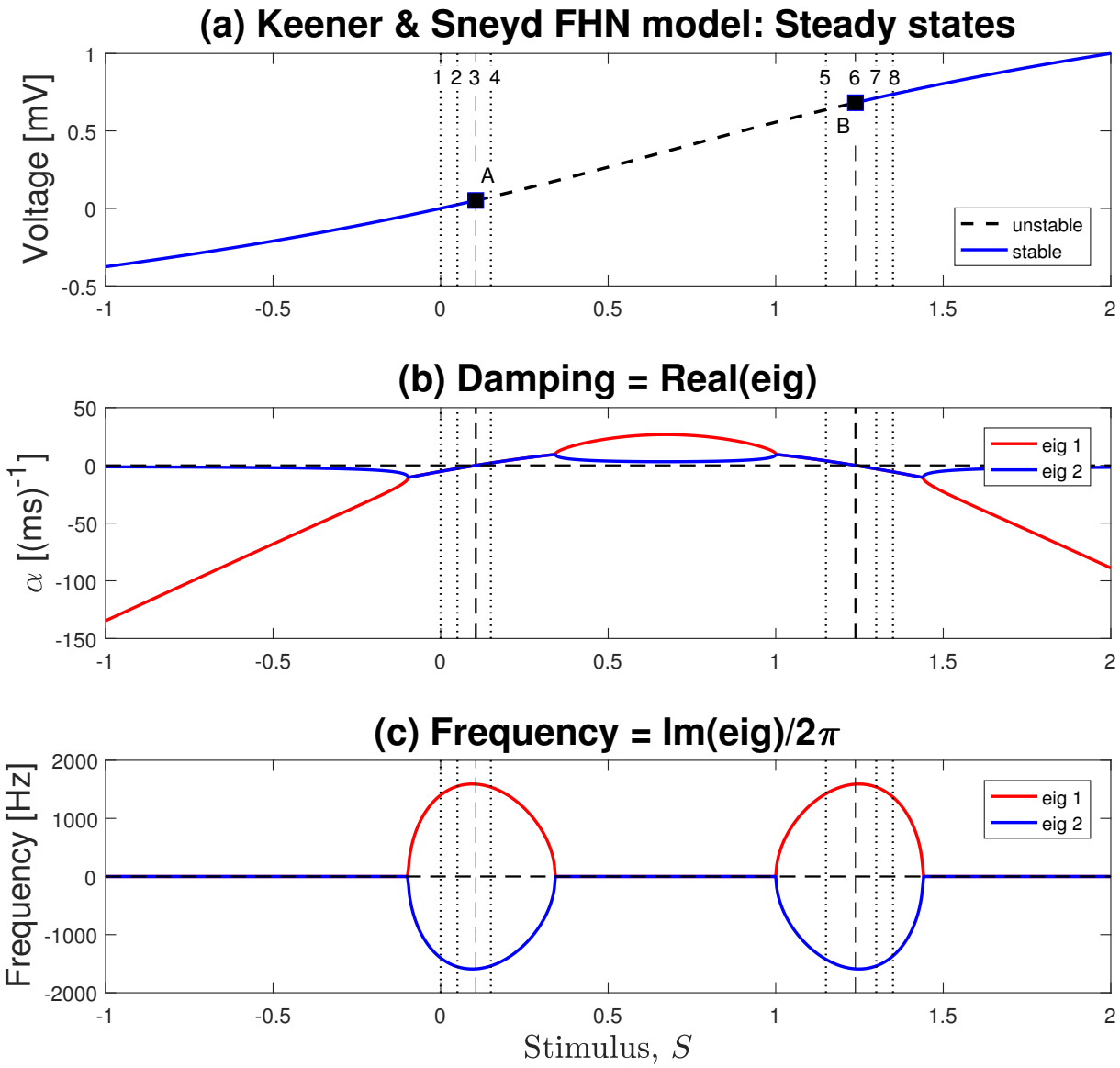

Figure 2.8: Steady-states and eigenvalues for the Keener & Sneyd FHN model. Lower and upper critical stimulus values are $S_1^{\mathrm{HB}} \simeq 0.1050$ (point A) and $S_2^{\mathrm{HB}} \simeq 1.2378$ (point B)

two critical points as identified by the zero-crossing of the α eigenvalue graph: there mark the birth (S_1^{HB}) and death (S_2^{HB}) of small linear oscillations representing the onset and offset of oscillatory behaviour. Intermediate values of drive stimulus, $S_1^{\mathrm{HB}} < S < S_2^{\mathrm{HB}}$, correspond to unstable steady states leading to nonlinear limit-cycle oscillations that are supposed to serve as action potential "spikes" in the FHN model neuron [42, 102].

Note that the steady state and eigenvalue distributions are sensitive to choice of parameter values in Equation 2.1. Parameter b_1 to b_5 determine the steady state, while τ_v and τ_r affect eigenvalues and therefore locations of critical points.

Figures 2.10–2.12 illustrate a series of impulse response simulations for the three FHN models. We added an impulse of 0.0001 V to the steady state at the start of the simulation

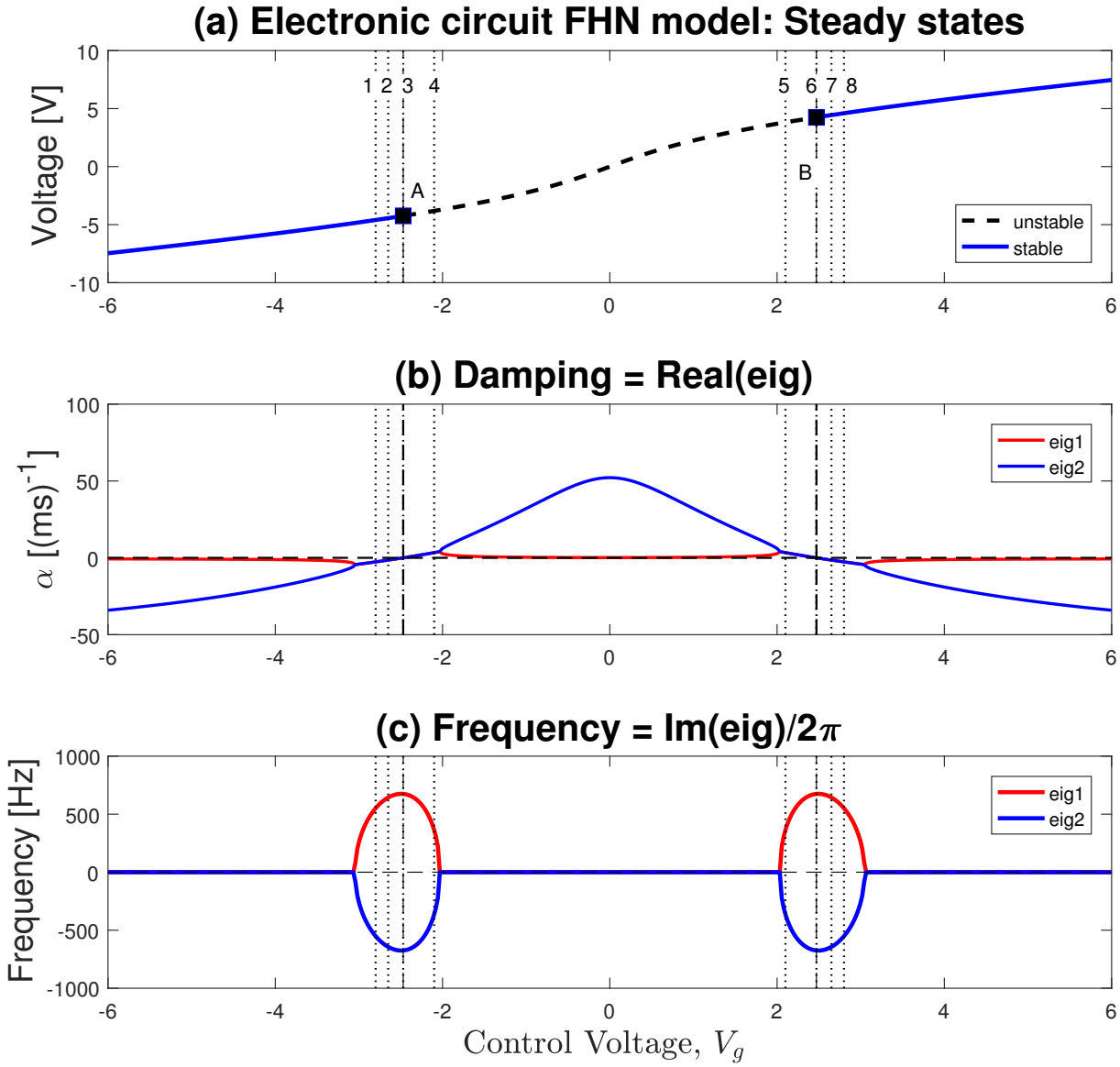

Figure 2.9: Steady-states and eigenvalues for the FHN electronic circuit model of Fig.2.3. Steady-states are symmetric around $V_g = 0$ axis and lower and upper critical control voltages are found at $S_1^{\mathrm{HB}} \simeq -2.0857$ V (point A) and $S_2^{\mathrm{HB}} \simeq 2.0857$ V (point B)

($v(t = 0) = v^0 + 0.0001$), and selected stimulus levels as indicated by the dotted/dashed vertical lines in Figures 2.7, 2.8, 2.9. The top row of Fig. 2.10 shows simulation near the first critical point. As stimulus S increases towards the lower critical point (panels (a) and (b)), we see a slowing of the relaxation to steady state. At the critical point of balance between decay and growth (panel (c)), we see persistent small amplitude sinewave oscillations. When S is within the unstable region (panels (d) and (e)) the equations generate a large-amplitude persistent spike train. A mirror of this behaviour is demonstrated near the second critical point (second row of Figure 2.10). At critical S, in panel (f), small 500 Hz oscillations can be seen. Further away from the second critical point,

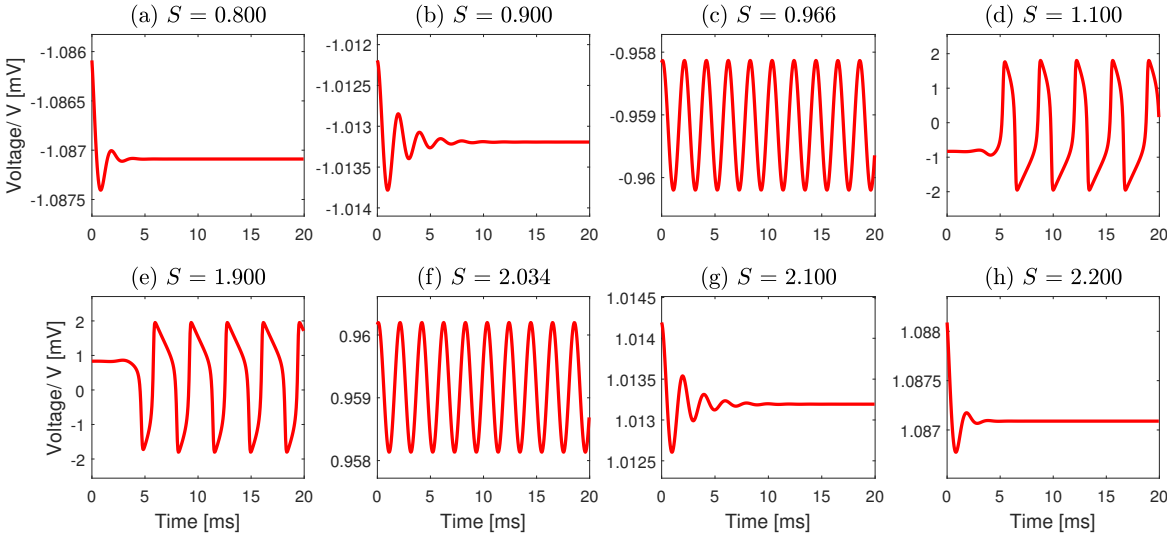

Figure 2.10: Small signal impulse response for Wilson FHN model for eight stimulus (S) levels. Upper four panels show responses near lower critical point ($S_1^{\mathrm{HB}} \simeq 0.9661$); lower four panels illustrate simulations near the higher threshold ($S_2^{\mathrm{HB}} \simeq 2.0339$). (d, e) At S of 1.1 and 1.9, the equations generate "spikes" since the system is now unstable. (a, b, g, h) When stimulus lies outside the unstable region, the neuron recovers steady state. Near threshold, oscillations persist for longer, evolving to ∼500 Hz sustained oscillations at thresholds (c, f), and spiking limit cycles (d, e)

the oscillations decay increasingly faster as the real part of the eigenvalue become more negative.

The Keener & Sneyd (Fig. 2.11) and op-amp FHN models (Fig. 2.12) show similar behaviour for a small signal impulse.

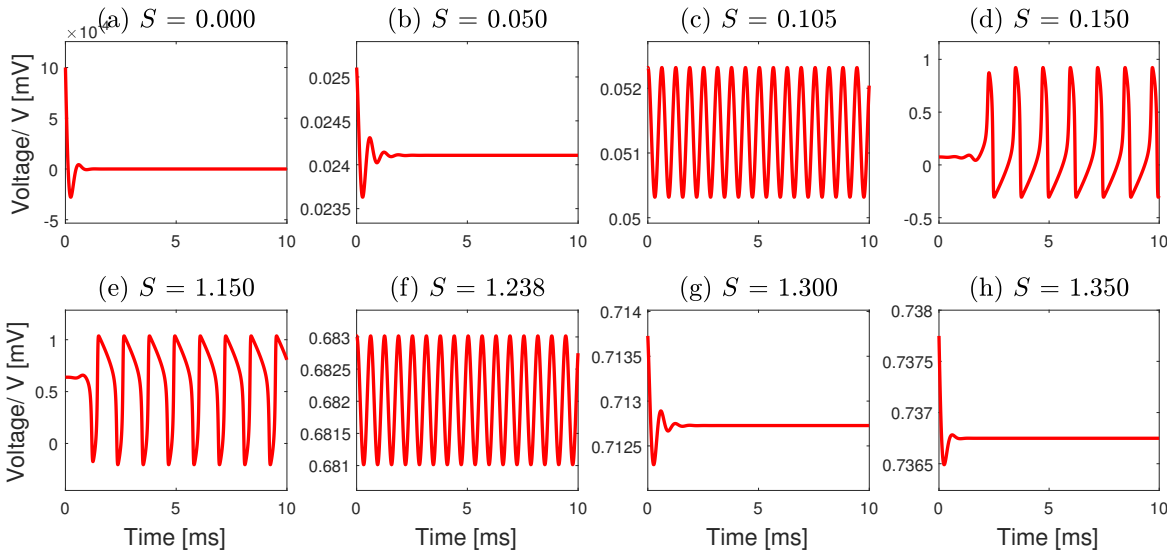

Figure 2.11: Small signal impulse response for Keener & Sneyd FHN model for eight settings of stimulus, S. Upper subplots show voltage time-series close to the lower critical point (S_1^{HB}); lower plots show responses near the second critical point (S_2^{HB}). (b, g) Impulse response is prolonged near threshold. (c, f) At threshold, small amplitude oscillations emerge. Oscillations are at frequency ∼1600 Hz which agrees with the eigenvalue prediction of Figure 2.8(c). (d, e) In the unstable region $S_1^{\mathrm{HB}} < I < S_2^{\mathrm{HB}}$ large-scale nonlinear oscillations appear

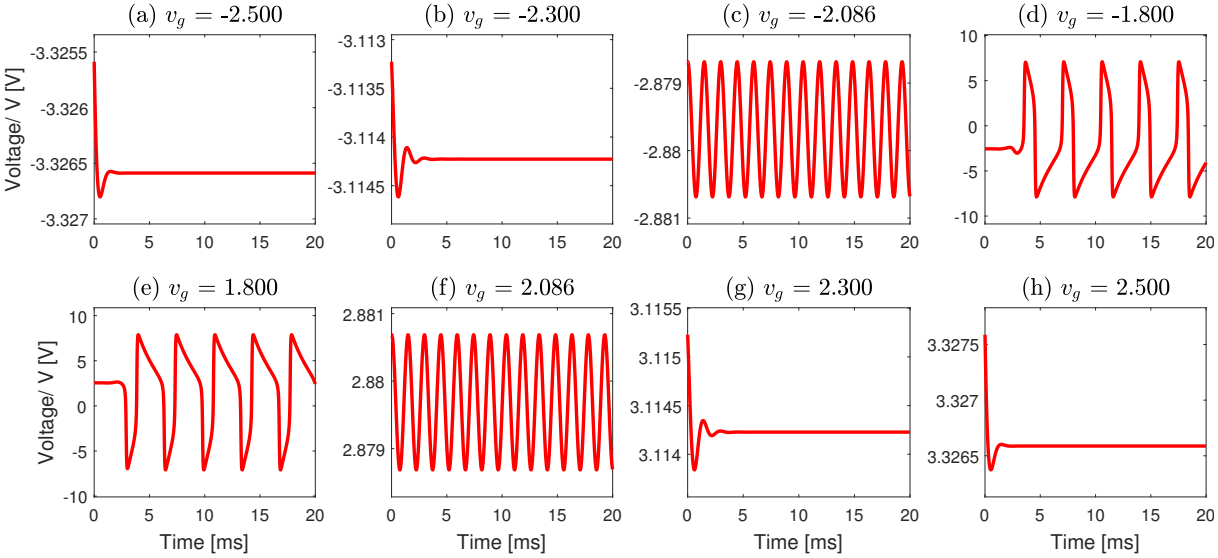

Figure 2.12: Small signal impulse response for op-amp FHN model for eight settings of gate voltages. Upper subplots are voltage time-series for four voltage settings near the lower critical gate voltage ($V_{\mathrm{g}}^{\mathrm{crit1}}$); lower subplots show responses near the second critical voltage ($V_{\mathrm{g}}^{\mathrm{crit2}}$). (c, f) Persistent oscillations appear with small amplitude and frequency ∼675 Hz, in agreement with the eigenvalue prediction of Figure 2.9(c)

2.4 Stochastic theory

In this section we examine the subthreshold response of the FHN "neuron" when exposed to low-intensity noise. Biological neurons are exposed to a continuous background of synaptic noise, and this randomness in the input stimuli might be expected to compromise the reliable encoding and transmission, via the firing of action potentials, of information to other neurons. In fact, we will show that there is a power-law growth in FHN neuron sensitivity to noisy stimulation as the critical point is closely approached from below.

2.4.1 Stochastic differential equations

We form the stochastic version of the FHN model by adding white-noise perturbations to the noise-free equations (2.1),

$$\frac{dv}{dt} = \frac{1}{\tau_v}(-f(v) - b_1 v - b_2 r + S) + \sigma_1 \xi_1(t) \tag{2.9a}$$

$$\frac{dr}{dt} = \frac{1}{\tau_r}(b_3 v - b_4 r + b_5 - b_6 S) + \sigma_2 \xi_2(t) \tag{2.9b}$$

where $\sigma_{1,2}$ are constants which scale the amplitude of the two noise terms; $\xi_{1,2}(t)$ are a pair of independent, Gaussian-distributed delta-correlated white-noise sources with zero-mean and infinite variance,

$$\langle \xi(t) \rangle = 0, \qquad \text{(zero mean)} \tag{2.10}$$

$$\langle \xi_1(t)\xi_2(t') \rangle = \delta_{1,2}\delta(t-t') \qquad \text{(delta correlation)} \tag{2.11}$$

where $\delta_{1,2}$ is the Kronecker delta and $\delta(t-t')$ is the Dirac delta function. The angle-bracket notation is short-hand for the temporal average

$$\langle [\cdots] \rangle = \lim_{T\to\infty} \frac{1}{T} \int_0^T [\cdots]\, dt$$

.

In our stochastic numerical simulations, the white-noise sources are approximated using a zero-mean, unit-variance Gaussian random number generator, $\mathcal{R}(0,1)$, divided by the square-root of the sampling time step, Δt,

$$\xi(t) = \frac{\mathcal{R}(0,1)}{\sqrt{\Delta t}}$$

This multiplication by $1/\sqrt{\Delta t}$ ensures that the stochastic Euler increment

$$\xi(t)\Delta t = \mathcal{R}(0,1)\sqrt{\Delta t}$$

scales with the square-root of the time step (as required for a Brownian motion process), and that $\xi(t)$ has a variance that diverges to infinity as $\Delta t \to 0$ (as required for white noise).

Here we are are specifically looking at the subthreshold dynamics, where fluctuations are quite small. Therefore linearisation is applied to predict the subthreshold behaviour of these nonlinear functions. We linearise the stochastic FHN equations about a given subthreshold steady state to form an Ornstein–Uhlenbeck (OU) system [29],

$$\frac{d}{dt}\begin{bmatrix} v \\ r \end{bmatrix} = -\mathbf{A}\begin{bmatrix} v \\ r \end{bmatrix} + \sqrt{\mathbf{D}}\begin{bmatrix} \xi_1(t) \\ \xi_2(t) \end{bmatrix} \tag{2.12}$$

where $\mathbf{A}$ is the 2×2 drift matrix equal to the negative of the Jacobian matrix ($\mathbf{A} = -\mathbf{J}$) evaluated at steady state. Here, $\mathbf{D}$ is the diffusion matrix,

$$\mathbf{D} = \begin{bmatrix} \sigma_1^2/\tau_v^2 & 0 \\ 0 & \sigma_2^2/\tau_r^2 \end{bmatrix} \tag{2.13}$$

2.4.2 Variance

For the Ornstein–Uhlenbeck process, Gardiner [29] derived a theoretical expression for the covariance matrix $\mathbf{\Sigma}$,

$$\mathbf{A\Sigma} + \mathbf{\Sigma A}^{\mathrm{T}} = \mathbf{D} \tag{2.14}$$

For a two-variable OU process, this implicit equation for $\mathbf{\Sigma}$ can be written out explicitly,

$$\mathbf{\Sigma} = \frac{\det(\mathbf{A})\mathbf{D} + [\mathbf{A} - (\mathrm{tr}(\mathbf{A})\mathbf{I}]\mathbf{D}[\mathbf{A} - \mathrm{tr}(\mathbf{A})\mathbf{I}]^{\mathrm{T}}}{2\mathrm{tr}(\mathbf{A})(\det\mathbf{A})} \tag{2.15}$$

where $\mathbf{I}$ is the 2×2 identity matrix. Here $\det(\cdot)$ and $\mathrm{tr}(\cdot)$ are determinant and trace operators that can expressed in terms of matrix eigenvalues,

$$\begin{aligned} \det(\mathbf{A}) &= \det(\mathbf{J}) = \lambda_1\lambda_2 \\ \mathrm{tr}(\mathbf{A}) &= -\mathrm{tr}(\mathbf{J}) = -(\lambda_1 + \lambda_2) \end{aligned}$$

where $\lambda_{1,2}$ are the eigenvalues of the Jacobian matrix $\mathbf{J}$. Then the theoretical expression for the variance of the noise-induced voltage fluctuations can be obtained form the Σ_{11} entry of the 2×2 covariance matrix,

$$\mathrm{var}\{v\} = \frac{\lambda_1\lambda_2 D_{11} + A_{22}^2 D_{11} + A_{12}^2 D_{22}}{-2(\lambda_1 + \lambda_2)\lambda_1\lambda_2} \tag{2.16}$$

2.4.3 Cross-correlation

The 2×2 time-correlation matrix can be computed directly from the $(v(t), r(t))$ fluctuations time-series,

$$\mathbf{C}(\tau) = \begin{bmatrix} \mathrm{cov}\{v(0), v(\tau)\} & \mathrm{cov}\{v(0), r(\tau)\} \\ \mathrm{cov}\{r(0), v(\tau)\} & \mathrm{cov}\{r(0), r(\tau)\} \end{bmatrix} \tag{2.17}$$

where τ is the lag-time. The theoretical expression for the time-correlation matrix is defined,

$$\mathbf{C}(\tau) = e^{-\mathbf{A}\tau}\mathbf{\Sigma}, \quad \text{where } \tau \geq 0 \tag{2.18}$$

and where $e^{-\mathbf{A}\tau}$ denotes a matrix exponential that can be evaluated using the `expm` function in MATLAB. The $\mathbf{C}_{11}(\tau)$ element from time-correlation matrix, $\mathbf{C}(\tau)$ provides the theoretical expression for the autocorrelation function of the $v(\tau)$ voltage fluctuations.

2.4.4 Frequency spectrum

Gardiner writes the spectrum matrix for the Ornstein–Uhlenbeck process as,

$$\mathbf{S}(\omega) = \frac{1}{2\pi}(\mathbf{A} + i\omega\mathbf{I})^{-1}\mathbf{D}(\mathbf{A}^{\mathrm{T}} - i\omega\mathbf{I})^{-1} \tag{2.19}$$

Our two-dimensional FHN system of equations has a 2×2 spectrum matrix, with the $\mathrm{S}_{11}(\omega)$ providing the power spectral density for voltage fluctuations about steady state,

$$\mathrm{S}_{11}(\omega) = \frac{1}{2\pi}\frac{\mathrm{A}_{22}^2\mathrm{D}_{11} + \mathrm{A}_{12}^2\mathrm{D}_{22} + \mathrm{D}_{11}\omega^2}{(\lambda_1\lambda_2 - \omega^2)^2 + (\lambda_1 + \lambda_2)^2\omega^2} \tag{2.20}$$

2.5 Subthreshold stochastic analysis

We now investigate the stochastic behaviour of the FHN model near the critical point. We perform a series of numerical simulations and analyse the noise-induced subthreshold fluctuation statistics comparing these results against the predictions of OU stochastic theory.

Wilson FHN model

Figure 2.13(a) shows the voltage fluctuations near the first critical point for 2000 individual simulations of the Wilson FHN model. Stochastic fluctuations are induced by white-noise sources of amplitudes $\sigma_1, \sigma_2 = 1 \times 10^{-6}$. These noise amplitudes are chosen to be sufficiently small to allow close approach to critical points.

The stochastic DEs were simulated using Euler–Maruyama integration with time-step $\Delta t = 10$ μs and with stimulus settings evenly spaced across the range from 0.8 to 0.9660. Each simulation ran for 2000 ms, with the largest positive and negative

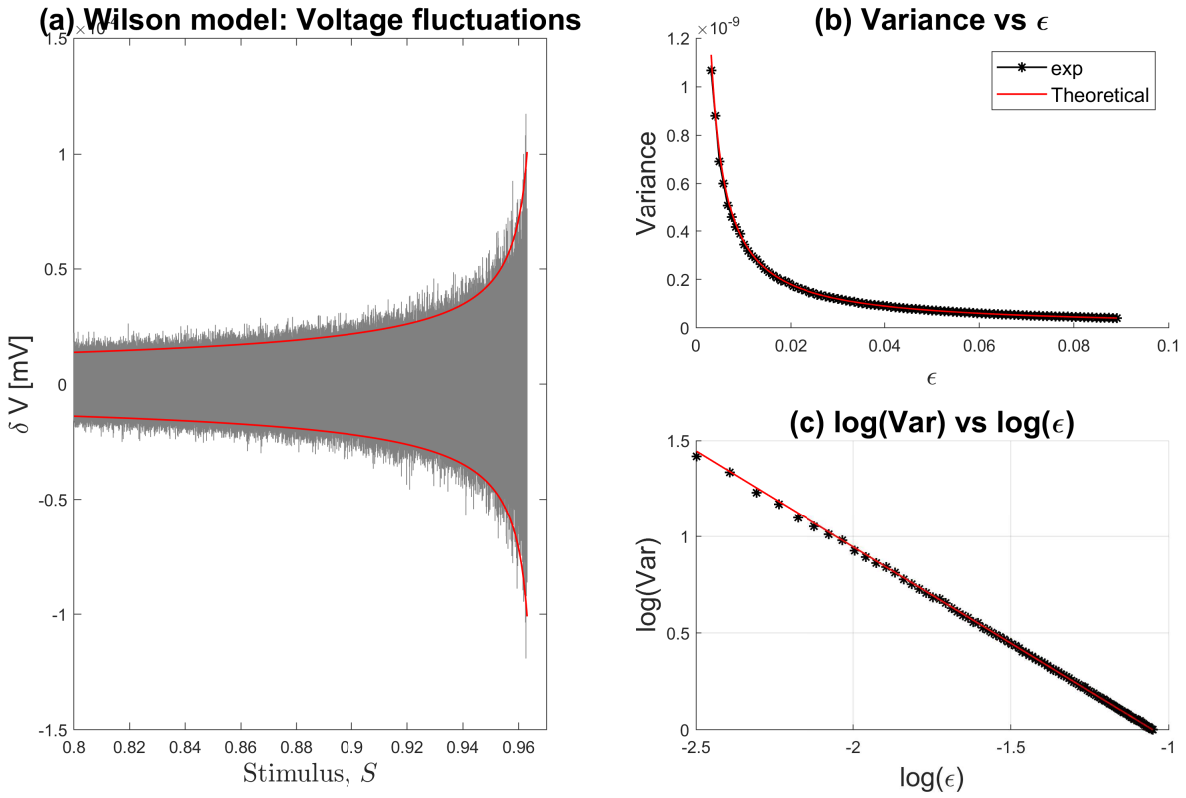

Figure 2.13: Voltage fluctuation as a function of stimulus S for the Wilson FHN equations near the first critical point. (a) Each vertical grey line shows maximum excursions recorded in a 2000-ms simulation; red curves display predicted $\pm 3\sigma_v$ limits. (b) Variance vs epsilon $\epsilon = (S^{\mathrm{HB}} - S)/S^{\mathrm{HB}}$ approaching critical point. Red curve shows the theoretical predictions, black circles show the measured variance. (c) Log-log variation between variance and epsilon; OU theory predicts a straight line with gradient -1

deviations ($\delta v^+$and δv^-) away from the v_0 equilibrium being recorded as signed offsets $(\delta v^+, \delta v^-) = (v_{\max} - v_0, v_{\min} - v_0)$, and plotted in panel (a) as vertical grey lines. On this was superimposed the $\pm 3\sigma$ theoretical predictions representing three standard deviation limits. The standard deviation was computed from Eq. (2.16) as $\sigma_v = \sqrt{\mathrm{var}\{v\}}$. Figure 2.13(a) manifests pronounced growth of voltage fluctuations on close approach to threshold, with good agreement between simulation and theory. The time-step, Δt was chosen to be a small fraction of the τ_v time-constant in order to ensure numerical stability.

To quantify distance from criticality, we define a dimensionless measure $\epsilon = (S^{HB} - S)/S^{HB}$ which tends to zero as $S \to S^{HB}$, the (lower) critical point. Panel (b) predicts that fluctuation variance will diverge strongly as $\epsilon \to 0$, and the log-log $\mathrm{var}\{v\}$ vs ϵ graph of panel (c) indicates that the divergence follows power-law

$$\mathrm{var}\{v\} \sim \frac{1}{\epsilon}$$

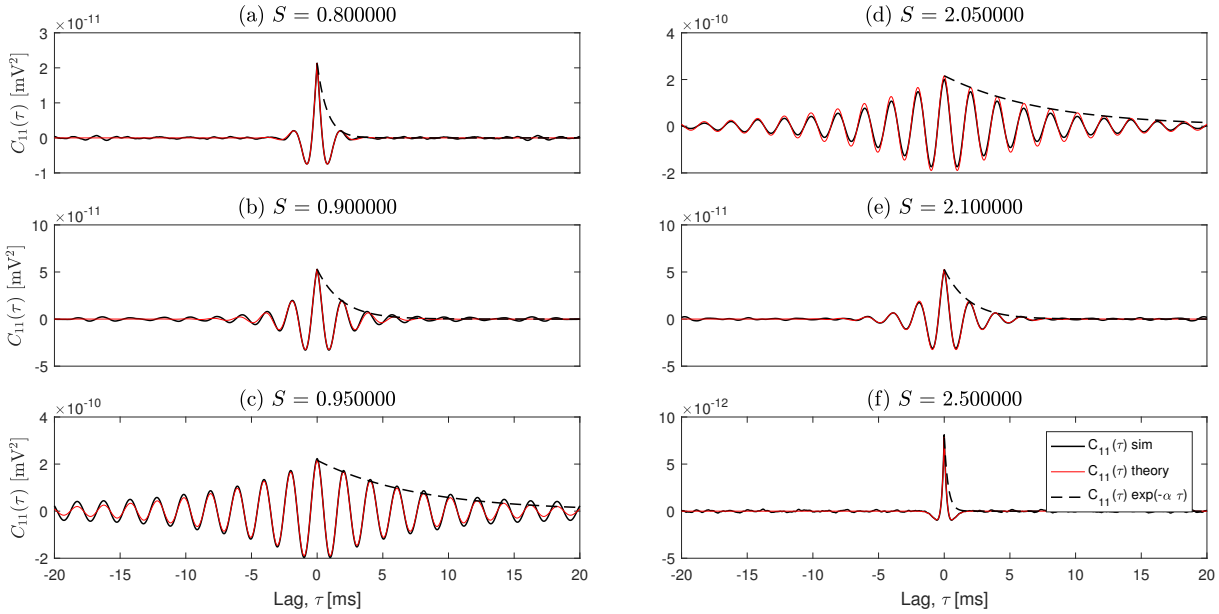

Figure 2.14: Autocorrelation of white noise-driven subthreshold Wilson FHN equations for six levels of S near first and second critical points: (a) 0.80; (b) 0.90; (c) 0.95; (d) 0.205; (e) 2.10; (f) 2.50. Red solid curves show numerical results; black solid curve represents the theoretical OU predictions; dashed curve shows the exponential ($\exp(-\alpha\tau)$) decay envelope, evaluated using the real part of the eigenvalue, $\alpha = -\mathrm{Re}(\lambda_{1,2})$

with excellent agreement between measurement and OU theory across ∼1.5 decades of ϵ values.

Growth of critical fluctuations in the FHN model also can be visualized by computing their temporal autocorrelation (see Figure 2.14). We selected six different S settings, three for approach to the lower threshold ($S_1^{\mathrm{HB}} \simeq 0.9660$) and three for departure from the upper threshold ($S_2^{\mathrm{HB}} \simeq 2.0339$). For each setting of S, we ran 2000-ms nonlinear stochastic simulations, then computed the C_{11} autocorrelation function for the time series using Eqs. (2.17) and (2.18). Simulation results (black) are in good agreement with theoretical predictions (red). We observe highly damped oscillations when far from threshold, and much lower damping near threshold, consistent with the notion that oscillations would become infinitely prolonged when precisely at the critical point where damping vanishes.

For the final demonstration of critically enhanced fluctuations, we compute the fluctuation spectrum for the Wilson FHN neuron from the time-series, and compare with the OU spectral prediction of Eq. (2.20). In Figure 2.15 we plot the root-mean-square voltage amplitude spectra $V_{\mathrm{rms}}(f) = \sqrt{S_{11}(f)}$, and note the strengthening resonance at frequency $\omega_0/2\pi \simeq 500$ Hz, consistent with the eigenvalue frequency trend of Fig. 2.7(c).

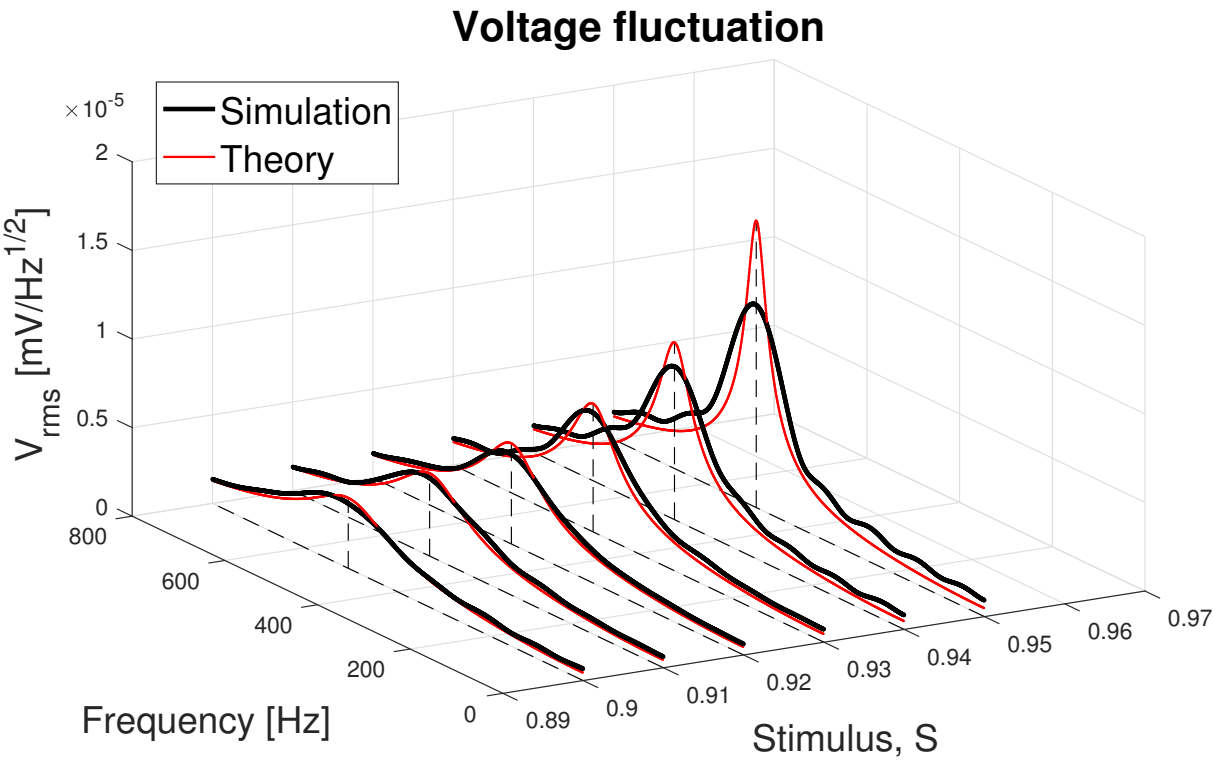

Figure 2.15: Fluctuation spectrum for Wilson FHN equations near firing threshold. One sided spectrum calculated for six different stimulus settings. Black curves show PSD of simulation data, evaluated using Euler integration with time step of 10 μs. Red curves show the $\sqrt{S_{11}}$ theoretical predictions using Ornstein–Uhlenbeck theory. Each curve exhibit noticeable resonance at ∼500 Hz, which strengthens and narrows when approaching the critical stimulus, $S \backsimeq 0.9660$

Keener & Sneyd FHN model

The subthreshold fluctuation dynamics for the Keener & Sneyd FHN neural model are qualitatively similar to that of the Wilson FHN model. Figure 2.16 displays: (a) variation of voltage fluctuations; (b, c) variance; (d) autocorrelation; and (e) power spectrum near the first critical point ($S_1^{\mathrm{HB}} = 0.1050$). Consistent with the Wilson FHN neuron, we see increased susceptibility to small perturbations when approaching threshold. The fluctuation spectrum (theory and numerical results) narrows and strengthens when approaching the critical point to reveal a resonant frequency $\simeq 1500$ Hz.

Electronic circuit model

We repeated the previous analyses for the mathematical model of the op-amp circuit of Fig. 2.3. The results presented in Figure 2.17 are consistent with both the Wilson and the Keener & Sneyd subthreshold characteristics. In panel (a) the extremes of voltage fluctuation for 2000 independent stochastic simulations ($\Delta t = 5$ μs) were recorded for stimulus v_g ranging from -2.5 to -2.087.

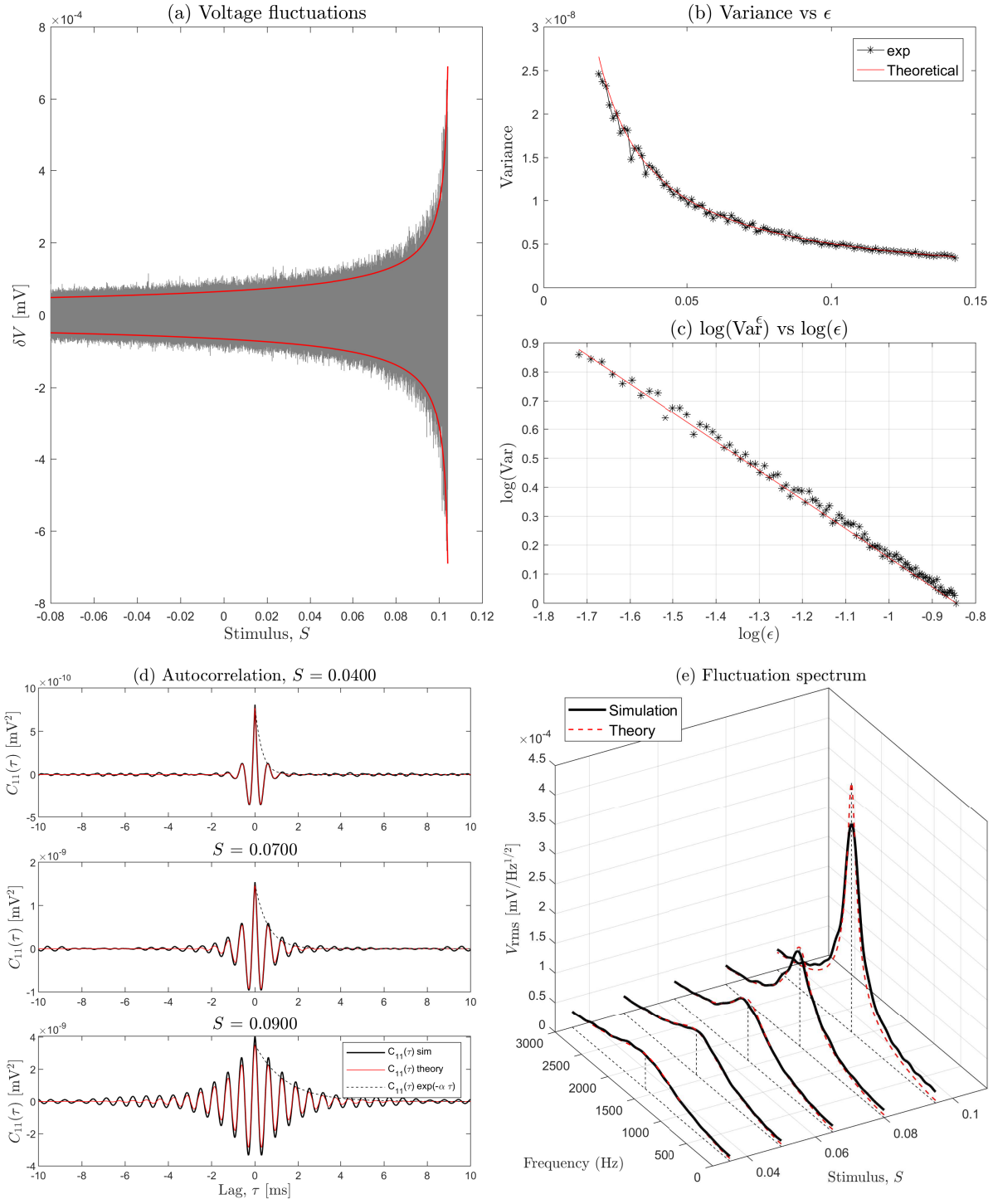

Figure 2.16: Subthreshold impulse response for Keener & Sneyd FHN model. (a) Each vertical grey line shows the maximum excursion for 2000 individual simulations that each ran for 2000 ms with time-step $\Delta t = 1$ μs. Red curves display predicted $\pm 3\sigma$ limits. (b),(c) Calculated variance against ϵ ($\epsilon = (S^{\mathrm{HB}} - S)/S^{\mathrm{HB}}$) using theory (red line) and simulation (black). Variance increases towards threshold, S_1^{HB} ($S_1^{\mathrm{HB}} \simeq 0.1050$ V) and log-log relationship aligns with a straight line of slope -1. (d) Autocorrelation for three control voltages levels near to $S_1^{\mathrm{HB}} \simeq 0.1050$. Red lines denote theoretical predictions; these align with simulation results (black lines). (e) Fluctuation spectrum for five control voltage settings. Both theory and experimental results show peaks at frequency ∼1500 Hz and power increases as stimulus is increased towards the critical point, S_1^{HB}

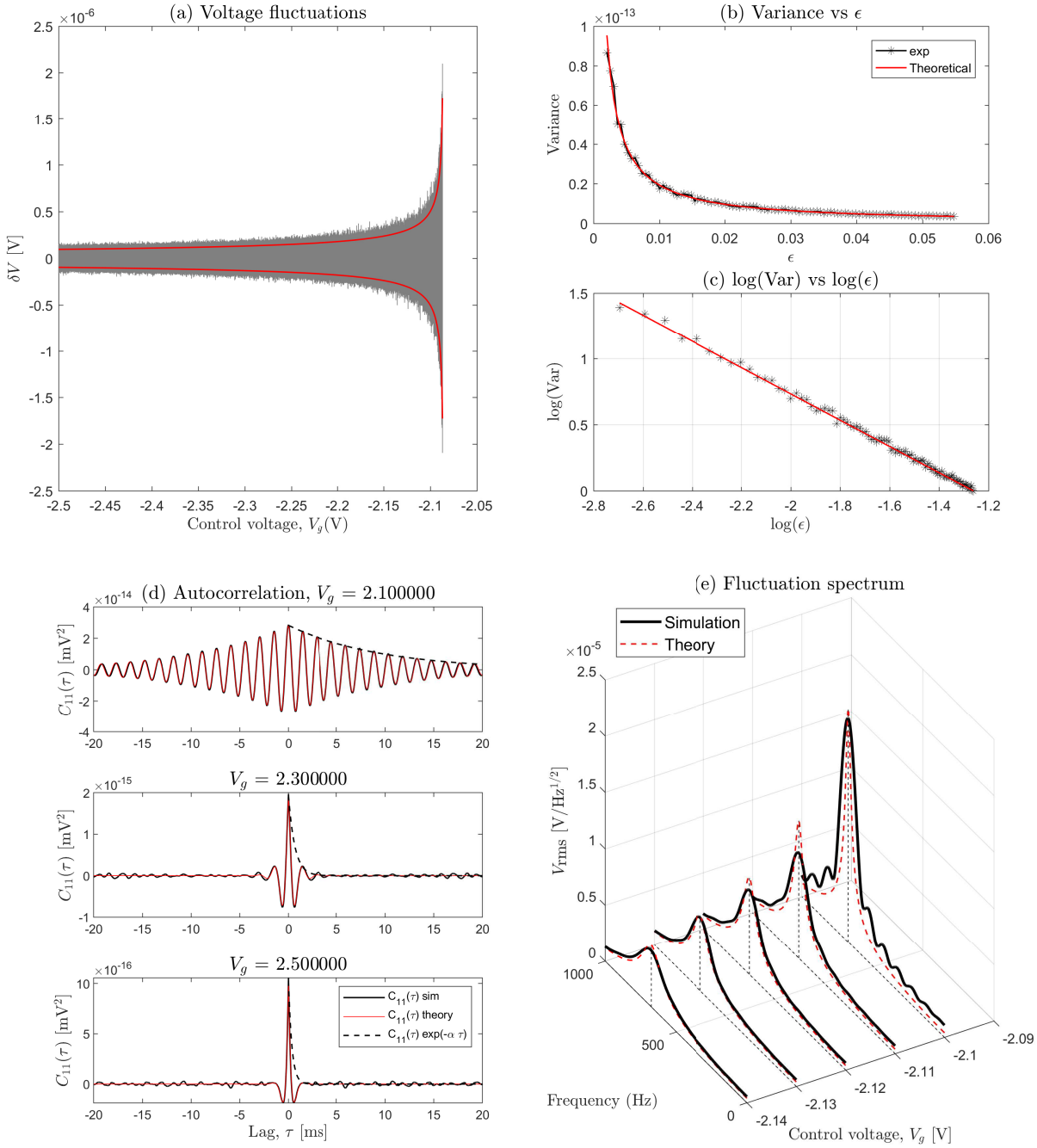

Figure 2.17: Subthreshold impulse response for FHN op-amp circuit model. (a) Grey vertical lines mark extremes of voltage fluctuation for each control voltage for 2000 ms runs with $\Delta t = 5$ μs timestep; red curves show theoretically predicted limits of voltage fluctuations ($\pm 3\sigma$). (b), (c) Calculated variance against ϵ ($\epsilon = (S^{\mathrm{HB}} - S)/S^{\mathrm{HB}}$) using theory (red line) and simulation (black). Variance increases towards threshold, S_2^{HB} ($S_2^{\mathrm{HB}} \simeq 2.0857$ V) and log-log relationship shows a power law with exponent -1. (d) Autocorrelation for three control voltages near to S_2^{HB}. Theoretical predictions (red) align with the simulation results (black). (e) Noise-induced fluctuation spectra for five control voltage settings. Red dashed lines are theoretical predictions, and thick black lines are simulation spectra. Peak activity occurs at frequency ~675 Hz with power increasing as control voltage approaches the second critical point, S_2^{HB} from above

The panels (b) and (c) illustrate the fluctuation variance (linear and log-log plots respectively). Variance vs ϵ reveals a power-law with exponent of -1. The fluctuation autocorrelation of the FHN circuit model in the time domain is illustrated in panel (d) for three values of v_g control voltage near the upper critical point, $S_2^{\rm HB}$. Panel (e) compares the theoretical and experimental power spectra for close approach to the upper critical point $S_2^{\rm HB}$ from above. A strengthening resonance emergences at frequency ~ 675 Hz.

2.6 Chapter summary

In this chapter we investigated the nonlinear dynamics and subthreshold stochastics of the FitzHugh-Nagumo (FHN) neural model using three different parameterisations: Wilson, Keener & Sneyd, and op-amp equivalent circuit. First we compared nonlinear oscillations and computed steady states and analysed linear stability at each equilibrium state. Then we examined the low-intensity white-noise induced voltage fluctuations for close approach to and departure from spiking threshold.

As discussed in Chapter 1, Steyn-Ross *et al.* [87] investigated onset of spiking in the two types of neuron elucidated by Wilson [102]: type-I integrator and type-II resonator (Note that they did not examine the death of spiking that occurs when stimulus current becomes excessively high). The FHN models investigated in the present chapter all exhibit type-II resonant behaviour. This arises from the Andronov-Hopf bifurcation at the critical points corresponding to the birth (onset at $S_1^{\rm HB}$) and death (offset at $S_2^{\rm HB}$) of large amplitude nonlinear oscillations, which are sustained in the unstable region $S_1^{\rm HB} < S < S_2^{\rm HB}$. The critical stimulus is located at the equilibrium point where the real part of the eigenvalue becomes zero, while the imaginary part (frequency) is non-zero.

Subthreshold stochastic analyses of all three FHN models concludes with the following results:

- Variance of voltage fluctuations increases on approach to threshold and aligns to a power-law with exponent -1 : $\text{var}\{v\} \sim \epsilon^{-1}$
- PSD also evinces the increase of fluctuation amplitude at a resonant frequency near the critical point: growth of spectral power simultaneous with a narrowing of spectral width
- Autocorrelation manifests a prolongation of settling time when approaching the critical point.

Unlike the type-I integrator neuron, FHN does not exhibit critical slowing down to zero frequency. Instead, it shows increasingly resonant behaviour and prolongation of settling time on approach to the critical point. Although FHN is the simplest model to represent the single spiking neuron, it retains the subthreshold stochastic characteristics of more biophysically realistic and mathematically more complicated spiking neuron models such as the Wilson and Hodgkin–Huxley point neurons.

Chapter 3

Critical fluctuations in the Waikato mean-field cortical model

In this chapter, we examine the dynamical behaviour of Waikato mean-field (WMF) model of the cerebral cortex as it approaches the anaesthetic induced phase-transition. Mean-field cortical models describe the spatially-averaged behaviour of *populations* of excitatory and inhibitory neurons, and make no attempt to describe single neuron events such as the birth and axonal propagation of individual spike events. The WMF model has been in continuous development since 1999 [85, 89, 91, 92], drawing on ideas from the continuum models of Liley *et al.* [52], Rennie *et al.* [72] and Robinson *et al.* [77]. Recently the model was extended to incorporate electrical gap-junction synapses [93, 94] to complement communication via standard chemical synapses.

The primary state parameter of the model is mean excitatory firing rate, which is presumed to represent the scalp-measured EEG [90]. The smallest cortical element is considered to be the "macrocolumn" containing ∼100,000 neurons that are grouped into excitatory (85%) and inhibitory (15%) populations according to their effect on other neurons. These populations communicate locally via both chemical and electrical synapses (gap junctions), and over longer ranges via myelinated axons.

The WMF model consists of a set of coupled partial differential equations. Flux activity generated by excitatory and inhibitory neuronal populations is received at a dendritic synapses. Axonal flux transmission is modelled as a 2-D wave equation with Macdonald-function connectivity [77]. The transmission efficiency of these chemical synapses is modified by the difference between the membrane voltage and its reversal potential [52, 72]. The net neuron voltage is determined by axono-dendritic activity at chemical synapses plus diffusive current from adjacent neurons coupled via gap junctions.

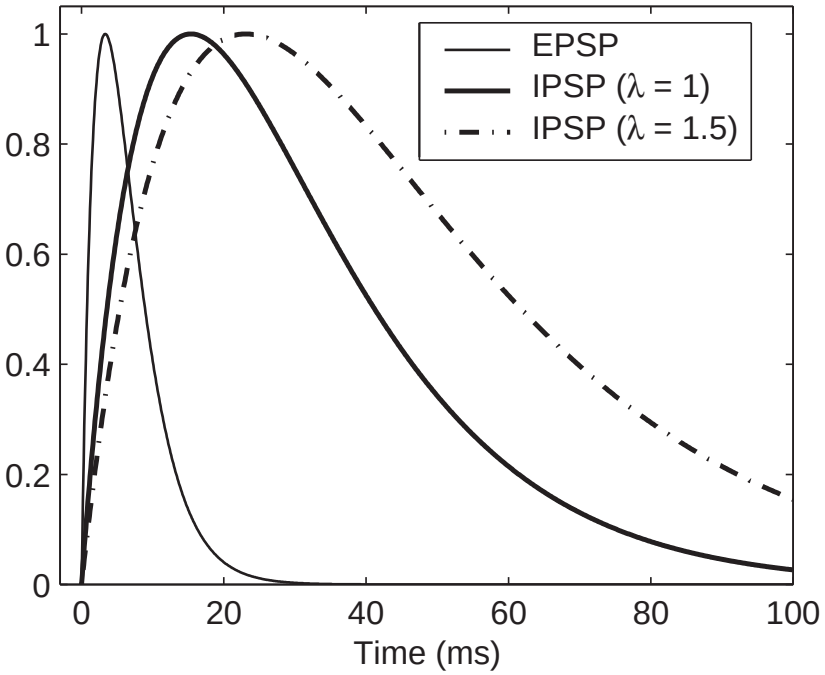

Figure 3.1: Unit-height impulse response for excitatory (light curve), inhibitory (bold), and anaesthetic enhanced inhibitory (dashed) post synaptic potentials. λ is the anaesthetic effect scale factor [89]

The postsynaptic potential at chemical synapses depends on $(V - V^{\text{rev}})$, the voltage of the receiving neuron V relative to its reversal potential V^{rev}. If this difference is large, firing activity is more effectively evoked by incoming stimuli; if this difference tends to zero then transmission efficiency is diminished. For excitatory events $V^{\text{rev}} \simeq 0$ mV, and for inhibitory events $V^{\text{rev}} \simeq -70$ mV [86].

General anaesthetic drugs reduce neural activity of the cortex by boosting the strength of inhibitory synaptic events. In the WMF model, propofol-induced anaesthesia is modelled by prolonging the duration of the inhibitory postsynaptic potential (IPSP) by a dimensionless scale factor λ, assumed to be proportional to anaesthetic concentration. The effect of λ on IPSP is shown in Figure 3.1.

The two contrasting states in the WMF anaesthesia model are termed "high-firing" and "low-firing", and are taken to represent the "conscious" and "unconscious" states respectively. The transition from high-firing "conscious" state to a low-firing "unconscious" state can be either smooth or abrupt, depending on the anaesthetic inhibitory effect and on the level of background cortical excitation. For a certain range of anaesthetic concentrations, the model predicts multiple steady states for brain activity, and that at a critical

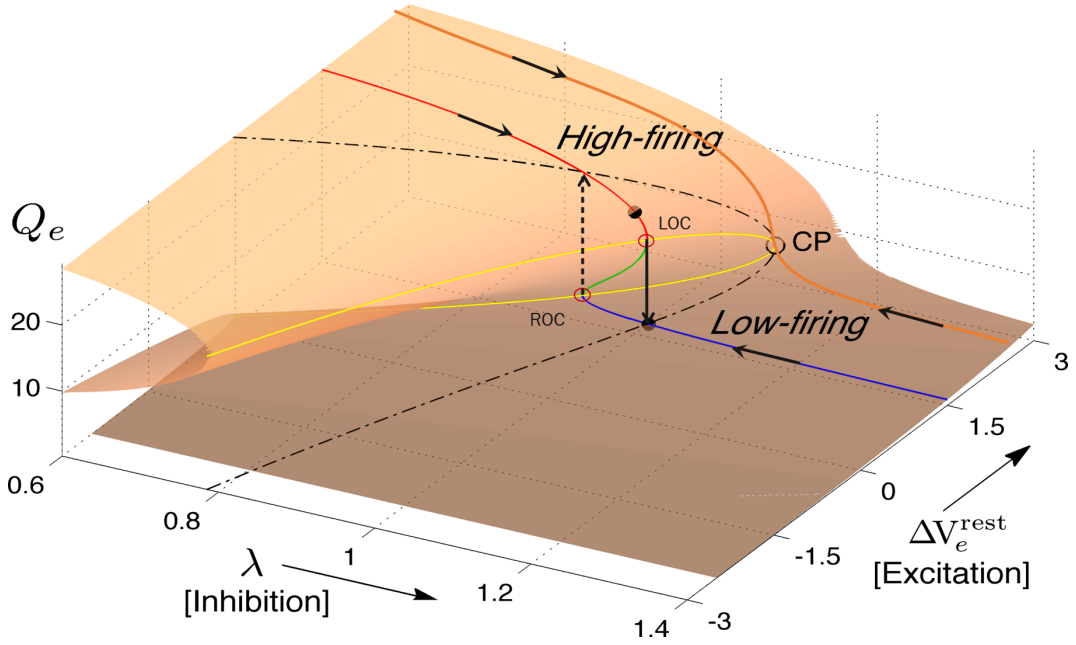

Figure 3.2: Steady-state manifold of excitatory firing rate Q_e as a function of anaesthetic inhibition (λ) and cortical tone (ΔV^{rest}). λ is used as control parameter and ΔV_e^{rest} is the additive offset representing cortical excitation. The yellow curve marks the edge of the reentrant fold; dashed-black curve shows the projection of this edge onto the lower and upper surfaces, bounding the zone of multiple steady states. Red-green-blue curve shows distribution of steady states for varying anaesthetic inhibition at constant cortical excitation. CP marks the critical point at which high- and low-firing states become indistinguishable. (From [90])

point of anaesthetic inhibition, the system can switch from a high-firing to a low-firing state.

The smooth or abrupt change of cortical activity at phase transition can be understood by studying the distribution of equilibrium states as a function of anaesthetic inhibition λ and background excitation ΔV_e^{rest} (see Fig. 3.2). These equilibrium states are located by setting all time and space dependencies in WMF equations (3.1)–(3.10) to zero; then there is no noise, no gap junction diffusion and no wave propagation through the cortical sheet. Figure 3.2 shows the manifold of equilibrium states as a function of anaesthetic inhibition λ and cortical tone ΔV_e^{rest}. The yellow line indicates the reentrant fold, which shows that for certain range of λ and ΔV_e^{rest} the cortex can access three alternative states: high-firing, low-firing, and an unstable intermediate state which separates the "conscious" (high-firing) and "unconscious" (low-firing) states [21, 89].

In this chapter, we analyse the loss of consciousness (LOC) and recovery of consciousness (ROC) phase transitions, focusing on the changes of variance and spectral power for small noise-induced voltage fluctuations on close approach to transition. Fluctuation statistics are predicted using Ornstein–Uhlenbeck theory, then validated using numerical

simulation of the stochastic WMF equations on a 25- × 25- cm square grid of cortical tissue.

Previous investigations of the WMF equations have studied emergence of temporal (Hopf) and spatial (Turing) bifurcations by respectively lowering the background (i.e., no anaesthetic) rate constant γ_i^0 of the inhibitory postsynaptic potential (IPSP), and by raising the diffusion strength D_2 that couples inhibitory neurons via gap junctions [21]. Since our emphasis here is on detecting and quantifying signs of critical slowing down near transition, we choose to suppress both temporal and spatial instabilities by setting $\gamma_i^0 = 100$ s^{-1} (no temporal oscillations via Hopf bifurcation) and $D_2 = 0$ cm^2 (no spatial pattering via Turing bifurcation).

3.1 Waikato mean-field model equations

The Waikato mean-field cortical model represents the flattened cortex as a 2D network of excitatory and inhibitory neurons (see Fig. 3.3). Neurons are connected locally through both gap junctions and neurotransmitter-mediated chemical synapses, and over distance via long-range myelinated axons. The cortex is represented as a continuum of excitable tissue whose parameters are coarse grained over a spatial extent of order 1 mm^2 which is the area of a cortical macrocolumn [90]. The spatially-averaged excitatory and inhibitory soma potentials V_e and V_i are expressed in the following pair of differential equations,

$$\begin{aligned}\tau_e \frac{\partial V_e(\vec{r},t)}{\partial t} =& V_e^{\text{rest}} + \Delta V_e^{\text{rest}} - V_e(\vec{r},t) \\ &+ [\rho_e \psi_{ee}(\vec{r},t)\Phi_{ee}(\vec{r},t) + \rho_i \psi_{ie}(\vec{r},t)\Phi_{ie}(\vec{r},t)] + D_1 \nabla^2 V_e(\vec{r},t) \end{aligned} \tag{3.1a}$$

$$\begin{aligned}\tau_i \frac{\partial V_i(\vec{r},t)}{\partial t} =& V_i^{\text{rest}} - V_i(\vec{r},t) \\ &+ [\rho_e \psi_{ei}(\vec{r},t)\Phi_{ei}(\vec{r},t) + \rho_i \psi_{ii}(\vec{r},t)\Phi_{ii}(\vec{r},t)] + D_2 \nabla^2 V_i(\vec{r},t) \end{aligned} \tag{3.1b}$$

Here $\tau_{e,i}$ is the soma (membrane) time constant, $V_{e,i}^{\text{rest}}$ is the soma resting voltage and $\rho_{e,i}$ is the chemical synaptic strength (see Table 3.1 for a list of symbol definitions and parameter values). Gap junction inputs are presented as diffusion terms $D_{1,2}\nabla^2 V_{e,i}$. The nabla-square symbols denotes the 2D Laplacian operator $\nabla^2 \equiv (\partial^2/\partial x^2 + \partial^2/\partial y^2)$. As explained above, we set diffusion to zero for the present work.

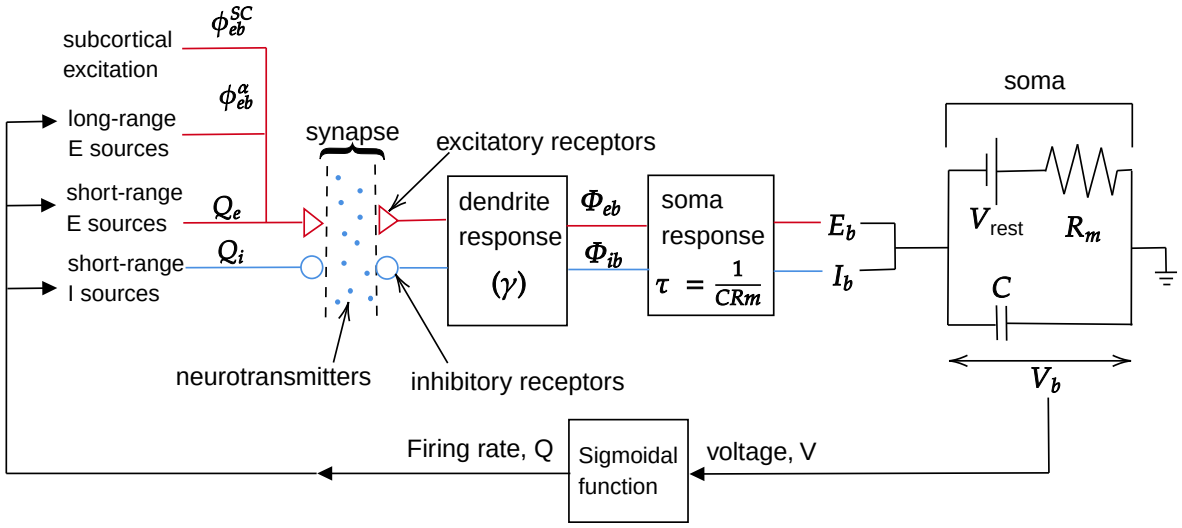

Figure 3.3: Schematic of the Waikato cortical model. The dendrite response is an alpha-function with rate constant γ; the soma response is an exponential function with time constant τ [98]

The terms in square brackets are chemical-synaptic voltage inputs. These strengths are scaled by dimensionless reversal-potential functions ψ_{ab} $(a = e, i; b = e, i)$,

$$\psi_{ab}(\vec{r}, t) = \frac{V_a^{\text{rev}} - V_b(\vec{r}, t)}{V_a^{\text{rev}} - V_b^{\text{rest}}} \tag{3.2}$$

The Φ_{eb}, Φ_{ib} functions are chemical-synaptic input fluxes obeying second-order differential equations,

$$\left(\frac{\partial}{\partial t} + \gamma_e\right)^2 \Phi_{eb}(\vec{r}, t) = \gamma_e^2 [N_{eb}^{\alpha} \phi_{eb}^{\alpha}(\vec{r}, t) + N_{eb}^{\beta} Q_e(\vec{r}, t) + \phi_{eb}^{\text{sc}}(\vec{r}, t)] \tag{3.3}$$

$$\left(\frac{\partial}{\partial t} + \gamma_i\right)^2 \Phi_{ib}(\vec{r}, t) = \gamma_i^2 N_{ib}^{\beta} Q_i(\vec{r}, t) \tag{3.4}$$

Here $\gamma_{e,i}$ are rate constants for the chemical synapses. The α and β superscripts label longer-range (cortico-cortical) and local connectivity with $N_{eb}^{\alpha}, N_{eb}^{\beta}$ being the number of these input connections, and $\phi_{eb}^{\alpha}, Q_{e,i}$ the long-range and local spike-rate fluxes. ϕ_{eb}^{sc} represents the unstructured subcortical stimulus entering from subcortical sources. This background stimulus is modelled as a small spatiotemporal white-noise variation ξ_{eb} about

a constant tone $\langle\phi_{eb}^{\rm sc}\rangle$,

$$\phi_{eb}^{\rm sc}(\vec{r},t) = \langle\phi_{eb}^{\rm sc}\rangle + a\sqrt{\langle\phi_{eb}^{\rm sc}\rangle}\xi_{eb}(\vec{r},t) \tag{3.5}$$

where a is a dimensionless noise-amplitude scale-factor, the $\xi_{eb}(\vec{r},t)$ is a zero-mean, Gaussian-distributed spatiotemporal white noise source, [62, 88]

$$\langle\xi(\vec{r},t)\rangle = 0 \tag{3.6}$$

$$\langle\xi_m(\vec{r},t)\xi_n(\vec{r}',t')\rangle = \delta_{mn}\delta_{\vec{r}\vec{r}'}\delta(t-t') \tag{3.7}$$

In numerical simulations we approximate continuous noise $\xi(\vec{r},t)$ with discrete noise, ξ^k, using a MATLAB random number generator `randn`,

$$\xi^k = \texttt{randn}/\sqrt{\Delta t} \tag{3.8}$$

where Δt is the time-step.

The local spike-rate fluxes $Q_{e,i}$ are determined by a sigmoidal mapping from soma voltage to firing rate,

$$Q_{e,i}(\vec{r},t) = \frac{Q_{e,i}^{\max}}{1+\exp[-C(V_{e,i}(\vec{r},t)) - \theta_{e,i})/\sigma_{e,i}]} \tag{3.9}$$

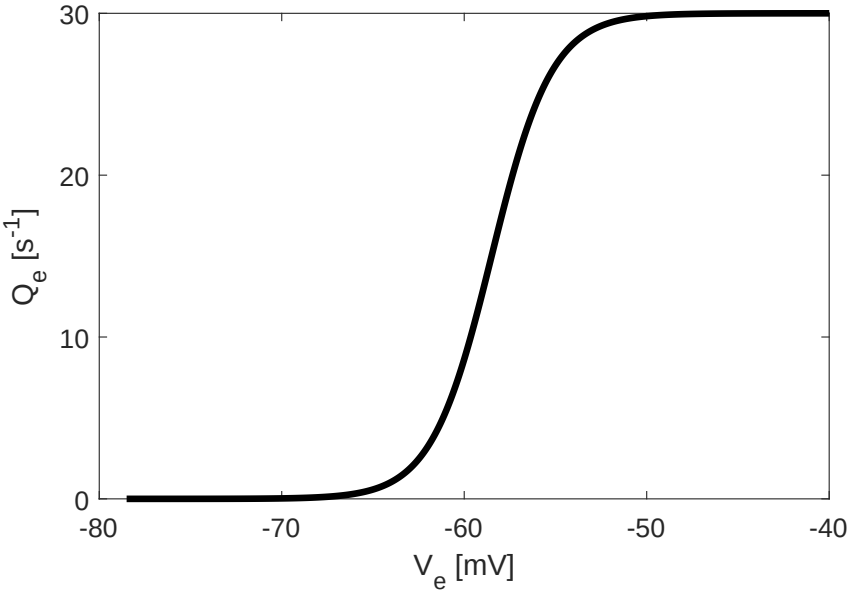

Figure 3.4: Sigmoidal mapping from soma voltage to firing rate

Table 3.1: Definitions of symbols and standard values of the WMF cortical model

Symbol	Description	Value	unit
τ_e, i	soma time constants	0.04, 0.04	s
$V_{e,i}^{\text{rest}}$	neuron resting potential	$-64, -64$	mV
$V_{e,i}^{\text{rev}}$	reversal potential at dendrite	0, -70	mV
ρ_e	excitatory synaptic gain	1.00×10^{-3}	mV
ρ_i^0	inhibitory synaptic gain at zero anaesthetic	-1.05×10^{-3}	mV
γ_e	excitatory rate constant	170	s^{-1}
γ_i^0	inhibitory synaptic gain at zero anaesthetic	100	s^{-1}
D_2	$i \leftrightarrow i$ gap-junction diffusive-coupling strength	0	cm^2
D_1	$e \leftrightarrow e$ gap-junction diffusive-coupling strength	$D_2/100$	cm^2
N_{eb}^{α}	longer-range $e \to b$ axonal connectivity	2000	...
$N_{eb,ib}^{\beta}$	local $e \to b$, $i \to b$ axonal connectivity	800, 600	...
$\langle \phi_{eb}^{\text{sc}} \rangle$	$e \to b$ tonic flux entering from subcortex	300	s^{-1}
a	subcortical noise scale factor	0.2	...
v	axonal conduction speed	140	cm s^{-1}
Λ_{eb}	inverse-length scale for $e \to b$ axonal connection	4	cm^{-1}
$Q_{e,i}^{\max}$	maximum firing rate	30, 60	s^{-1}
$\theta_{e,i}$	sigmoid threshold voltage	$-58.5, -58.5$	mV
$\sigma_{e,i}$	standard deviation for threshold	3, 5	mV
$L_{x,y}$	length and width of cortical sheet	25, 25	cm

where $C = \pi/3$, $\theta_{e,i}$ is population-average threshold for firing, $\sigma_{e,i}$ is its standard deviation and $Q_{e,i}^{\max}$ is the maximum firing rate. The sigmoidal $V_e \to Q_e$ mapping is illustrated in Fig. 3.4.

The cortico-cortical flux ϕ_{eb}^{α} is generated by distant excitatory sources $Q_{e,i}$ and obeys a 2-D damped wave equation,

$$\left[\left(\frac{\partial}{\partial t} + v\Lambda_{eb}\right)^2 - v^2\nabla^2\right]\phi_{eb}^{\alpha}(\vec{r},t) = (v\Lambda_{eb})^2 Q_e(\vec{r},t) \tag{3.10}$$

with Λ_{eb} being the inverse-length scale for axonal connectivity.

3.2 Modelling anaesthesia

As depicted in Fig. 3.1, the anaesthetic propofol prolongs the duration of inhibitory post synaptic potential (IPSP) without changing its peak amplitude. The propofol effect is modelled by scaling both the inhibitory rate constant γ_i and synaptic strength ρ_i by a dimensionless scale factor λ [90],

$$\gamma_i = \gamma_i^0/\lambda, \quad \rho_i = \lambda\rho_i^0 \tag{3.11}$$

where γ_i^0 and ρ_i^0 are default values with no anaesthetic presence, so $\lambda = 1$ corresponds to no propofol effect, and $(\lambda - 1)$ is proportional to propofol concentration. An increase of λ results in a decrease of γ_i and rise of ρ_i, enlarging the area of the IPSP response linearly with propofol concentration while maintaining a constant IPSP peak height. The IPSP responses shown in Fig. 3.1 are normalised alpha functions of the form

$$\mathrm{IPSP}(t) \sim \rho_i \gamma_i^2 t e^{-\gamma_i t} \quad \xrightarrow[\text{effect } \lambda]{\text{anaesthetic}} \quad \lambda \rho_i^0 \left(\frac{\gamma_i^0}{\lambda}\right)^2 t e^{-(\gamma_i^0/\lambda)t}$$

3.3 Equilibrium states

The homogeneous equilibrium states of the Waikato mean-field model are evaluated by setting the noise stimulus in Eq. (3.5) to zero and zeroing all space and time derivatives in the differential equations ($\nabla^2 = 0; \partial/\partial t = 0; \partial^2/\partial t^2 = 0$). Then the equations are solved numerically to locate the steady state firing rates (Q_e, Q_i) of the excitatory and inhibitory neural populations. Figure 3.2 shows the steady state manifold as a function of anaesthetic effect λ and excitation $\Delta V_e^{\mathrm{rest}}$, and Fig. 3.5 shows the steady state diagram for five different values of $\Delta V_e^{\mathrm{rest}}$. Each trajectory forms a reverse S-shaped reentrance, where top branch corresponds to the "conscious" high-firing state, and bottom branch corresponds to the "anaesthetised" low-firing state.

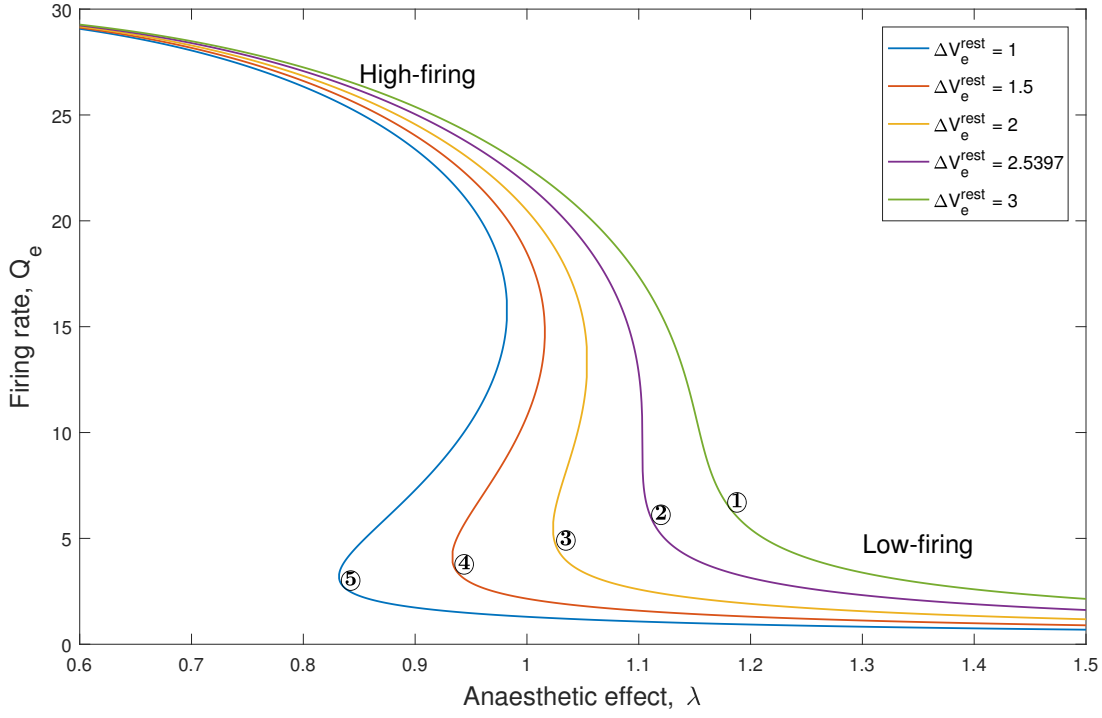

Figure 3.5: Steady state diagram of firing rate, Q_e, for five steps of $\Delta V_e^{\mathrm{rest}}$

3.4 Linear stability analysis

We wish to examine the linear stability properties of a given homogeneous steady state. We define the eight-variable state vector, $X = [V_e, V_i, \Phi_{eb}, \dot{\Phi}_{eb}, \Phi_{ib}, \dot{\Phi}_{eb}, \phi_{eb}, \dot{\phi}_{eb}]^{\mathrm{T}}$, then interrogate the stability of a given steady state X^0 by adding a small spatiotemporal disturbance,

$$X(\vec{r}, t) = X^{(0)} + \delta X(\vec{r}, t) \tag{3.12}$$

where δX is a plane-wave perturbation,

$$\delta X(\vec{r}, t) = \delta X(t)\, e^{i\vec{q}\cdot\vec{r}} = \delta X(0)\, e^{\Lambda t}\, e^{i\vec{q}\cdot\vec{r}} \tag{3.13}$$

with $\vec{q}$ being a wave vector with wave number $q = |\vec{q}|$. Λ is an eigenvalue whose real part determines the growth rate of the $\delta X(0)$ perturbation: if $\mathrm{Re}(\Lambda) > 0$, then the steady state is unstable. After substituting Eq. (3.12) into the WMF equations, then linearising, we obtain the matrix equation,

$$\frac{d}{dt}\delta X(\vec{r}, t) = \mathbf{J}(q)\, \delta X(\vec{r}, t) \tag{3.14}$$

where $\mathbf{J}$ is the 8×8 Jacobian matrix evaluated at the given steady state (see Appendix B for a listing of the Jacobian matrix elements). The ∇^2 Laplacians for excitatory and inhibitory diffusion and wave propagation appear in $\mathbf{J}$ as $-q^2$ terms. In this analysis, we suppress spatial instabilities, therefore diffusion terms are disabled ($D_1, D_2 = 0$), but we retain the wave equation.

3.4.1 Eigenvalue analysis

The eigenvalues characterise the linear stability of a given equilibrium state of the homogeneous cortex. Since the eigenvalues are derived from the 8×8 Jacobian matrix, there will be eight eigenvalues, each of which will be wavenumber dependent. For each wavenumber we rank the eigenvalues in terms of their real part, $\mathrm{Re}(\Lambda_1) > \mathrm{Re}(\Lambda_2) > ... > \mathrm{Re}(\Lambda_8)$ and

select the dominant eigenvalue $\Lambda \equiv \Lambda_1$ since it represents the most strongly growing (or most slowly decaying) mode at a given spatial frequency. Writing Λ in terms of its real and imaginary parts,

$$\Lambda(q) = \alpha(q) + i\omega(q)$$

If α is negative, the steady state is stable (exponential damping); if α is positive, the equilibrium is unstable. Near the transition points the eigenvalues approach zero, so these points become marginally stable meaning that small perturbations produce a prolonged response.

The stability of bifurcations marking the LOC (loss of consciousness) and ROC (recovery of consciousness) transition points are analysed in Figures 3.6 and 3.7 respectively. For the LOC transition, the dominant eigenvalue of the top branch is precisely zero at $q = 0$, and the same is true for the ROC transition (Fig. 3.7) on the bottom branch. At both LOC and ROC, α and ω become zero at $q = 0$ indicating that the transition is a saddle–node bifurcation. This indicates that the lifetimes and amplitudes of noise-induced fluctuations are predicted to increase significantly as the transition points are closely approached.

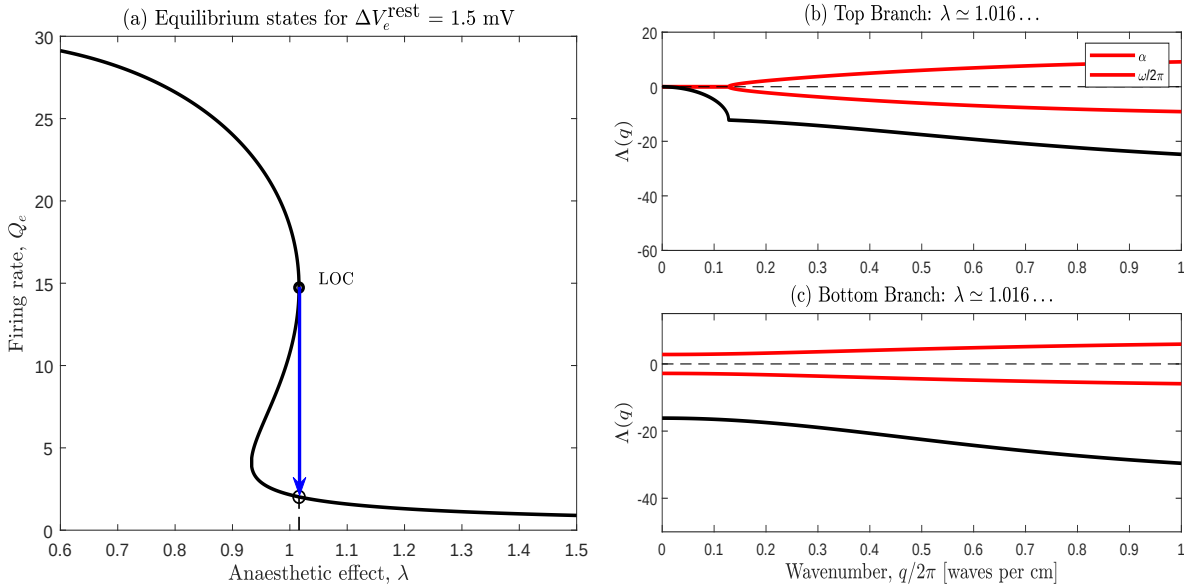

Figure 3.6: Linear stability predictions for homogeneous Waikato mean-field cortical model at the LOC transition point $\lambda \simeq 1.0160\,6379\,0864\,507$. (a) Steady state trajectory for $\Delta V_e^{\text{rest}} = 1.5$ mV with LOC transition point (solid black circle). (b), (c) Eigenvalue distribution: black and red curves shows the real (α) and imaginary (ω) parts respectively of the dominant eigenvalue (Λ) as a function wave number q. (b) Top branch is marginally stable as Λ approaches zero from below (at $q = 0$). (c) Bottom branch is strongly stable ($\alpha < 0$)

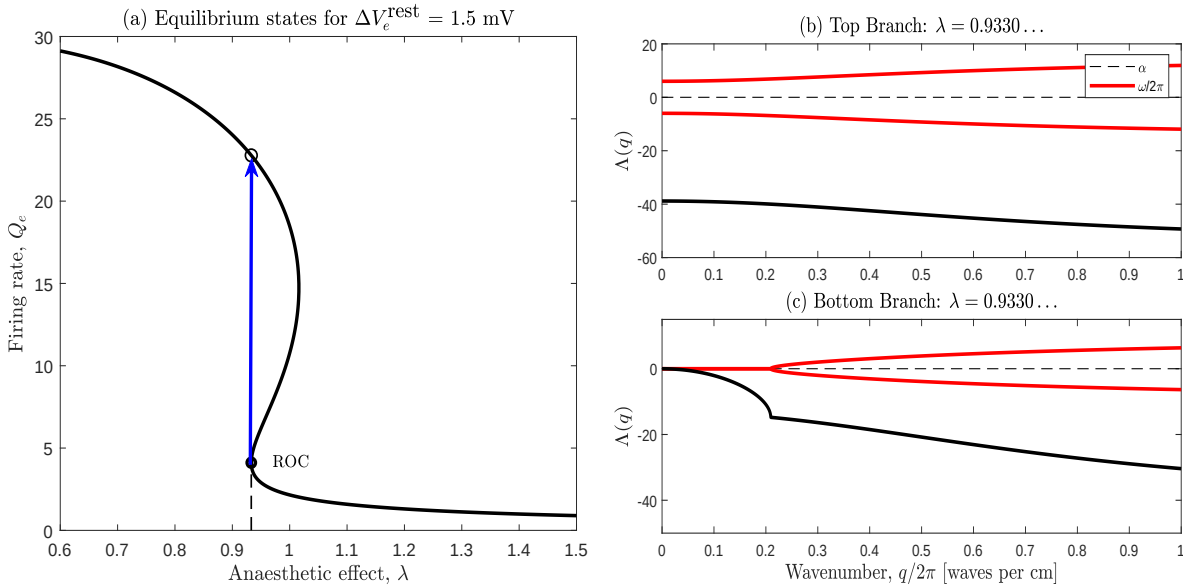

Figure 3.7: Linear stability predictions for WMF model at the ROC transition point $\lambda \simeq 0.9330\,1029\,7130\,724$. (a) Steady states for trajectory of $\Delta V_e^{\text{rest}} = 1.5$ mV with ROC transition point (solid black circle). Top branch (b) is strongly stable, the bottom branch (c) is marginally stable as α and ω approach zero for $q \to 0$

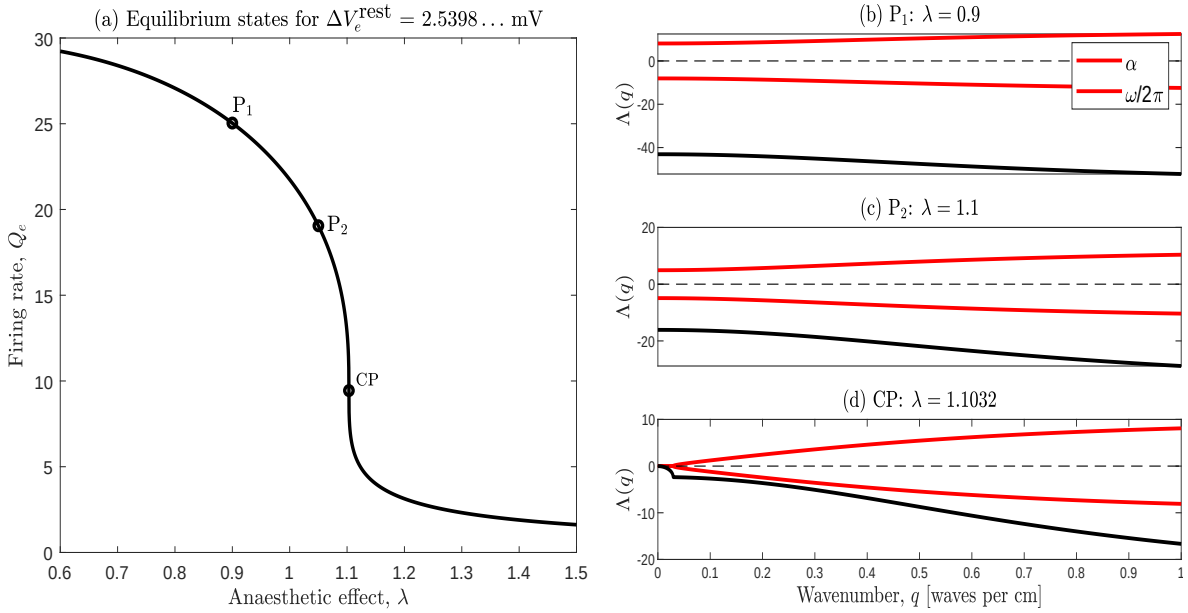

Figure 3.8: Stability predictions of WMF model approaching the critical point CP at (Eq. 3.15)). (a) Equilibrium states and selected points. (b) (c) Dispersion curves for points away from the critical point and (d) at the critical point (CP). P_1 is strongly stable; P_2 is weakly stable. At the critical point, eigenvalue components $(\alpha, \omega) \to (0, 0)$ at zero wavenumber (i.e., infinite wavelength)

Figure 3.8 shows the eigenvalue dispersion graphs for points along the trajectory P_1-P_2-CP passing through the critical point. P_1 and P_2 are points along the trajectory, where P_2 is closer to the CP than P_1. This codimension-2 cusp marks the point where the

three-root region evolves into a "single" root. Locating this point requires simultaneous tuning of λ and ΔV_e^{rest} through the three root region of the equilibrium manifold until the narrowing peninsula of distinct multiple roots converges into three identical roots. Its coordinate, accurate to double precision, is

$$(\lambda^{\text{CP}}, \Delta V_e^{\text{rest, CP}}) \simeq (1.1032\,3341\,8766\,981,\ 2.5397\,7880\,8756\,027\ \text{mV}) \tag{3.15}$$

These turning point coordinates need to be as accurate as possible in order to quantify variance vs ϵ power-law divergences (refer Section 3.6). However the true turning point cannot be locate to be better than ∼16 significant figures due to numerical limitations in MATLAB (double precision). It is evident from Fig. 3.8(a) that point P_1 is strongly stable as $\alpha(q)$ is significantly negative across all wavenumbers. At P_2, α approaches (but does not reach) zero as $q \to 0$ as the P_2 equilibrium is closer to the critical point. At the critical point, α and ω are precisely zero at $q = 0$, implying infinitely prolonged perturbative recovery times and extreme low frequency responsiveness corresponding to a "resonance" at zero frequency. Note that unlike the first-order "jump" transitions at LOC and ROC, the passage through CP is smooth and continuous, so does not exhibit hysteresis separation between LOC and ROC transitions since these effectively merge at CP.

3.4.2 Correlation time

The correlation time, t_{corr} determines the $(1/e)$ time period over which fluctuations from steady state die away, and can be defined as the inverse of the dominant eigenvalue decay rate,

$$t_{\text{corr}} = -\frac{1}{\text{Re}(\Lambda)} \tag{3.16}$$

Figure 3.9 illustrates the correlation t_{corr} in the vicinity of the LOC, ROC, and CP phase transition points. Correlation times increase on approach, diverging to infinity as $\text{Re}(\Lambda) \to 0$ at transition. Compared to LOC and ROC, critical point correlation times show a much larger domain of slowed decay. This increase of correlation time near phase transition is often described as "critical slowing down".

Close to each transition point the correlation time graphs show a break in the flow (see zoomed views in Figs. 3.9–3.11). This deviation corresponds to a change in the eigenvalue

structure: real parts of the first and second eigenvalues have same value until the break point, then the dominant eigenvalue approaches zero while second eigenvalue drops away to more negative values.

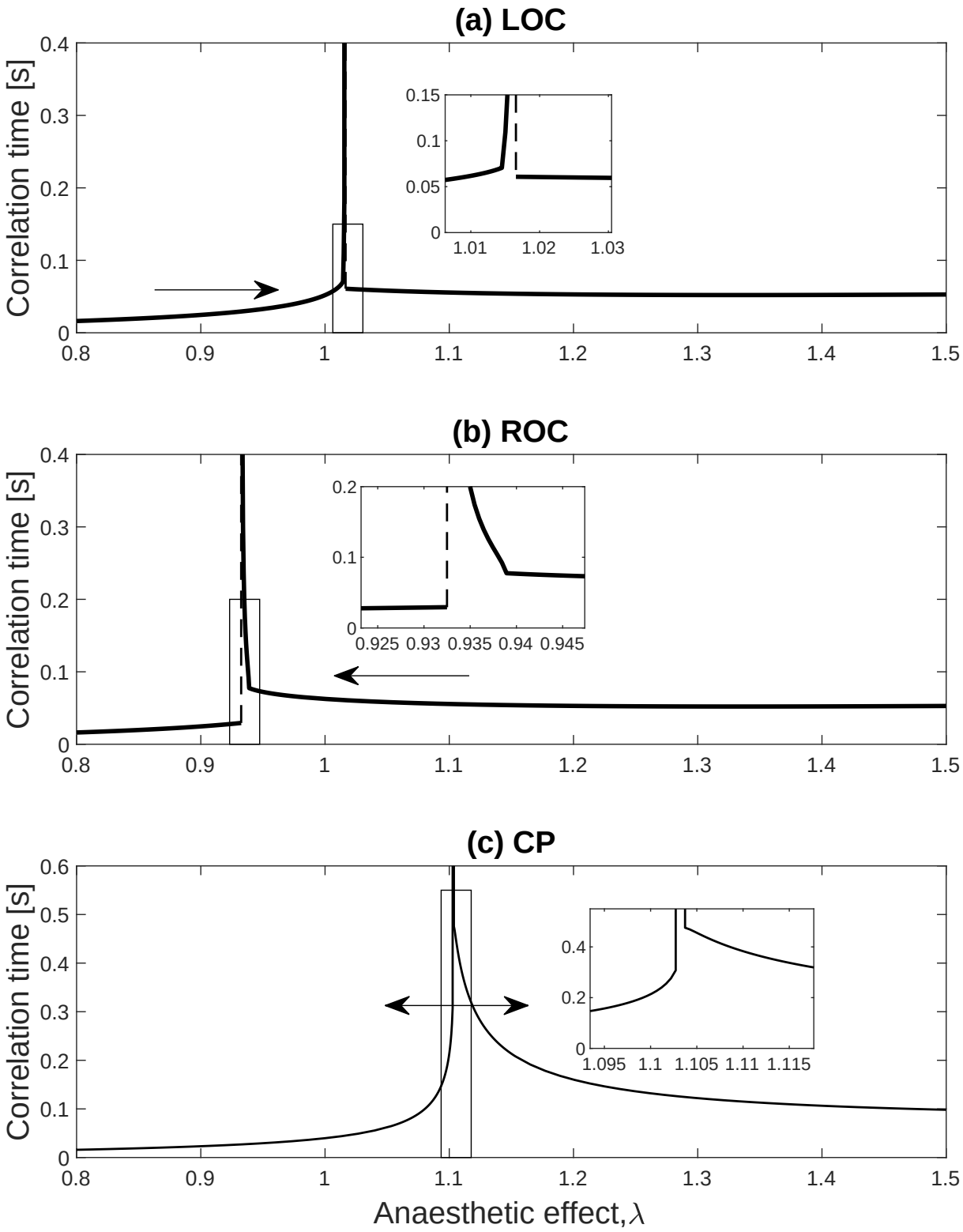

Figure 3.9: Change of theoretical correlation time on close approach to anaesthetic induced phase transitions: (a) loss of consciousness; (b) recovery of consciousness; (c) critical point. The domain of prolonged slowing is much larger for the CP transition than for LOC or ROC

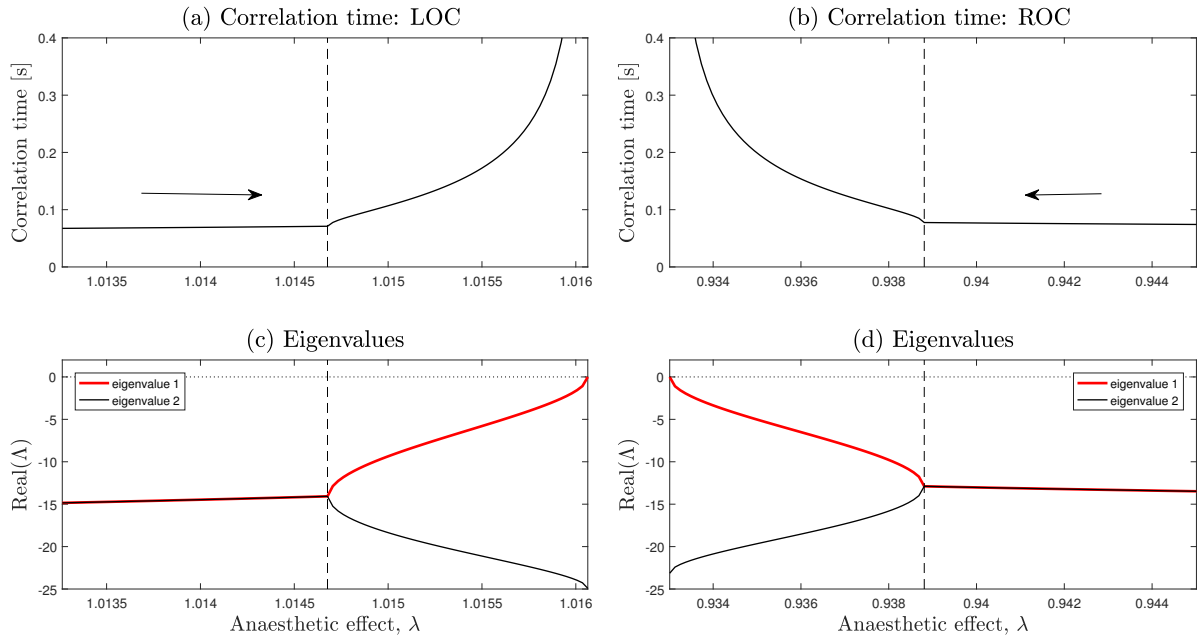

Figure 3.10: Correlation time (a), (b) and eigenvalue (c), (d) (dominant (red) and second (black)) variation on close approach to LOC and ROC transition points. Dashed line marks the break point

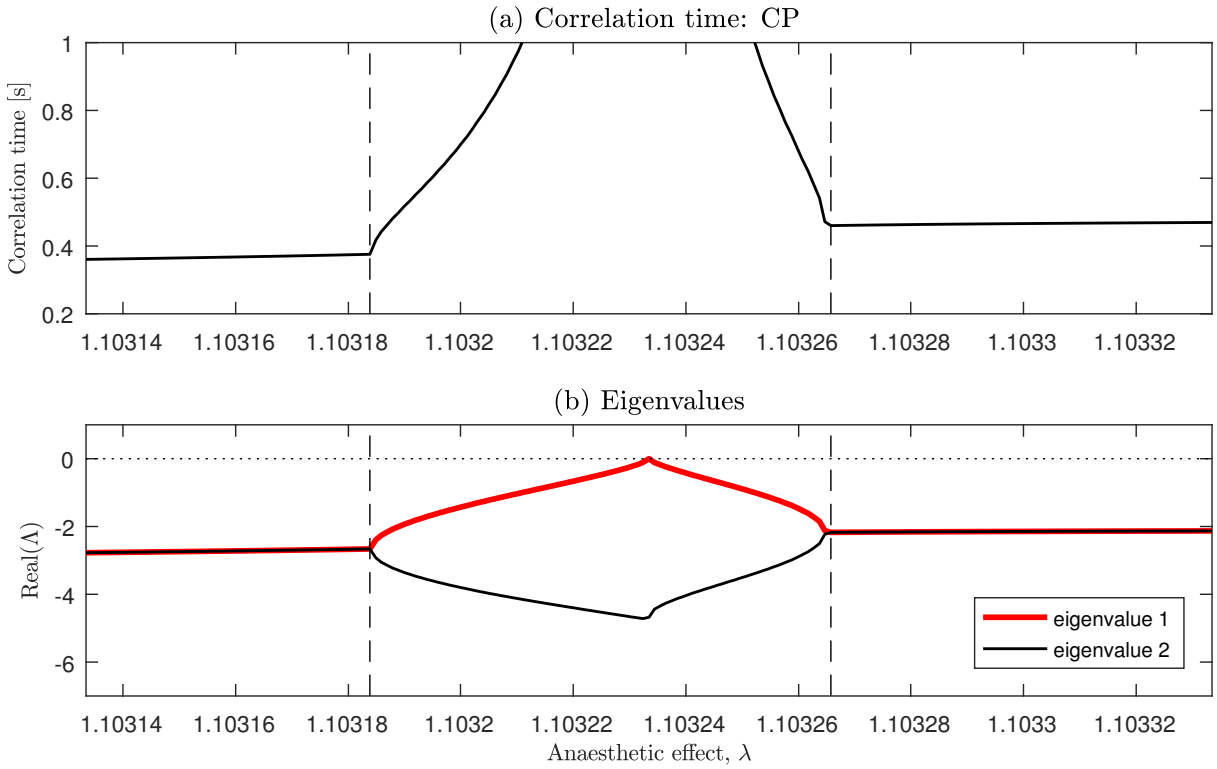

Figure 3.11: Correlation time (a) and eigenvalue (b) (dominant (red) and second (black)) variation on close approach to CP. The correlation time has distinct break points when approaching from left ($\lambda < \lambda_{CP}$) right ($\lambda > \lambda_{CP}$)

3.4.3 Theoretical expression for spatial variance

Gardiner [29] gives an implicit matrix equation for the covariance matrix, $\mathbf{\Sigma}$ of a multivariate noise-driven Ornstein–Uhlenbeck (OU) process,

$$\mathbf{A}(q)\mathbf{\Sigma}(q) + \mathbf{\Sigma}(q)\mathbf{A}^{\mathrm{T}}(q) = \mathbf{D} \tag{3.17}$$

where the drift matrix $\mathbf{A} = -\mathbf{J}$, the negative of the Jacobian matrix, and $\mathbf{D}$ is the 8×8 diffusion (noise intensity) matrix. Only the (4, 4) element of $\mathbf{D}$ is non-zero,

$$D(i,j) = \begin{cases} \gamma_e^4 a^2 \langle \phi_{eb}^{\mathrm{sc}} \rangle, & \text{for} \quad i = 4,\ j = 4 \\ 0, & \text{otherwise} \end{cases} \tag{3.18}$$

For the special case of a two-variable OU process, Eq. (3.17) can be solved explicitly for the $\mathbf{\Sigma}$ covariance matrix (e.g., the FHN model, see Eq. (2.15)), but for our eight-variable linearised WMF equation set there is no analytic solution, so must be solved numerically. Equation (3.17) is a form of Lyapunov equation that can be solved in MATLAB using the `sylvester` function,

$$\mathbf{\Sigma} = \texttt{sylvester}(\mathbf{A}, \mathbf{A}^{\mathrm{T}}, \mathbf{D}) \tag{3.19}$$

The (1, 1) element of the covariance matrix gives the fluctuation variance of excitatory soma potentials V_e at wave number q,

$$\sigma_{V_e}^2(q) = \Sigma_{11}(q)$$

and the spatial variance across the cortical grid is obtained by averaging across the full range of accessible wavenumbers between $q_{\min}$ and $q_{\max}$,

$$\sigma_{V_e,\mathrm{theory}}^2 = \frac{\int_{q_y} \int_{q_x} \Sigma_{11}(q)\, dq_x\, dq_y}{\int_{q_y} \int_{q_x} dq_x\, dq_y} \tag{3.20}$$

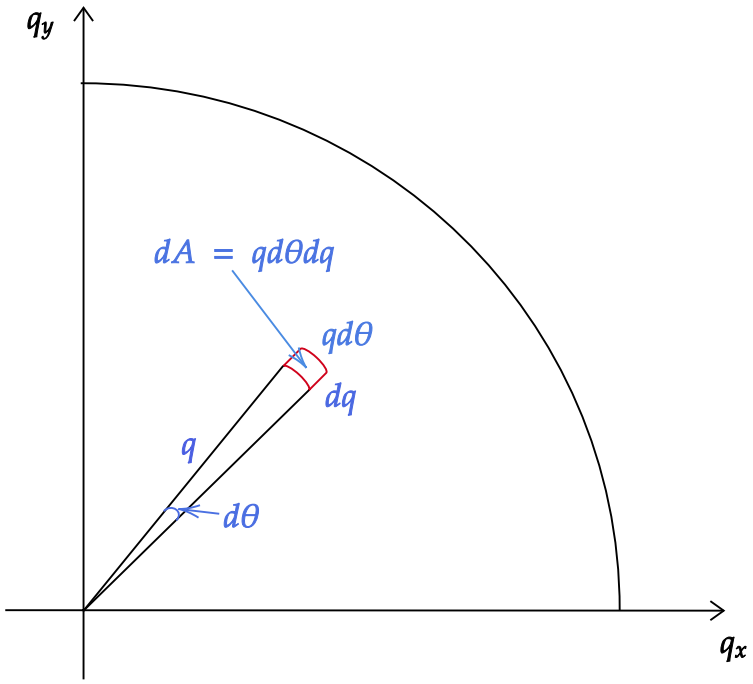

Figure 3.12: Demonstration of radial integration.

where $q^2 = q_x^2 + q_y^2$, and Σ_{11} has cylindrical symmetry in (q_x, q_y) space since it only depends on q^2. Converting to polar coordinates, the double integral of $\Sigma_{11}(q)$ can be rewritten,

$$\int_{q_y}\int_{q_x} \Sigma_{11}(q)\, dq_x\, dq_y = \int_{\theta=0}^{2\pi}\int_{q}^{q_{\max}} \Sigma_{11}(q)\, q\, dq\, d\theta \tag{3.21}$$

$$= 2\pi \int_{q}^{q_{\max}} q\, \Sigma_{11}(q)\, dq \tag{3.22}$$

Similarly the double integral of q can be written as,

$$\int_{q_y}\int_{q_x} dq_x\, dq_y = 2\pi \int_{q}^{q_{\max}} q\, dq \tag{3.23}$$

$$= 2\pi \frac{q^2}{2}\Big|_{q_{\min}}^{q_{\max}} = \frac{2\pi}{2}(q_{\max}^2 - q_{\min}^2) \tag{3.24}$$

giving

$$\sigma^2_{V_e,\text{theory}} = \frac{2}{(q_{\max}^2 - q_{\min}^2)} \int_{q=q_{\min}}^{q_{\max}} \Sigma_{11}(q)\, q\, dq \tag{3.25}$$

where $q_{\min}$ is set by the side length $L = L_x = L_y$ of the square cortical grid,

$$q_{\min} = \frac{2\pi}{L} \qquad \text{(longest representable wavelength} = L) \tag{3.26}$$

and $q_{\max}$ is determined by the grid resolution $\Delta x = \Delta y = L/N_x = L/N_y$

$$q_{\max} = \frac{2\pi}{2\Delta x} \qquad \text{(shortest representable wavelength} = 2\Delta x) \tag{3.27}$$

with $N_{x,y}$ being the number of cells along the (x, y) axis directions respectively. Table 3.2 summarizes the three different grid configurations used in our numerical experiments:

- 250×250 resolution, $L = 25$ cm (for variance calculations)
- 60×60 resolution, $L = 25$ cm (for spectral calculations)
- 60×60 resolution, $L = 250$ cm ("giant brain" tests near CP opalescent point)

We choose $L = 25$ cm as a reasonable side length for the flattened cortical tissue of an adult cortex, and $L = 250$ cm as a "giant" test case to allow exploration of the critical point.

We find that setting $q_{\min} \simeq 0$ makes little difference to the variance and spectral calculations, except when closely approaching the critical point. However, to obtain a good match between theory and simulation we needed to raise $q_{\max}$ (see Table 3.2). This adjustment is probably partly compensating for spatial aliasing effects in which high spatial frequency components $q > q_{\max}$ are reflected about the $q_{\max}$ Nyquist mirror to appear as (spurious) $q < q_{\max}$ activity. This is consistent with our finding that the higher resolution grid (250×250) requires a smaller relative adjustment than the lower resolution (60×60) grid.

The theoretical fluctuation variance of the excitatory firing rate is calculated by linearising about the steady-state fixed point on the sigmoidal $V_e \to Q_e$ curve (Fig. 3.4).

Table 3.2: The calculated and used values for $q_{\min}$ and $q_{\max}$

Grid	L	Δx	Theory	
	[cm]	[cm]	$q_{\min}/2\pi$ [cm^{-1}]	$q_{\max}/2\pi$ [cm^{-1}]
250×250	25	0.1	0.04	5
60×60	25	0.417	0.04	1.2
60×60	250	4.17	0.004	0.12

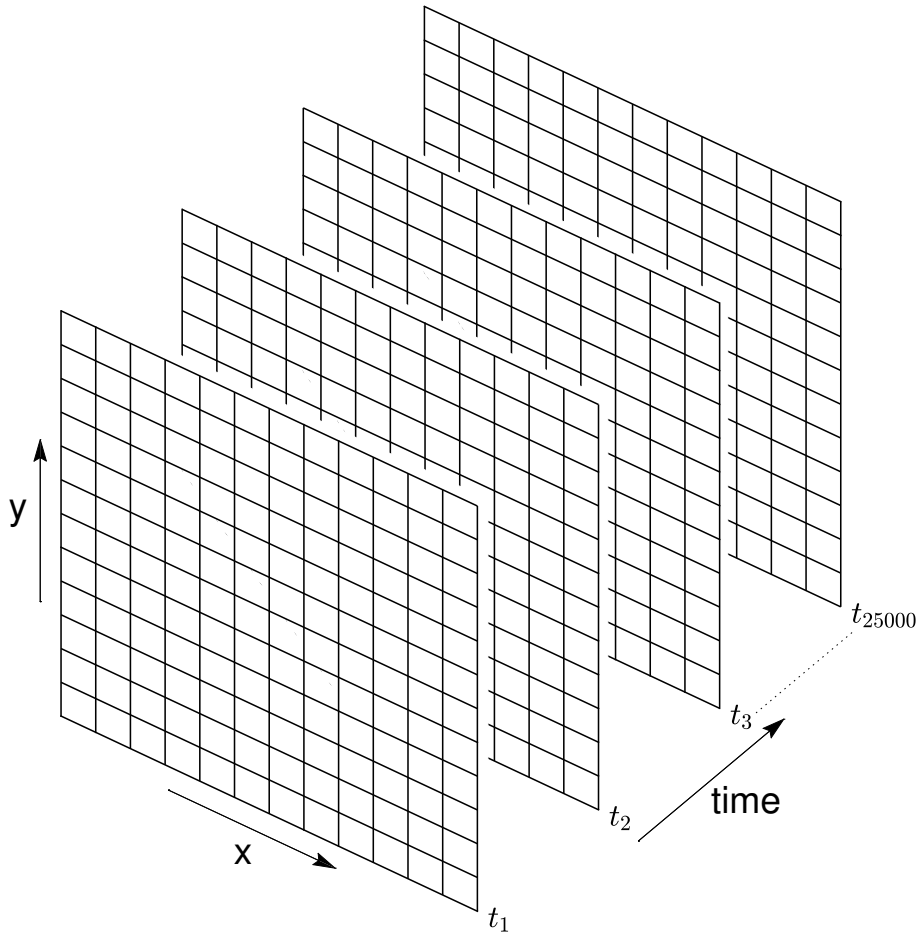

Figure 3.13: Illustration of the grid used for numerical experiments. Simulations are run on a 250×250 square grid with spatial resolution $\Delta x = \Delta y = 1$ mm (length of the grid = 25 cm). The variance is calculated across the grid for one time instance, then averaged across all 25,000 time-samples

This allows us to map voltage standard deviation σ_{V_e} to firing rate standard deviation σ_{Q_e},

$$\sigma_{Q_e,\text{theory}} = \left.\frac{dQ_e}{dV_e}\right|_{\text{ss}} \sigma_{V_e,\text{theory}} \tag{3.28}$$

and hence the variance mapping reads

$$\sigma^2_{Q_e,\text{theory}} = \left(\left.\frac{dQ_e}{dV_e}\right|_{\text{ss}}\right)^2 \sigma^2_{V_e,\text{theory}} \tag{3.29}$$

This expected to be valid provided that fluctuations remain small.

We test the theoretical predictions using numerical simulations of a 25- $\times$ 25-cm cortex on a 250×250 grid, giving an areal resolution of 1 mm^2 corresponding to the nominal area of a cortical macrocolumn. The time-step is set at $\Delta t = 0.4$ ms, generating 2500

grid updates per second. We run the simulation for 20 s but only analyse the final 10 s of $V_e(x, y, t)$ and $Q_e(x, y, t)$ membrane voltage and firing rate data. We compute the spatial variance at each time step, then average across all time samples. For the simulated membrane voltage V_e, the fluctuation variance is given by,

$$\sigma^2_{V_e,\text{sim}} = \frac{1}{N}\sum_{i=0}^{N-1} \text{var}\{V_e(x, y)\}_i \tag{3.30}$$

and for firing rate Q_e,

$$\sigma^2_{Q_e,\text{sim}} = \frac{1}{N}\sum_{i=0}^{N-1} \text{var}\{Q_e(x, y)\}_i \tag{3.31}$$

where index i denotes time $t = i\Delta t$, and N =25,000 is the number of grid-slice samples.

3.5 Variance analysis

3.5.1 Loss of consciousness (LOC)

For a closely-spaced range of λ values, we step the anaesthetic effect through the high-firing upper branch of the $\Delta V_e^{\text{rest}} = 1.5$ mV trajectory (arrowed curve of Figure 3.14(a)) towards the LOC turning point, then jump (dashed vertical line) to follow the trajectory

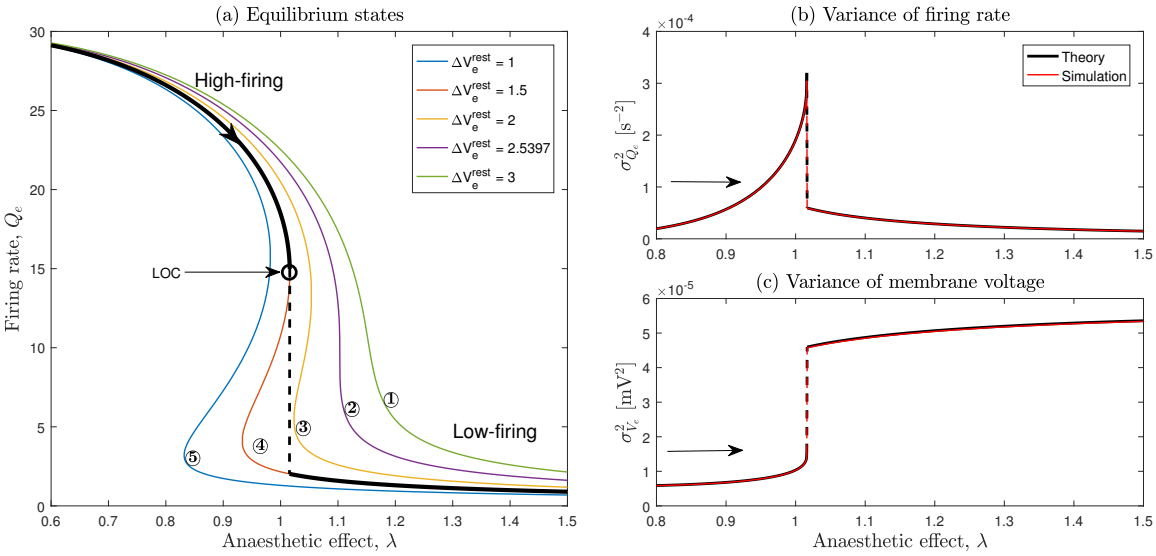

Figure 3.14: WMF fluctuation variance for passage through anaesthesia LOC. (a) Steady state trajectories for five values of ΔV_e^{rest}. Cortex approaches LOC along the $\Delta V_e^{\text{rest}} = 1.5$ mV top branch (arrow), then makes a jump transition (dashed vertical) to the bottom branch. (b), (c) Variance versus λ trends for fluctuations in firing rate (upper panel) and membrane voltage (lower panel), comparing OU prediction (black) with numerical simulation (red)

along the low-firing bottom branch. For each value of λ, we compute the OU predictions for V_e and Q_e fluctuation power (Eqs. (3.25), (3.29)), and compare with spatial variance values measured directly from the 250×250 grid and averaged over 10 s (i.e., 25,000 temporal samples at each equilibrium point).

The spatial variance trends for noise-induced fluctuations are illustrated in Fig. 3.14(b) and (c). We observe strong growth in fluctuation power in Q_e and V_e for close approach to the LOC transition point. The simulation measurements track the OU predictions very well.

3.5.2 Recovery of consciousness (ROC)

Now the transition point is approached from right to left along the bottom branch by decreasing the anaesthetic effect, λ. We note that the ROC bifurcation point occurs at a lower anaesthetic concentration compared to LOC (this is anaesthetic hysteresis: the patient awakens at a lower concentration than that required to put her to sleep). The trajectory of steady states ROC (for $\Delta V_e^{\text{rest}} = 1.5$ mV) is shown in Figure 3.15(a) (black arrowed curve). At ROC, the system jumps to the high-firing upper branch (dashed vertical line).

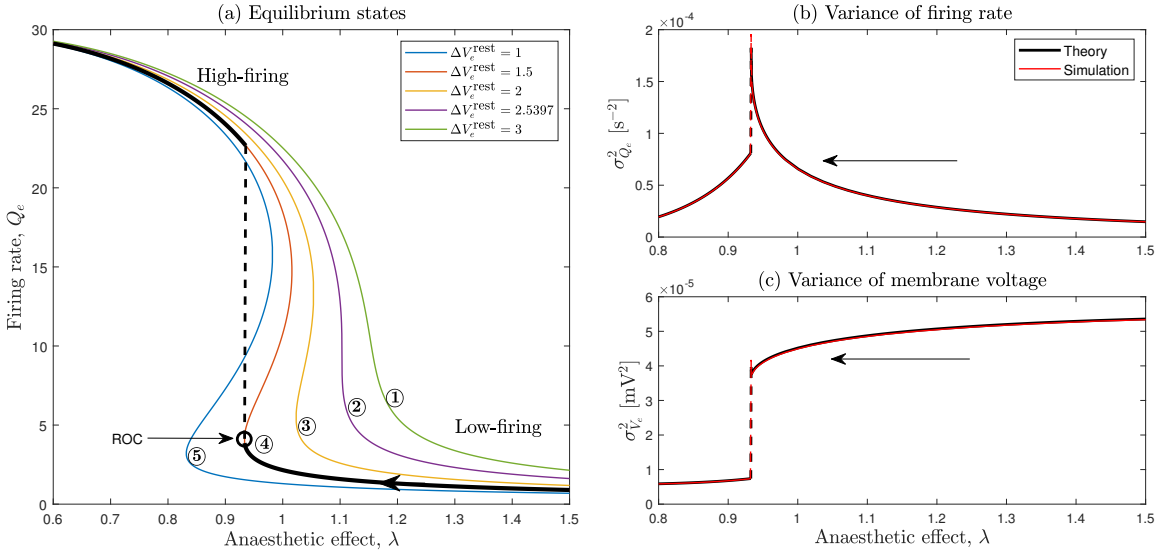

Figure 3.15: WMF fluctuation variance for passage through anaesthesia ROC. (a) Cortex approaches ROC transition through the $\Delta V_e^{\text{rest}} = 1.5$ mV trajectory along the bottom-branch (arrow), then jumps to the top branch (dashed line). (b), (c) Fluctuation variance of firing rate (upper panel) and membrane voltage (lower panel), where OU predictions (black) and numerical simulations (red) are compared

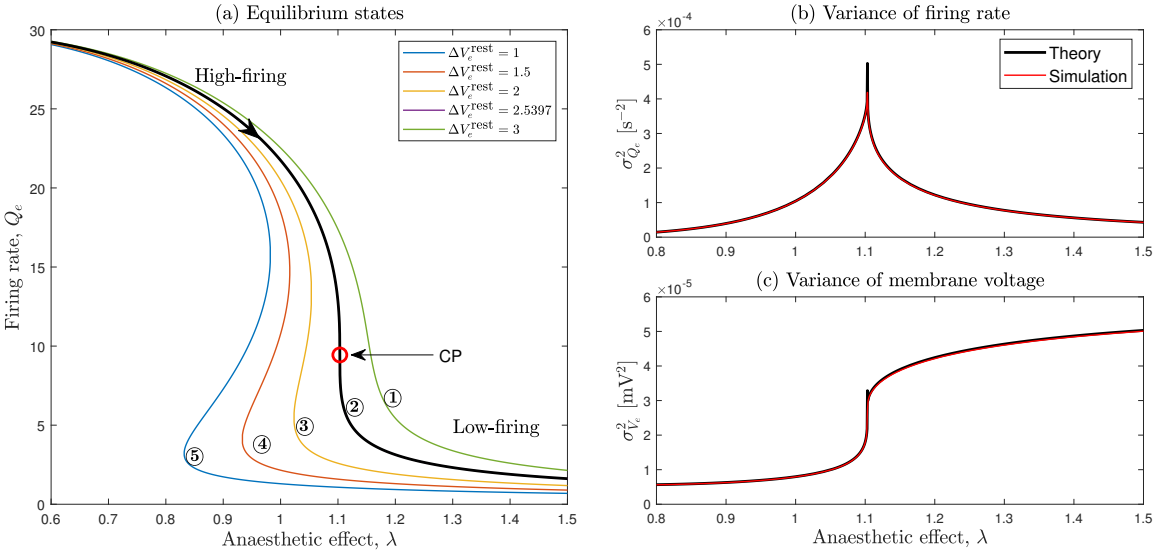

Figure 3.16: WMF fluctuation variance along the trajectory through opalescent point CP. (a) Equilibrium states vs anaesthetic inhibition for stepped values of ΔV_e^{rest}. (b) Fluctuation variance of excitatory firing rate, Q_e. (c) Fluctuation variance of excitatory soma voltage, V_e

Panels (b) and (c) illustrate the variance trends for firing rate and membrane voltage respectively. As was the case for LOC, we see pronounced increases in fluctuation power as the saddle–node bifurcation point is closely approached. Simulations results follow theoretical predictions quite well.

3.5.3 Critical fluctuations through the opalescent point (CP)

The $\Delta V_e^{\text{rest}} = \Delta V_e^{\text{rest, CP}}$ trajectory through CP is highlighted in black in Fig. 3.16(a). We increase λ in small steps, starting from the high-firing branch. Panels (b) and (c) illustrate the variance trends for firing rate and membrane voltage respectively. We see increases in fluctuation power on close approach to the critical point. Simulations results follow the theoretical predictions well.

3.6 Scaling law divergence for WMF fluctuation variance

In this section, we wish to establish the scaling laws governing the divergence of fluctuation power near transition. For each of LOC, ROC, and CP, we compute theoretical and numerical variances var$\{Q_e\}$, and var$\{V_e\}$ as a function of epsilon,

$$\epsilon = |\lambda - \lambda_{\text{crit}}|/\lambda_{\text{crit}} \tag{3.32}$$

the normalised distance to the relevant turning point, and plot the results on logarithmic scales in Figures 3.17 and 3.18. The measured scaling-law exponents for theoretical variance are listed in Table 3.3. All three transitions exhibit scale-free divergences with variance $\sim 1/\epsilon^{\alpha}$.

The exponents for LOC and ROC are closely similar for both membrane voltage V_e and firing rate Q_e fluctuations: $\alpha \simeq 0.0075$. The rate of divergence near the CP opalescent point $\alpha^{\mathrm{CP}} \simeq 0.02$, about three times steeper than for LOC and ROC. We attribute this to the fact that CP is a double-sided saddle-node bifurcation.

We plotted the variance trends for a wide range of ϵ values. If ϵ is set too low ($< 10^{-9}$), the theoretical variance calculations become saturated (not shown). This behaviour is probably due to the limitations of double-precision calculations in MATLAB.

We note that the WMF exponent values listed in Table 3.3 are much lower than the well-established value of $\alpha = 0.5$ for a type-I neuron that transits to spiking via a saddle–node bifurcation [58, 87]. This difference arises because the WMF cortex has two spatial dimensions to model a sheet of tissue, whereas the point neuron, by definition, is zero-dimensional (i.e., occupies no space). The mean-field model integrates variance

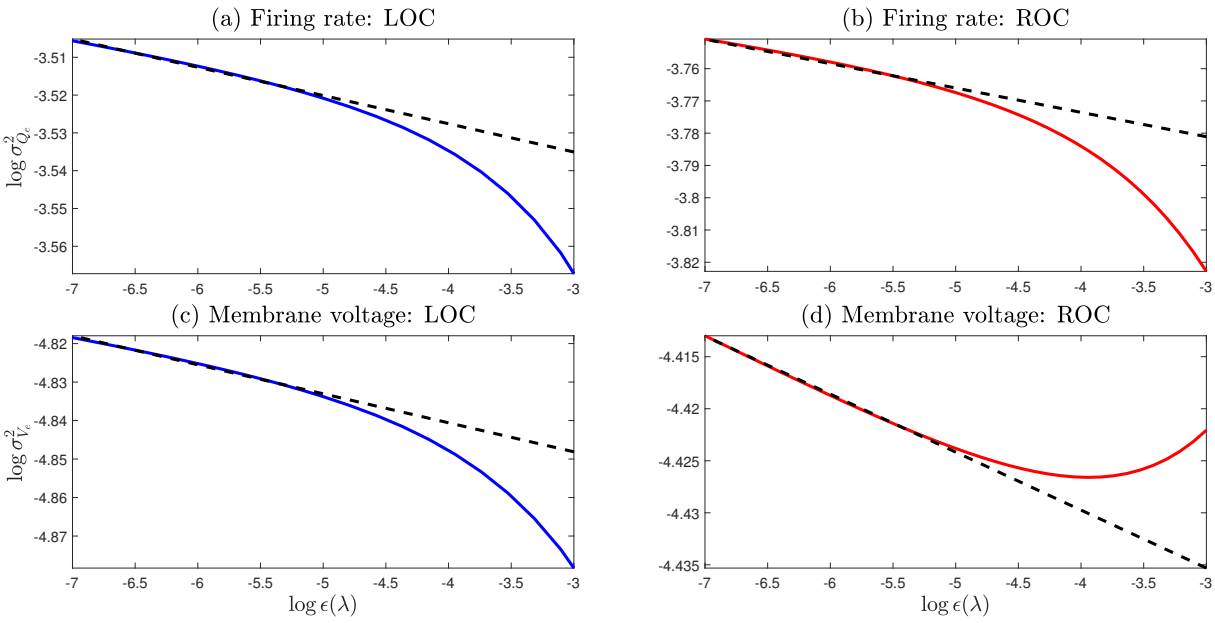

Figure 3.17: Log-log plot of variance of Q_e and V_e as approaches to the transition point. Thick lines and dots indicate theoretical and simulation results respectively. Panels (a) and (c) shows the variance near to the LOC transition point, where power-law exponents are calculated from theoretical predictions for each log-distribution as 0.0075 ± 0.0005, 0.0075 ± 0.0006 for $\sigma^2_{Q_e}$ and $\sigma^2_{V_e}$ respectively. Panels (b) and (d) illustrate the log-log plots of variance near ROC tipping point and power-laws as 0.0075 ± 0.0004, 0.0056 ± 0.0006 for $\sigma^2_{Q_e}$ and $\sigma^2_{V_e}$ respectively

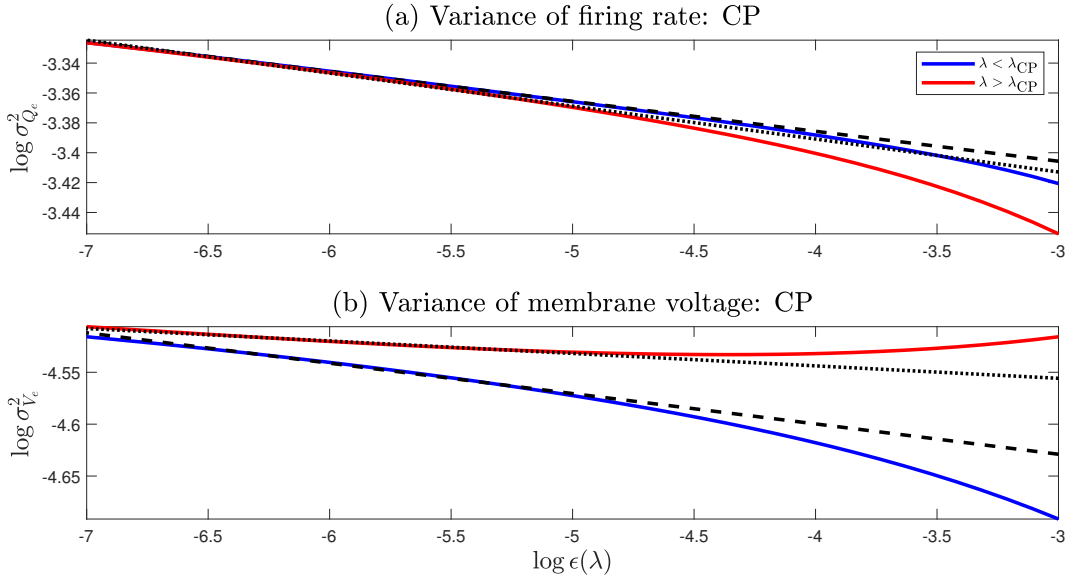

Figure 3.18: Log-log plot of variance of Q_e and V_e as approaches to the critical point CP for $\lambda < \lambda_{\rm CP}$ and $\lambda > \lambda_{\rm CP}$. Calculated power-law exponents are mentioned in Table 3.3

contributions from all possible wave numbers, reducing the slope of the power-law. Note that, only the $q = 0$ variance gives a slope of 0.5 for LOC and ROC (consistent with a homogeneous cortex); for CP, we found a slope of $\alpha \simeq 2/3$ (not shown).

Table 3.3: WMF scaling-law exponents α for OU predicted variance: var $\sim 1/\epsilon^{\alpha}$

transition point	$\lambda < \lambda_{\rm critic}$	$\lambda > \lambda_{\rm critic}$
LOC	$\alpha(\sigma^2_{Q_e}) = 0.0075 \pm 0.0004$ $\alpha(\sigma^2_{V_e}) = 0.0075 \pm 0.0004$	
ROC		$\alpha(\sigma^2_{Q_e}) = 0.0075 \pm 0.0005$ $\alpha(\sigma^2_{V_e}) = 0.0056 \pm 0.0001$
CP	$\alpha(\sigma^2_{Q_e}) = 0.020 \pm 0.0007$ $\alpha(\sigma^2_{V_e}) = 0.029 \pm 0.0012$	$\alpha(\sigma^2_{Q_e}) = 0.022 \pm 0.0023$ $\alpha(\sigma^2_{V_e}) = 0.012 \pm 0.0007$

3.7 Fluctuation power spectra

3.7.1 Theoretical expression for power spectral density

The Ornstein-Uhlenbeck expression for the power spectrum matrix given in Eq. (2.19) is now generalized to include wavenumber q dependence,

$$\mathbf{S}(\omega, q) = \frac{1}{2\pi}(\mathbf{A}(q) + i\omega)^{-1}\mathbf{D}(\mathbf{A}(q)^{\rm T} - i\omega)^{-1} \tag{3.33}$$

where $\mathbf{A}$ is the 8×8 drift matrix, and $\mathbf{D}$ is the sparse 8×8 noise intensity matrix (see Eq. (3.18)).

The power spectrum for V_e fluctuations is provided by the $\mathbf{S}_{11}$ element of the spectrum matrix.

$$S_{V_e}(\omega, q) = \mathbf{S}_{11} \tag{3.34}$$

We apply the sigmoidal mapping of Eq. (3.9) to obtain the spectral density for firing rate fluctuations,

$$S_{Q_e}(\omega, q) = \left(\left. \frac{dQ_e}{dV_e} \right|_{\text{ss}} \right)^2 S_{11}(\omega, q) \tag{3.35}$$

then average across the full range of accessible wave numbers to compute the temporal power spectrum,

$$S_{Q_e}(\omega) = \frac{2}{(q_{\max}^2 - q_{\min}^2)} \int_{q=q_{\min}}^{q_{\max}} S_{Q_e}(\omega, q)\, q\, dq \tag{3.36}$$

the wavenumber limits $q_{\min}, q_{\max}$ are listed in Table 3.2.

For simulations, we calculate the temporal power spectral density for the time-series generated by each grid cell, then average over the grid. Simulations are run in 60×60, 25-cm length grid for 10 s (record for 20 s and extract the last 10 s) using Euler–Maruyama integration with a time step of 0.4 ms.

3.7.2 Power spectrum analysis

Figures 3.19, 3.20 show the $S_{Q_e}(\omega)$ power spectral density (PSD) as a function of wave number q and frequency $f = \omega/2\pi$ for different λ values along the $\Delta V_e^{\text{rest}}/\text{mV} = 2.5398\ldots$ trajectory through the critical point. For λ values that are distant from λ^{CP} (e.g., Fig. 3.19(a–c) and Fig. 3.20(f)), we see fluctuation activity in the range ∼4–12 Hz across a broad range of wavenumbers. This activity narrows dramatically as CP is approached (Fig. 3.20(e) → (d)), focusing and strengthening at $(q, f) = (0,\ 0)$. This particularly evident in Fig. 3.21 with $\lambda = 1.1032$, very close to λ^{CP} (Eq. (3.15)), showing a spectral peak that is $\sim 10^6$ times larger than that for $\lambda = 0.8$ (Fig. 3.19(a)).

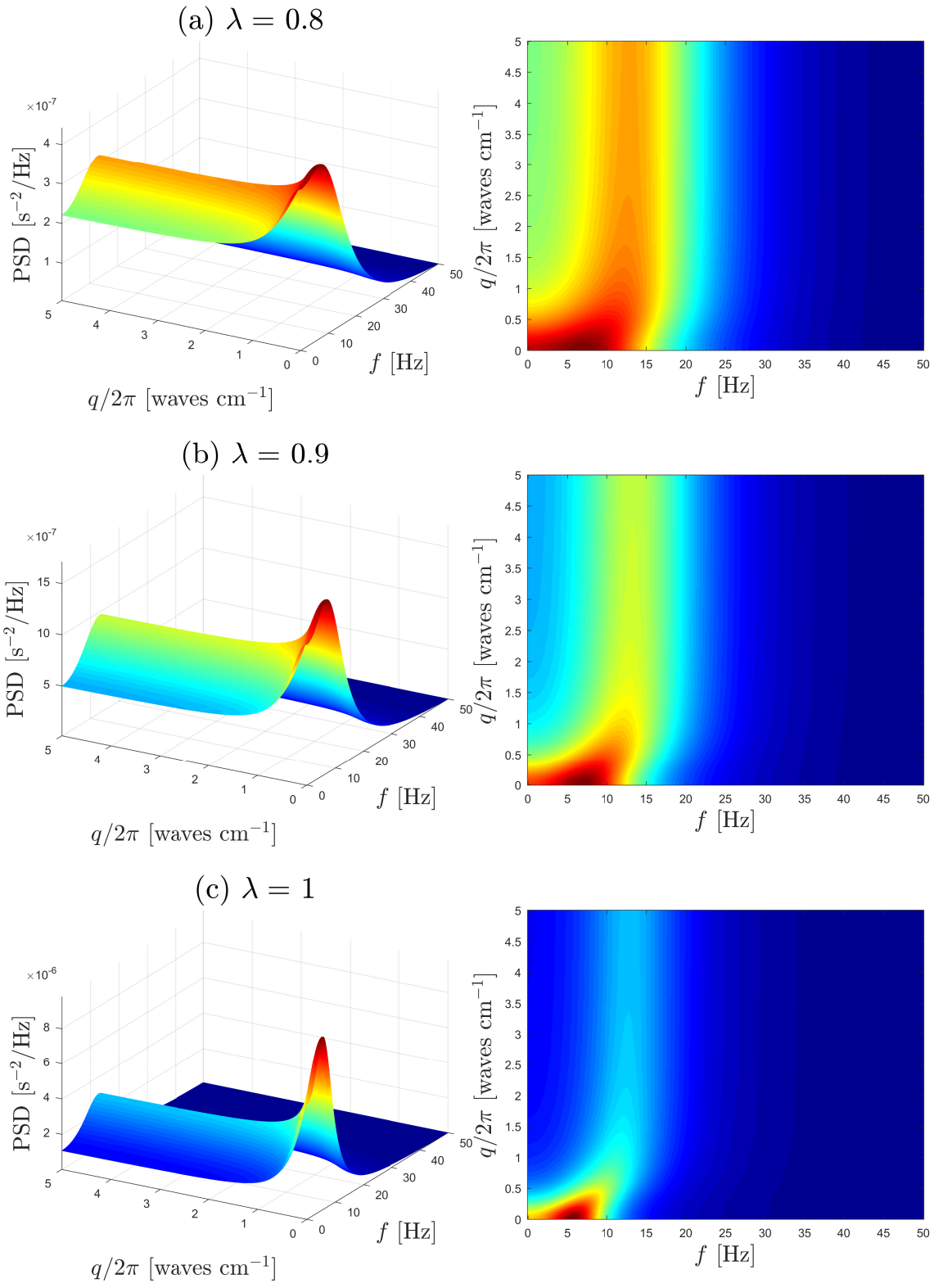

Figure 3.19: Theoretical PSD of Q_e firing rate fluctuations as a function of wave number q and frequency f for different settings of anaesthetic effect along the CP trajectory (curve ② of Fig. 3.16(a): $\Delta V_e^{\text{rest}}/\text{mV} = 2.5398\ldots$) (a) At $\lambda = 0.8$, there is a broad resonance around 12 Hz at faster spatial frequencies that migrates and peaks at ∼6 Hz for smaller q-values. This trend towards higher power at low wavenumber becomes more pronounced as λ increases to (b) 0.9, and (c) 1.0. Note the change in vertical scale

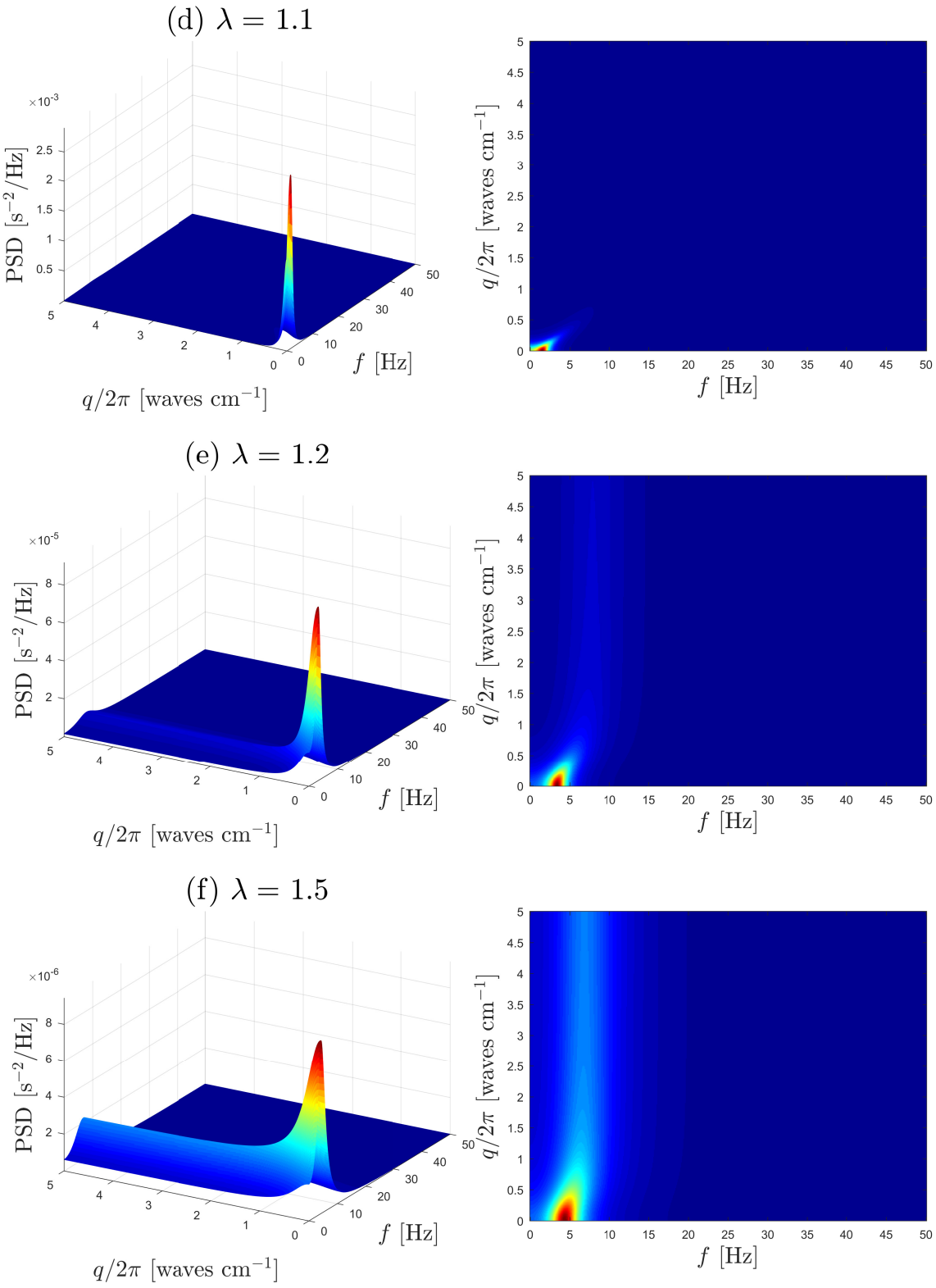

Figure 3.20: (Continuation of Fig. 3.19). The trend towards narrowing and strengthening resonance at lower temporal and spatial frequencies is evident in (d) $\lambda = 1.1$, which is reasonably close to the critical value (but compare with Fig. 3.21). (e, f) Points on the $\Delta V_e^{\text{rest, CP}}$ trajectory that are further from CP show a relaxing spectrum, with development of significant spectral power in the ∼4–9 Hz range in (f)

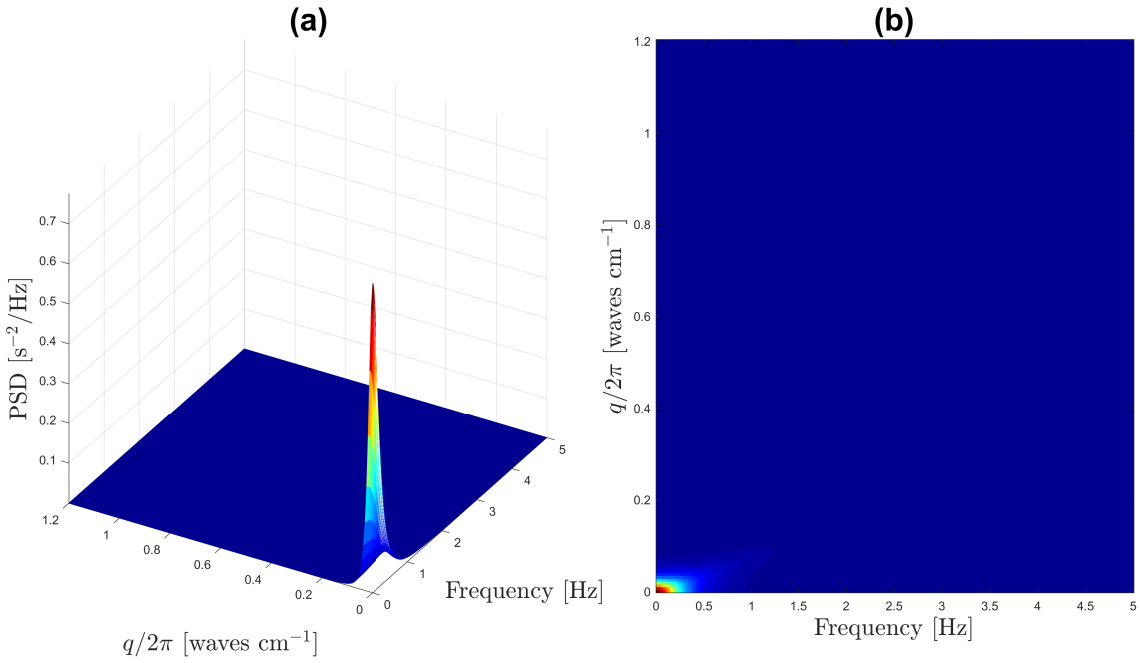

Figure 3.21: Theoretical PSD at $\lambda = 1.1032$ on the $\Delta V_e^{\text{rest,CP}}$ trajectory, very close to the critical point. Extremely high spectral power predicted at $f \simeq 0$ and $q \simeq 0$. Axes have been zoomed to get a better view

To validate the theoretical PSD predictions, we elected to compute the wavenumber-averaged $S_{Q_e}(\omega)$ spectra of Eq. (3.36) since there can be plotted in 2D graphs. Simulations are performed for each λ value and the PSD is calculated for each cell using the `spectrogram` function in MATLAB, then averaged across the grid (3600 cells for 60×60 grid). The grid length is set at 25 cm. The $q_{\min}$ and $q_{\max}$ limits for the averaging over wavenumber are as set out in Table 3.2.

Figure 3.22 illustrates the power spectrum for six distinct λ values in the vicinity of the critical point. As expected, low-frequency spectral power surges strongly on approach to the critical point. We see good agreement between simulation and theory when λ is distant from λ^{CP} (panels (a), (b), (f)), but increasing mismatch on close approach (panel (d)). This discrepancy is caused by the inability of an $L = 25$-cm cortex to sustain an oscillation whose wavelength exceeds 25 cm, corresponding to a minimum wavenumber $q_{\min} = 2\pi/L = 0.251$ cm^{-1}. Figures 3.20(e) ($\lambda = 1.1$) and 3.21 ($\lambda = 1.1032$) clearly predict development of substantial spectral activity at q-values smaller than $q_{\min}$. Because the simulation uses periodic (toroidal) boundaries, these over-long waves will wrapped around and interfere, resulting in distorted and inaccurate spectral estimates for grid simulations very near CP.

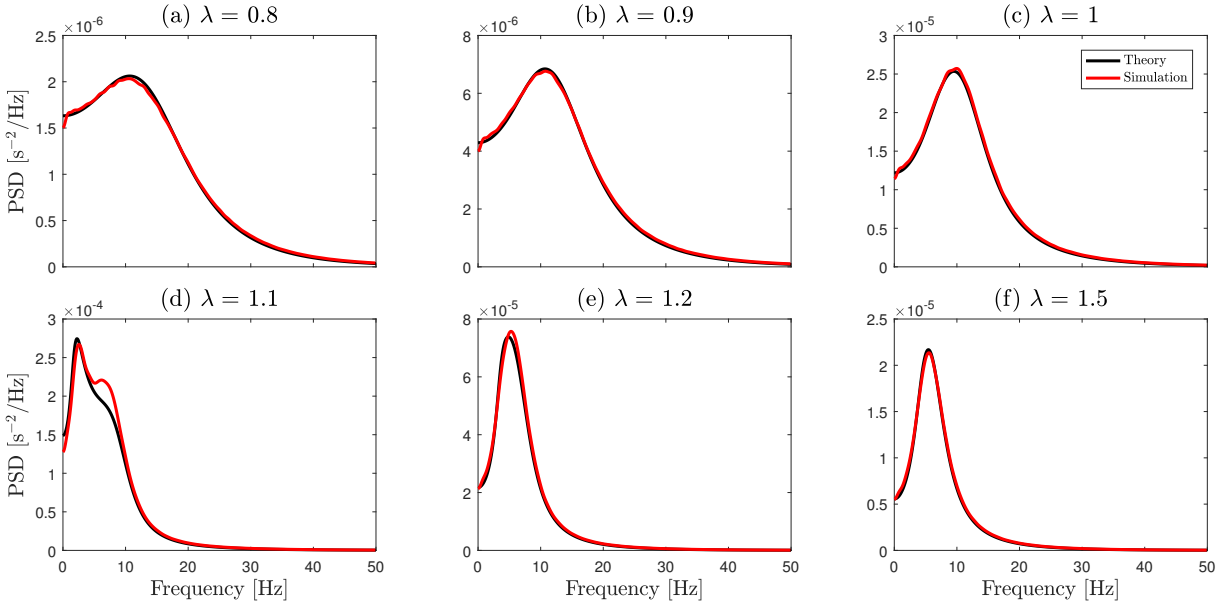

Figure 3.22: Wavenumber-averaged PSD for Q_e fluctuation, comparing theory vs simulation for 25 cm length 60×60 grid. Simulations run for 10 s using Euler–Maruyama integration with $\Delta t = 0.4$ ms. Theory and simulations are better aligned when away from the CP (at $\lambda = 0.8, \lambda = 0.9$, $\lambda = 1.5$). Closer to the critical point, simulations deviate from theory

To check the validity of this statement we have run another set of simulations for $\lambda = 1.0, 1.1, 1.2$ on a "giant cortex" of length $L = 250$ cm. This ten-fold increase in cortical length results in a ten-fold decrease in minimum wavenumber: $q_{\min} \to 0.0251$ cm^{-1}. As shown in Fig. 3.23, spectral agreement between simulation and theory is much improved for these near-CP numerical experiments.

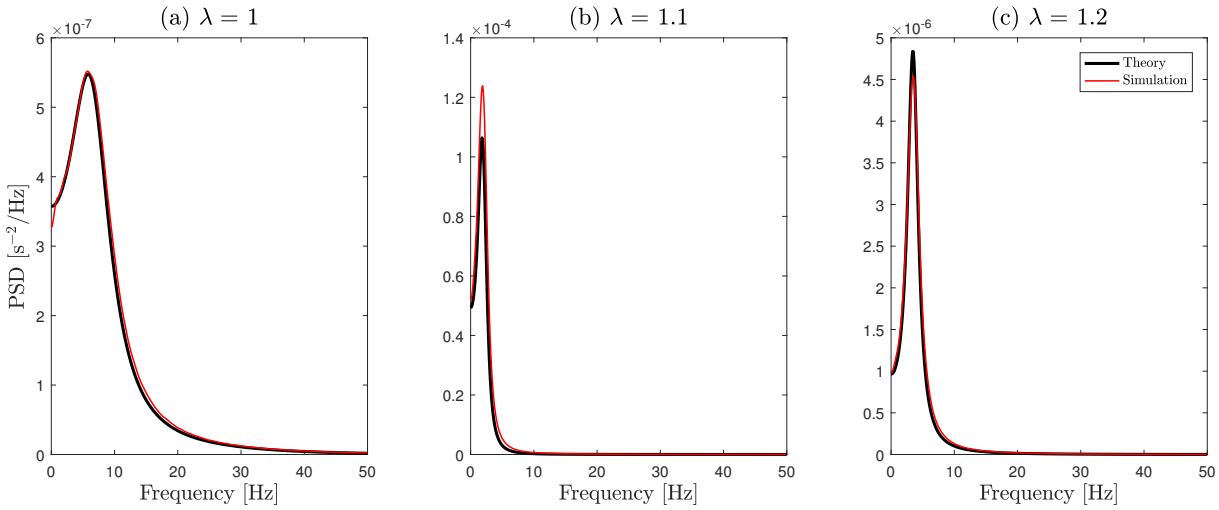

Figure 3.23: Wavenumber-averaged PSD theory vs "giant cortex" simulation for 250 cm length 60×60 grid. Simulations show much better agreement with theory when grid length is increased by a factor of 10 (compare Fig. 3.22) for close approach to CP

We can draw the following conclusions:

- close approach to the critical point leads to divergent growth of spectral power at low spatial and temporal frequencies
- very close to the critical point, peak power occurs at $q = 0, f \simeq 0$, corresponding to zero-frequency waves of infinite extent.

These results confirm that the Waikato mean-field model is showing signs of criticality: increase of fluctuation power associated with critical slowing down on close approach to the critical point.

3.8 Chapter summary

In this chapter we analysed anaesthetic induced phase-transitions in the Waikato mean-field cortical model: loss of consciousness (LOC), recovery of consciousness (ROC), and approach to critical point (CP). Linear stability analysis of WMF reveals that at all three transition points, the real part and the imaginary parts of the dominant eigenvalue becomes zero, signalling a saddle–node bifurcation.

Fluctuation spectra and variance were measured from grid simulations and compared against Ornstein–Uhlenbeck theoretical predictions, and confirmed a consistent quantitative behaviour: close approach to transition (LOC, ROC or CP) leads to divergent growth in power at ever lower spatial and temporal frequencies. This "resonance at dc" at the transition point is the basis of critical slowing down. The power divergences at transition obey scaling laws of the form variance $\sim 1/\epsilon^{\alpha}$ with $\alpha^{\mathrm{LOC}} \simeq \alpha^{\mathrm{ROC}} \simeq 0.0075$, and $\alpha^{\mathrm{CP}} \simeq 0.02$.

Chapter 4

Anaesthetic-induced changes of rat local field potential recordings

The anaesthetic-induced phase transition using a mean-field neural model was analysed and discussed in detail in the previous chapter. This chapter examines anaesthetic-induced changes in electrocortical data in rats. For this investigation, I am using the local field potential (LFP) data of anaesthetised rats, reported by Sleigh, Hudetz and colleagues[1] in 2009 [82]. I will refer to this work as the Hudetz study.

Electroencephalogram (EEG) is a measure of electrical signals that represent electric potentials detected on the surface of the scalp using noninvasive macroelectrodes. Electrocorticogram (ECoG) is recorded from the subdural surface of the cortex using large metal, glass, silicon electrodes. The ECoG signal measures the averaged electric voltage or local field potential (LFP) of neuron populations that lie adjacent to the electrode. EEG is also a population average signal, but it samples a larger neural area compared to LFP. In addition, EEG detects signals that have been attenuated and filtered by propagating through cerebrospinal fluid, skull and skin layers, so is a low-pass filtered brain signal. ECoG eliminates this frequency loss by placing electrodes directly into the surface of the cortex, thereby bypassing the filtering media [16, 97]. Despite their differences, EEG and LFP show similar behaviour in voltage fluctuations.

Anaesthetic drugs alter brain activity by reducing neural processing, interrupting interactivity within and between neural populations. The transition from consciousness to unconsciousness due to anaesthetic drugs can be visualised in EEG recordings as a

[1] Sleigh, J. W., Vizuete, J. A., Voss, L., Steyn-Ross, A., Steyn-Ross, M., Marcuccilli, C. J., & Hudetz, A. G. (2009). The electrocortical effects of enflurane: experiment and theory. Anesthesia and analgesia, 109(4), 1253.

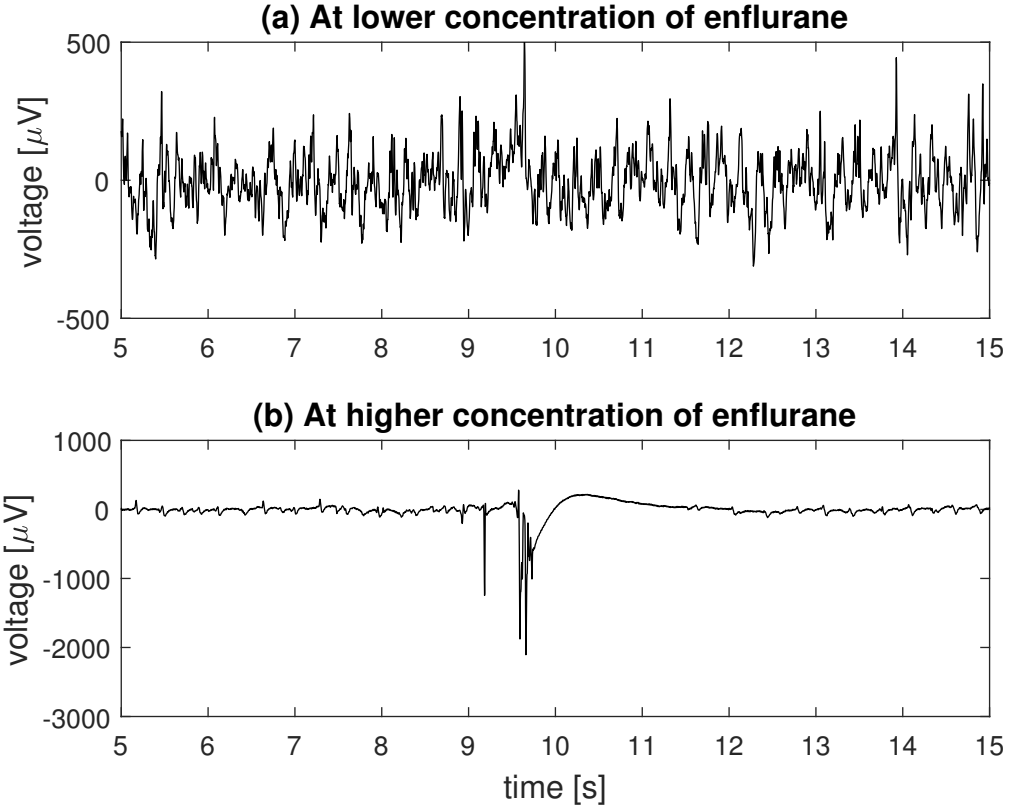

Figure 4.1: Change of local field potential (LFPs) patterns from low to high enflurane concentration. (a) Low concentration enflurane (0.5 MAC) exhibits low-amplitude, high frequency voltage fluctuations. (b) High concentration enflurane (2 MAC) shows PED pattern with periods of suppression of activity. (Data supplied by J. Sleigh from Hudetz experiment [82])

change from low amplitude, high frequency to high amplitude, low-frequency electrical fluctuations [82, 97].

The Hudetz study induced enflurane anaesthesia in rats. Enflurane is a volatile (breathable gas) general anaesthetic, which is not currently used in clinical practice due to its pro-convulsant effects. Enflurane produces the same EEG patterns as most general anaesthetic drugs: increasing amplitude and slowing of EEG as the concentration is increased. At higher concentration, enflurane induces different patterns known as paroxysmal epileptiform discharges (PEDs). PEDs are high-amplitude abrupt waves, alternating with periods of suppression (Figure 4.1). In the Hudetz paper, the main aim was to compare PEDs generated by a theoretical model with real local field potential (LFP) data.

The Hudetz experiment acquired multichannel LFP from rats at different enflurane concentrations: 0.5, 1.0, 1.5, 2.0 and 2.5 MAC (minimum alveolar anaesthetic concentration). This is a measure of anaesthetic potency, with a MAC of 1.0 representing the median concentration required to prevent patient movement in response to a surgical

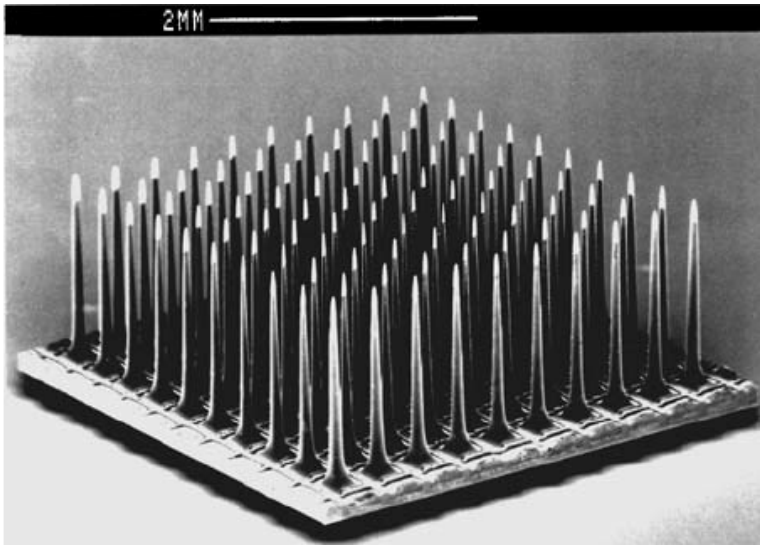

Figure 4.2: Example of a microelectrode array [47]. This 10×10 array contains 100 electrodes.

stimulus in 50% of patients. Loss of consciousness typically occurs earlier at 0.3–0.5 MAC.

In this chapter I examine the Hudetz LFP data to investigate the changes that occur with anaesthetic. Specifically, I will apply histogram analysis, temporal correlation, power spectral and detrended fluctuation analysis (DFA). In the following chapter, I will present investigations of the avalanche behaviour for the Hudetz LFP data.

4.1 Electrophysiological recording methods and measurements

This section describes the methods used in the Hudetz study. The LFP electrophysiological data for four rats under different concentrations of enflurane anaesthesia were captured using a two-dimensional 8×8 square array of electrodes (similar to that shown in Figure 4.2) inserted into the visual cortex.

4.1.1 Experimental procedure

Preparing rats

Adult male Sprague-Dawley rats weighing 270–330g were used for the experiment. Inspiratory and expiratory gas concentrations (oxygen, anaesthetic, and carbon dioxide) were recorded using a clinical anaesthesia monitor. The head was secured in a stereotaxic apparatus.

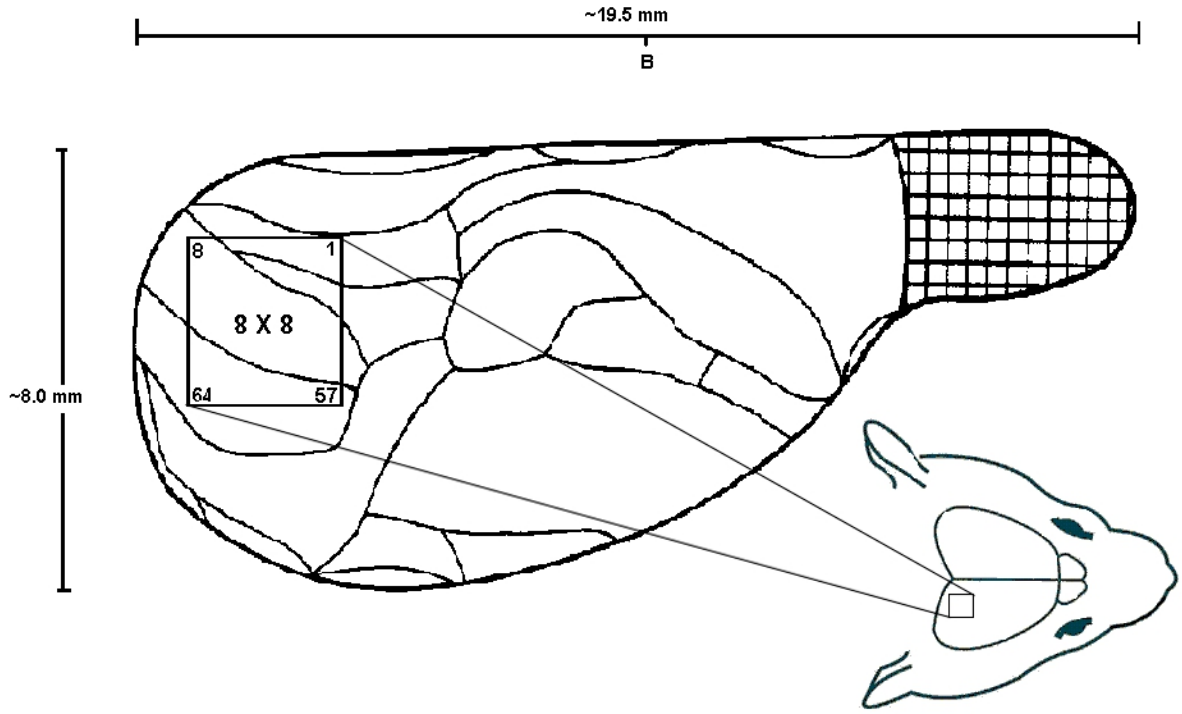

Figure 4.3: Placement of electrode array of 64 electrodes inserted into the cortex, viewed from the top. In the 8×8 array spacing between electrodes was 400 μm.

Electrode placement

The electrodes were placed at the occipital cortex of the right hemisphere. A 4×4 mm rectangular section of the skull bone was surgically removed in a craniotomy to uncover the brain, but the dura, one of the membrane layers that protects the brain, was not removed. An 8×8 square electrode array (Cyberkinetics Inc) was inserted into the cortex through the dura using a pneumatic device that inserted the electrode tips 0.3 mm deep into the cortex. The cortex was then further pierced approximately 1 mm beneath the dura into the layer V pyramidal cells using a fine micromanipulator. The reference electrode was a platinum wire inserted into the scalp. The spacing between adjacent pairs of electrodes is 400 μm and the height from electrode base to tip is 1.5 mm. Figure 4.3 shows the placement of the electrode array on the cortex.

Change of enflurane concentrations

Electrical signals were recorded while increasing the enflurane concentration from 0.5 MAC to 2.5 MAC in 5 steps. Data were saved for 60 s following a 15-min settling time after each increase in concentration level.

Date: 10.01.2006

64	56	48	40	32	24	16	8
63	55	47	39	31	23	15	7
62	54	46	38	30	22	14	6
61	53	45	37	29	21	13	5
60	52	44	36	28	20	12	4
59	51	43	35	27	19	11	3
58	50	42	34	26	18	10	2
57	49	41	33	25	17	9	1

Date: 17.01.2006

64	56	48	40	32	24	16	8
63	55	47	39	31	23	15	7
62	54	46	38	30	22	14	6
61	53	45	37	29	21	13	5
60	52	44	36	28	20	12	4
59	51	43	35	27	19	11	3
58	50	42	34	26	18	10	2
57	49	41	33	25	17	9	1

Date: 23.01.2006

64	56	48	40	32	24	16	8
63	55	47	39	31	23	15	7
62	54	46	38	30	22	14	6
61	53	45	37	29	21	13	5
60	52	44	36	28	20	12	4
59	51	43	35	27	19	11	3
58	50	42	34	26	18	10	2
57	49	41	33	25	17	9	1

Date: 01.02.2006

64	56	48	40	32	24	16	8
63	55	47	39	31	23	15	7
62	54	46	38	30	22	14	6
61	53	45	37	29	21	13	5
60	52	44	36	28	20	12	4
59	51	43	35	27	19	11	3
58	50	42	34	26	18	10	2
57	49	41	33	25	17	9	1

Figure 4.4: Location of active electrodes for each day are shown with white background (inactive electrodes have grey shading). A different rat was used on each day.

Measurements

Electrical signals acquired by the electrodes were recorded using a Cerebus data acquisition system, amplified, and filtered. LFP data were sampled at 500 Hz and bandpass filtered between 1 Hz to 250 Hz.

4.1.2 Data availability

Data were recorded on four days for four different rats. For each array, it was found that only a fraction of the 64 electrode sites were actually active, varying from 13/64 (20%) to 37/64 (58%). Table 4.1 shows the available data for each day.

Table 4.1: Data availability for LFP measurements

Day	Recording date (dd.mm.yyyy)	Concentrations (MAC)	# active electrodes (of 64)
rat 1	10.01.2006	0.5, 1.0, 1.5, 2.5	37 (58%)
rat 2	17.01.2006	0.5, 1.0, 1.5	19 (30%)
rat 3	23.01.2006	0.5, 1.0, 1.5, 2.0	13 (20%)
rat 4	01.02.2006	0.5, 1.0, 1.5, 2.0	22 (34%)

4.2 Statistical analyses of the anaesthetic-induced transition

This section presents the analysis of LFP at distinct concentrations to quantify the voltage fluctuations that occur in the cortex with increase of anaesthetic. Investigations are accompanied by statistical analyses: histograms of amplitude distribution, time-correlation analysis (auto-correlation) and variance analysis.

4.2.1 Amplitude distribution

We examine the change of probability distribution (PDF) of LFP amplitude with anaesthetic concentration. We quantify the variation of PDF by computing skewness and kurtosis statistics.

The LFP patterns reflects the change of behaviour of the cortex with anaesthetic concentration by gradual increase of the LFP amplitude and decrease of frequency. At higher anaesthetic concentrations, LFP exhibit high-amplitude burst patterns, with long suppression periods. Figure 4.5 exhibits these differences of voltage patterns for different anaesthetic concentration. These changes are clearly visualised in the histograms of LFP amplitudes.

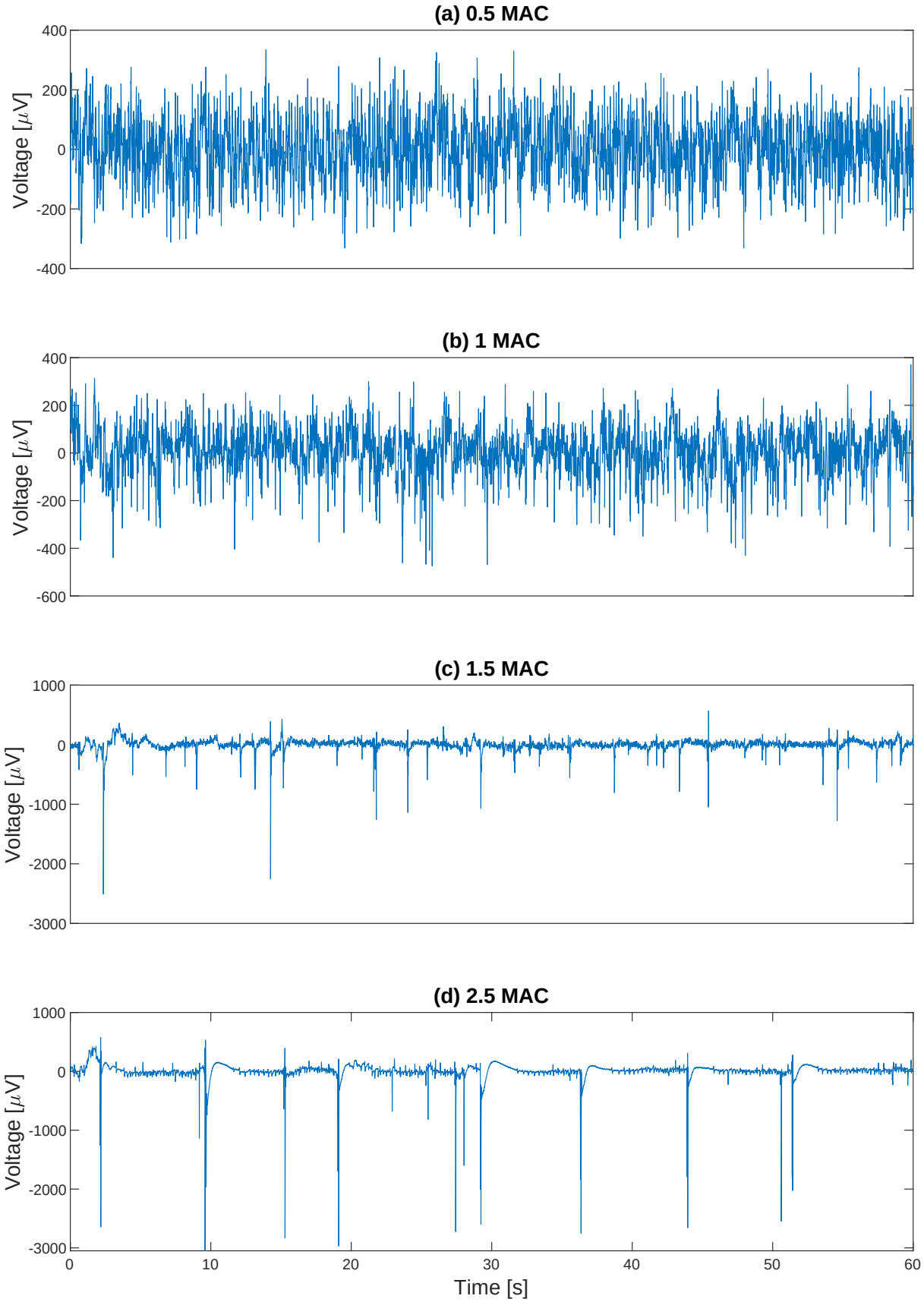

Figure 4.5: Change of voltage patterns with increase of anaesthetic concentration. LFP data are from electrode number 61 of rat 4. Burst-suppression patterns are clearly seen at deeper levels of anaesthesia (> 1 MAC)

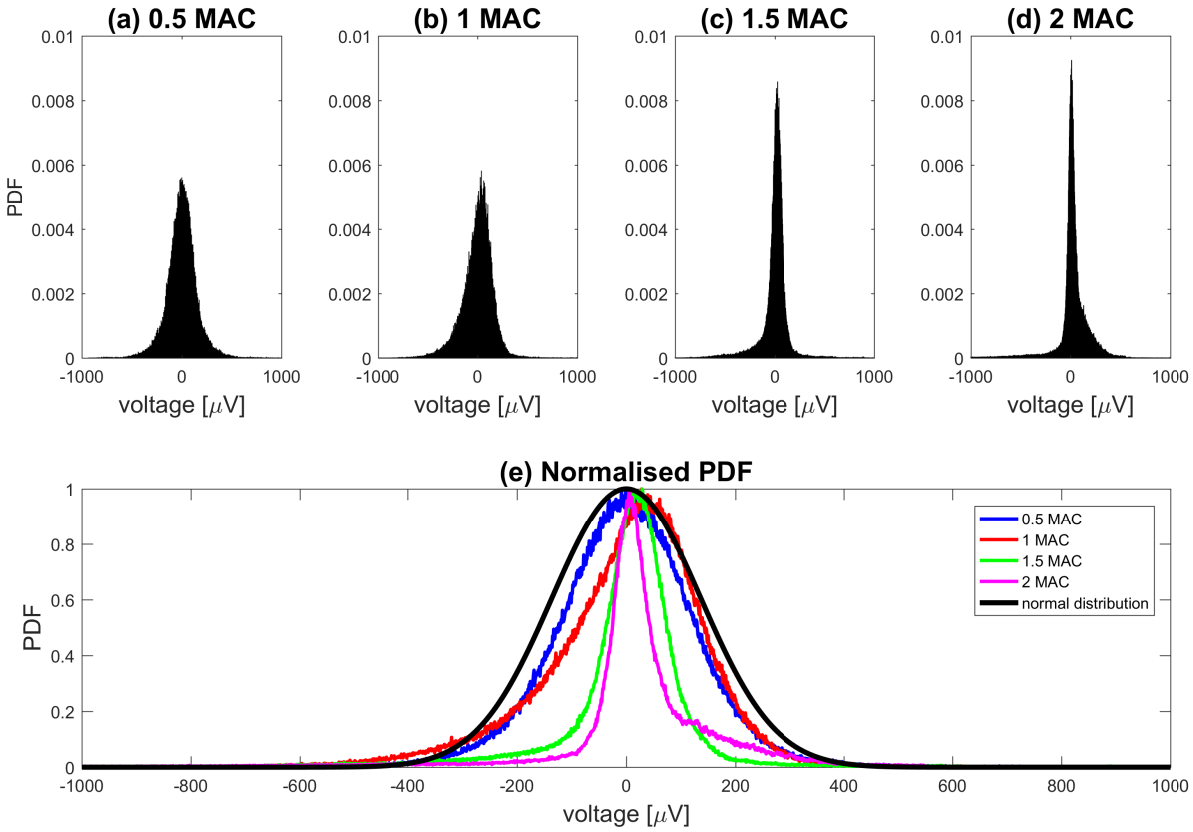

Figure 4.6: Probability density of the local field potential at different anaesthetic concentrations for rat 4. Panels (a) - (d) show narrowing PDF patterns and increasingly negative skewness as anaesthetic concentration increases. (e) PDFs are normalised in height and compared with normal distribution ($\mu = 0, \sigma = 136$). These patterns deviate from normal distribution with higher anaesthetic

Figure 4.6 illustrates the change of probability distribution for LFP voltage fluctuations with anaesthetic concentration. Here I used the data of rat 4, aggregating the LFP signals from all 22 active channels. The probability density functions (PDF) were calculated for mean-subtracted LFP time-series to eliminate any residual DC offset. At the lower anaesthetic concentrations 0.5 and 1 MAC, the LFP fluctuations are symmetric about zero. Higher anaesthetic concentrations lead to more narrowed and asymmetric distributions with a higher peak as a result of the emergence of burst-suppression patterns seen in Figure 4.5(d). Distributions are skewed negatively because of the negative high amplitude burst transients. These PDF patterns are compared in Figure 4.6(e) with a unit-height normal distribution that approximately matches that of 0.5 MAC distribution ($\mu = 0, \sigma = 136$). Deeper anaesthetic increases the deviation, with higher concentrations becoming increasingly narrower and more skewed.

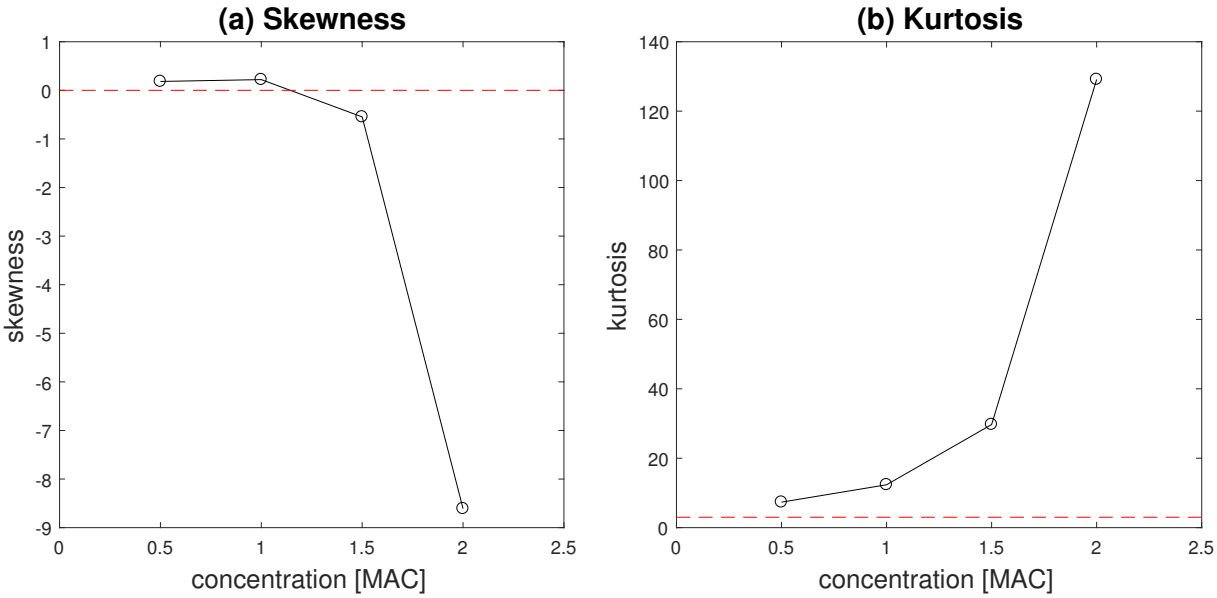

Figure 4.7: Skewness and kurtosis for LFP patterns for different anaesthetic concentration on rat 4. (a) LFP distributions become increasingly negatively skewed at higher anaesthetic concentrations. (b) The increase of the kurtosis parameter indicates the development of a heavy tail in the PDF at high anaesthesia

Skewness and kurtosis for this data set are illustrated in Figure 4.7. Skewness quantifies the degree of asymmetry in the distribution [23, 31]. For this data set, skewness increases negatively to -9 at 2 MAC, while being close to zero at lower concentrations (0.5, 1 MAC).

Kurtosis quantifies the shape and tailedness of the distribution [59, 100]. A normal distribution has kurtosis value of 3. Lower anaesthetic concentrations produce fewer non-normal outliers, so has a kurtosis of around 3. Kurtosis increases with anaesthetic, exhibiting a high value around 130 as a result of infrequent high amplitude burst events.

Figure 4.8 summarises the skewness and kurtosis using the rat data across all four rats. Skewness and kurtosis have been calculated for each electrode separately (black dots); red circles mark the mean value for each concentration.

In general, at low anaesthetic concentrations, the LFP fluctuations are symmetric and approximately normally distributed, while at high concentrations fluctuations become increasingly heavy-tailed and negatively skewed.

4.2.2 Variance analysis

The variance of the rat data was calculated to track the changes of fluctuation amplitude of LFP with anaesthetic concentration. The variance is a measure of LFP fluctuation

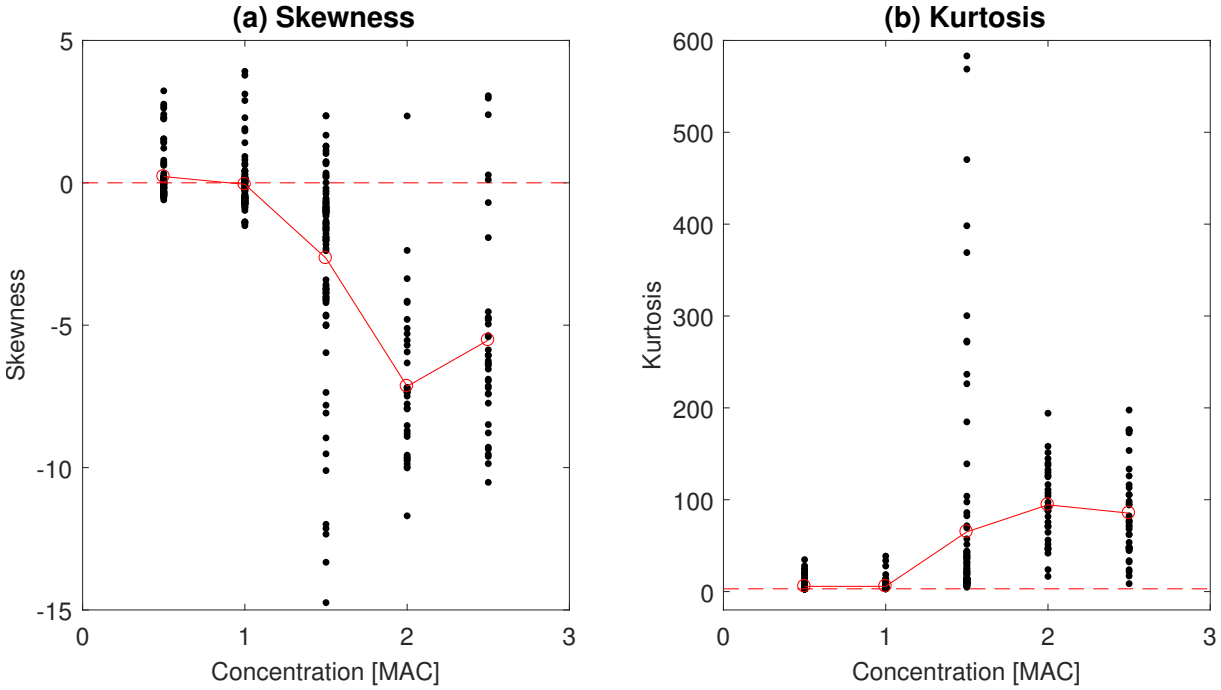

Figure 4.8: Summarised (a) skewness and (b) kurtosis for the rat data aggregated across all four rats. Circles show the mean values. Red dashed lines indicate skewness and kurtosis values for normal distribution (0 and 3 respectively)

energy. Figure 4.9 illustrates the deviation of variance with anaesthetic concentration for rats 1 to 4. We calculated the variance for each electrode separately (black dots) and computed the electrode-averaged variance for each concentration. The average variance peaks at 1 MAC, then drops at 1.5 MAC, before rising strongly at 2 MAC due to emergence of burst-suppression patterns. Similar anaesthetic-vs-concentration trends are evident for the data for rats 1, 2 and 3. The phase transition is expected to happen around 1 MAC, and this is consistent with the observe variance increases for three of the four rats.

However for the rat-1, the variance exhibits a quite dissimilar trend (Fig. 4.9(b)), showing a gradual decrease in fluctuation intensity towards 1.5 MAC. This rat performs differently, and it may have a different transition point which occurs before 0.5 MAC or at 2 MAC where data are unavailable.

In conclusion, for three of the four rats, fluctuation variance tends to increase on approach to the nominal 1.0 MAC phase transition point, but this pattern was not evident for the fourth rat. As with humans, rats have differing sensitivities to anaesthetic, thus different rats have distinct brain responses. Therefore, the transition point can vary from rat to rat.

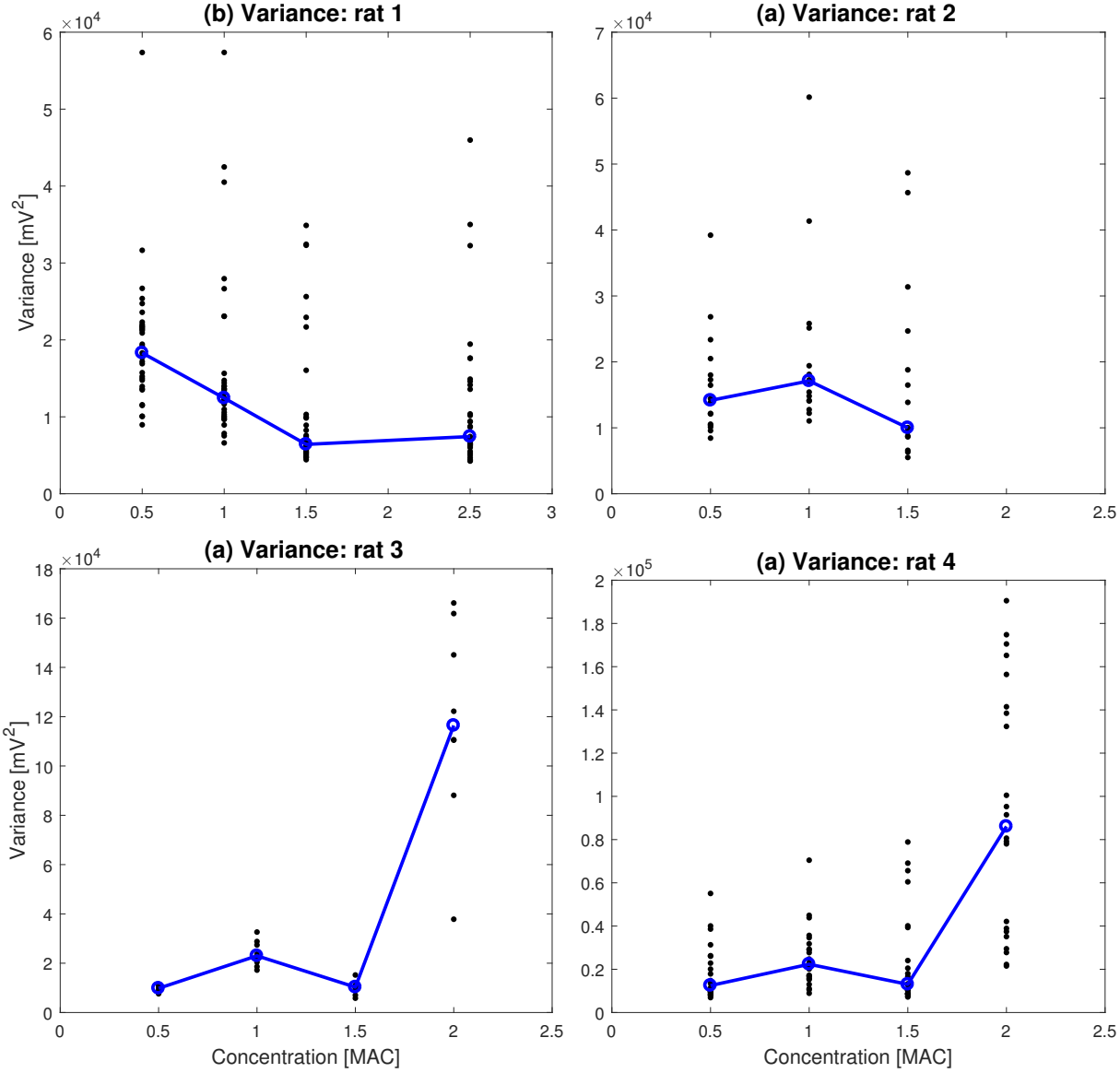

Figure 4.9: LFP variance as a function of anaesthetic concentration. Variance calculated for each electrode separately (black dots) and median across all electrodes in each concentration (blue circles). For rats 3 to 4, median LFP variance peaks strongly at 2.0 MAC because of bursting events; a smaller peak is evident at 1.0 MAC for rats 2, 3 and 4. In contrast, rat-1 median activity decreases with anaesthetic depth, unlike data of rats 2, 3, 4

4.2.3 Temporal correlation analysis

This section investigates the change of temporal correlation of rat LFP with depth of anaesthetic agent, and applies autocorrelation and spectral analysis of LFP to identify LFP oscillation patterns.

First, the correlation coefficient (auto-correlation) is computed for different time-lags for each electrode separately. Then to understand the overall behaviour of the temporal correlation, I averaged the coefficient across all electrodes for each concentration; see

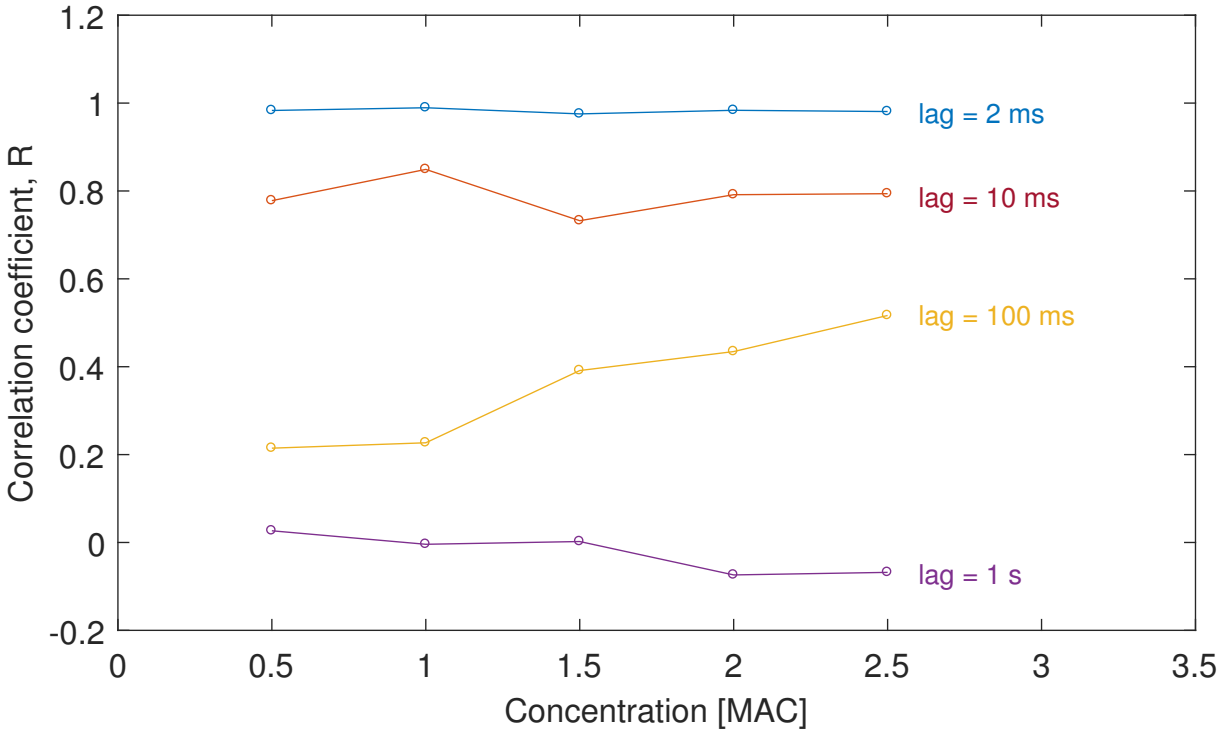

Figure 4.10: Averaged correlation coefficient (auto-correlation) across all data sets for different anaesthetic concentrations and different lags. Correlation decreases with lag. At lowest time-lag of 2 ms correlation coefficient ∼1 indicating high correlation; there is a near zero correlation at the highest time-lag of 1 s

Figure 4.10. The smallest time-lag of 2 ms gives a coefficient close to unity independent of enflurane concentration. However, for the highest time-lag of 1 s, the correlation coefficient is around zero. At 100 ms, higher concentrations show higher correlations (∼0.5) than seen at lower concentrations, indicating slower, more prolonged LFP fluctuations.

This change of correlation is evident in the time-lagged phase plots of LFP (Fig. 4.11). Here I used an LFP data set of one channel for rat-4 data. The phase-plots tend to align with the unity-slope line at smaller time-lags. As time-lag increases, phase-plot points become scattered and do not fit the line. At higher time-lags, these broaden into a roughly circular cloud indicating absence of any correlation. At the highest anaesthetic concentrations, points are scattered into bands because of the transient high-amplitude burst events.

These averaged correlations give a basic idea about how LFP autocorrelations change with lag and concentration. Now we investigate the correlation for different dates individually; we find that the rat data for different dates contain distinct frequency patterns. The rat LFP autocorrelation patterns for two selected dates (rats 4 and 1) are shown in Figures 4.12 and 4.13 respectively.

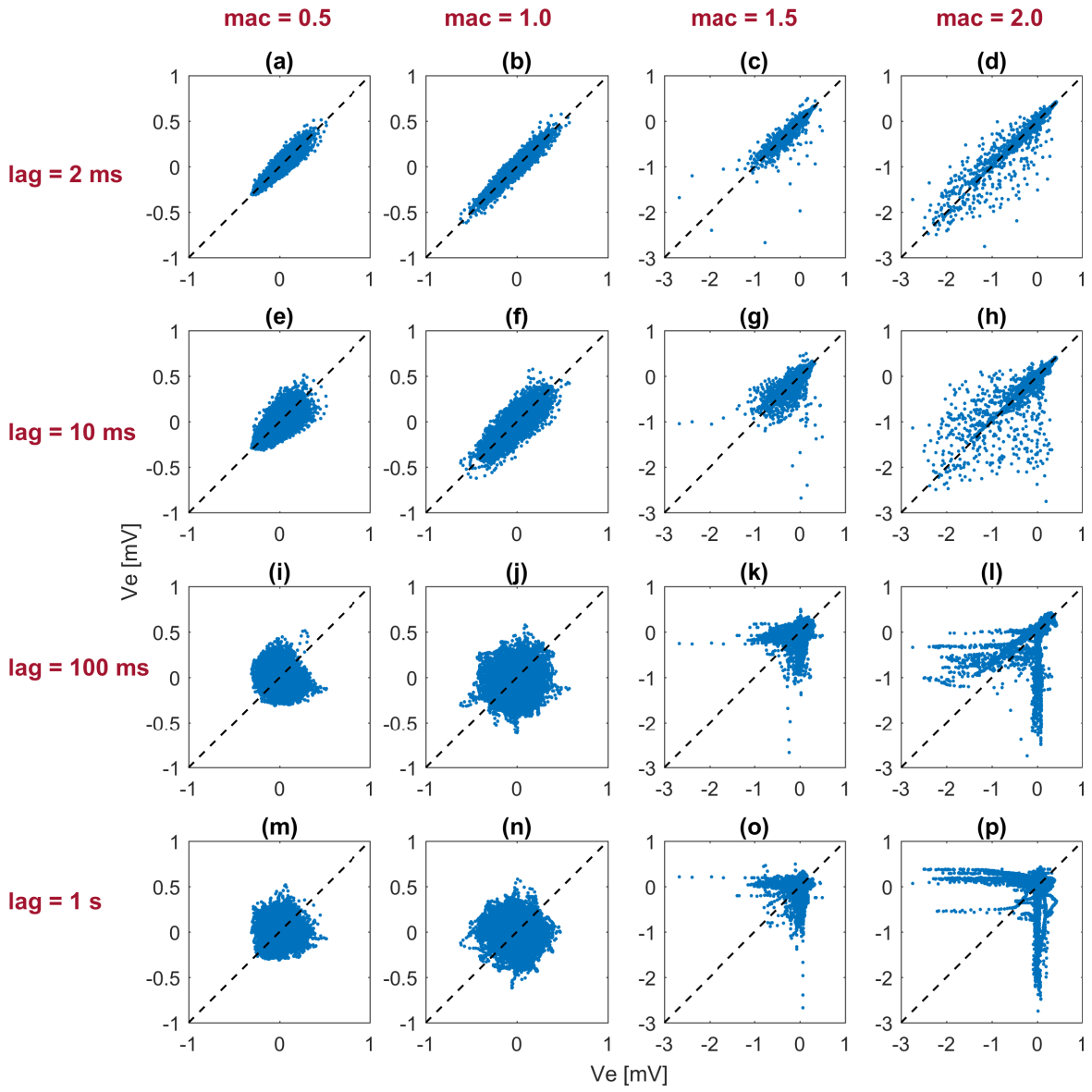

Figure 4.11: Phase plots for different time-lag and different anaesthetic concentrations (electrode 2 in rat 4). Each row corresponds to the distinct time-lags (2 ms, 10 ms, 100 ms, 1 s). Black dashed line shows the line with slope of 1

Red curves in rat 4 (Figure 4.12) illustrate an exponential fit to each autocorrelation. The $1/e$ correlation times were calculated for each exponential decay (red dashed line). Increases of anaesthetic concentration lead to increases of correlation time of LFP fluctuations.

The time-domain autocorrelation was computed for each electrode at each concentration and then averaged across all active electrodes. These patterns unveiled oscillations that are unique to each rat. The rat recorded on rat 4 (Fig. 4.12) shows a frequency

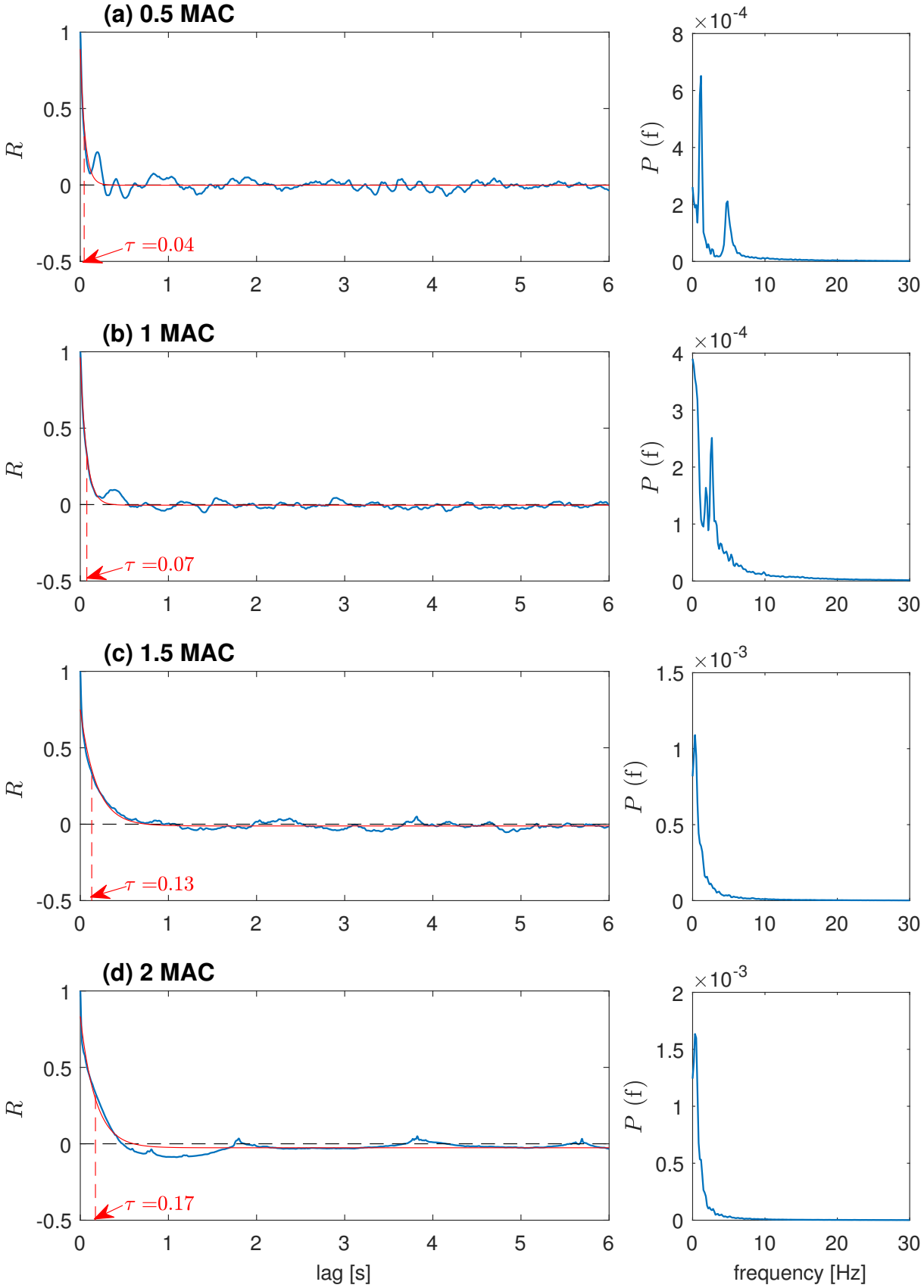

Figure 4.12: The autocorrelation of LFP data for rat-4 data (left-hand side panels) and corresponding power spectra (right-hand side panels). The ∼5 Hz resonance evident at low anaesthetic concentration moves to lower frequencies, then disappears at greater anaesthetic depth. Red curves shows the exponential fit and dashed line indicates the $1/e$ correlation time

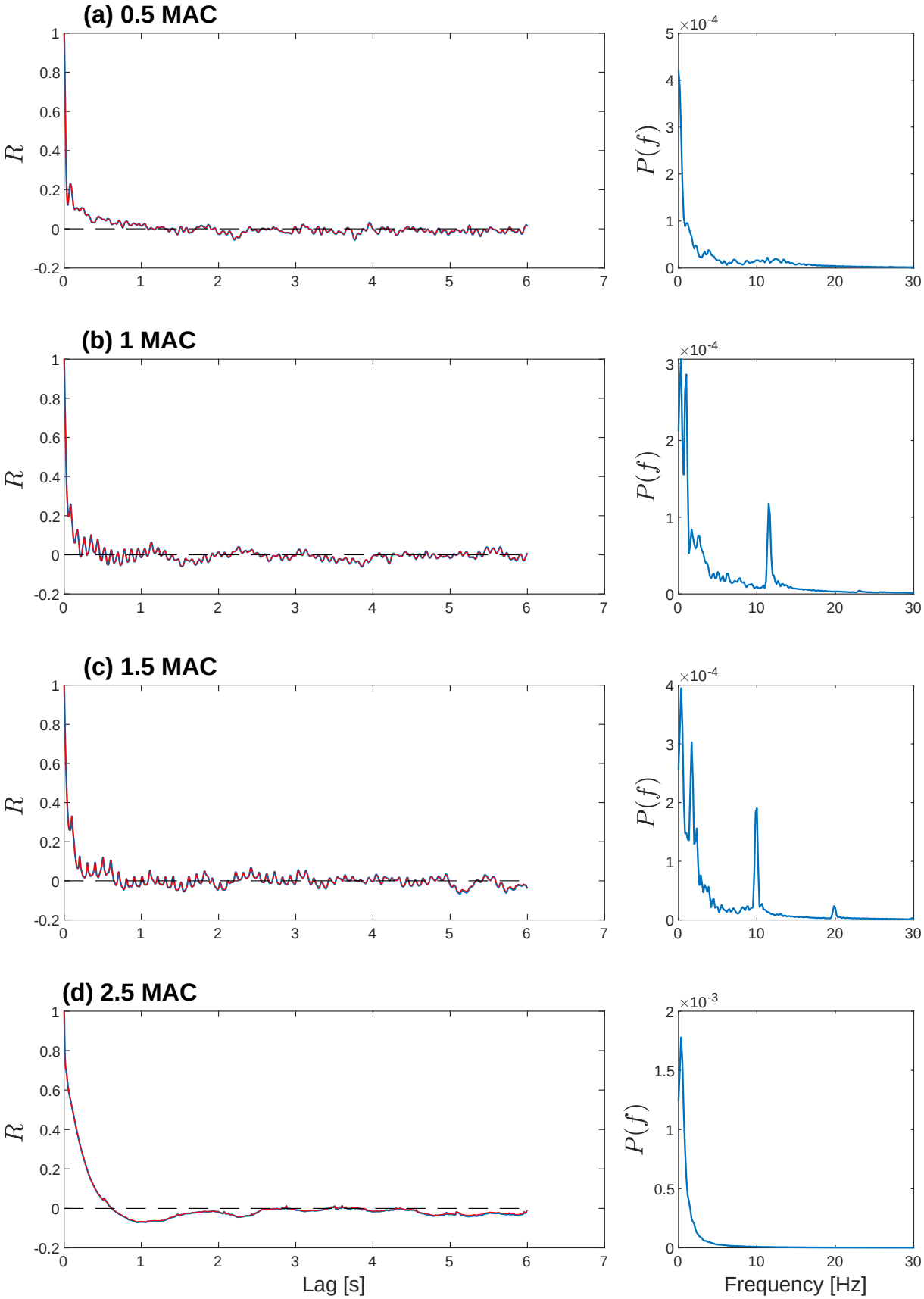

Figure 4.13: Autocorrelation and spectra for rat-1 data. Oscillations at ∼11 Hz emerge at 1 MAC, slow to ∼10 Hz at 1.5 MAC, and disappear completely at 2.5 MAC

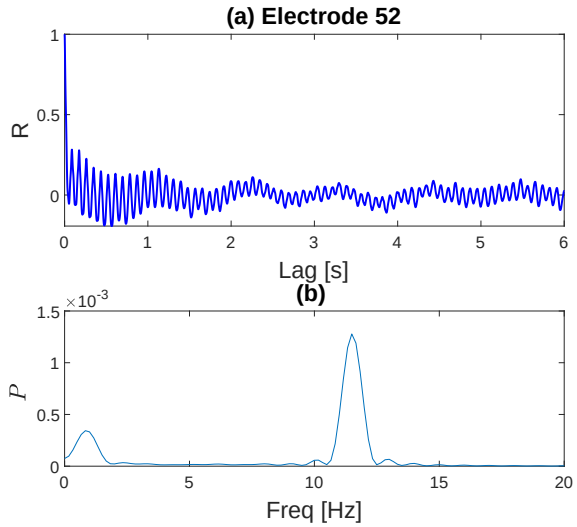

64	56	48	40	32	24	16	8
63	55	47	39	31	23	15	7
62	54	46	38	30	22	14	6
61	53	45	37	29	21	13	5
60	52	44	36	28	20	12	4
59	51	43	35	27	19	11	3
58	50	42	34	26	18	10	2
57	49	41	33	25	17	9	1

Figure 4.14: (a) Correlation coefficient and power spectrum for electrode 52 at 1 MAC (rat 1). The grid in the right-side panel shows the electrode map. Electrodes marked in blue reveal the same frequency patterns as selected electrode 52 (red dashed lines)

around 5 Hz at 0.5 MAC concentration, and this frequency decreases with concentration (∼3 Hz at 1 MAC), then disappears at higher concentrations with only very slow oscillations remaining. (All active electrodes show the same frequency patterns.)

In contrast the rat recorded on rat 1 shows a resonance near 11 Hz at 1 MAC which slows to ∼10 Hz at 1.5 MAC, then vanishes at 2.5 MAC. For these rat-1 data these frequency patterns only appeared on a subset of electrodes (marked in blue on the right-side panel in Figure 4.14).

The time-series and spectrogram of the LFP for electrode 52 are illustrated in Figures 4.15 and 4.16 respectively. It is hard to identify oscillations in the time-series, but these are clearly evident in the power spectra. The ∼11 Hz resonance at 1 MAC lowers to 10 Hz (plus harmonics) at 1.5 MAC. At the highest anaesthetic concentration of 2.5 MAC, these resonances disappear, and burst-suppression patterns override the spectrum.

The question arises: Are these frequency patterns of real biological origin, or are they an artefact due to external noise interference? The fact that the frequency diminishes, then disappears at higher concentrations, strongly suggests that these signals originate in the rat brain.

From the results of correlation and spectral analysis, we come to the following conclusions:

- Temporal auto-correlation decreases at increasing lag times
- At higher concentrations these correlations become more prolonged

- Oscillations that appear at lower concentrations become suppressed at higher concentrations.

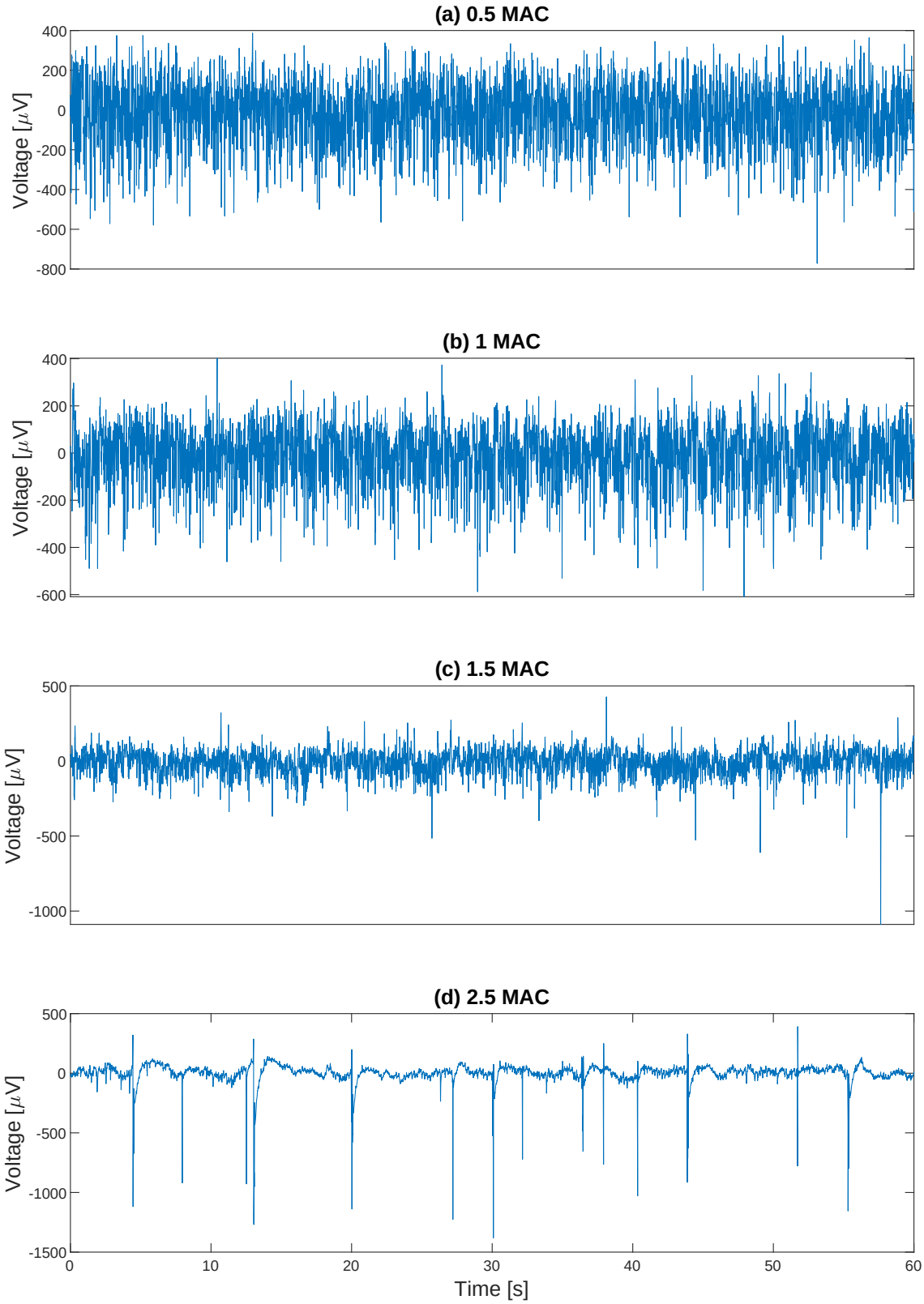

Figure 4.15: Time series for selected electrode 52 in Fig. 4.14 for rat-1 data. Corresponding spectrograms are illustrated in Fig. 4.16

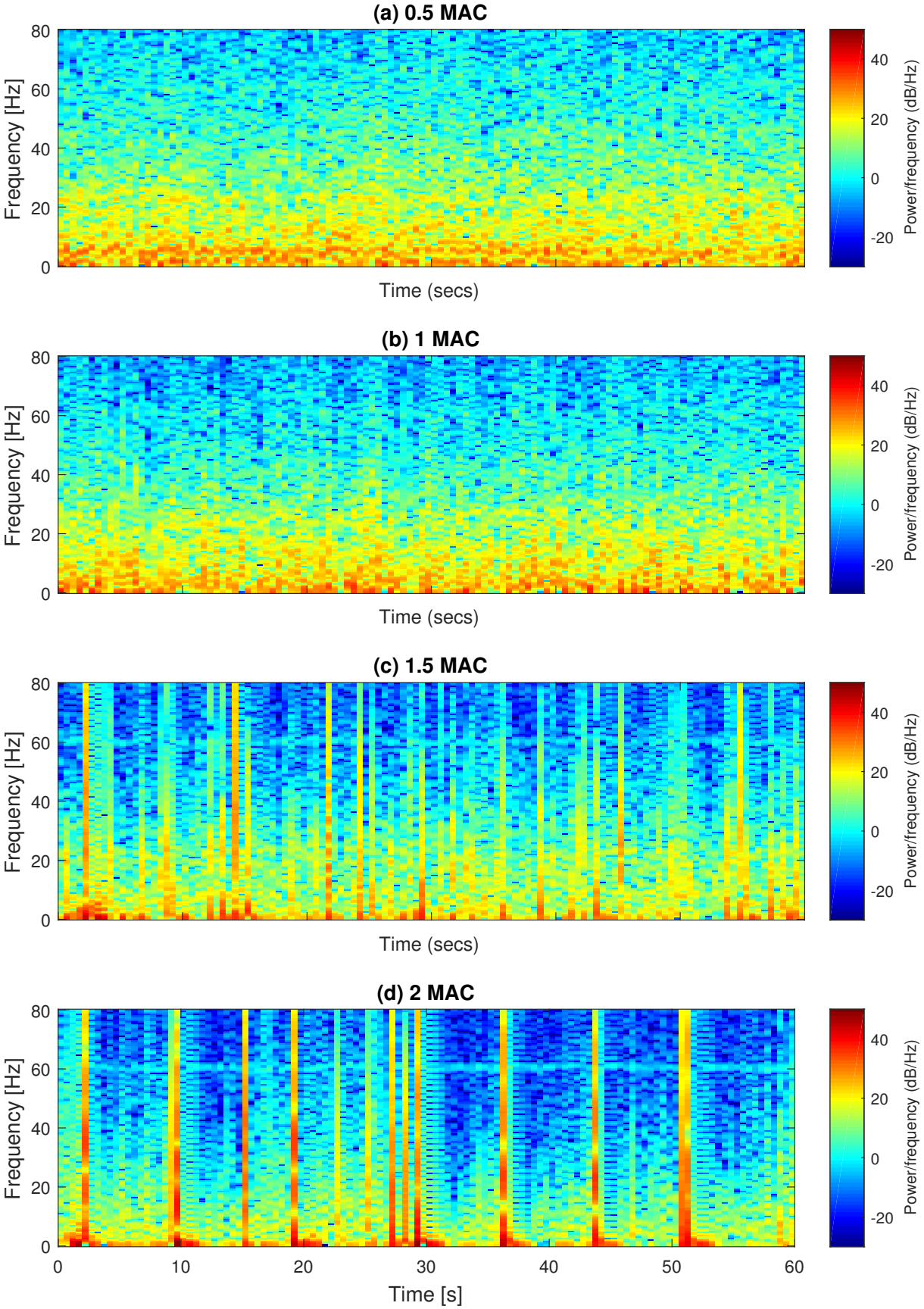

Figure 4.16: Spectrograms for electrode 52 for different anaesthetic concentrations. (a) Concentration = 0.5 MAC: no dominant frequency, most spectral power at low frequency. (b) 1 MAC: spectral peaks at ∼11 Hz and its harmonics. (c) 1.5 MAC: harmonics at 10, 20, 30 and 40 Hz. (d) 2.5 MAC: bursting patterns dominate the spectrum

4.3 Detrended Fluctuation Analysis

Detrended fluctuation analysis (DFA) is a method to quantify the self-correlation or long-range dependence in a time-series. DFA was introduced by Peng *et al.* in 1994 to identify the long-range mosaic correlations of DNA sequences [65]. DFA has been used for wide range of applications such as heartbeat dynamics [66,67,106], neuron spiking [3,9], studies on weather [40, 60], economic time-series [53, 75]. DFA is also been applied to EEG and LFP signals to detect self-similarity in the time-series [11, 57, 76].

DFA is a form of root mean square analysis. Advantages of this analysis over other methods include the fact that it can be applied to non-stationary time-series and also it avoids false detection of long-range correlations caused by transient artefacts.

Here we use DFA to quantify the long-range correlation in LFP data of anaesthetised rats. Our main focus is to determine the change of long-range correlation with anaesthetic concentration. The LFP data sampled at the rate of 500 Hz and recorded for 60 s, so each recording contains 30000 samples.

4.3.1 The DFA Algorithm

A continuous time-series $x(t)$ is sampled and reduced to a discrete-time signal $x(k)$, where $t = k\Delta t$. First we ensure $x(k)$ has zero mean by subtracting its mean,

$$u(k) = x(k) - \bar{x} \tag{4.1}$$

where $u(k)$ is the resulting zero-mean time-series. Then compute $y(k)$, the cumulative sum by summing $u(k)$,

$$y(k) = \sum_{i=1}^{k} u(i) \tag{4.2}$$

The cumulated signal $y(k)$ is broken into m non-overlapping blocks, each of length n, then the linear-fit trend for each block is computed before combining all trends into a single time-series, $y_{\text{trend}}(k)$. Figure 4.17(b) illustrates $y(k)$ with its trend (red lines) for $m = 30$ blocks each containing $n = 2500$ samples. The root-mean-square fluctuation of

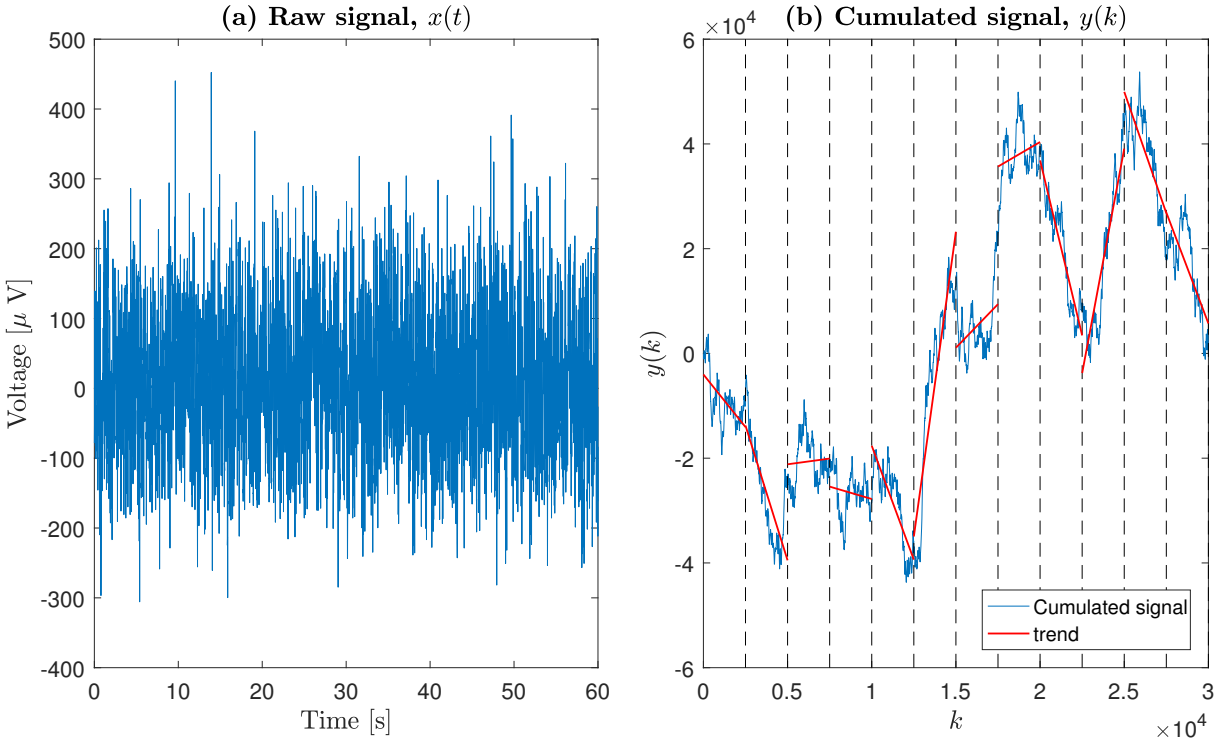

Figure 4.17: Illustration of DFA algorithm. (a) Raw signal, $x(t)$. (b) Cumulated zero-mean signal, $y(k)$, illustrated in blue. Here the signal has been broken into $m = 30$ non-overlapping blocks of length $n = 2500$, then the trend is calculated for each block (red line segments)

this summed and detrended time series is calculated by subtracting the local trend of each box from $y(k)$,

$$F(n) = \sqrt{\frac{1}{N}\sum_{k=1}^{N}[y(k) - y_{\text{trend}}(k)]^2} \tag{4.3}$$

where N is the length of $x(t)$. Typically the detrended fluctuation function, $F(n)$ increases with box size n. If a plot of $\log F(n)$ vs $\log n$ displays a linear relationship, then we deduce the existence of a power-law connection between $F(n)$ and n of the form,

$$F(n) = n^{\alpha} \tag{4.4}$$

where α is the DFA exponent.

The correlation of the fluctuations can be categorized by the value of the exponent α [66]:

- $\alpha < 0.5$: anti-correlated signal

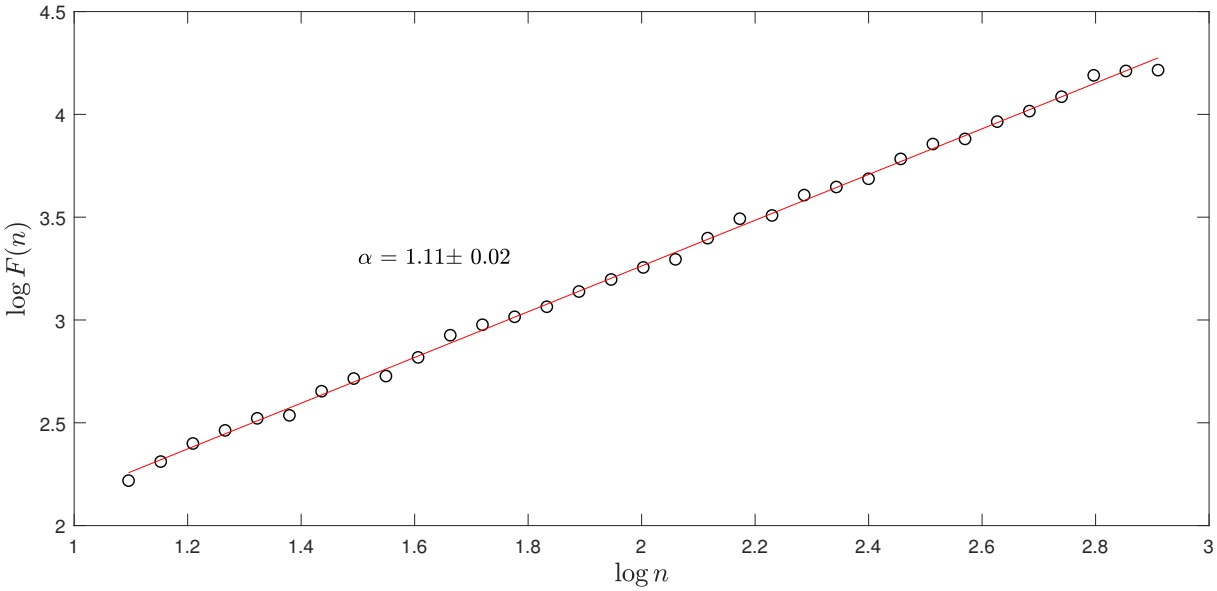

Figure 4.18: Detrended fluctuation analysis (averaged over all the active electrodes) for 2 MAC on rat 4 (date: 01.02.2006). The plot of $\log f(n)$ vs $\log n$ aligns with a linear-fit of slope $\alpha = 1.11$

- $\alpha \approx 0.5$: fluctuations are completely uncorrelated (e.g., white-noise)
- $0.5 < \alpha \lesssim 1$: time-series is correlated
- $\alpha \approx 1$: $1/f$ ("pink") noise, with power spectral density inversely proportional to frequency, f
- $\alpha > 1$: fluctuations are unbounded and nonstationary
- $\alpha = 1.5$: Brownian noise.

We analysed the DFA signatures of the local field potential data of anaesthetised rats to clarify the nature of the underlying correlations. Figure 4.18 shows the calculated DFA at concentration of 2 MAC on rat 4. A plot of $\log f(n)$ vs $\log n$ (n changing from 12 to 800) aligns to a linear-fit of slope 1.11 so we deduce a DFA exponent $\alpha = 1.11$ indicating that the signal is correlated and nonstationary.

4.3.2 Change of DFA for different anaesthetic concentrations

Our motivation for using DFA is to identify how long-range LFP temporal correlations vary with anaesthetic concentration. Here I compute DFA for each concentration; the results are illustrated in Figure 4.19 for rat-4 data. Calculated DFA exponent values increase slightly with concentration, but all lie within $\alpha = 1.05 \pm 0.1$, indicating temporal correlation.

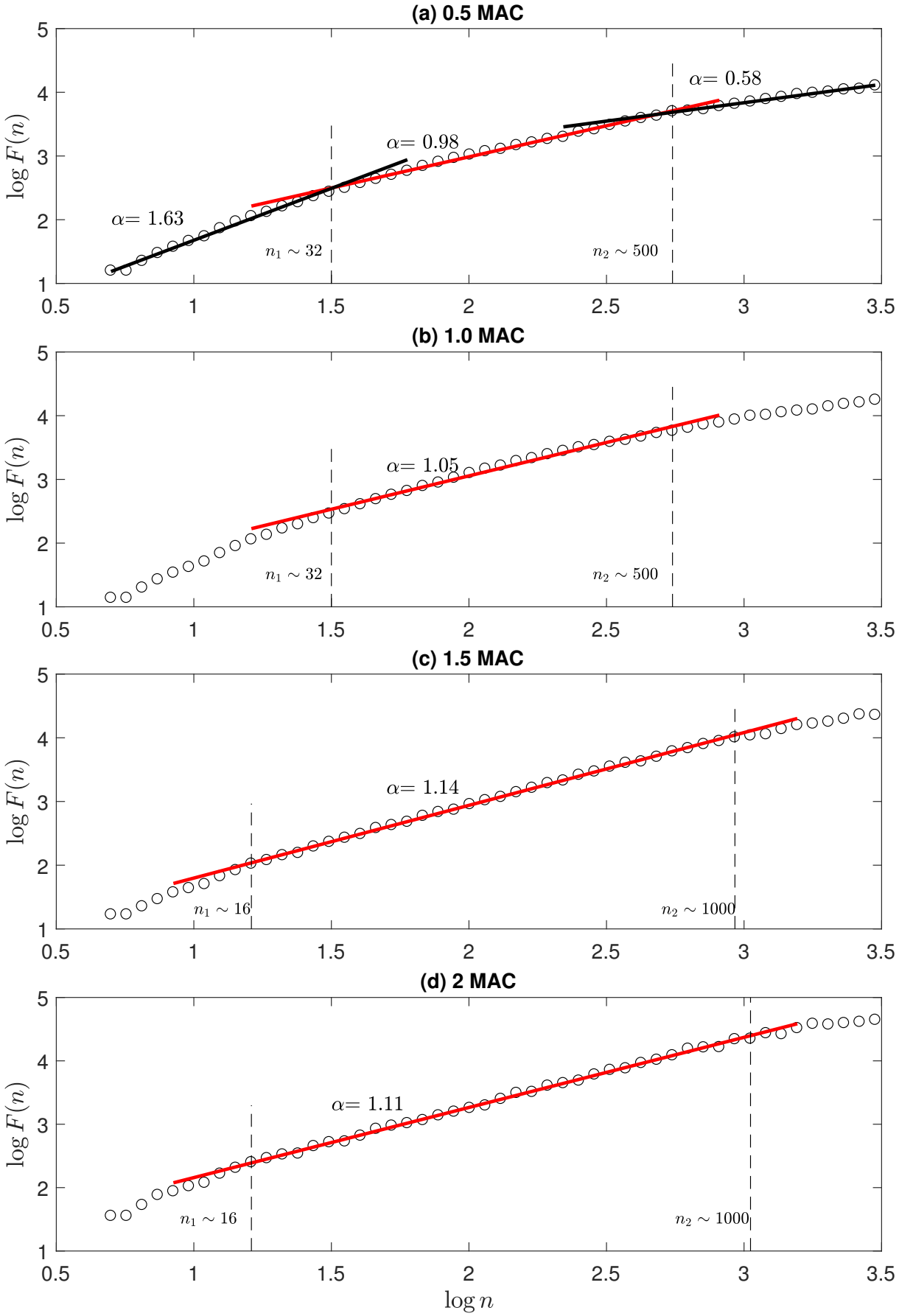

Figure 4.19: Logarithmic plot DFA vs block size n for different concentrations on rat 4. Cut-off points are marked by the dashed lines. The value of α is calculated for the range bounded by the cut-off points n_1 and n_2. This range expands for higher concentrations. The DFA exponent is approximately unity at all four concentrations, increasing slightly at higher concentrations. For smaller and larger n the DFA trends deviate to steeper and shallower slopes respectively

The DFA exponent was calculated for the mid-range linear-fit with $16 \lesssim n \lesssim 1000$ corresponding to block durations 0.03 s $\lesssim n\Delta t \lesssim$ 2 s . We see deviations away from the mid-range trend for smaller and larger n. These lower and upper break-points relate naturally to the spectral characteristics of the LFP signal; this is discussed further in Section 4.3.3.

We draw the following conclusions from the rat DFA trends:

- Increase of anaesthetic depth leads to a slight increase in the value of α, suggesting an increased degree of nonstationarity. This is consistent with the emergence of bursting patterns for deeper anaesthesia
- For block durations 0.06 s $\lesssim n\Delta t \lesssim$ 1 s, detrended fluctuations for 0.5 and 1.0 MAC are well fitted with a DFA exponent that is close to unity, suggesting a $1/f$ spectrum.

4.3.3 Power spectral density analysis

Power spectral density (PSD) is a measure of the distribution of signal power as a function of frequency and is one of the oldest signal processing methods. Although PSD was not designed to measure long-range correlation, here we focus on its relation to the more modern method of detrended fluctuation analysis.

We assume that there exists a simple power-law relationship between spectral density, $S(f)$, and frequency of the form [35],

$$S(f) \propto f^{-\beta} \tag{4.5}$$

where β is the PSD power-law exponent.

Figure 4.20 illustrates the log-log plot of PSD vs frequency. We note the presence of three spectral regions, and three distinct slopes. We calculate the power-law exponent β from the mid-frequency range (0.5 Hz to 40 Hz), as this range is minimally affected by the various filtering processes.

The low-frequency breakpoint at 0.5 Hz results from the 1 Hz highpass component of the 1 – 250 Hz bandpass filter that was applied during data acquisition. The 40 Hz upper breakpoint may be biological in origin, but could also be due to a spatial smoothing (lowpass filtering effect) by the electrode elements. Each element of the multi-electrode array has a finite area so detects a spatially-averaged signal.

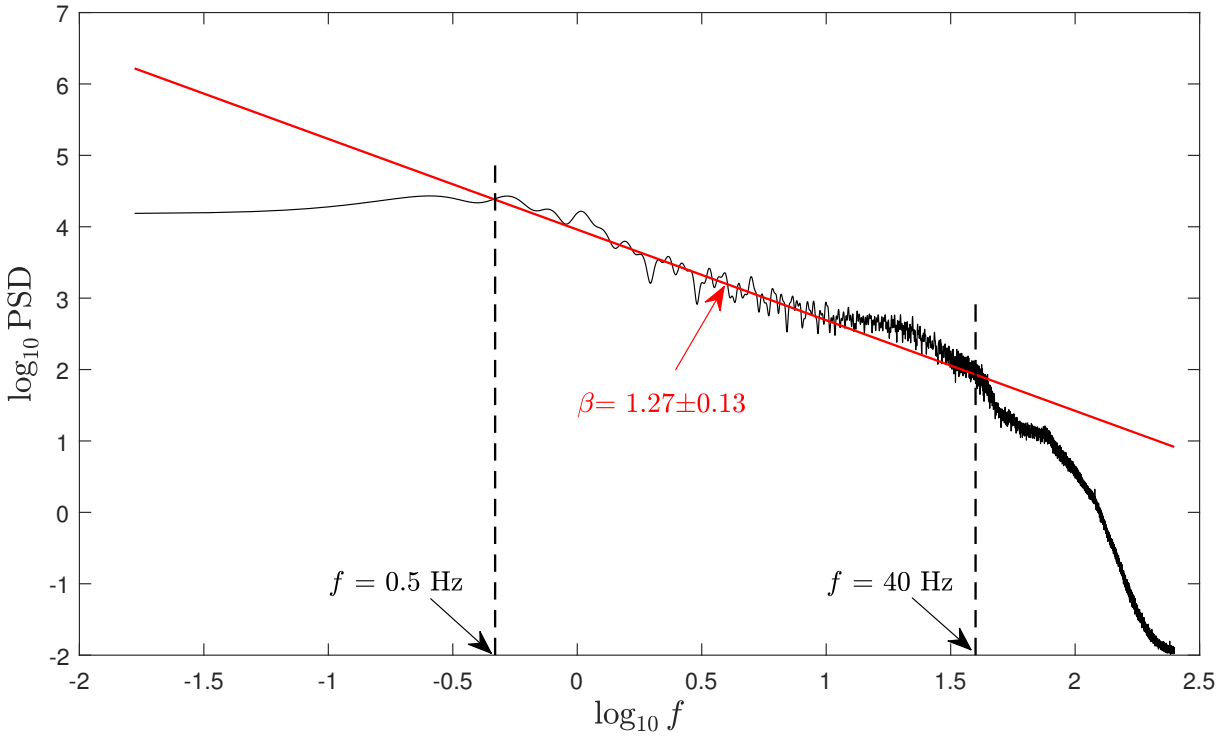

Figure 4.20: Log-log plot power spectral density (PSD) vs frequency (f) for concentration of 2 MAC on rat 4. A straight line is aligned to PSD in mid-frequency range, where slope is the power-law exponent, $\beta = 1.27 \pm 0.13$

We now compute the power-law exponent of PSD β for each concentration of each rat, then compare against an established analytical relationship between PSD and DFA exponents.

4.3.4 Comparison between DFA and PSD for rat LFP data

The analytic relationship between DFA and spectral analysis was introduced by Buldyrev *et al.* in 1995 [15], and later proved by Heneghan and McDarby in 2000 [34]. The link between DFA power-law exponent α and PSD power-law exponent β is given by,

$$2\alpha = \beta + 1. \tag{4.6}$$

(See Appendix C for an outline of the proof.)

Figures 4.19 and 4.21 illustrate the DFA and PSD for trends different anaesthetic concentrations for rat 4 respectively. Dashed lines represent the limits of block size n and frequency f within which DFA exponent α and PSD exponent β were calculated. The frequency limits found in the PSD, due to lowpass and highpass filters, is related to the cut-off points in the DFA distribution. We compute the characteristic period for

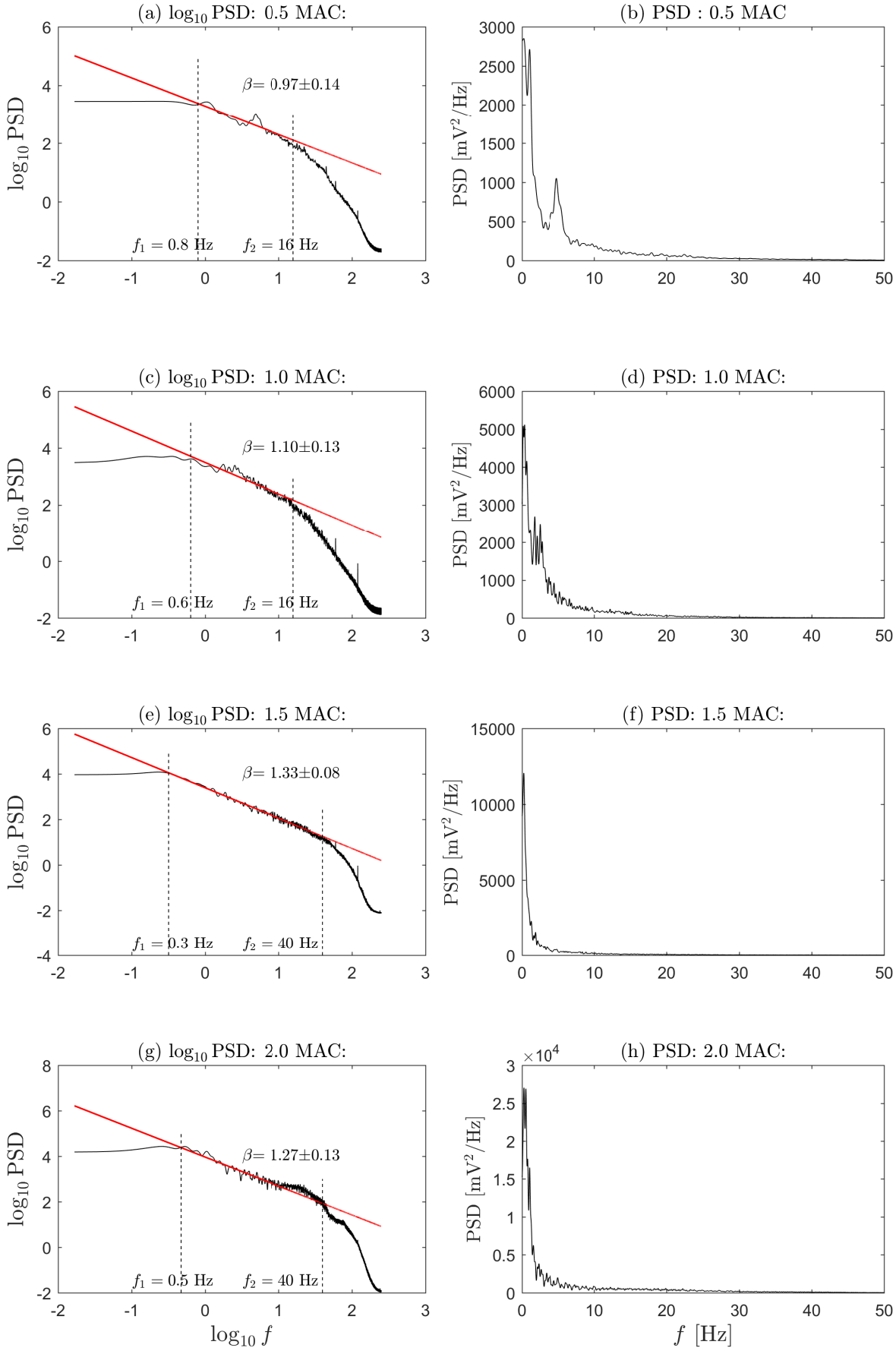

Figure 4.21: Power spectral density vs frequency for different concentrations on rat 4. Left panels illustrate the log-log plot of PSD vs f, right panels show linear plots. The power-law exponent β was calculated for the mid-frequency range bounded by the upper and the lower frequency limits f_1 to f_2 (shown by the dashed lines)

Table 4.2: Comparison between $\alpha_1 = \frac{1}{2}(\beta + 1)$ computed from PSD exponent β and DFA α. Error bounds are calculated using the `polyfit` MATLAB function

MAC		rat 1	rat 2	rat 3	rat 4
0.5	α	0.87 ± 0.01	0.95 ± 0.02	1.18 ± 0.02	0.98 ± 0.03
	α_1	0.91 ± 0.11	1.04 ± 0.12	1.25 ± 1.12	0.98 ± 0.16
1.0	α	0.95 ± 0.03	0.98 ± 0.02	1.23 ± 0.05	1.05 ± 0.02
	α_1	1.00 ± 0.11	1.02 ± 0.08	1.35 ± 0.07	1.05 ± 0.13
1.5	α	1.02 ± 0.03	1.01 ± 0.02	1.15 ± 0.04	1.14 ± 0.04
	α_1	1.05 ± 0.15	1.08 ± 0.11	1.27 ± 1.14	1.16 ± 0.07
2.0	α			1.09 ± 0.03	1.11 ± 0.06
	α_1			1.13 ± 0.09	1.13 ± 0.11
2.5	α	1.18 ± 0.03			
	α_1	1.25 ± 0.06			

each cut-off n ($t_{\text{cut-off}} = n\Delta t$, dt is the sampling time), and calculate the corresponding frequency ($f_{\text{cut-off}} = 1/t_{\text{cut-off}}$). We find that the frequency limits in PSD and $f_{\text{cut-off}}$ values are similar.

In the previous analysis we found that, at higher concentrations, the rat brain generates burst suppression patterns. However, DFA analysis shows linear behaviour and is not noticeably affected by the burst-suppression events. The reason for this behaviour is that DFA systematically removes trends in order to distinguish long-range fluctuations.

We computed the DFA exponent and PSD exponent for rat LFP data sets (averaged across all electrodes) as summarised in Table 4.2. Exponent α_1 was calculated from the PSD exponent β using $\alpha_1 = \frac{1}{2}(\beta + 1)$, then compared with the DFA-derived value of α.

Days 1, 2 and 4 provide consistent results as the α_1 and α values are closely similar. Moreover, DFA performs in the same manner as α shows lower values at lower concentrations and slightly higher values at higher concentrations. However, the data for rat 3 is less consistent.

These results give good support to the analytical relationship between DFA and PSD exponents. Our DFA and PSD study leads to the following conclusions:

- DFA exponent is close to unity for anaesthetised rat LFP data, which indicates the existence of long-range temporal correlations
- Slight increase of α at higher concentrations
- Experimental results validate the analytical relationship between DFA and PSD.

In Section 4.2.3 we computed the $1/e$ correlation times for autocorrelation exponential decay to give the short-range correlation $R(\text{lag}) \sim \exp(-\text{lag}/\tau)$. If there are long-range correlations present, these should be maps to a power-law decay $R(\text{lag}) \sim \text{lag}^{-\gamma}$ [44]. However, it is not possible to calculate power-law decay γ directly from a log-log plot of the autocorrelation function because of the noisy oscillations about zero at larger lag times.

4.4 Chapter Summary

This chapter investigated anaesthetic induced changes in electrophysiological data in rats. Examination of the LFP amplitude histograms showed that:

- At lower concentrations, LFP fluctuations are symmetric and approximately normally distributed
- At higher concentrations, the distributions become increasingly negatively skewed and heavy-tailed due to emergence of high-amplitude burst-suppression patterns.
- Fluctuation variance tends to peak at the nominal phase-transition point of 1.0 MAC. However, the rat of day-1 shows a different pattern, possibly due to a difference in anaesthetic sensitivity.

The autocorrelation investigations showed that correlation time increases with anaesthetic concentration. Interesting resonance patterns in LFP at lower anaesthetic concentrations become suppressed at higher concentrations.

Detrended fluctuation analysis (DFA) of the LFP fluctuations revealed:

- A mid-range DFA exponent value near 1 for the time range 0.03 s to 2 s, indicating long-range temporal correlations in the anaesthetised LFP data
- Slight increase in the DFA exponent with anaesthetic concentration, suggesting onset of unbounded non-stationary fluctuations.

Finally, we showed that the DFA and power spectral density power-law exponents (α and β respectively) were in reasonable agreement with theoretical relationship $\alpha = (\beta + 1)/2$. Three out of four rats validate the relationship, while the fourth rat shows poorer agreement.

Chapter 5

Neuronal avalanches and scaling behaviour

5.1 Introduction

Avalanches are cascades of events that propagate spatially and temporally through an assembly of connected "units". One unit reaches threshold for change of state, and communicates this information to other units which may also change state, resulting in outward propagation to larger areas. Avalanche behaviour can be seen in many dynamical complex systems, such as forest fires, earthquakes, magnets and nuclear reactions [7, 27, 55]. Avalanches can also propagate through an assembly of neurons: an individual neuron integrates inputs from thousands of neurons; when the summed input exceeds threshold, the neuron generates an action potential that is distributed back to the network to influence firing of other neurons. This integration and redistribution allows neuronal activity to propagate through the cortex to create spreading cascades of neuronal activations [7, 27].

Neuronal avalanches are spontaneous events that propagate along the superficial layers of the cortex. These random events are correlated in space and time [81] but do not take the form of waves or oscillations [7, 96]. Avalanches manifest as irregular and isolated population bursts occurring across a wide range of spatial and time scales. The variations in length and durations have characteristic statistical properties, chief among these being so-called "power-law behaviour" [7, 69, 73, 96].

Power-law distribution in avalanches is a characteristic behaviour of *self-organised critical* (SOC) systems. If a system can approach a critical state without any external perturbation or tuning of a control parameter, it is called as a self-organised critical system. The concept of self-organised criticality was first introduced in the sandpile model

by Bak, Tang, and Wiesenfeld in 1987 [4]. This model displayed spatial and temporal power-law and scale-invariant properties [4, 71].

Although the term "avalanche"is applied to both SOC systems and neural networks, it actually refers to different classifications of activity. In SOC systems, an avalanche is a cascade of activities that initiate from a single point and that is separated from other avalanches by a distinct pause in activity. In contrast, neuronal avalanches typically overlap, with no clear pauses between them, so it can be challenging to identify the end of one avalanche event and the start of another. Therefore, it is standard practice in neuronal avalanche analysis to segment the data into "bins", investigating how the distribution of avalanche events varies with epoch length and spatial extent. For this reason, neuronal avalanche statistics are described as being bin dependent [71].

Neuronal avalanche analysis has been applied to both *in vitro* and *in vivo* models. Initial work focused on cell cultures and slices [6, 7, 69, 81]. Later studies progressed to anaesthetised and freely behaving rats [48, 73], awake monkeys [68], cats [96] and human brain [2, 64].

In this chapter we will be applying avalanche analysis to two distinct types of data: electrophysiological recordings from anaesthetised rats, and simulation results from the Waikato mean-field cortical model placed close to its critical point.

5.2 Properties of avalanches and their statistics

5.2.1 Power-law distribution

The term "power-law" is a statistical relationship between two variables in which a relative change in one variable results in a proportional change in the other. A random variable x is said to follow a power-law distribution when its probability distribution, $p(x)$, obeys the following equation [19, 63, 96],

$$p(x) = C\frac{1}{x^{\alpha}}$$

where α is a constant exponent known as the *scaling parameter* of the power-law. C is a normalisation constant that ensures $p(x)$ has unit area,

$$\int p(x)\,dx = 1$$

Taking the logarithm of the power-law distribution,

$$\log p(x) = -\alpha \log x + \log C$$

showing that a plot of $\log p(x)$ vs $\log x$ gives a straight line of slope α.

Because of the anticipated scatter in the $\log p(x)$ vs x distribution, there will be uncertainty in the "best" value of the power-law slope. We choose to use the maximum likelihood method [19, 63], then evaluate goodness-of-fit between the data and evaluated power-law using the Kolmogorov–Smirnov (KS) test [19].

Before applying power-law analysis to avalanche size distributions, first we will investigate power-law behaviour using an idealised data set: random real numbers generated using a power-law probability distribution for a specific value of α. The following calibration experiment is drawn from the review article by Newman (2005) [63].

Calibration experiment using artificial data

Following Newman [63], we generate random numbers r uniformly distributed in the range $0 \leq r < 1$, then produce power-law-distributed random numbers in the range $x_{\min} \leq x < \infty$ with exponent α using,

$$x = x_{\min}(1-r)^{\frac{-1}{(\alpha-1)}} \tag{5.1}$$

Here we set $\alpha = 2.5$ and $x_{\min} = 1$. The histogram for uniformly distributed r and the probability density for power-law distributed x are shown in figure 5.1. Sample MATLAB code is shown below.

```
alpha = 2.5;          % define power-law exponent
x_min = 1;                  % minimum of x
n = 1000000;          % 1 milion samples
% generate uniformly distributed random numbers
r = rand(n,1);

% generate power-law distributed random numbers
x = x_min*(1-r).^(-1/(alpha-1));

figure(1)
% first subplot: histogram for r
subaxis(1,3,1);
```

```
h = histogram(r, [0:0.02:1]); % compute and plot histogram for r
title('(a) Histogram for r')

% Calculate histogram for x with 50000 number of bins
bins = linspace(1,max(x),50000);
[freq,edges] = histcounts(x,bins);        % generate histogram

Prob = freq/sum(freq);        % Calculate probability distribution

% second subplot: PDF for x
subaxis(1,3,2);
plot(edges(2:end), Prob, 'ok')
title('(b) PDF for x')

% third subplot: log-log PDF for x
subaxis(1,3,3);
loglog(edges(2:end), Prob, 'ok')
title('(c) log-log PDF for x')

% calculate cumulative probability
cumProb = cumsum(prob,'reverse');

figure(2)
loglog(edges(2:end), Prob, 'ok')
loglog(edges(2:end), cumProb, '*b')
```

To illustrate the power-law nature of the probability density of x, we plot the probability density function (PDF), $p(x)$ on logarithmic scales. Figure 5.1(c) shows that the log-log plot $p(x)$ is aligned with a straight-line of slope -2.5. However, the results get noisy in the right-hand tail for $x \gtrsim 100$. This is because for larger values of x, the number of samples in the bins becomes small or even zero. This fluctuating bin count results in an increasingly noisy distribution for large x. To alleviate this problem, we construct the *cumulative distribution* (CDF), $P(x)$ denoting the probability of encountering a value larger than x,

$$\begin{aligned} P(x) &= \int_x^\infty p(\lambda)\, d\lambda \\ &= \int_x^\infty C\lambda^{-\alpha}\, d\lambda \\ &= \frac{C}{\alpha - 1} x^{-(\alpha-1)} \end{aligned} \tag{5.2}$$

We note that the cumulative distribution, $P(x)$ also follows a power-law, but with an exponent $(\alpha - 1)$ which is 1 less than that for $p(x)$. Figure 5.2 shows that for $\alpha = -2.5$, the cumulative distribution has a slope -1.5. We observe that the cumulative distribution has

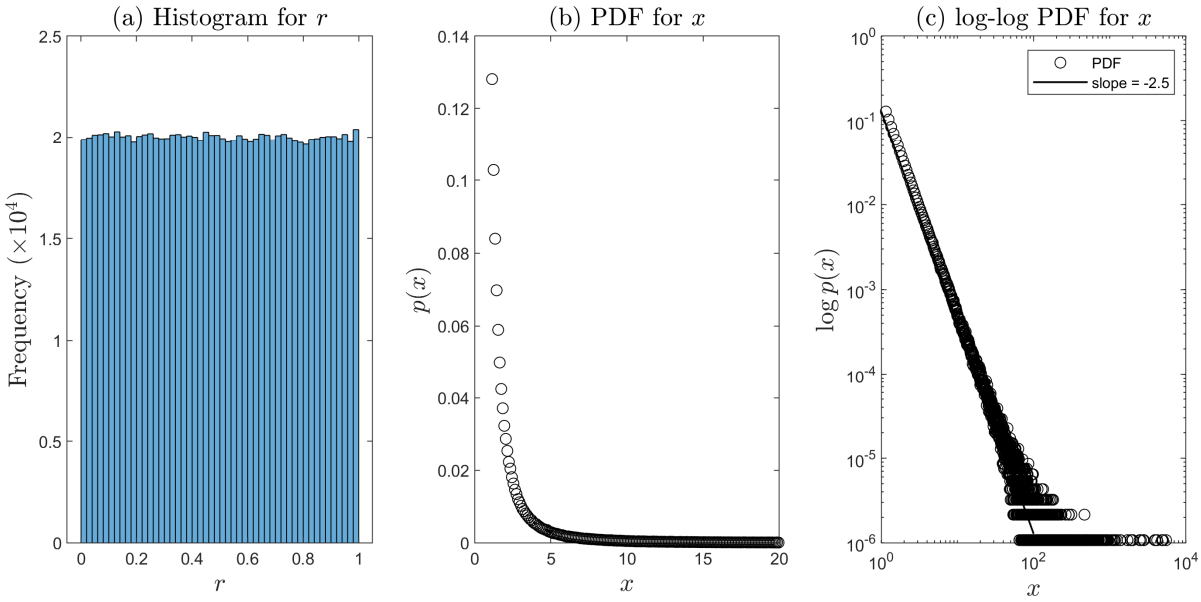

Figure 5.1: Histograms and distribution for calibration data. (a) Random numbers r, are uniformly distributed in the range $0 \leq r < 1$. (b) Probability density for power-law distributed numbers with $\alpha = 2.5$. Smaller numbers are common and larger numbers are rare. (c) Log-log plot of the probability distribution of x. Straight line has a slope of -2.5

a smoother shape because of the integration. This reduces the noise in the tail, thereby extending the range of analysis by $\sim$2 orders of magnitude.

Calculating the exponent of the power-law

The artificial data were generated using a predetermined α value. In practical situations the exponent is unknown so we need to estimate α from the data. The standard method is to fit a straight line to the log-log plots and determine the slope of that line. However this method is not reliable and can be biased because of the uneven variations in the tail. Instead, Newman [63] provides a simple and reliable numerical method to estimate α:

$$\alpha = 1 + n\left[\sum_{i=1}^{n} \ln \frac{x_i}{x_{\min}}\right]^{-1} \tag{5.3}$$

where n is the number of data points and $x_{\min}$ is the minimum of x. The statistical error in the exponent σ is given by,

$$\sigma = \sqrt{n}\left[\sum_{i=1}^{n} \ln \frac{x_i}{x_{\min}}\right]^{-1} = \frac{\alpha - 1}{\sqrt{n}}. \tag{5.4}$$

These equations are derived by using maximum likelihood estimation of power-law distribution [63]. For our artificial data set of one million random numbers Eqs (5.3) and

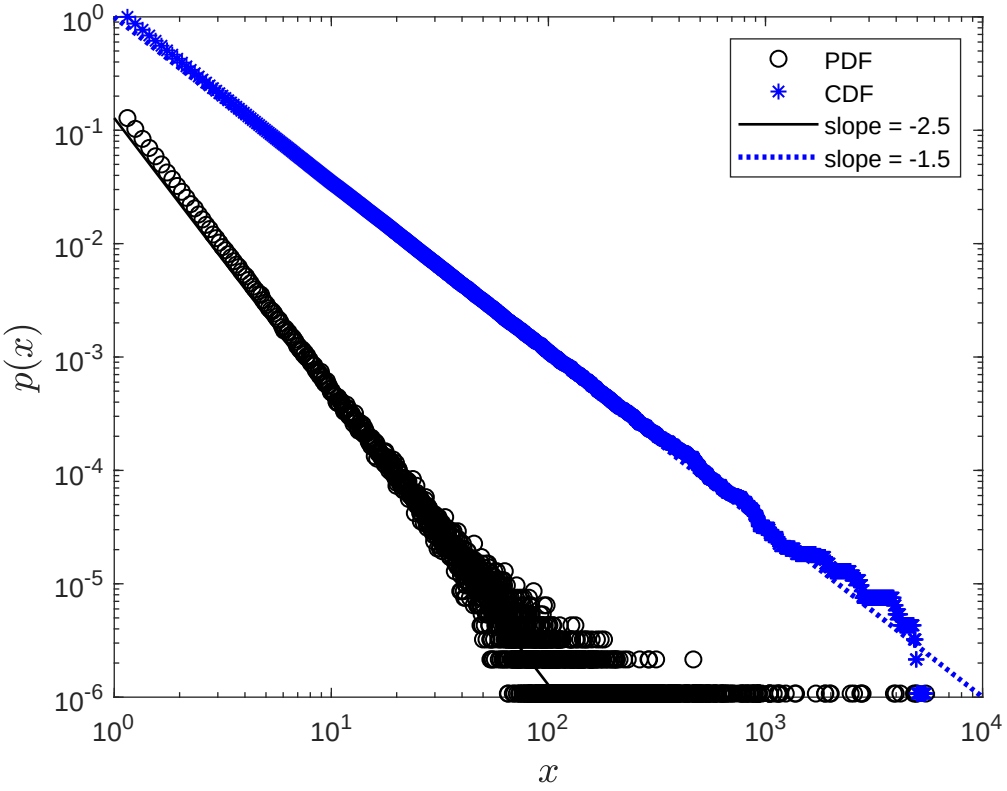

Figure 5.2: Comparison between probability distribution $p(x)$ (black circles) and cumulative distribution $P(x)$ (blue asterisks). Data are well fitted by straight lines of slopes -2.5 and -1.5 respectively

(5.4) estimate the exponent to be $\alpha = 2.499 \pm 0.001$.

We use Eqs (5.3) and (5.4) to estimate the power-law exponent of the avalanches with $x_{\min}$ being chosen to give a best power-law fit for the distribution.

5.2.2 Detection of an avalanche

In this chapter we analyse local field potential (LFP) data from rat electrophysiological recordings and from numerical simulations of the Waikato mean-field model. Here we discuss the signal processing methods required to detect peaks and avalanche events in the respective time-series.

Signal processing

The first step in processing the sampled LFP signals is to ensure that each recording has zero mean. This is done by subtracting the whole-of-recording mean from each sample value x,

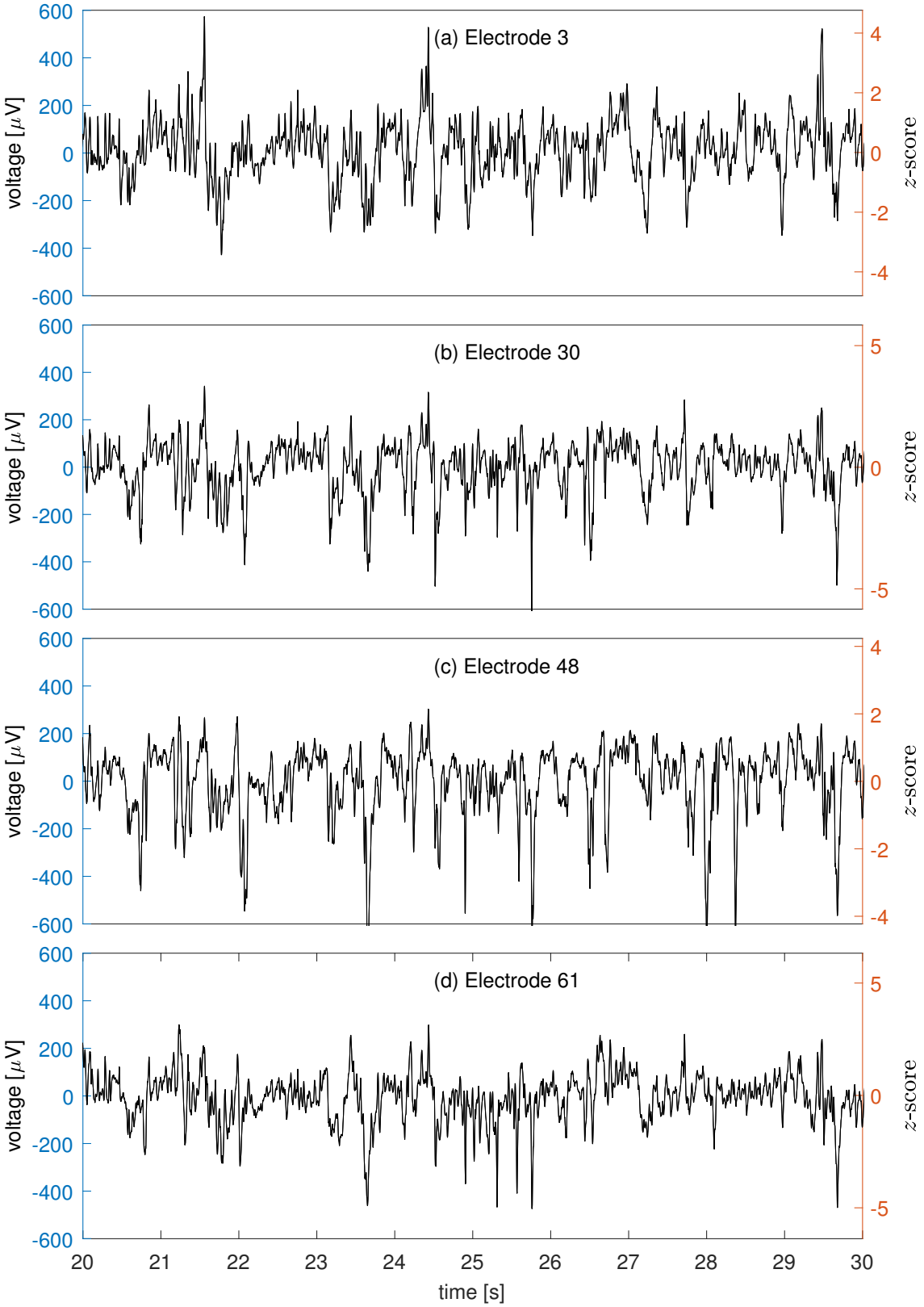

Figure 5.3: LFP time-series for four selected electrodes for 1 MAC on day 4 (01.02.2006). Left scale shows raw LFP voltage in μV, right scale applies a z-score normalisation to compensate for differing electrode sensitivities: $z = (x - \bar{x})/s$ with mean $\bar{x}$ and standard deviation s calculated for each channel

$$x'_i = x_i - \bar{x} \quad \text{with} \quad \bar{x} = \frac{1}{N}\sum_{i=1}^{N} x_i$$

where N is the number of samples per LFP recording. For sample rate of 500 s^{-1} and duration of 60 s, $N = 30000$.

We then map to a z-score by dividing by the standard deviation,

$$z_i = \frac{x'_i}{s} = \frac{x_i - \bar{x}}{s} \quad \text{with} \quad s = \sqrt{\frac{\sum_{i=1}^{N}(x_i - \bar{x})^2}{N-1}}$$

The LFP data are collected from different electrodes which evidently have different sensitivities. Converting to z-scores is an attempt to compensate for these variations in effective channel gains.

Figure 5.3 shows a comparison between raw signal (in μV – see left-hand scale) and z-normalized signal (right-hand scale) for four representative LFP channels.

Peak detection

Peaks are defined as the extremes of the time-series which cross a specified positive or negative amplitude threshold. We record the amplitude and time of occurrence of each peak.

The selection of an appropriate threshold requires some care: if the value is set too low then the algorithm will be triggered by peaks of noise content, but if the threshold is too high, we may lose important events. The influence of threshold selection in avalanche analysis is further explained in Section 5.2.5.

Definition of an avalanche

In our standard LFP avalanche analysis we consider all active electrodes for a given rat on a given day (the number of active electrodes varied from 13 to 37). But to clarify the methods used for extracting avalanche statistics, we have chosen to use a subset of just four selected electrodes in the following discussion of what is meant by the "size" of an avalanche. This tutorial introduction will then be followed by an analysis of the full LFP data.

Detected peaks for four chosen electrodes are shown in the Figure 5.5. Events were binned into time-bins or *frames* of width Δt. We define an avalanche as a sequence of

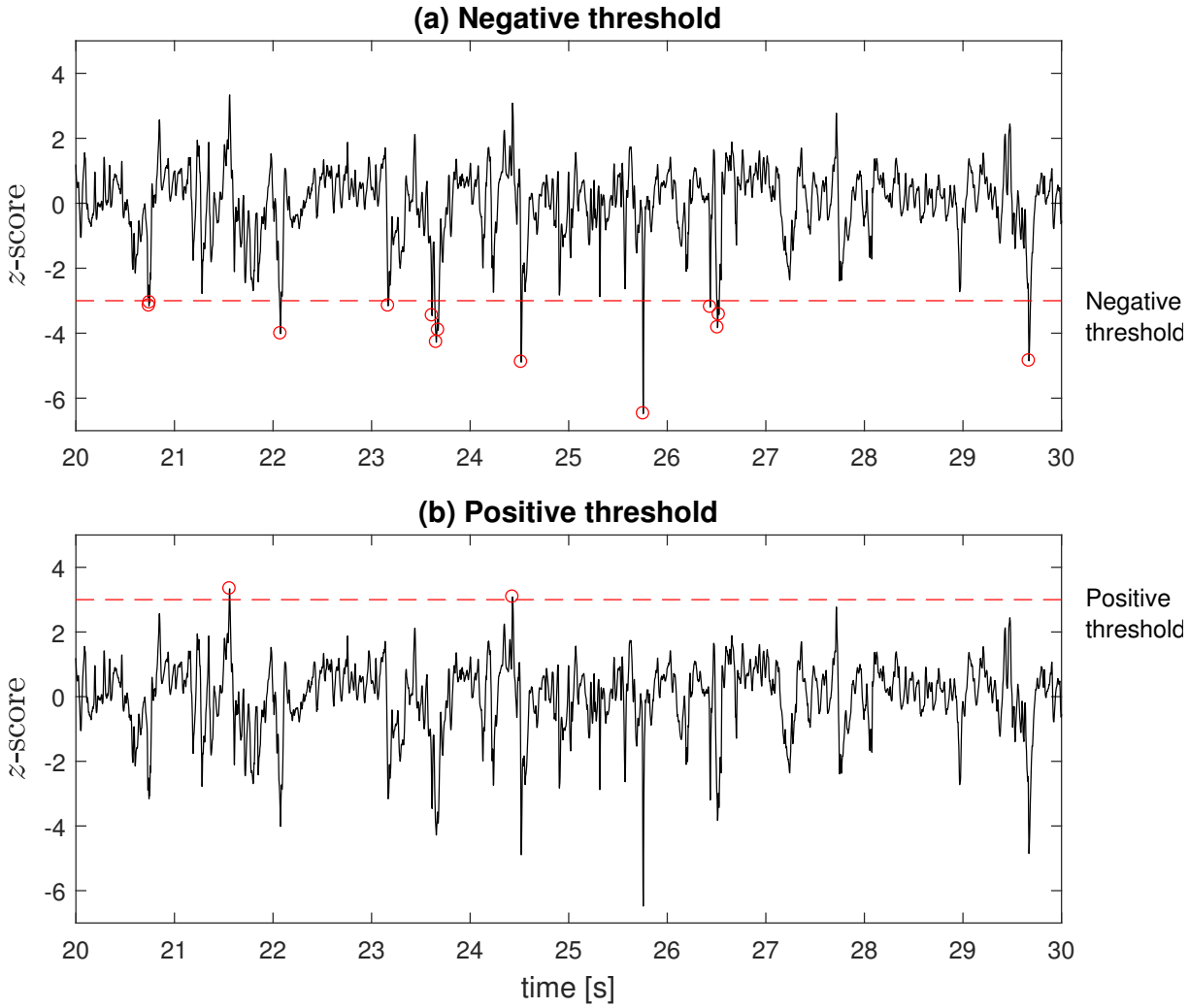

Figure 5.4: Detected negative and positive peaks with threshold (in z-score units) of (a) -3 and (b) $+3$. Dashed lines indicate threshold setting, red circles are the detected peak events

consecutively active frames which are bounded by "blank" or inactive frames containing no peak events. Figure 5.5(e) shows the ten detected avalanches.

In this illustration we select a bin width $\Delta t = 0.2$ s. Altering the width of the time bin changes the apparent size of avalanches. Smaller time bins result in smaller avalanches, while longer Δt captures larger-size avalanches resulting from the combination of many small events [7]. Therefore the extracted avalanche behaviour and size distribution depends on bin size. This is further discussed in Section 5.2.4.

5.2.3 Size distributions of avalanches

Avalanche behaviour quantified by its size distribution. The size of an avalanche can be defined in three distinct ways. The most popular definition is the total number of peaks in an avalanche [7]. Also used is the absolute-sum of amplitudes of LFP peaks [7,96]. The

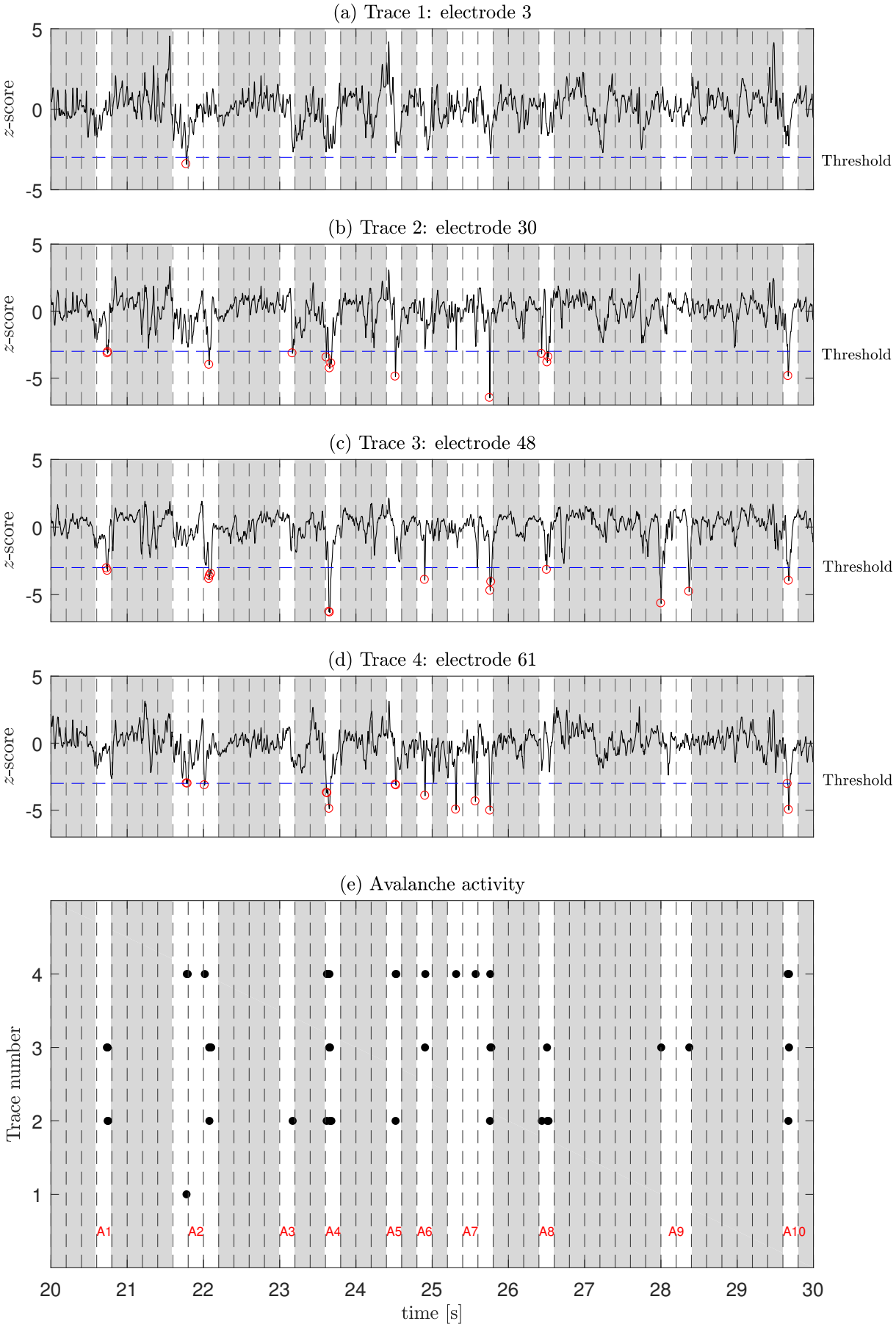

Figure 5.5: Defining an avalanche using peak detections across four selected electrodes. Vertical-dashed lines show temporal binning with a time resolution of 0.2 s. (e) An avalanche is defined as a sequence of active time-frames bounded by blank frames (grey areas) in which no activity present. The ten avalanches detected here are labelled A1, A2, ... A10

Table 5.1: Sizes of detected avalanches according to three definitions: number of peaks (n_{pk}), the summation of amplitudes (n_{amp}), number of active electrodes (n_{elec}).

Event	A1	A2	A3	A4	A5	A6	A7	A8	A9	A10
n_{pk}	2	5	1	3	2	2	5	2	2	3
n_{amp}	6.40	17.45	3.15	15.51	8.04	7.85	25.56	7.00	10.45	13.82
n_{elec}	2	4	1	3	2	2	3	2	1	3

third definition is the number of active electrodes, ignoring any repeated activity in the avalanche by same electrode [48]. Table 5.1 illustrates these three measures of avalanche size for the four selected electrodes of Figure 5.5.

Once all avalanche events for a given (multichannel) LFP recording have been extracted, we convert the size distribution to a probability distribution $p(n)$, the probability of an avalanche of size n. The power-law exponent can then be extracted from a log-log plot of $p(n)$ vs n (or equivalently, by applying Eqs (5.3) and (5.4)).

The following sections apply avalanche analysis to all active electrodes of a selected rat LFP data set (date 01.02.2006) for 1 MAC.

64	56	48	40	32	24	16	8
63	55	47	39	31	23	15	7
62	54	46	38	30	22	14	6
61	53	45	37	29	21	13	5
60	52	44	36	28	20	12	4
59	51	43	35	27	19	11	3
58	50	42	34	26	18	10	2
57	49	41	33	25	17	9	1

Figure 5.6: Electrode placement in the 8×8 grid. The 22 active electrodes for date 01.02.2006 are shown with a white background

Number of peaks during the avalanche (n_{pk})

Initially, we set avalanche size to be number of peaks per avalanche. Figure 5.7 presents the size distribution for rat LFP data on day 01.02.2006 (dd.mm.yyyy) concentration of 1 MAC. Here $\Delta t = 0.01$s and we fixed the z-score threshold at -1.5. We recorded and analysed the events detected at the active 22 electrodes shown in Fig. 5.6.

Note that the size of avalanches is not limited by the number of electrodes in the grid: some avalanche sizes are *larger* than the maximum number of electrodes. This is because some electrodes appear more than once in the same avalanche. Beggs and Plenz [7] explained that this unusual behaviour can occur when the avalanche travels through the grid then returns to the initial point, creating another event at the same electrode.

The log-log plot of $p(n_{\text{pk}})$ vs n_{pk} reveals a power-law with $\alpha = 1.50 \pm 0.02$ (calculated using Eqs (5.3), (5.4)). As per previous studies, this linear relationship should have a cut-off point determined by the maximum number of electrodes available within the array [7,48,68]. It is evident in our analysis that the line breaks earlier than the expected cut-off point (vertical dotted line), and this is most obvious in the cumulative distribution (Fig. 5.7(b)). Only 22 electrodes were active from the 8×8 electrode array, and they are

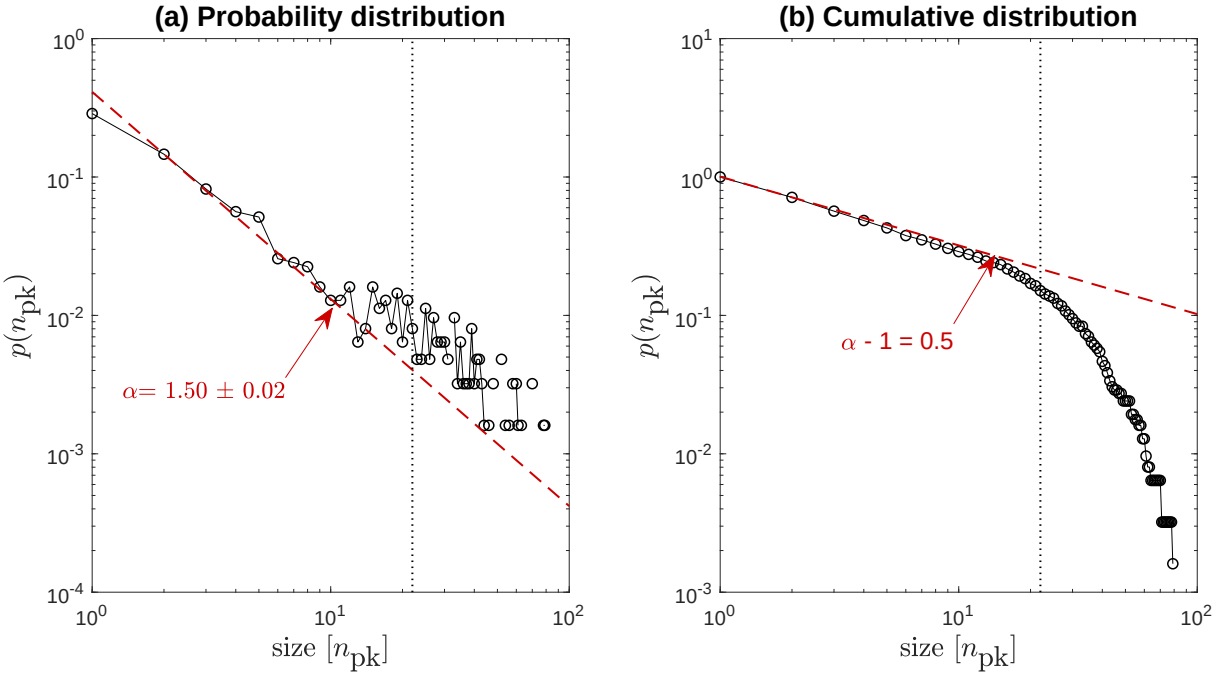

Figure 5.7: (a) Probability distribution of avalanche size expressed as number of peaks per avalanche. Bin width Δt is equal to 0.01 s; threshold is -1.5. Red dashed line illustrates the linear-fit to the log-log plot. Black dotted line indicates the cut-off size set equal to 22, number of electrodes available. (b) Cumulative probability distribution. The linear-fit fails prior to the cut-off point

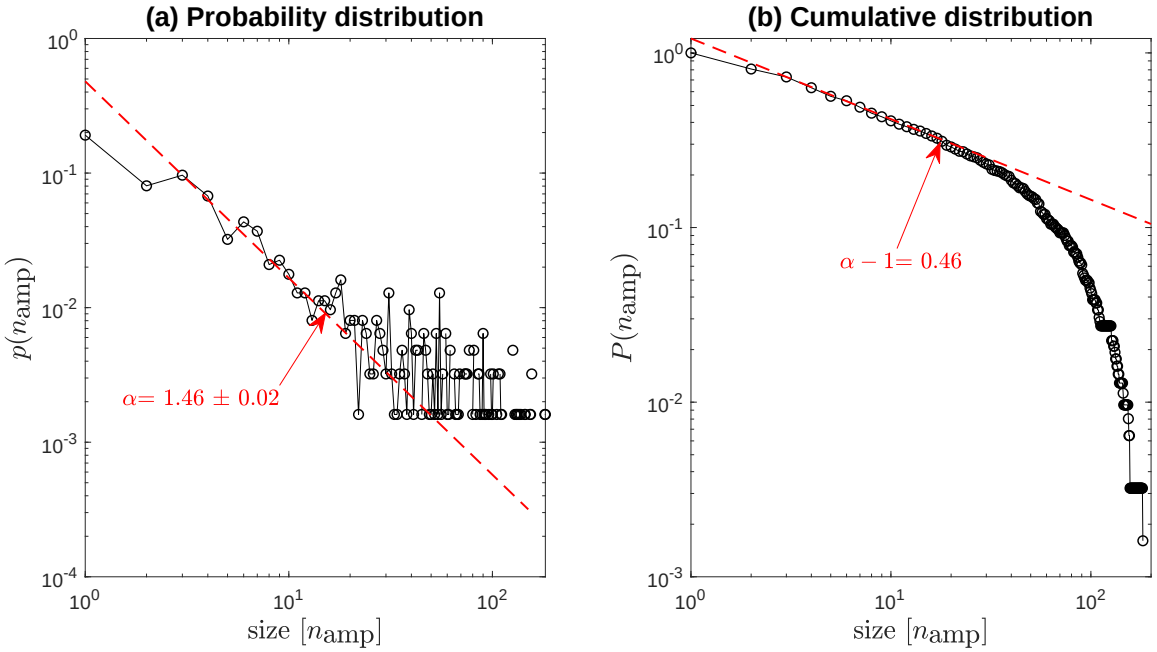

Figure 5.8: (a) Probability distribution of size based on summation of amplitude of peaks per avalanche. Peak amplitudes are measured in (dimensionless) z-score units. Time-bin width = 0.01 s, threshold = −1.5 (b) Cumulative probability distribution

not spread evenly across the grid (see Fig. 5.6). Therefore we might miss some avalanche events, causing the misalignment with the expected cut-off.

We evaluated the power-law exponent using Eq (5.3), restricting the fitting to one order of magnitude in avalanche size, as points in the tail are scattered, then applied the KS criterion to test for agreement between the fitted power-law and the avalanche distribution.

Sum of amplitudes (n_{amp})

Here avalanche size is expressed as the absolute summation of the z-score amplitudes of those peaks that exceed the defined threshold. Figure 5.8 presents the size distribution, showing power-law behaviour with exponent $\alpha = 1.46 \pm 0.02$.

Number of electrodes activated (n_{elec})

To eliminate repetitive events from the same electrode we now count, n_{elec}, the number of *unique* active electrodes in the avalanche. Figure 5.9 illustrates the size distribution for the same data set used in the previous sections. Note that the size of an avalanche cannot exceed the maximum cluster size of 22 active electrodes.

All three definitions gives power-law distributions exponents falling within ±0.04 of the average value $\alpha = 1.5$. Among the three definitions, number of peaks shows best

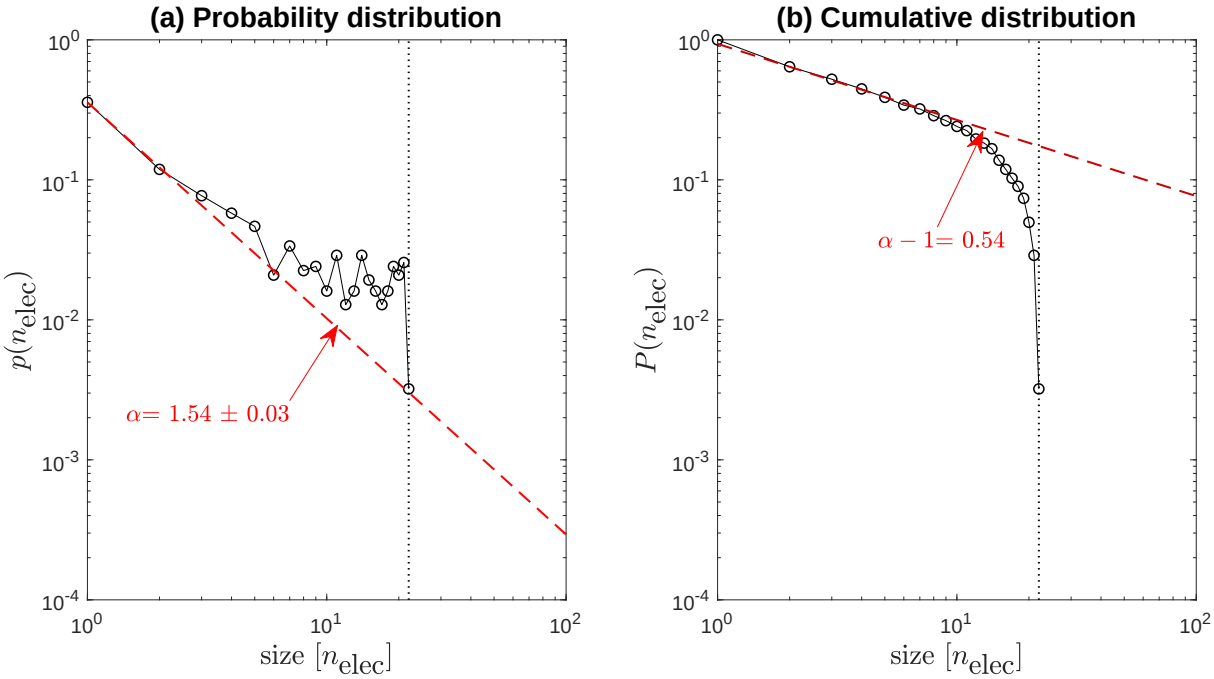

Figure 5.9: The size distribution of avalanches, when size is the number of active electrodes per avalanche (Δt = 0.01 s, threshold = -1.5). The red dashed line denotes the slope with power-law exponent, $\alpha = 1.54 \pm 0.03$. Here size is limited to the cluster size

alignment with the linear fit. Therefore, where there is a choice, we preferred to use the size definition n_{pk}, the number of peaks per avalanche.

5.2.4 Impact of width of the time bin

As explained earlier in Section 5.2.2, the apparent behaviour of avalanches varies with the width of time-bin, Δt. This section investigates this claim in more detail. We use rat LFP data at concentration of 1 MAC.

Figure 5.11 illustrates the variation of size distribution with Δt for the three size definitions. Left side figures, (a), (c), (e) show the size distributions, with different colours for different time-bin sizes. The z-score threshold for peak detection is set at -1.5. Although it seems all distributions align to a power-law, the value of α decreases slightly by a few percent ($\sim 6\%$) as Δt is increased by a factor of 2.

Figure 5.10 elucidates of the impact of variations in time-bin width on avalanche sizes. Here we consider three values for Δt: 0.2 s, 0.4 s, 0.8 s. When the time-bin width is short, it separates longer avalanche sequences into smaller avalanches. This is clearly illustrated in box A where a longer avalanche breaks into three smaller avalanches. Increasing the number of smaller avalanches leads to a power-law with a steeper slope. If Δt is long, then

smaller avalanches integrate into longer avalanches resulting in more long avalanches and fewer small avalanches, thus decreasing the slope of the power-law. Box B illustrates this phenomenon: five identified avalanches at $\Delta t = 0.4$ s combine into one long avalanche when Δt is doubled to 0.8 s. Therefore we need to establish an optimal time-bin width for avalanche analysis.

Previous studies have suggested that the averaged inter-event interval (IEI_{avg}) provides the optimum time-bin width [7, 68]. The inter-event interval is defined as the interval between two events. The averaged interval between LFP activity peaks across all the electrodes defines the averaged inter-event interval, IEI_{avg}. It has been established experimentally in previous studies of rat LFP that $\alpha = 1.5$ when $\Delta t = \text{IEI}_{\text{avg}}$ [7]. It has been argued theoretically that when the system is at criticality the power-law exponent should be $\alpha = 1.5$ [7, 68]. This will be discussed further in Section 5.2.6.

In our analysis, $\text{IEI}_{\text{avg}} = 0.017$ s for a z-score threshold $= -1.5$. Setting $\Delta t = \text{IEI}_{\text{avg}}$ gives $\alpha = 1.43 \pm 0.02$ for first two size definitions (number of peaks and summation of amplitudes) and $\alpha = 1.50 \pm 0.02$ for the third definition (number of unique electrodes).

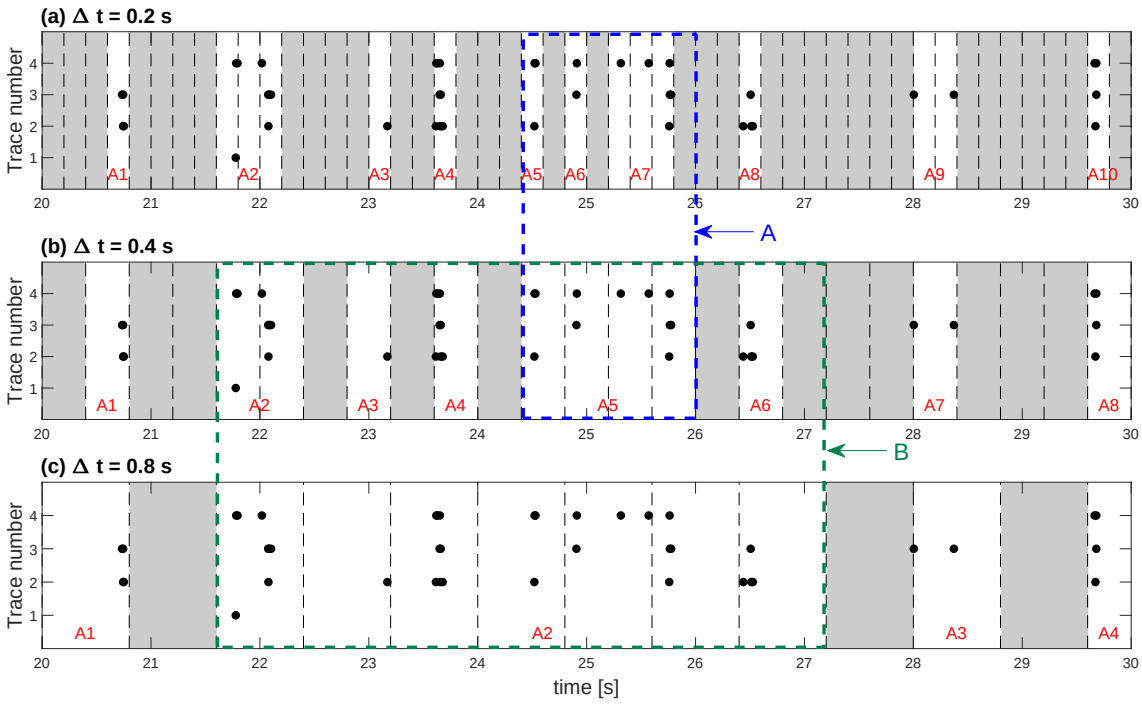

Figure 5.10: Detecting avalanches for three different time-bin widths. (a) $\Delta t = 0.2$ s; (b) $\Delta t = 0.4$ s; (c) $\Delta t = 0.6$ s. If the time-bin width is short then one long avalanche divides into several shorter avalanches as illustrated in box A for $\Delta t = 0.6$ s to $\Delta t = 0.2$ s. Box B exhibits the integration of smaller avalanches into one long avalanche when Δt changes from 0.4 s to 0.6 s

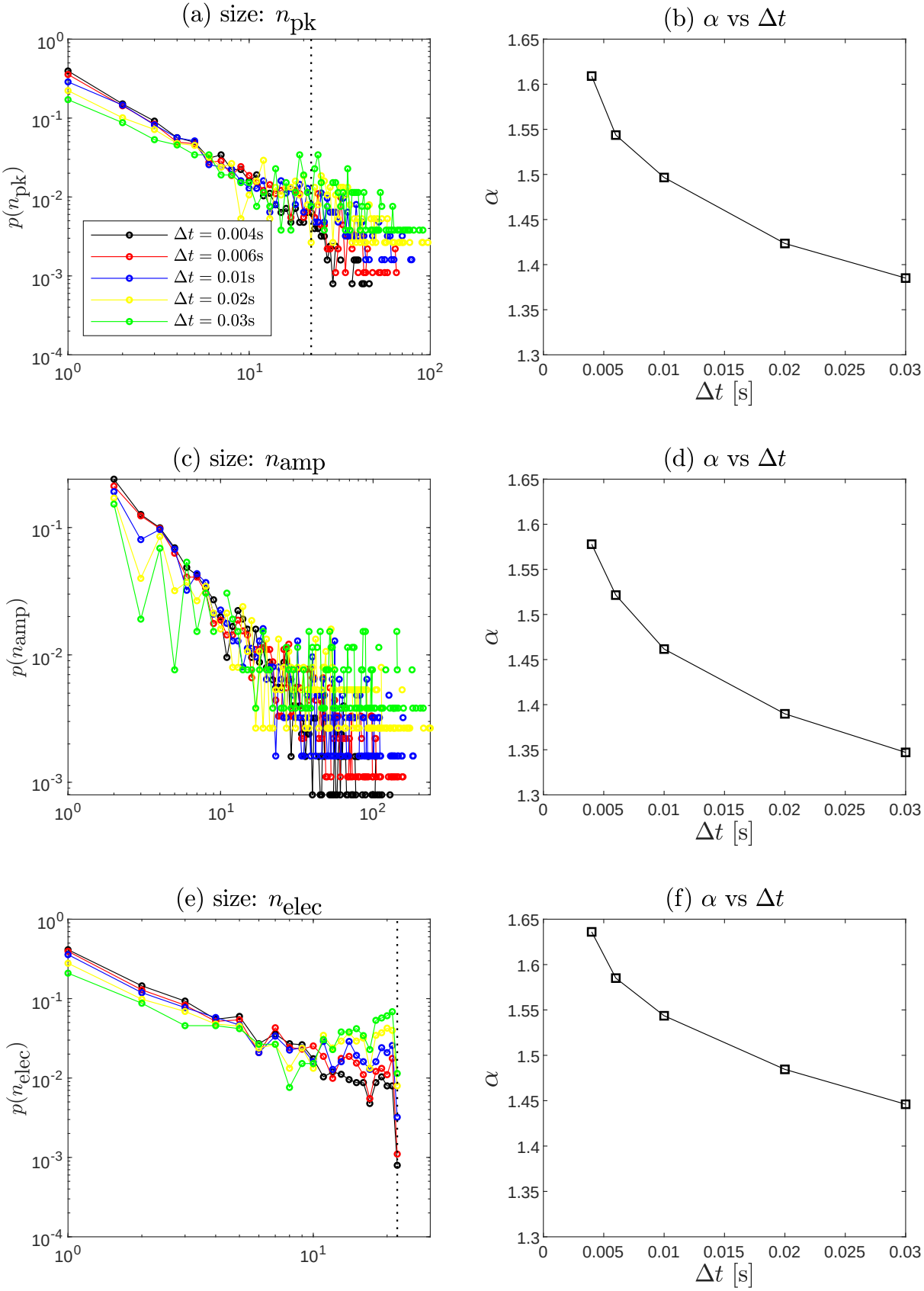

Figure 5.11: Size distributions for different time-bin widths, Δt. Left figures (a), (c), (e) demonstrate the probability distribution of avalanche sizes for five values of Δt. The slope of the power-law, α decays with Δt as shown in right-side figures (b), (d), (f)

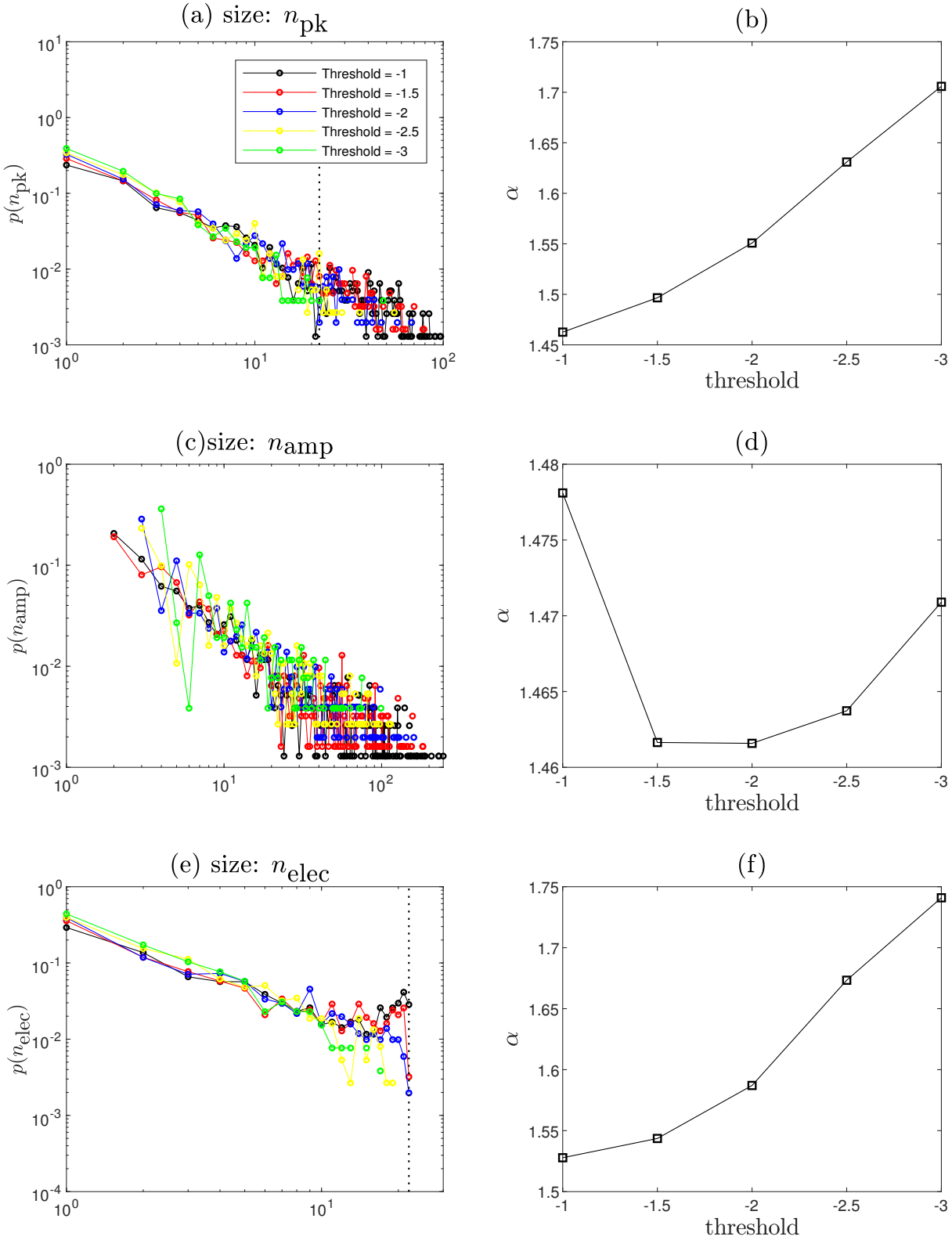

Figure 5.12: Change of power-law with different *negative* thresholds for rat LFP data from date 01.02.2006 at 1 MAC. Left-hand panels show probability distribution for (a) $p(n_{\mathrm{pk}})$: number of peaks; (b) $p(n_{\mathrm{amp}})$: sum of absolute amplitude; (c) $p(n_{\mathrm{elec}})$: number of unique electrodes. In all three cases power-law exponent tends to increase with absolute threshold (right-hand panels)

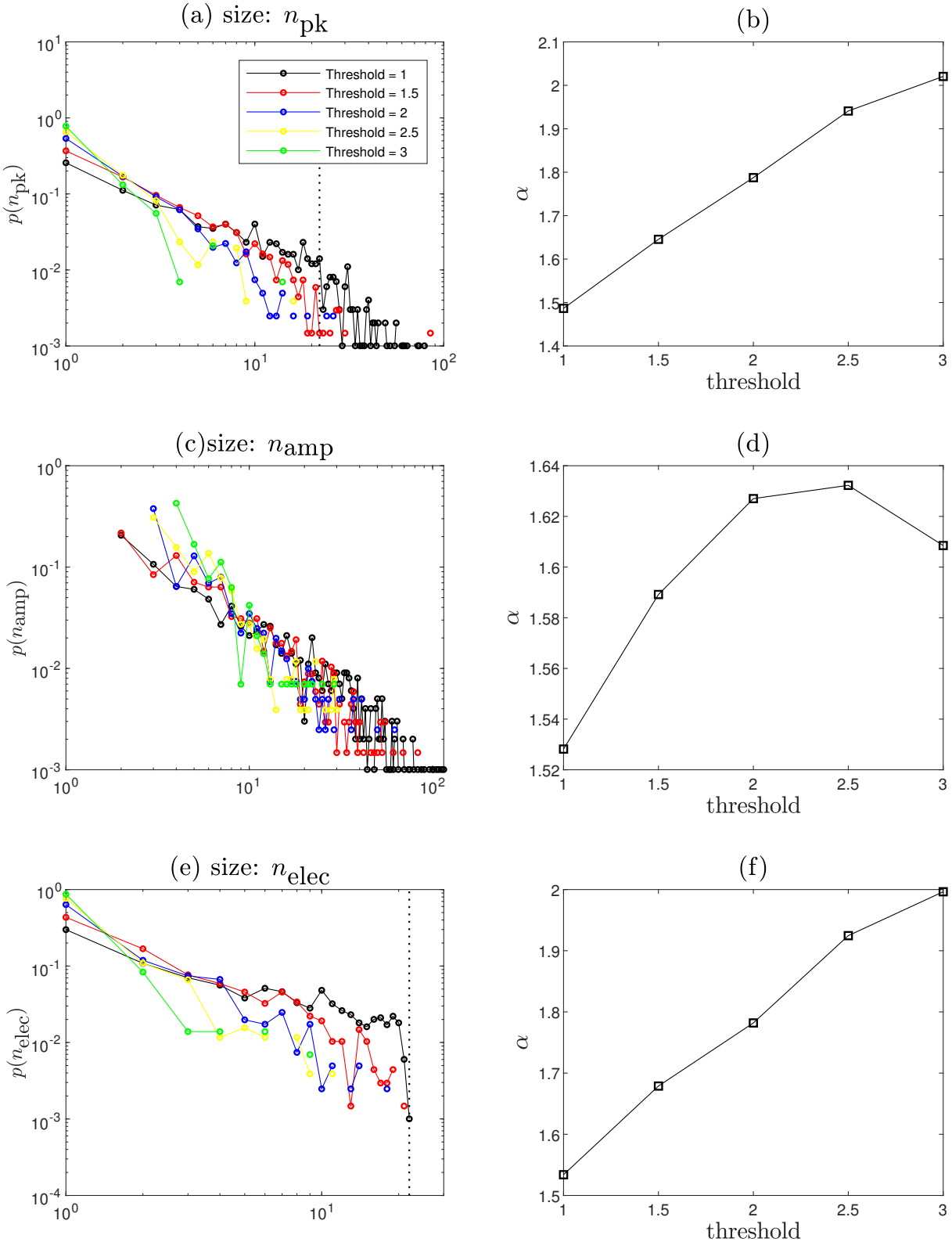

Figure 5.13: Power-law dependence on choice of *positive* z-score threshold for same rat LFP data referenced in Fig 5.12. Left-hand panels illustrate the probability distribution for each definition: (a) $p(n_{\mathrm{pk}})$; (b) $p(n_{\mathrm{amp}})$; (c) $p(n_{\mathrm{elec}})$. The exponent α increases with the threshold level in all three cases

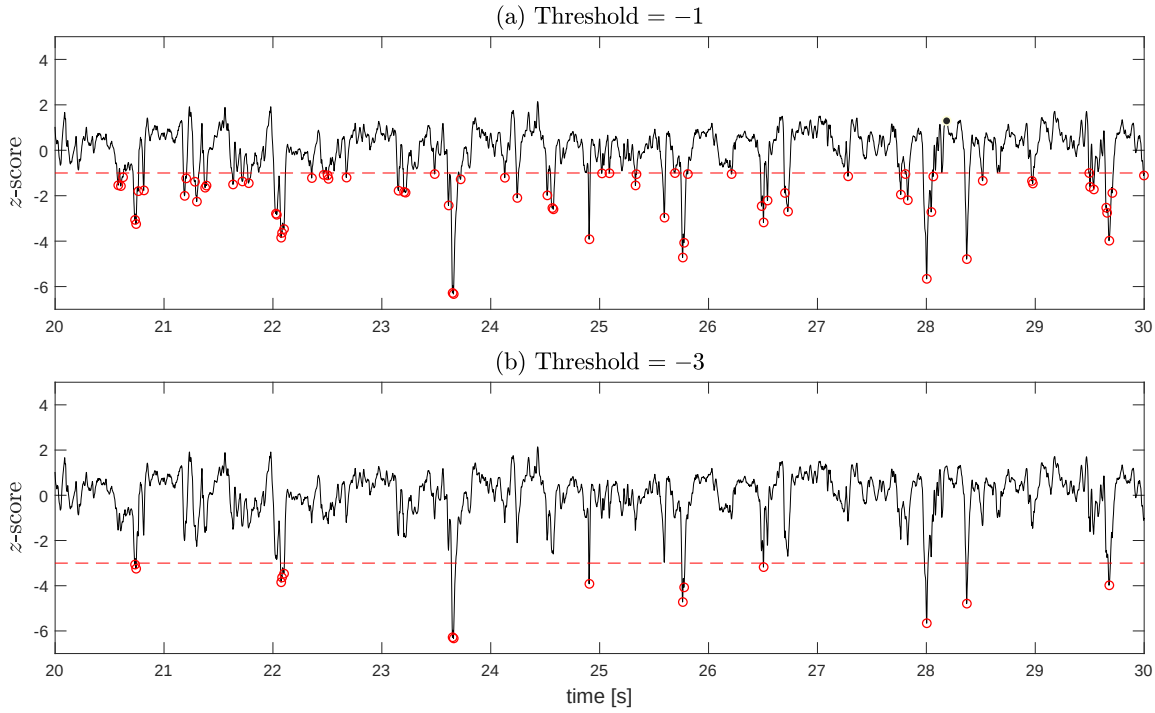

Figure 5.14: Detection of peaks with (a) low threshold and (b) high threshold. At low z-score threshold of -1, more events with shorter separations are revealed. The higher threshold of -3 results in few peaks with huge amplitude and larger time-gap

5.2.5 Change of size distribution with threshold

The previous section showed how the value of the power-law exponent depends on the choice of bin-width Δt. Our studies reveal that α also depends on the chosen threshold level. Here we analyse power-law distributions for rat LFP recordings for both negative and positive thresholds.

The threshold determines the number of events: signal extremes that exceed threshold define the events. As threshold level increases, events with lower amplitude are ignored. Figure 5.14 shows the change of peak detection with the threshold level. Lower thresholds reveal more peaks (Figure 5.14(a)). The time-gap between events is very low, and possibly it contains unwanted events not related to actual neuronal activity. At high threshold (Figure 5.14(b)) few events are spotted and they are well apart.

Unsurprisingly, the power-law distribution of avalanche sizes also depends on detection threshold. Low thresholds allow detection of more low-amplitude events: this tends to increase the size of the avalanches while decreasing the slope of the power-law. On the other hand, a high detection threshold detects events with higher amplitude and long time-gap reducing the number of larger events leading to a steeper slope. This can be

seen in Figures 5.12 and 5.13. These figures compare the size distribution for different *negative* thresholds and *positive* thresholds respectively. Both show an increase of α with higher thresholds. Interestingly the positive thresholds are associated with *larger* power-law slopes than those for negative thresholds ($\alpha_+ \simeq 1.65 \pm 0.03$ versus $\alpha_- \simeq 1.50 \pm 0.02$), and this is probably related to the apparent asymmetry between the positive and negative portions of the LFP waveform (e.g., see Fig. 5.14). Previous studies have focused more on the negative LFP peaks [7, 68], as they are thought to be more related to neuronal activity. Therefore negative LFP peaks are used for subsequent analysis here.

Inter-event Interval (IEI)

A further explanation for the variation of α with threshold would be changing of inter-event interval (IEI). Figure 5.15 shows the variation of IEI with z-score threshold. When the absolute level rises, IEI grows, albeit asymmetrically, with stronger growth for positive thresholds. Raised thresholds will detect fewer events, and event pairs will have longer time gaps between them, which corresponds to higher IEI.

In Section 5.2.4, it was explained how time-bin width effects α, with the suggestion that IEI would be the optimal time-bin width. For shorter IEI the events are closer. Therefore it creates larger size avalanches as more events are binned together. If IEI is

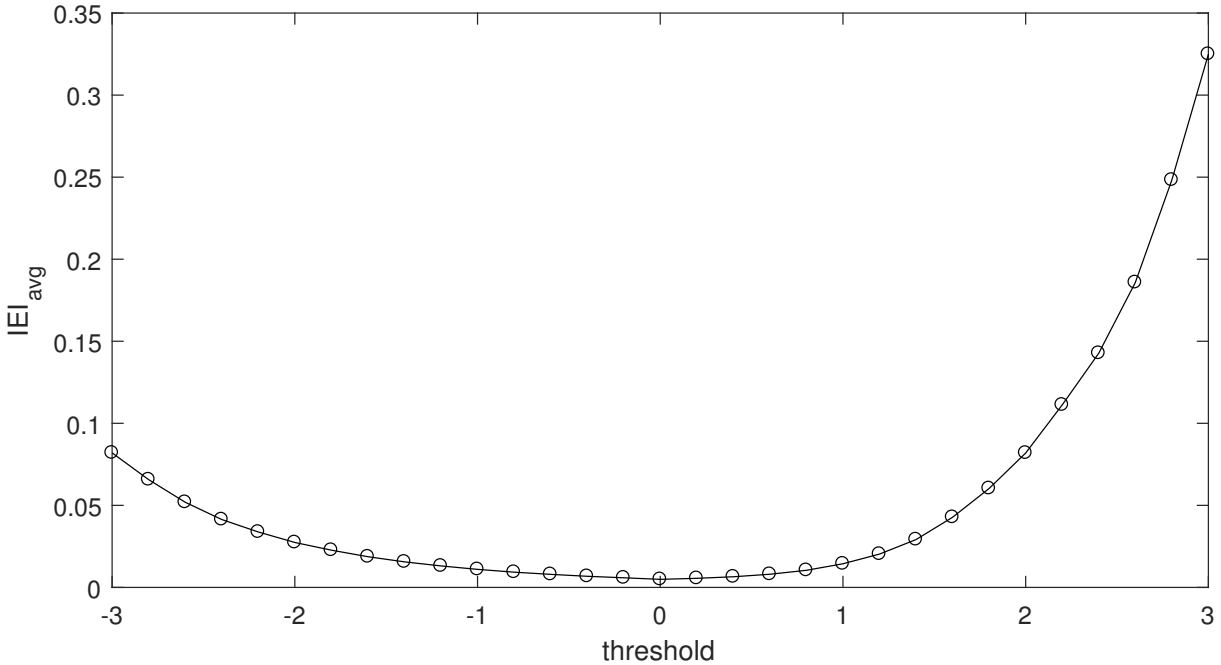

Figure 5.15: Inter-event interval (IEI) variation with detection threshold. Threshold was varied from -3 to 3. Here we used rat LFP data for 1 MAC (at 01.02.2006). Note the strong asymmetry between right (positive) and left (negative) halves of the IEI graph

longer, then events are more isolated, resulting in more smaller size avalanches. Therefore changes to IEI change the probability distribution of avalanche sizes, and α changes with it. This suggests that in order to retain a fixed value of α, we need to tune Δt for the different thresholds.

Applying a polynomial curve fit to the left and right portions of Fig. 5.15 we find that the IEI_{avg} versus threshold θ relationship maps to a pair of cubic equations for negative and positive thresholds:

$$\text{IEI}_{\text{avg}} = \begin{cases} 0.0034|\theta|^3 - 0.0079|\theta|^2 + 0.0077|\theta| + 0.0024, & \theta < 0 \\ 0.0196|\theta|^3 - 0.0386|\theta|^2 + 0.0246|\theta| + 0.0012, & \theta > 0 \end{cases} \tag{5.5}$$

5.2.6 Power-law exponent for the critical state

The behaviour of a system can often be characterised into qualitatively different phases with transitions between phases achieved by varying a control parameter. A *critical state* marks the edge of these phase transitions and the behaviour of the system at this point is described as being critical.

In previous studies it has been argued that $\alpha = 1.5$ should be the characteristic power-law exponent for avalanche size distribution of neural activity at a critical state [7]. This was verified by some experimental analysis [6, 7, 68, 83, 84], but this exponent value was only shown for a specific time-bin set to be equal to the averaged inter-event interval (IEI). For example, Beggs and Plenz [7] show $\alpha = 1.5$ at $\Delta t = 4$ ms, but these results exhibit clear dependence on Δt, with α ranging from 2 to 1 as Δt ranges from 1 to 16 ms. In our analysis at MAC 1.0, α varies from 1.4 to 1.7 for bin sizes ranging from 4 to 30 ms at z-score threshold setting of -1.5. For this threshold, $\text{IEI}_{\text{avg}} = 17$ ms, giving $\alpha_{\text{pk}} = 1.43 \pm 0.02$ for first two size definitions (number of peaks and summation of amplitudes) and $\alpha_{\text{elec}} = 1.50 \pm 0.02$ for the third definition (number of unique electrodes). Obtaining a power-law value of 1.5 required "tuning" of Δt between 10 to 15 ms for the three different size definitions.

Although the concept of using IEI as the optimum bin size appears in several previous studies [6, 7, 68], there is no theoretical explanation to choose this over other bin sizes. Therefore there is no specific rule to choose an appropriate value of Δt to justify the $\alpha = 1.5$ power-law exponent hypothesis quoted in the literature [71].

In fact, it has been shown that in general, the power-law exponent is not necessarily equal to 1.5 in different neural systems. As examples, $\alpha = 1.8$ for spike avalanches in anaesthetised cats [32], and $\alpha = 1.9$ for EEG of human brain [2]. There are different arguments for the reasons behind this discrepancy, one is being finite-size effects, using a limited number of electrodes compared to original works by Beggs and Plenz [2]. Moreover, has been suggested that using different systems might result in different power-law behaviour [32].

From these earlier works and from our own work reported here, we conclude that the power-law for neuronal avalanches depends fundamentally on the choice of time-bin size and that unfortunately there is no specific method to choose the optimum time-bin. Consistent with this conclusion, Priesemann [71] and Benayoun [8] argue that there is no specific or unique value of α for critical avalanche activities. Benayoun also states that avalanche distributions from any good neuronal network model must produce variation with respect to temporal bin width [8].

Alternative to estimating the critical exponents, Friedman [27] and Sethna [80] suggest a universal scaling function which determines the shape of the mean temporal profile of avalanches via data collapse. This method is independent of the exact value of the critical exponent. Note that we did not attempt data collapse on our avalanche measurements.

5.3 Impact of anaesthetic on avalanche size distributions for rat LFP

We analysed the LFP data of rats for anaesthetic concentrations in Chapter 4. Here we extend our analysis to see whether avalanche statistics are sensitive to anaesthetic concentration. As the animal transits from awake to anaesthetised, voltage waveforms change to high amplitude, low-frequency patterns. We will show that the size distribution of neuronal avalanches is indeed sensitive to the transition to deep anaesthesia, showing a pronounced deviation from the expected power-law behaviour. Here we use the number of peaks (n_{pk}) size definition as this gives better alignment with a power-law distribution than the other two definitions; also this is the most common definition used in the literature [7, 68, 70].

The electrophysiological data consist of multichannel LFP recordings from different rats under different anaesthetic concentrations (full details given in Chapter 4). Figure

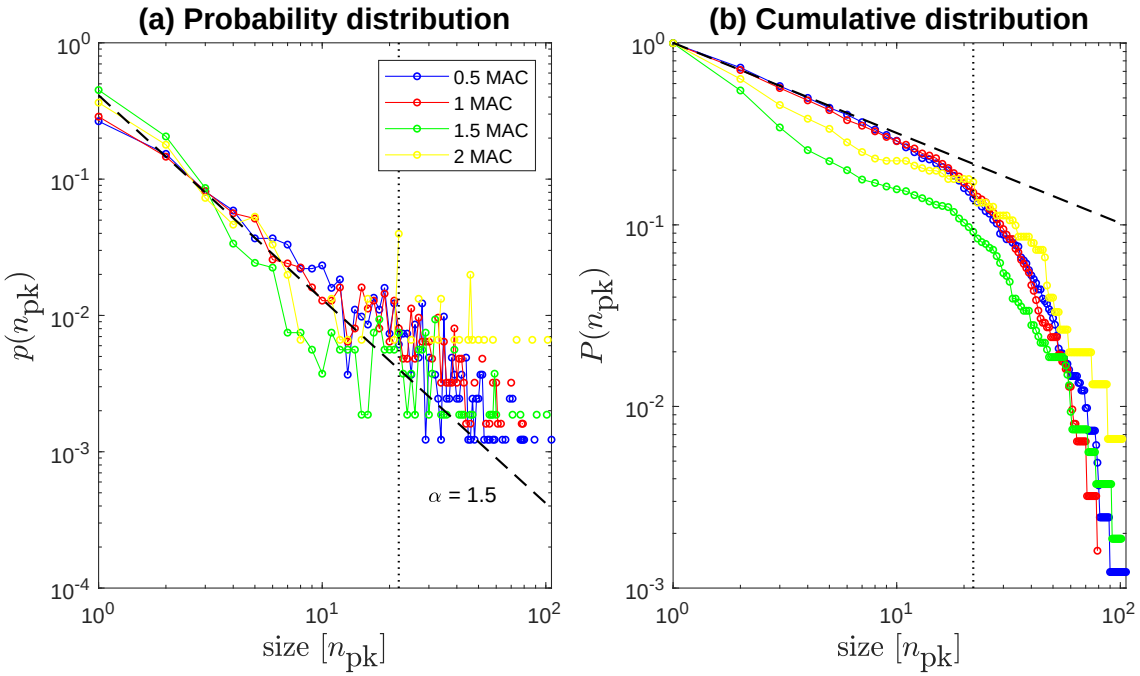

Figure 5.16: Probability distribution of avalanches with different anaesthetic concentrations: 0.5 MAC, 1 MAC, 1.5 MAC, 2 MAC. At lower concentrations (0.5 MAC and 1 MAC) probability distribution follows the expected $\alpha = 1.5$ power-law (blue and red lines). At higher anaesthetic concentrations (1.5 MAC and 2 MAC) the distribution deviates away from the power-law (green and yellow lines) as burst-suppression patterns emerge, with bursting activity tending to boost the number of large amplitude events. Time-bin width = 0.01 s and z-score threshold = -1.5. (b) Cumulative probability distribution illustrates clear visualisation of divergence from power-law distribution at higher anaesthetic concentrations

5.16(a) presents the size distribution from a selected rat for four anaesthetic concentrations: 0.5 MAC, 1 MAC, 1.5 MAC, 2 MAC. Dark colours, red and blue, represent the lower anaesthetic concentrations; these show alignment with the $\alpha = 1.5$ power-law. At higher concentrations (green and yellow), LFP events are not well described as scale-free power-law behaviour. This is clearly illustrated in the cumulative distributions, Figure 5.16(b). For low anaesthetic concentrations, the cumulative distributions align to a linear-fit line of slope of $\alpha - 1 = 0.50$. However, the size distribution at higher concentrations deviates from the power-law, showing a roughly bimodal shape. A higher number of small avalanches leads to higher slope at lower avalanche sizes. $P(x)$ generally decreases with an increase in avalanche size, interrupted by a sudden increase of $P(x)$ corresponding to higher avalanche sizes.

Increased anaesthetic concentration leads to characteristic burst-suppression patterns

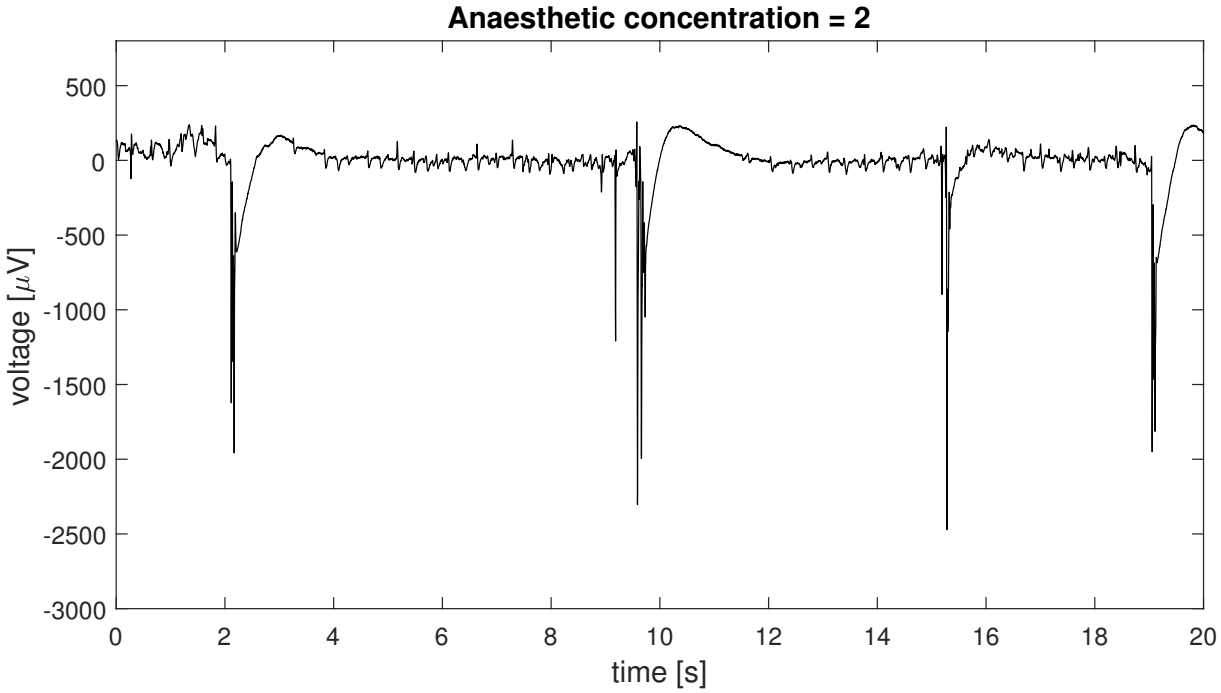

Figure 5.17: LFP recording at concentration of 2 MAC. Burst suppression patterns are visualised as intermittent large amplitude events interspersed with long quiet periods

in LFP recordings at high concentrations. Burst suppression manifests as high amplitude events with longer quiet periods (Figure 5.17). Therefore events are well-apart, so avalanches contain fewer events. Anaesthesia disrupts the dynamics of the cortex, transforming the brain from a critical conscious state to a non-critical unconscious state. This explains why the size distribution of avalanches diverges from power-law behaviour at deep anaesthesia. At lower anaesthetic concentrations, 0.5 MAC and 1 MAC, the system exhibits critical behaviour with avalanche size distributions that align with a power-law.

Figure 5.16 showed the avalanche distribution for rat LFP data recorded on day 01.02.2006 ("Rat 4"). In Figure 5.18 we show the corresponding distribution for the data recorded on days 10.01.2006 ("Rat 1") and 23.01.2006 ("Rat 3") using the same values for bin-width ($\Delta t = 0.01$ s) and z-score threshold (-1.5). All three rats shows consistent behaviour: at deep anaesthesia, the cumulative distributions diverge from power-law behaviour.

5.3.1 Summary of rat LFP avalanche statistics

Our avalanche analysis of LFP recordings of anaesthetised rats, reported by Sleigh, Hudetz and colleagues (2006), revealed the following general characteristics:

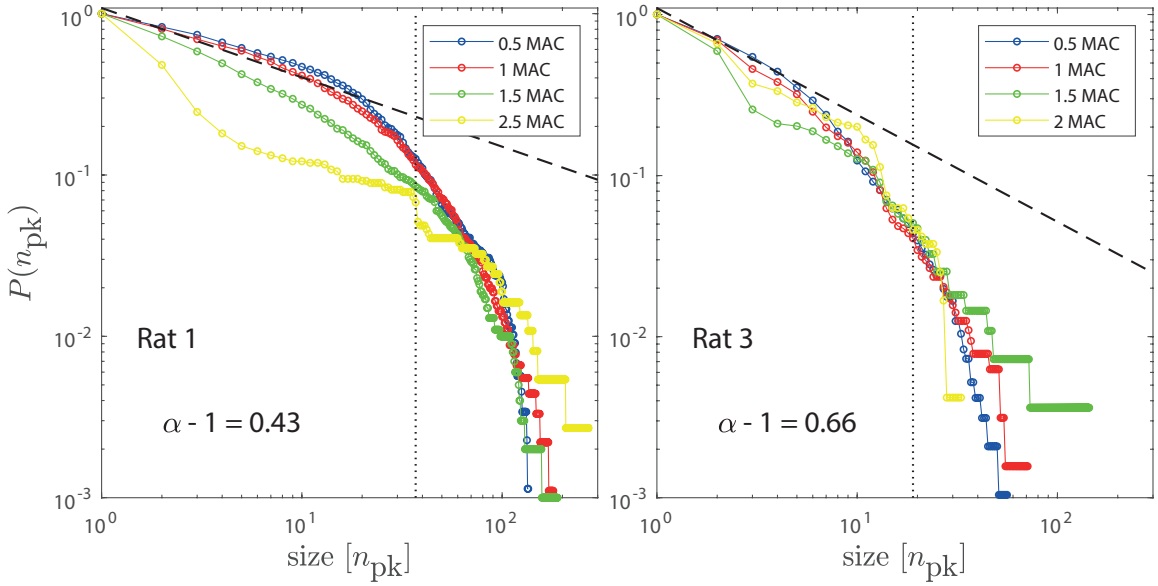

Figure 5.18: Cumulative probability distribution for different anaesthetic concentrations of two different rats recorded on days 10.01.2006 ("Rat 1") and 23.01.2006 ("Rat 3"). Four colours represents four different anaesthetic concentrations. Here dashed lines shows the slope of $\alpha - 1$

- Avalanche size can have three distinct definitions: number of peaks (n_{pk}), sum of amplitudes (n_{amp}), number of unique active electrodes (n_{elec})
- The power-law exponent for avalanche size distribution across all three definitions was found to fall within ± 0.04 of a characteristic value of $\alpha = 1.50$
- The value of α is not unique: it varies with the choice of time-bin width ranging from 1.3 to 1.65 for the selected z-score threshold of -1.5
- The power-law exponent also depends on the z-score threshold chosen to detect peaks. For positive thresholds α lies in a higher range (1.5 – 2) and for negative thresholds varies within a lower range (1.4 – 1.7).

Our main focus was to identify the characteristic changes that emerge with deepening anaesthetic concentrations. Following are our two main findings:

- At lower anaesthetic concentration the avalanche probability distribution follows a power-law with $\alpha = 1.50 \pm 0.02$
- For higher anaesthetic concentrations ($\geq$ 1.5 MAC), avalanche size distribution fails to show a power-law characteristic, indicating that the fluctuations are no longer scale-free.

In concluding sections of this chapter, we will apply avalanche analysis to pseudoLFP waveforms generated by the Waikato mean-field model.

5.4 Avalanche analysis of Waikato mean-field model

In previous sections, we analysed the electrophysiological data from rats and examined the avalanche statistics in the vicinity of the anaesthetic induced phase transition. In this section, we will analyse avalanches extracted from numerical simulations of the Waikato mean-field model as it traverses the point of anaesthesia induction. (The model equations were detailed in Chapter 3.) The point of phase transition in the model is determined by the two control parameters anaesthetic inhibition λ (anaesthetic drug effect) and subcortical excitation ΔV_e^{rest}. For particular combinations of λ and ΔV_e^{rest}, the cortex can exist in one of three alternative states: either high-firing, or low-firing, or an intermediate unstable state. The upper (high-firing) state is identified with consciousness, and the low-firing state is considered to be the anaesthetised unconscious state of the brain. The main aim of the present analysis to investigate cortical avalanche behaviour close to various phase transitions.

In this section, we investigate avalanche behaviour close to several transition points corresponding to either induction of, or emergence from, anaesthesia. A numerical simulation is run for each situation, and the resulting pseudo-LFP recordings are analysed for power-law distribution of avalanches. Here we simulate on a 60×60 grid with periodic boundaries for 10 s with time-step = 0.0004 s. Each grid point is continuously stimulated with low-intensity spatiotemporal white noise.

5.4.1 Avalanche distribution at different states: high-firing, low-firing and at critical point

In our first experiment, five different points were selected on the steady-state trajectory ABCDE (black curve in Figure 5.19) that passes through the critical point C with $\Delta V_e^{\text{rest}} = 2.54$ mV. C marks the critical or "opalescent" point, at which high-firing and low-firing states are indistinguishable. The selected points are circled in Figure 5.19: two points on the high-firing branch (A, B), one at the opalescent point (C), and two points on the low-firing branch (D, E). Representative simulation time-series are shown in Fig. 5.20, and the corresponding avalanche distributions are illustrated in Figure 5.21. The z-score threshold was set at -3, with $\Delta t = 0.0045$ s. Each of the 3600 grid points was treated as an LFP electrode.

A power-law distribution is evident only at the opalescent point (red line, C: $\lambda_i = 1.1032$). At the high-firing states (A, B), only a few smaller avalanches occurred, and the probability distribution fails to manifest a power-law distribution. Meanwhile, at the low-firing states (D, E), a higher number of smaller avalanches were detected, breaking the power-law at the very beginning. These power-law failures can be clearly visualised in the cumulative distribution figure (Figure 5.21(b)).

The power-law nature of the probability distribution at the opalescent point supports the notion of criticality, while equilibrium states far from the critical point fail to show critical behaviour as their avalanche distributions do not align to a power-law. For the high-firing states, the pseudo-LFP has high-frequency voltage patterns, so events have a short quiet time, resulting in more large avalanches and fewer smaller avalanches. On the other hand, at the low-firing states, voltage patterns show slower patterns which produce smaller avalanches resulting in rapid breakdown of the distribution.

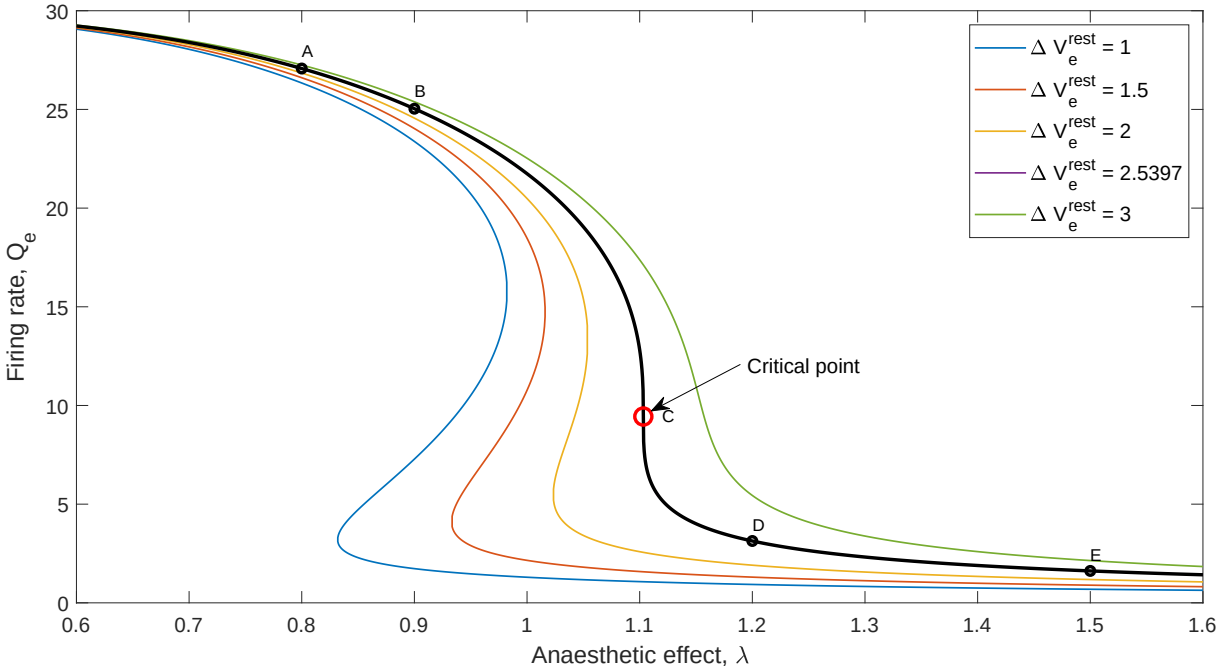

Figure 5.19: Equilibrium states for mean-field model. Points A, B, C, D and E are selected for avalanche analysis. C marks the critical ("opalescent") point. Sample time-series are displayed in Fig. 5.20, and avalanche results are shown in Figure 5.21

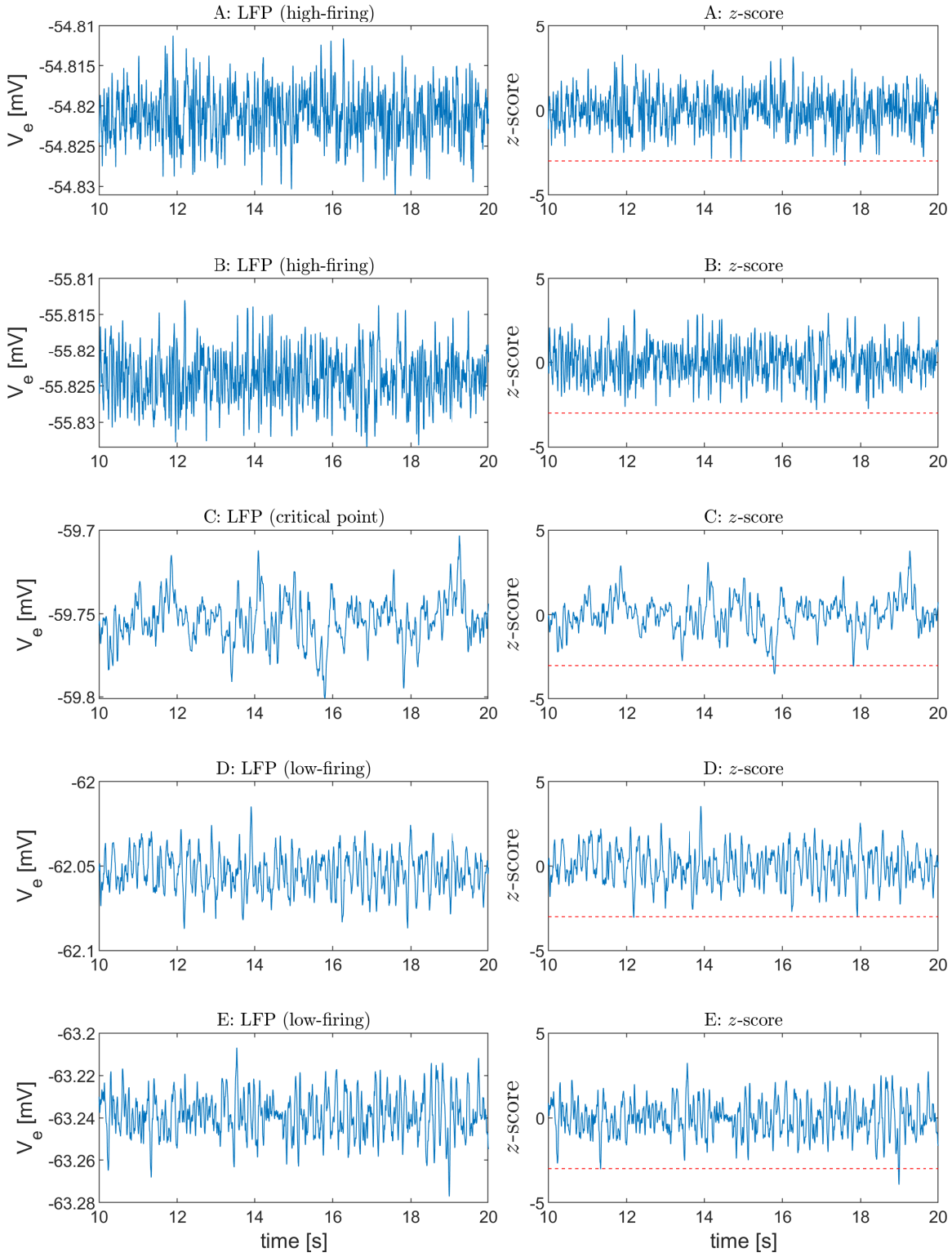

Figure 5.20: Time-series of a selected grid point for five steady-state coordinates A…E labelled in Fig. 5.19. Left panels show the raw LFP patterns and right panels show the computed z-score with the chosen threshold (red dashed line). High-firing states A and B present high frequency, low amplitude voltage patterns, while low-firing states D and E show low frequency, higher amplitude voltage patterns. Critical point C exhibits the slowest and largest voltage fluctuations

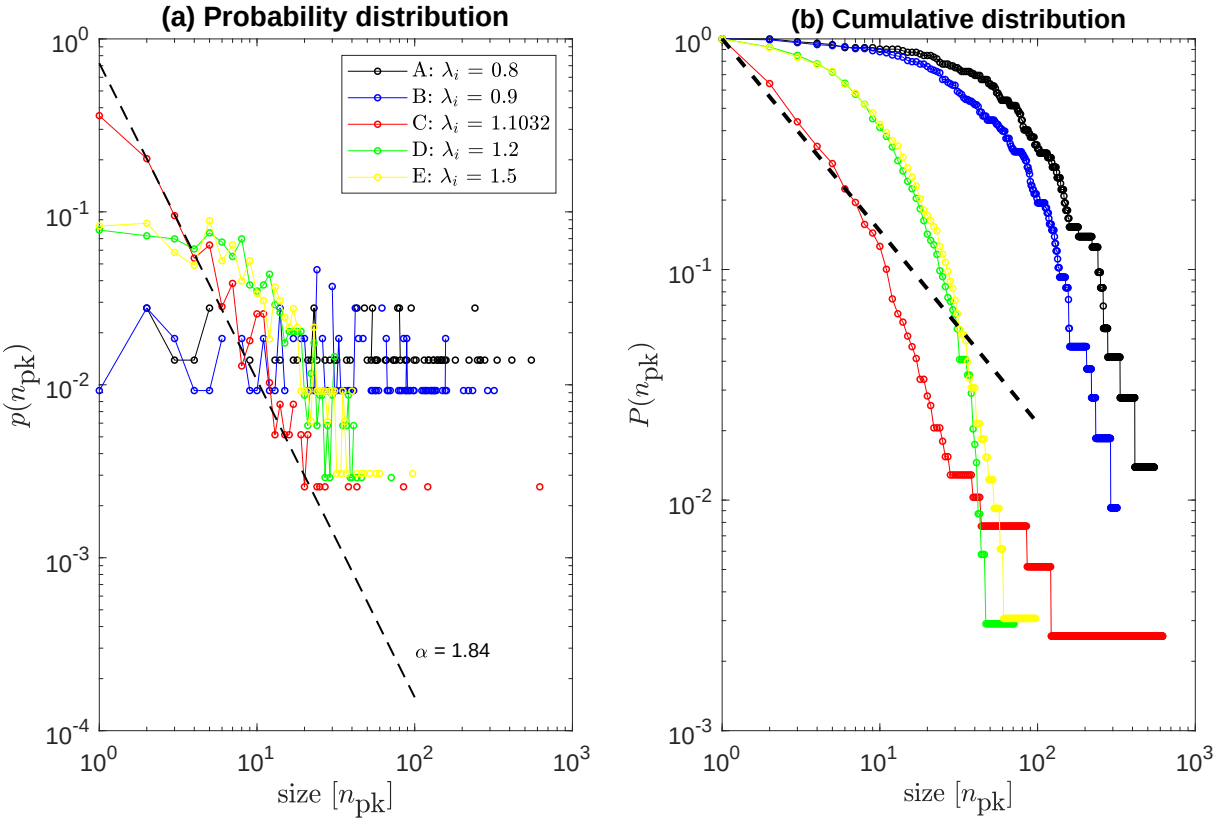

Figure 5.21: Avalanche size distribution for the five different λ values in the trajectory through the opalescent point ($\Delta V_e^{\rm rest} = 2.5398$). (a) Probability distribution of avalanche sizes $n_{\rm pk}$. Only the distribution at the opalescent point ($\lambda_i = 1.1032$) exhibits a power-law: $\alpha = 1.84 \pm 0.06$. The low-firing state ($\lambda_i > 1.1032$) shows a higher number of smaller avalanches, while the high-firing state ($\lambda_i < 1.1032$) shows a higher number of larger avalanches

5.4.2 Avalanche size distributions at secondary phase-transition points

A limited range power-law for avalanche size distribution at the opalescent point was evident in the previous analysis. It is of interest to know whether or not other saddle-node turning points also exhibit scale-free fluctuation statistics. Therefore in this section, power-law behaviour of avalanches at the secondary turning points: H1, H2, H3 (induction) and L1, L2, L3 (recovery) will be investigated. These points are marked in Figure 5.23. CP shows the opalescent point.

Numerical simulations ran for 20 s for each turning point. The cortex was stimulated by low-intensity subcortical spatiotemporal white noise. Since these points are only marginally stable, if the noise intensity is set too high the system will promptly jump to its preferred state (H1, H2, H3 $\rightarrow$ unconscious; L1, L2, L3 $\rightarrow$ conscious). Therefore the

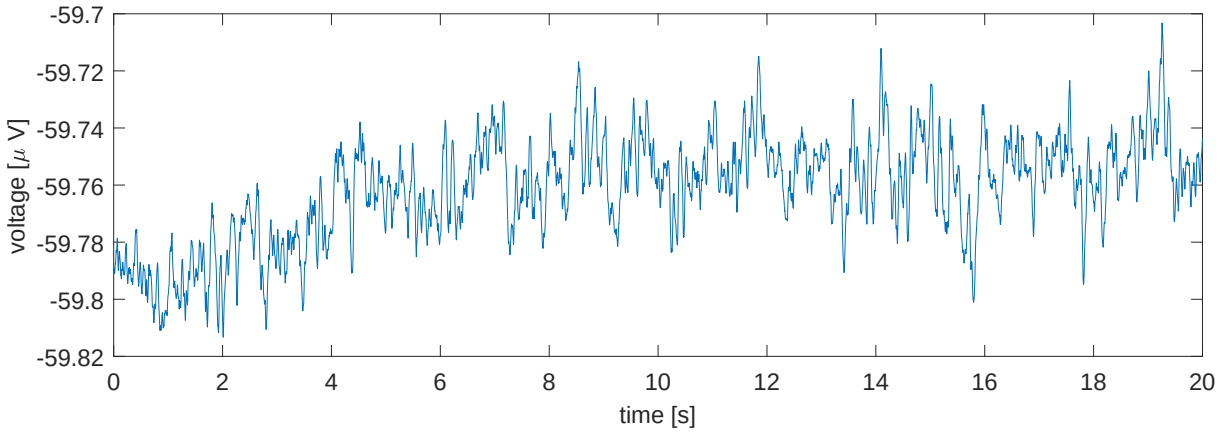

Figure 5.22: Raw voltage patterns at CP for 20 s. For the first 6 s the baseline voltage is increasing and after 8 s it stabilizes

noise scaling was reduced to extend the dwell time at the selected turning point (noise-scale factor = 0.1). Each time-series was inspected, and if the cortex showed a jump transition, that pseudoLFP record was rejected and the simulation was run again. For the H and L secondary phase transition points, only the first 10 s of the simulation was used for the analysis. At the CP critical point, the final 10 s of simulation was used, as it takes a few seconds for the cortex to evolve to its equilibrium baseline. This slow drift may be an artefact of the periodic boundaries. The baseline drift at the opalescent point is illustrated in Figure 5.22.

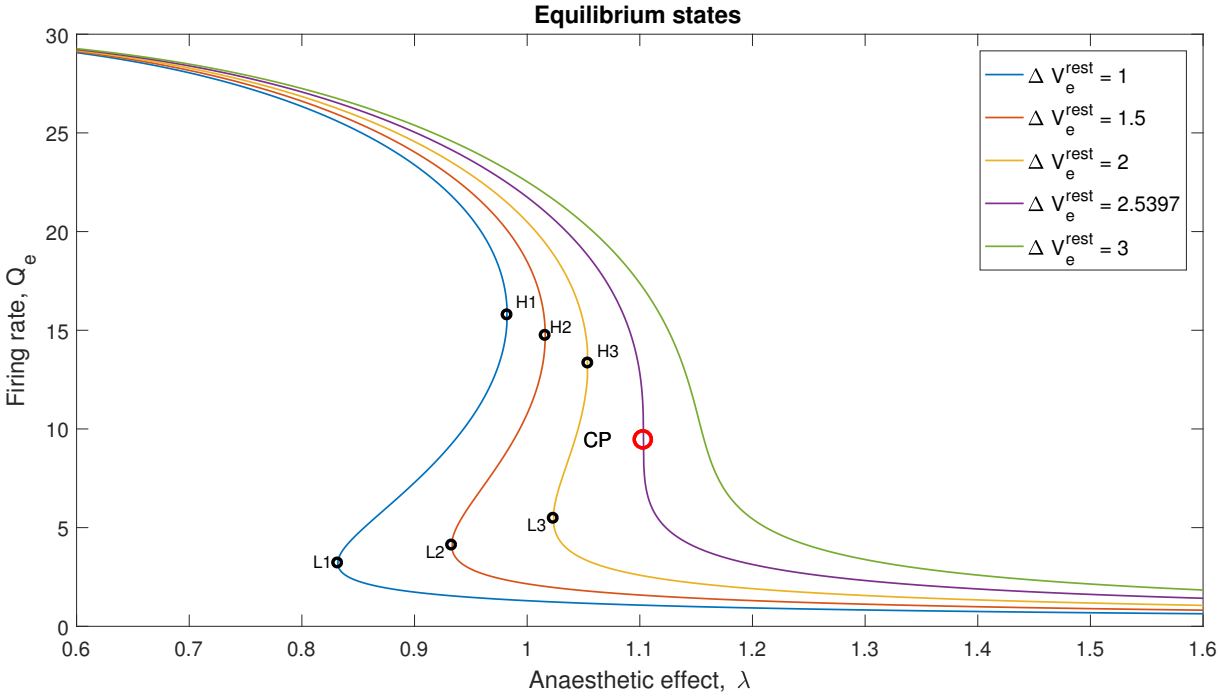

Figure 5.23: The equilibrium states of mean-field model and phase transition points for selected ΔV_e^{rest}. H1, H2, H3 mark the transition point for induction of anaesthesia and L1, L2, L3 mark the transition for emergence from anaesthesia. CP marks the opalescent point

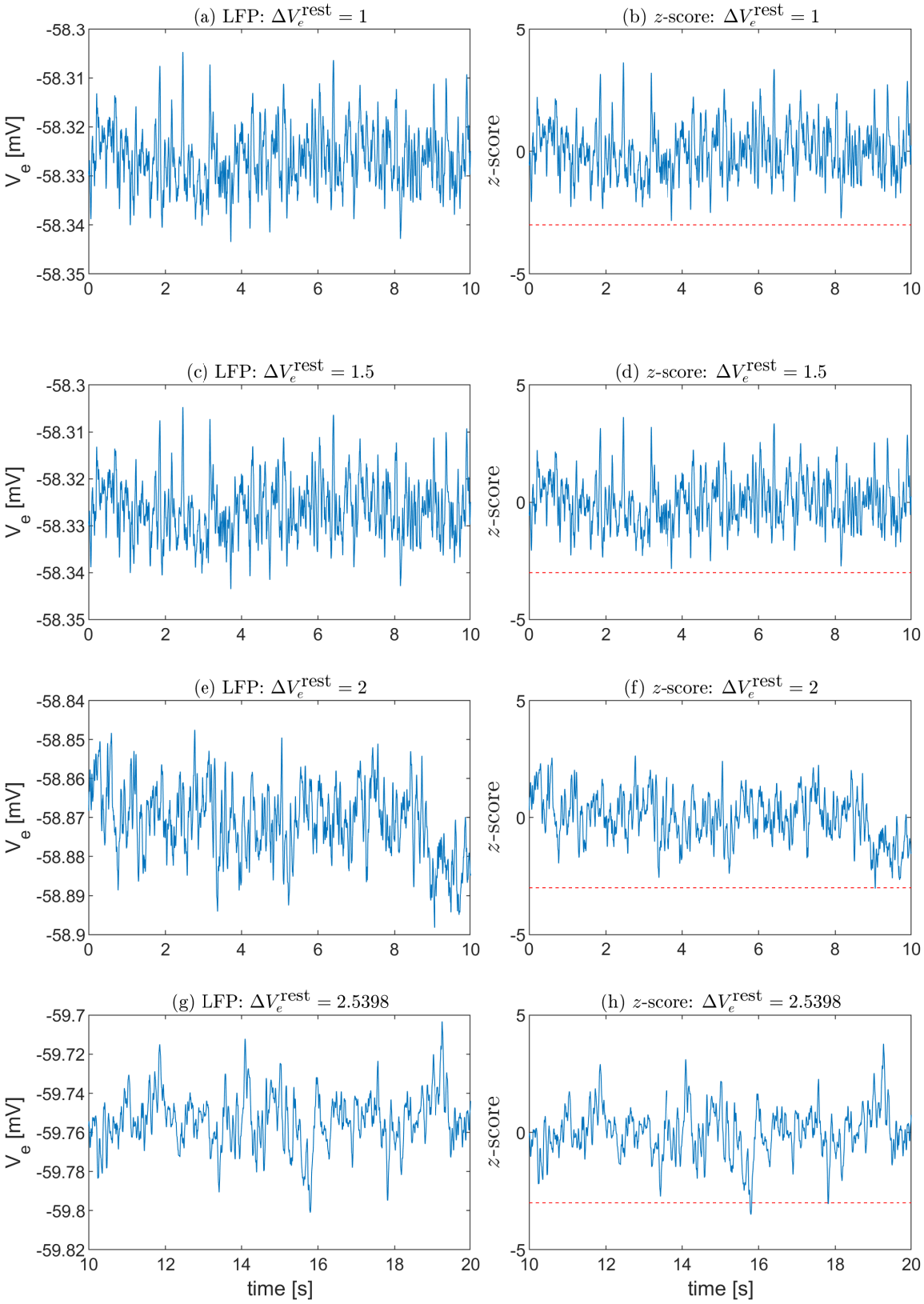

Figure 5.24: Time-series at loss of consciousness (LOC) phase-transition points, H1, H2, H3 (first three rows). Raw LFP patterns are at left-side panels and z-score at right-side panels. Last row exhibits the LFP and z-score patterns at CP

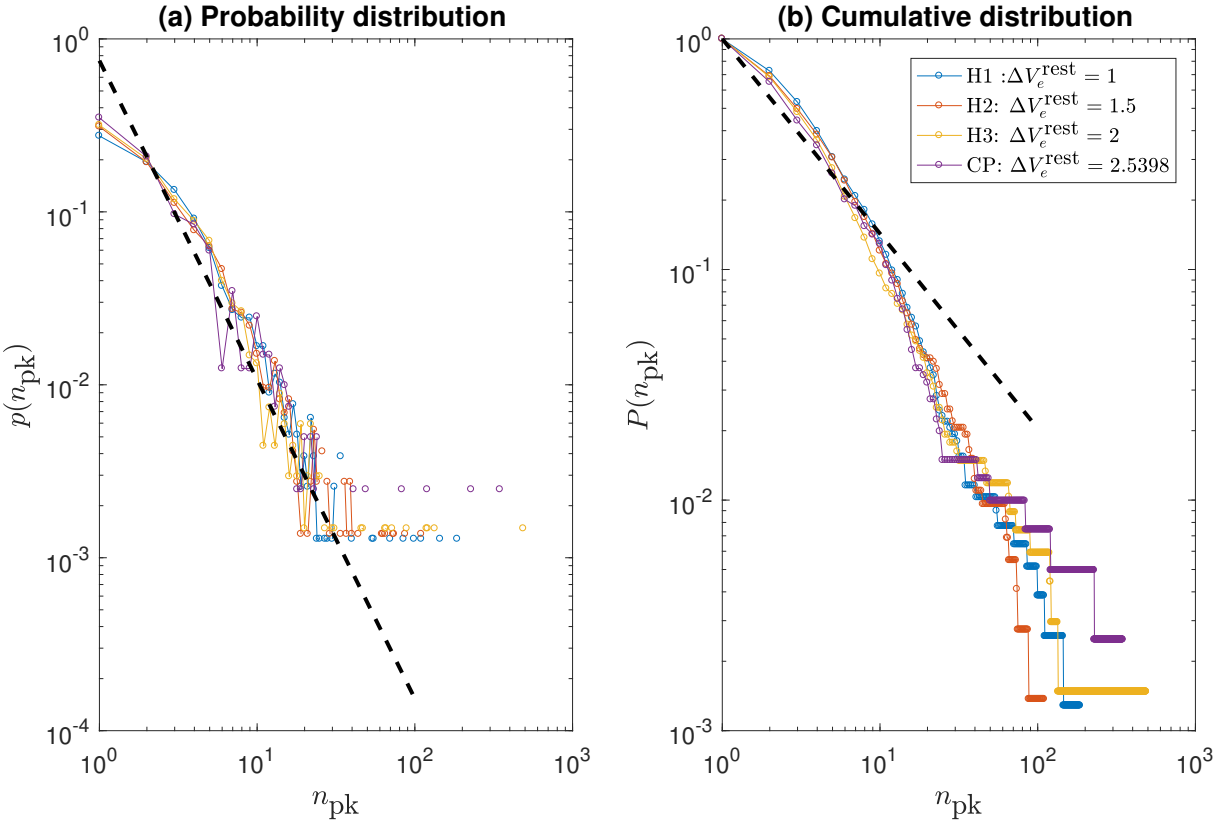

Figure 5.25: Avalanche size distribution for LOC (loss of consciousness) phase transition points (H1, H2, H3). (a) Probability distribution of avalanche size. Power-law exponents vary within the range of 1.84 to 1.90. The black dashed line shows the slope with $\alpha = 1.84 \pm 0.06$ (at opalescent point). (b) Cumulative distributions for LOC turning points

Avalanche behaviour at phase-transition point for loss of consciousness (LOC)

As per our previous studies (Chapter 3), the model cortex shows critical slowing down characteristics, with high-amplitude and slower fluctuations and higher susceptibility to small perturbations when approaching the opalescent point. Similar critical slowing has also been manifest in Chapter 3 when approaching the secondary saddle-node turning points for induction of, and recovery from, anaesthesia. Therefore we expect to find evidence of power-law avalanche behaviour at the LOC and ROC transition points.

We selected three ΔV_e^{rest} values and found the values of λ_i where the top branch steady states were marginally stable (i.e., the real part of the dominant eigenvalue approaches zero from below at zero wavenumber). The simulation was held at the selected turning point by ensuring the noise was sufficiently small. The pseudoLFP data from 3600 grid points were analysed to obtain the probability distribution of avalanche sizes; the results are presented in Figure 5.25. Averaged IEI was calculated at each equilibrium point, and then used as the time-bin width. As expected, the distributions of avalanche sizes

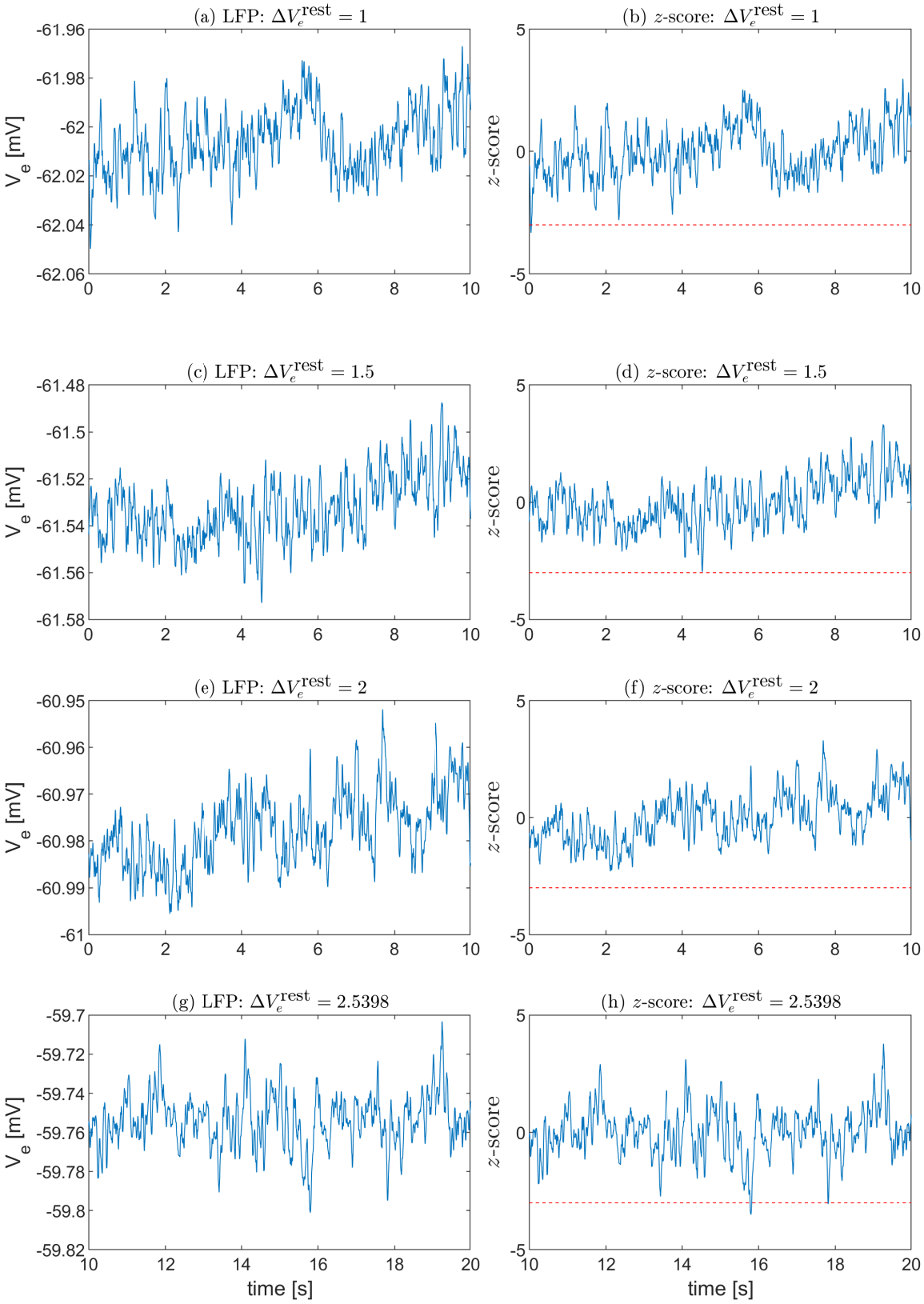

Figure 5.26: LFP and z-score at recovery of consciousness (ROC) turning points. These time-series show a low-frequency patterns compared to LOC turning points

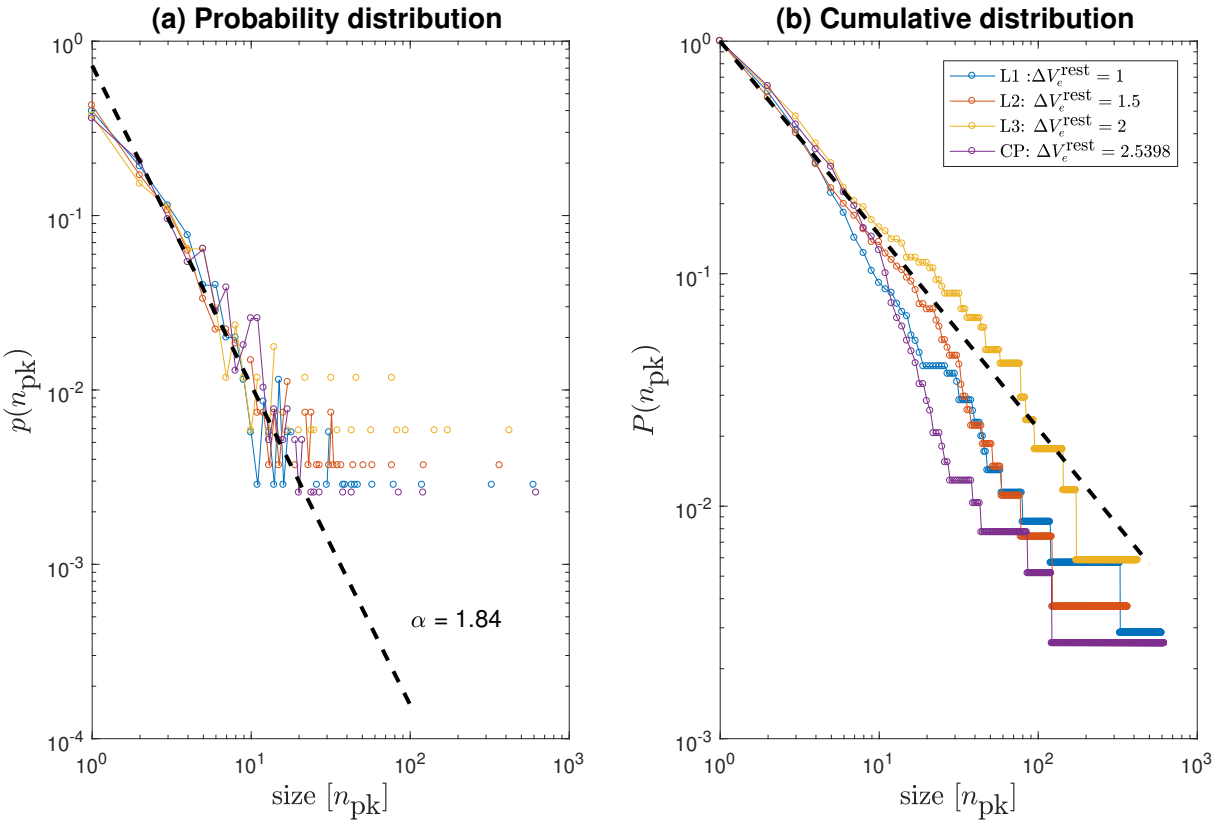

Figure 5.27: (a) Probability distribution of avalanche sizes at ROC transition points (L1, L2, L3). Slopes vary from 1.6 to 1.85. Power-law behaviour is manifested by each turning point (black dashed line is for the CP power-law, where slope is fitted within one order of magnitude. (b) Cumulative distributions for ROC turning points

align with a power-law with α ranging from 1.8 to 1.9 for the three LOC phase-transition points, very close to the critical-point exponent value of $\alpha = 1.84$.

Avalanche behaviour at phase-transition point for recovery of consciousness (ROC)

We now examine ROC phase-transition points for the same selection of $\Delta V_e^{\mathrm{rest}}$ trajectories. We observe similar behaviour, albeit less tightly clustered, as for the LOC turning points, but at lower anaesthetic inhibition. The probability distributions of avalanche sizes obeys a power-law with α ranging from 1.6 to 1.85.

5.4.3 Summary of Waikato mean-field model avalanche behaviour

We analysed simulation data generated by the Waikato mean-field cortical model for probability distributions of avalanche sizes across a range of anaesthetic induced phase-transitions. We now summarise the important findings from these analyses:

- The probability distribution of extracted avalanches shows unambiguous power-law behaviour at the critical opalescent point : $\alpha = 1.8 \pm 0.2$
- The secondary turning points, loss of consciousness (LOC) and recovery of consciousness (ROC), also exhibited power-law behaviour, with α lying in the same range
- If the model is not at a phase transition point (high-firing state or low-firing state that is not close to a turning point), then the probability distribution of avalanche sizes does not follow a power-law.

The value of the power-law exponent for the Waikato mean-field model was close to -1.8, quite different from the "expected" value of -1.5 reported in a previous study [7].

In our Waikato mean-field analyses we found that we needed to use a rather high z-score threshold of -3; lower threshold settings detected a larger number of events which destroyed the power-law.

For all the above analyses we used the membrane voltage (V_e) extracted from the simulations (which we assume to be equivalent to LFP in experimental recordings). As a cross-check we repeated the analysis using firing rates (Q_e) instead of membrane voltage. The avalanche size distribution for Q_e also exhibited the same behaviour as V_e and showed nearly the same power-law exponent, α.

5.5 Chapter summary

Most experimental and numerical studies have supported the idea that the brain operates near a critical point, implying that the sizes of neuronal avalanches should follow a scale-free power-law distribution [6, 7, 69, 81]. Neuronal avalanches are a burst of activities spread through the network, and they are considered to be in the same avalanches if the activity bursts have occurred in temporal proximity. Initially, Beggs and Plenz in 2003 [7] proposed the notion of a characteristic power-law exponent of -1.5 for cortical networks at critical state using experimental data from acute slice of a rat.

In this chapter, we have presented avalanche analyses of both experimental and numerical data. For experimental data, we used LFP recordings of anaesthetised rats for different anaesthetic concentrations. The numerical simulation data were generated by the Waikato mean-field model placed close to various phase-transition points.

The rat LFP data were used to determine the properties of neuronal avalanches with avalanche size being defined in three distinct ways: number of peaks (n_{pk}), summation of amplitudes (n_{amp}) and number of unique active electrodes (n_{elec}). Our findings are as follows:

- α The power-law exponent is close to $\alpha = 1.5$ for all three definitions
- The value of α depends on the time-bin width (Δt) chosen to separate the events into avalanches: α decreases slightly with increases in Δt
- The z-score threshold used to detect peaks affects the avalanche distribution: higher thresholds lead to larger values of α, and vice versa.

The main focus of the rat study is to identify the change of power-law behaviour of neuronal avalanches when the cortex closely approaches the transition points of anaesthetised to bursting. For lower anaesthetic concentrations, power-law behaviour is manifest with $\alpha = -1.5$. However, at higher anaesthetic concentrations avalanche size distribution fails to align with a power-law nature. This failure coincides with the emergence of strongly negatively skewed burst suppression LFP patterns characteristic of deep anaesthesia.

Then we analysed the anaesthetic-induced phase-transition of Waikato mean-field model. The avalanche analysis of the simulation data shows the following characteristics:

- Power-law behaviour is evident at the CP critical point, and also at the secondary phase-transition points: loss of consciousness (LOC) and recovery of consciousness (ROC)
- Equilibrium points far from CP, LOC, or ROC transition points states fail to support a power-law.

The mean-field model produced higher α around 1.8 compared to rat LFP data, where $\alpha = 1.5$. For the mean field model, we had to use a larger threshold as too many peaks were detected when the threshold was set as low as -1.5. Moreover, mean-field $\text{IEI}_{\text{avg}} \simeq 0.004$ s was quite small compared to IEI_{avg} found in rat LFP recordings ($\text{IEI}_{\text{avg}} \simeq 0.01$ s). This is because the mean-field data is obtained for a vastly larger number of parallel channels (3600), therefore registering many more events compared to LFP recordings (which typically have only 22 active channels).

Neuronal avalanches are defined using a temporal binning that separates avalanches by pauses of a few ms. Priesemann in 2014 [71] has stated that if events are recorded

from a large number of parallel channels, then all pauses would vanish. Therefore it is necessary to enforce pauses by raising thresholds. Another approach is to apply spatial subsampling to reduce the number of parallel channels, thereby reducing the number of detected events.

The power-law curves exhibited a cut-off point which is related to the number of electrodes available. However, the cut-off points for CDF and PDF are different. This is because we are computing the complementary CDF, which accumulates from the tail, leading to misalignment with the power-law trend. We calculated the power-law for PDF distribution for only one order of magnitude of size range, and this avoids the uncertainty associated with cut-off variabilities.

Chapter 6

Summary and future work

6.1 Summary

In this thesis, we have examined critical dynamics associated with neuronal phase transitions between distinct neural states using computer-based mathematical modelling and electrophysiological data analysis. We selected four topics for close analysis: transition to spiking in a FitzHugh-Nagumo (FHN) point neuron; induction of, and recovery from, anaesthesia in the Waikato mean-field (WMF) cortical model; anaesthetic-induced changes in rat local-field potential (LFP) signals; and avalanche statistics under anaesthesia for the WMF and rat models.

Transition to spiking in a point neuron

The nonlinear dynamics and subthreshold stochastics of FHN single spiking neuron model were investigated for these different implementations: Wilson, Keener & Sneyd, and op-amp equivalent circuit. The nonlinear oscillations were compared for all three models and we observed closely similar behaviours. Linear stability analysis of the steady states revealed type-II resonant behaviour, with an Andronov–Hopf bifurcation at the critical points marking onset and offset of spiking. At spiking threshold, the real part of the eigenvalue becomes zero, while the imaginary part (frequency) is non-zero.

Low-intensity noise-induced voltage fluctuations of the three FHN models were investigated for close approach to onset and death of spiking. Critical slowing down was manifest as a divergent growth of variance of voltage fluctuations simultaneous with a prolongation of autocorrelation settling time when approaching the transition point. The variance trends unveiled a scaling-law with exponent of -1: $\mathrm{var}\{v\} \sim 1/\epsilon$.

Anaesthetic-induced phase transitions in the Waikato cortical model

Anaesthetic induced phase-transitions in the two-dimensional Waikato mean-field cortical model were investigated, focusing on loss of consciousness (LOC), recovery of consciousness (ROC), and approach to critical point (CP) transitions. Linear stability analysis of all three transition points revealed saddle–node bifurcations: a purely real dominant eigenvalue which goes to zero at the turning point.

Critical slowing down near these turning points were demonstrated by comparing subthreshold stochastic analysis of grid simulations against Ornstein–Uhlenbeck (OU) theoretical predictions. The fluctuation variance and power spectra exhibited divergent growth at ever lower spatial and temporal frequencies on close approach to transition (LOC, ROC or CP).

The LOC and ROC critical fluctuations obeyed a common scaling law $\mathrm{var}\{Q_e\}^{\mathrm{LOC}} \sim \mathrm{var}\{Q_e\}^{\mathrm{ROC}} \sim 1/\epsilon^{0.0075}$, while that for CP fluctuations exhibited a power-law exponent that was about twice as large, $\mathrm{var}\{Q_e\}^{\mathrm{CP}} \sim 1/\epsilon^{0.02}$, consistent with the observation that the opalescent point is a double-sided saddle–node bifurcation.

Anaesthetic-induced changes in electrophysiological data in rats

We examined local field potentials (LFP) recorded from anaesthetised rats under different anaesthetic concentrations looking for evidence of critical fluctuations. Different characteristic patterns were identified at each discrete level of anaesthetic concentration. LFP amplitude histograms showed that at lower concentrations, LFP fluctuations are symmetric and approximately normally distributed. The appearance of burst-suppression patterns at higher anaesthetic concentrations resulted in a negatively skewed, heavy-tailed distribution. Correlation time increased with anaesthetic concentration, and resonance patterns found at lower concentrations were suppressed at higher concentrations.

The scaling laws of LFP fluctuations were established for different concentrations by detrended fluctuation analysis (DFA) and power spectral density (PSD) analysis. The DFA power-law exponent was found to be $\alpha \sim 1$, indicating the existence of long-range temporal correlations in the anaesthetised LFP data. The exponent tended to increase with anaesthetic concentration, suggesting the onset of unbounded nonstationary fluctuations. The DFA α-exponents were consistent with β-exponents obtained using PSD analysis, confirming the $\alpha = (\beta + 1)/2$ relationship between PSD and DFA statistics.

Avalanche analysis

Criticality hypothesis of the anaesthetic induced phase transition was further investigated for both experimental and numerical data using avalanche analysis. We used LFP recordings of anaesthetised rats for different concentrations, and numerical simulation data generated by the Waikato mean-field cortical model for LOC, ROC, CP tipping points.

Analyses of the rat LFP data suggested an avalanche power-law exponent of around $\alpha \simeq 1.5$, presumed to be the critical value. However, it was found that this value depends on the choice of time-bin width used to separate events, and also on the z-score threshold used to detect peaks. Moreover, a power-law relationship was only evident at lower anaesthetic concentrations and disappeared at higher anaesthetic concentration.

The power-law behaviour for avalanches of Waikato mean-field model simulation data was observed at the CP opalescent point, loss of consciousness (LOC) and recovery of consciousness (ROC) tipping points. The common exponent value was $\alpha \simeq 1.8$. As expected, equilibrium states far from these transition points failed to show a power-law.

Unifying themes

These analyses unveiled the increase of amplitude and prolongation of noise-driven fluctuations on close approach to the transition point, not only in single-neuron and neural population models, but also in biological LFP signals. Detection of power-law behaviour of neuronal avalanches in rat LFP data for low anaesthetic concentrations and at the transition points of Waikato mean-field model provides further support for the criticality hypothesis.

The single spiking neuron model with Hopf bifurcation illustrated prolongation of settling time after a perturbation; a corresponding prolongation of fluctuation and autocorrelation time was seen in the saddle-node transition of the mean-field model. Both single neurons and neuronal populations exhibited power-law behaviour near the phase transitions. However, the different transitions revealed distinct critical exponent values.

Table 6.1 summarizes the range of scaling laws encountered or referenced in this thesis. It is noteworthy that the SN (saddle–node) exponents for WMF (LOC/ROC, CP) are very different from that for the type-I point neuron. This is probably because the point neuron has no spatial dependence.

Table 6.1: Summary of scaling laws

System	Bifurcation	Criticality measure & scaling law	Reference
FHN neuron	Hopf	variance $\sim 1/\epsilon^{1.0}$	Chapter 2
Type-II neuron	Hopf	variance $\sim 1/\epsilon^{1.0}$	[58, 87]
Type-I neuron	SN	variance $\sim 1/\epsilon^{0.5}$	[58, 87]
WMF LOC	SN	variance $\sim 1/\epsilon^{0.0075}$	Chapter 3
ROC	SN		
CP	double-SN	variance $\sim 1/\epsilon^{0.02}$	Chapter 3
Rat LFP		DFA: $F(n) \sim n^{1.0-1.2}$	Chapter 4
		PSD: $S(f) \sim f^{1.0-1.7}$	Chapter 4
		Avalanche: $p(x) \sim 1/x^{1.5}$ (but only for < 1.5 MAC)	Chapter 5
WMF LOC	SN	Avalanche: $p(x) \sim 1/x^{1.8}$	Chapter 5
ROC	SN		
CP	double-SN		

6.2 Future work

Theoretical analysis of the Waikato mean-field model focused exclusively on anaesthetic-induced phase transition between equilibrium states, and we suppressed spatial and temporal instabilities. Our criticality investigations could be extended to cortical transitions to nonequilibrium states: emergence of Hopf instability (coherent temporal oscillations), Turing instability (stationary spatial patterns), Turing–Hopf instability (spatiotemporal wave patterns). The rate-constant, γ_i^0, which controls the inhibitory impulse response at the postsynaptic membrane (IPSP) could be smoothly decreased to force a Hopf bifurcation. A Turing instability can be provoked by boosting the strength of inhibitory gap-junction diffusion, D_2. Spatiotemporal instabilities can then be generated by simultaneously lowering the IPSP rate-constant while raising the inhibitory diffusion strength.

In Chapter 3, when we examined the scaling-laws for variance we observed saturations (at LOC and ROC) and increasing scatter (at CP) for very close approach to the transition point. This may be due to numerical limitations in MATLAB when dealing with close-to-singular matrix operations and inversions (e.g., Eqs. (3.17, 3.33)), but should be further investigated to establish the underlying cause of the misbehaviour.

The rat LFP data are only available for three to five steps of anaesthetic concentration. Data should be collected for more finely spaced concentration steps to allow better identification of the critical signs for anaesthetic phase transition. Specifically, the critical dynamics of LFP data for lower anaesthetic concentrations should be investigated. Furthermore, the LFP data for "awake" rats should be analysed to obtain a baseline reference for investigation of anaesthetic changes.

Spatial subsampling is a common problem when analysing spatially extended dynamical systems, as it may cause loss of spatial information. This was certainly the case for our data with only $\sim$25% of the rat LFP electrodes being active. Wilting and Priesemann [105] introduced a multiple regression estimator that used autocorrelation times to correct subsampling errors in criticality analysis. Our avalanche analyses could be cross-validated using this novel estimator.

Appendix A

Fitzhugh-Nagumo model equations and codes

A.1 Derivation of differential equations for op-amp equivalent circuit

Voltage v across capacitor C_1 is the excitation variable, and current i_2 through resistor R_4 is the recovery variable (labelled as i in Eq. (2.2)). We are building the equations using these two-variables. Figure A.1 is obtained from page 228 of [45].

Op-amp 1 is a voltage follower, therefore $v_1 = v_2$ and voltage across the R_3 is a function of v: $F(v) = v - g(v)$ where $g(v)$ is the response of op-amp U2. Keener & Sneyd approximate $F(v)$ as a piecewise-linear function, but in our calculations we use $F(v) = v - V_r \tanh\left(\dfrac{v}{V_r/2.5}\right)$ (see Fig. 2.4).

Applying Ohm's law across resistor R_4,

$$v - v_1 = i_2 R_4 \tag{A.1}$$

Ohm's law across resistor R_3 gives,

$$i_3 = \frac{F(v)}{R_3} \tag{A.2}$$

Ohm's law across resistor R_5 gives,

$$i_1 = \frac{v_1 - V_g}{R_5} \quad \text{as } v_2 = v_1 \tag{A.3}$$

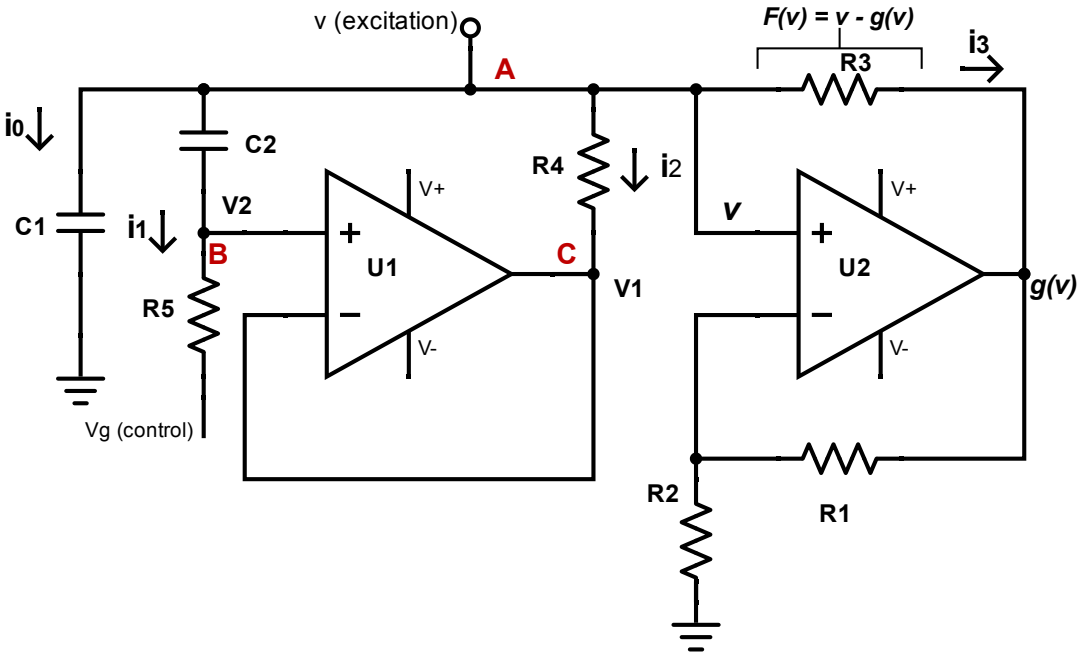

Figure A.1: Keener & Sneyd electronic circuit equivalent to FitzHugh–Nagumo model from page 228 of [45] (Same circuit is redrawn in Fig. 2.3)

Applying Kirchhoff's current law to node A,

$$i_0 + i_1 + i_2 + i_3 = 0 \tag{A.4}$$

where

$$i_0 = C_1 \frac{dv}{dt} \tag{A.5}$$

is the capacitive current through C_1.

Substituting Eqs. (A.5), (A.2), (A.1) and (A.3) respectively into (A.4) gives,

$$C_1 \frac{dv}{dt} + \frac{v - i_2 R_4}{R_5} - \frac{V_g}{R_5} + i_2 + \frac{F(v)}{R_3} = 0$$

rearranging the equation

$$C_1 \frac{dv}{dt} + i_2 \left(1 - \frac{R_4}{R_5}\right) + \frac{F(v)}{R_3} + \frac{v - V_g}{R_5} = 0$$

Rearranging the equations,

$$\begin{aligned}\frac{dv}{dt} &= \frac{1}{C_1 R_5}\left(-\frac{R_5}{R_3}F(v) - (R_5 - R_4)i_2 - v + V_g \right) \\ &= \frac{1}{C_1 R_5}\left(-f(v) - (R_5 - R_4)i_2 - v + V_g \right);\end{aligned}$$

which is Eq. (2.2(a)) with $f(v) = \dfrac{R_5}{R_3}F(v)$.

Applying Kirchhoff's current law to node B,

$$C_2 \frac{d}{dt}(v - v_1) = \frac{v_1 - V_g}{R_5}$$

from Eq. (A.1) $v_1 = v - i_2 R_4$

$$C_2 R_4 \frac{di_2}{dt} = \frac{v - iR_4 - V_g}{R_5}$$

So,

$$\frac{di_2}{dt} = \frac{1}{C_2 R_5}\left(\frac{v}{R_4} - i_2 - \frac{V_g}{R_4} \right)$$

which recovers Eq. (2.2(b)).

A.2 LTSpice simulation

In this section I list the sources of LTSpice simulations: Netlist and schematic diagram.

Netlist

```
C1 N001 0 0.01u
C2 N001 N004 0.5u
R5 N004 Vg 10k tol=1 pwr=0.1
R4 N001 N005 1k
R1 N007 0 100k
R2 N006 N007 100k
R3 N006 N001 3.9k
V1 0 N002 9V
V2 N009 0 9V
V3 Vg 0 1V
V4 N008 0 9V
V5 0 N003 9V
XU1 N004 N005 N008 N003 N005 LM741
XU2 N001 N007 N009 N002 N006 LM741
.tran 0 0.02 0 0.005m
.lib BEE215\LM741.lib
.backanno
.end
```

LTspice Schematic diagram

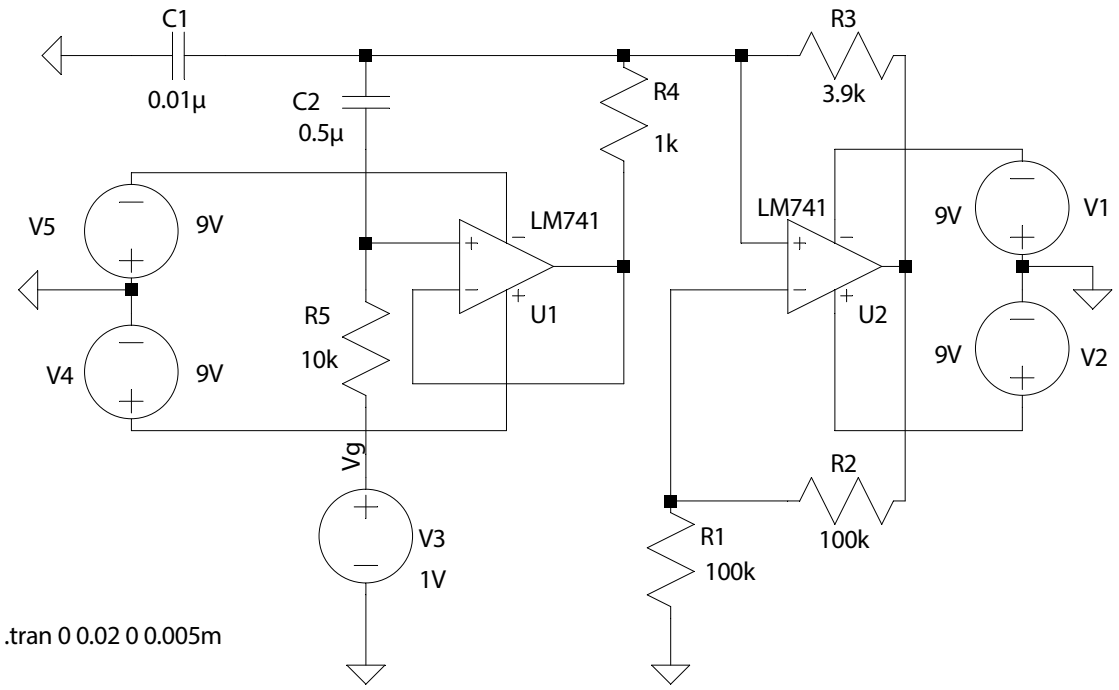

Figure A.2: Schematic diagram of Keener & Sneyd op-amp equivalent circuit drawn in LTSpice

A.3 Matlab codes for finding steady states

The code for calculation of steady states for the FHN model.

Steady states

```
function [V0 R0] = FHNSteadyStates(S, model)
% inputs:
% S: Stimulus
% model:
% W : Wilson FHN model,
% K: Keener & Sneyd model,
% C: op-amp circuit model

Switch model

        case  'W'
                %% steady state for Wilson FHN model
                % R_isocline = 1.25*V + 1.5; % R_isocline, dr/dt = 0
                %% V_isocline, dv/dt = 0
                % V_isocline = -R_isocline + V - ((V^3)/3) + S;

                V = [-1/3 0 -1/4 -1.5+S]; % Coefficients of V_isocline

                % finding the steady states(roots of the V_isocline)
                V0 = roots(V);          % steady state value for v
                V0(imag(V0) ~= 0) = [];
                R0 = 1.25*V0 + 1.5;        % steady state value for r

        case 'K'
                %% steady state for Keener and Sneyd FHN model
                % R_isocline = 2*V ;   % R_isocline, dr/dt = 0
                %% V_isocline, dv/dt = 0
                % V_isocline = -R_isocline + (V*(1-V)*(V-0.1)) + S;

                V = [-1 11/10 -21/10 S]; % Coefficients of V_isocline

                % finding the steady states(roots of the V_isocline)
                V0 = roots(V);  % steady state value for v
                V0(imag(V0) ~= 0) = [];
                R0 = 2*V0 ;        % steady state value for r

        case 'C'
                %% steady state for op-amp circuit FHN model
                %     Vout = (Vr*tanh(V/(Vr/2.5)));
                %     F = V-Vout;
                %     R_isocline = V - S;
                %     V_isocline = -(V - S) - (1/3.9)*F(V);
                Vr = 9:                % rail voltage = 9V

                % V_isocline function
                function  y = f(V)
                        y =  -(4.9/3.9)*V + S + ((Vr/3.9)*tanh(2.5*V/Vr));
                end

                fun = @f;
```

```
                % steady state value for v (finding roots of v_isocline)
                V0 = fzero(fun,0);
                R0 = V0 - Vg;         % steady state value for r
        end
end
```

Appendix B

Jacobian matrix elements for Waikato mean-field model

In this appendix, we develop the Jacobian matrix of the Waikato mean-field cortical model. We begin by splitting the second-order equations in time into pairs of first-order equations, to obtain a set of eight coupled first-order equations:

$$F_1 = \frac{\partial V_e}{\partial t} = \frac{1}{\tau_e}\left(V_e^{\text{rest}} + \Delta V_e^{\text{rest}} - V_e + [\rho_e \psi_{ee} \Phi_{ee} + \rho_i \psi_{ie} \Phi_{ie}]\right) \tag{B.1}$$

$$F_2 = \frac{\partial V_i}{\partial t} = \frac{1}{\tau_i}\left(V_i^{\text{rest}} - V_i + [\rho_e \psi_{ei} \Phi_{ei} + \rho_i \psi_{ii} \Phi_{ii}]\right) \tag{B.2}$$

$$F_3 = \frac{\partial \Phi_{eb}}{\partial t} = \dot{\Phi}_{eb} \tag{B.3}$$

$$F_4 = \frac{\partial \dot{\Phi}_{eb}}{\partial t} = -2\gamma_e \dot{\Phi}_{eb} - \gamma_e^2 \Phi_{eb} + \gamma^2 [N_{eb}^{\alpha} \phi_{eb}^{\alpha} + N_{eb}^{\beta} Q_e + \langle \phi_{eb}^{\text{sc}} \rangle] \tag{B.4}$$

$$F_5 = \frac{\partial \Phi_{ib}}{\partial t} = \dot{\Phi}_{ib} \tag{B.5}$$

$$F_6 = \frac{\partial \dot{\Phi}_{ib}}{\partial t} = -2\gamma_i \dot{\Phi}_{ib} + \gamma_i^2 N_{ib}^{\beta} Q_i \tag{B.6}$$

$$F_7 = \frac{\partial \phi_{eb}}{\partial t} = \dot{\phi}_{eb} \tag{B.7}$$

$$F_8 = \frac{\partial \dot{\phi}_{eb}}{\partial t} = -2v\Lambda_{eb} \dot{\phi}_{eb} - v^2(\Lambda_{eb}^2 - \nabla^2)\phi_{eb} + v^2 \Lambda_{eb}^2 Q_e \tag{B.8}$$

We define the 8-dimensional state vector $\vec{X}$,

$$\vec{X} = \begin{bmatrix} V_e & V_i & \Phi_{eb} & \dot{\Phi}_{eb} & \Phi_{ib} & \dot{\Phi}_{ib} & \phi_{eb} & \dot{\phi}_{eb} \end{bmatrix} \tag{B.9}$$

The Jacobian matrix corresponding to the small spatiotemporal disturbance of Eq. (3.12) replaces the ∇^2 Laplacian operator in Eq. (B.8) with a $-q^2$ term.

$$\mathbf{J}(q) = \begin{bmatrix} J_{11} & 0 & J_{13} & 0 & J_{15} & 0 & 0 & 0 \\ 0 & J_{22} & J_{23} & 0 & J_{25} & 0 & 0 & 0 \\ 0 & 0 & 0 & J_{34} & 0 & 0 & 0 & 0 \\ J_{41} & 0 & J_{43} & J_{44} & 0 & 0 & J_{47} & 0 \\ 0 & 0 & 0 & 0 & 0 & J_{56} & 0 & 0 \\ 0 & J_{62} & 0 & 0 & J_{65} & J_{66} & 0 & 0 \\ 0 & 0 & 0 & 0 & 0 & 0 & 0 & J_{78} \\ J_{81} & 0 & 0 & 0 & 0 & 0 & J_{87}(q^2) & J_{88} \end{bmatrix} \tag{B.10}$$

The non-zero elements of $\mathbf{J}$ are,

$$J_{11} = \frac{\partial F_1}{\partial V_e} = \frac{1}{\tau_e}(-1 + \text{term}_1 + \text{term}_2 + \text{term}_3)$$
$$\text{term}_1 = \rho_e \frac{\partial \psi_{ee}}{\partial V_e}\Phi_{ee} = \rho_e \frac{\partial \psi_{ee}}{\partial V_e}[(N_{ee}^{\alpha} + N_{ee}^{\beta})Q_e + \langle \phi_{ee}^{\text{sc}} \rangle]$$
$$\text{term}_2 = \rho_e \psi_{ee} \frac{\partial \Phi_{ee}}{\partial V_e} \equiv 0$$
$$\text{term}_3 = \rho_i \frac{\partial \psi_{ie}}{\partial V_e}\Phi_{ie} = \rho_i \frac{\partial \psi_{ee}}{\partial V_e} N_{ie}^{\beta} Q_i$$

$$J_{13} = \frac{\partial F_1}{\partial \Phi_{eb}} = \frac{1}{\tau_e}\rho_e \psi_{ee}$$
$$J_{15} = \frac{\partial F_1}{\partial \Phi_{ib}} = \frac{1}{\tau_e}\rho_i \psi_{ie}$$

$$J_{22} = \frac{\partial F_2}{\partial V_i} = \frac{1}{\tau_i}(-1 + \text{term}_4 + \text{term}_5 + \text{term}_6)$$
$$\text{term}_4 = \rho_e \frac{\partial \psi_{ei}}{\partial V_i}\Phi_{ei} = \rho_e \frac{\partial \psi_{ei}}{\partial V_i}[N_{ei}^{\alpha\beta} Q_e]$$
$$\text{term}_5 = \rho_i \psi_{ii} \frac{\partial \Phi_{ii}}{\partial V_i} \equiv 0$$
$$\text{term}_6 = \rho_i \frac{\partial \psi_{ii}}{\partial V_i}\Phi_{ii} = \rho_i \frac{\partial \psi_{ii}}{\partial V_i} N_{ii}^{\beta} Q_i$$

$$J_{23} = \frac{\partial F_2}{\partial \Phi_{eb}} = \frac{1}{\tau_i}\rho_e \psi_{ei}; \qquad J_{25} = \frac{\partial F_2}{\partial \Phi_{ib}} = \frac{1}{\tau_i}\rho_i \psi_{ii};$$
$$J_{34} = \frac{\partial F_3}{\partial \dot{\Phi}_{eb}} = 1;$$

$$J_{41} = \frac{\partial F_4}{\partial V_e} = \gamma_e^2 N_{eb}^{\beta} \frac{\partial Q_e}{\partial V_e}; \qquad J_{43} = \frac{\partial F_4}{\partial \Phi_{eb}} = -\gamma_e^2;$$
$$J_{44} = \frac{\partial F_4}{\partial \dot{\Phi}_{eb}} = -2\gamma_e; \qquad J_{47} = \frac{\partial F_4}{\partial \phi_{eb}} = \gamma^2 N_{ee}^{\alpha};$$

$$J_{56} = \frac{\partial F_5}{\partial \dot{\Phi}_{eb}} = 1;$$
$$J_{62} = \frac{\partial F_6}{\partial V_i} = \gamma_i^2 N_{ib}^{\beta} \frac{\partial Q_i}{\partial V_i}; \qquad J_{65} = \frac{\partial F_4}{\partial \Phi_{eb}} = -\gamma_i^2; \qquad J_{66} = \frac{\partial F_4}{\partial \dot{\Phi}_{eb}} = -2\gamma_i;$$
$$J_{78} = \frac{\partial F_7}{\partial \dot{\phi}_{eb}} = 1;$$
$$J_{81} = \frac{\partial F_8}{\partial V_e} = (v\Lambda_{eb})^2 \frac{\partial Q_e}{\partial V_e}; \qquad J_{87} = \frac{\partial F_8}{\partial \phi_{eb}} = -v^2 q^2 - v^2 \Lambda_{eb}^2; \qquad J_{88} = \frac{\partial F_8}{\partial \dot{\phi}_{eb}} = -2v\Lambda_{eb}$$

Appendix C

Relationship between DFA and PSD

The analytical relationship between detrended fluctuation analysis (DFA) and power spectral density (PSD) was first derived by Heneghan and McDarby [34]. The proof is detailed in this Appendix.

We write the power spectrum of a zero-mean time-series $u(t)$ as,

$$S_u(\omega) = \begin{cases} 0, & \text{for } \omega = 0 \\ S_x(\omega), & \text{for } \omega \neq 0 \end{cases} \tag{C.1}$$

where S_x is the power spectrum of original time-series. For DFA analysis we compute the running sum of the time-series $u(t)$,

$$y(k) = \sum_{i=1}^{k} u(i) \tag{C.2}$$

In the z-domain, the transfer function for the cumulative summing sequence, $y(k)$, can be expressed,

$$H(z) = \frac{Y(z)}{U(z)} = \frac{1}{1 - z^{-1}} \tag{C.3}$$

with power spectrum,

$$\begin{aligned} S_y(\omega) &= |H(e^{jw})|^2 S_u(\omega) \\ &= \begin{cases} 0, & \text{for } \omega = 0 \\ \dfrac{S_u(\omega)}{2(1 - \cos(\omega))}, & \text{for } \omega \neq 0 \end{cases} \end{aligned} \tag{C.4}$$

where

$$|H(e_{jw})|^2 = \frac{1}{|1 - e^{-jw}|^2} = \frac{1}{2(1 - \cos(w))} \tag{C.5}$$

By Taylor-expansion,

$$\cos(\omega) = 1 - \frac{\omega^2}{2!} + \frac{\omega^4}{4!} - \frac{\omega^6}{6!} + ... \simeq 1 - \frac{\omega^2}{2} \qquad \text{for small } \omega$$

Therefore for small ω,

$$S_y(\omega) = \begin{cases} 0, & \text{for } \omega = 0 \\ \dfrac{S_u(\omega)}{\omega^2}, & \text{for } \omega \neq 0 \end{cases} \tag{C.6}$$

Assuming a PSD power-law exponent of β, the spectral power $S_u(\omega)$ can be written as,

$$S_u(\omega) = \frac{C}{\omega^\beta}; \qquad C = \text{constant.} \tag{C.7}$$

Hence,

$$S_y(\omega) = \begin{cases} 0, & \text{for } \omega = 0 \\ \dfrac{C}{\omega^{\beta+2}}, & \text{for } \omega \neq 0 \end{cases} \tag{C.8}$$

The detrended fluctuation function, $F(n)$ increases with box size n. The power-law connection between $F(n)$ and n takes the form,

$$F(n) = n^\alpha \tag{C.9}$$

where α is the DFA exponent.

The squared $F(n)$ is the average of all the variances of detrended signals of each block,

$$F(n)^2 = \frac{1}{N}\sum_{k=1}^{N}[y(k) - y_{\text{trend}}(k)]^2 \tag{C.10}$$

which is equivalent to taking the variance of the detrended signal $y(k)$, therefore

$$F(n)^2 = \text{var}\{y(k)\} \tag{C.11}$$

Thus,

$$\text{var}\{y(k)\} = \int_{\omega=1/k}^{\infty} S_y(\omega)\, d\omega \tag{C.12}$$

$$= \int_{\omega=1/k}^{\infty} \frac{C}{\omega^{\beta+2}}\, d\omega, \qquad \text{for} \quad \omega \neq 0 \tag{C.13}$$

$$= \frac{C}{\beta+1}\, \omega^{-(\beta+1)} \tag{C.14}$$

therefore,

$$F(n)^2 = n^{2\alpha} = \frac{C}{\beta+1}\left(\frac{1}{\omega}\right)^{\beta+1} \tag{C.15}$$

giving the relationship between DFA power-law exponent α and PSD power-law exponent β as,

$$2\alpha = \beta + 1 \tag{C.16}$$

-

References

[1] Abbott, L.F.: Lapicque's introduction of the integrate-and-fire model neuron (1907). Brain Research Bulletin **50**(5-6), 303–304 (1999)

[2] Allegrini, P., Paradisi, P., Menicucci, D., Gemignani, A.: Fractal complexity in spontaneous EEG metastable-state transitions: new vistas on integrated neural dynamics. Frontiers in Physiology **1**, 128 (2010)

[3] Bahar, S., Kantelhardt, J., Neiman, A., Rego, H., Russell, D., Wilkens, L., Bunde, A., Moss, F.: Long-range temporal anti-correlations in paddlefish electroreceptors. EPL (Europhysics Letters) **56**(3), 454 (2001)

[4] Bak, P., Tang, C., Wiesenfeld, K.: Self-organized criticality: An explanation of the 1/f noise. Physical Review Letters **59**(4), 381 (1987)

[5] Bak, P., Tang, C., Wiesenfeld, K.: Self-organized criticality. Physical Review A **38**(1), 364 (1988)

[6] Beggs, J.M.: Neuronal avalanches are diverse and precise activity patterns that are stable for many hours in cortical slice cultures. Journal of Neuroscience **24**(22), 5216–5229 (2004), doi:10.1523/jneurosci.0540-04.2004

[7] Beggs, J.M., Plenz, D.: Neuronal avalanches in neocortical circuits. Journal of Neuroscience **23**(35), 11167–11177 (2003)

[8] Benayoun, M., Cowan, J.D., van Drongelen, W., Wallace, E.: Avalanches in a stochastic model of spiking neurons. PLoS Computational Biology **6**(7), e1000846 (2010)

[9] Blesić, S., Milošević, S., Stratimirović, D., Ljubisavljević, M.: Detrended fluctuation analysis of time series of a firing fusimotor neuron. Physica A: Statistical Mechanics and its Applications **268**(3-4), 275–282 (1999)

[10] Bonachela, J.A., De Franciscis, S., Torres, J.J., Munoz, M.A.: Self-organization without conservation: are neuronal avalanches generically critical? Journal of Statistical Mechanics: Theory and Experiment **2010**(02), P02015 (2010)

[11] Botcharova, M., Farmer, S.F., Berthouze, L.: Markers of criticality in phase synchronization. Frontiers in Systems Neuroscience **8**, 176 (2014)

[12] Brown, E.N., Flores, F.J.: General anesthesia causes telltale brain activity patterns (2019), URL `https://tinyurl.com/y2pb9ts9`

[13] Brown, E.N., Lydic, R., Schiff, N.D.: General anesthesia, sleep, and coma. New England Journal of Medicine **363**(27), 2638–2650 (2010)

[14] Bukoski, A., Steyn-Ross, D.A., Steyn-Ross, M.L.: Channel-noise-induced critical slowing in the subthreshold Hodgkin–Huxley neuron. Physical Review E **91**(3), 032708 (2015)

[15] Buldyrev, S., Goldberger, A., Havlin, S., Mantegna, R., Matsa, M., Peng, C.K., Simons, M., Stanley, H.: Long-range correlation properties of coding and noncoding DNA sequences: Genbank analysis. Physical Review E **51**(5), 5084 (1995)

[16] Buzsáki, G., Anastassiou, C.A., Koch, C.: The origin of extracellular fields and currentsEEG, ECoG, LFP and spikes. Nature Reviews Neuroscience **13**(6), 407 (2012)

[17] Cencini, M., Falcioni, M., Olbrich, E., Kantz, H., Vulpiani, A.: Chaos or noise: Difficulties of a distinction. Physical Review E **62**(1), 427 (2000)

[18] Chavarette, F.R., Balthazar, J.M., Peruzzi, N.J., Rafikov, M.: On non-linear dynamics and control designs applied to the ideal and non-ideal variants of the Fitzhugh–Nagumo mathematical model. Communications in Nonlinear Science and Numerical Simulation **14**(3), 892–905 (2009)

[19] Clauset, A., Shalizi, C.R., Newman, M.E.: Power-law distributions in empirical data. SIAM Review **51**(4), 661–703 (2009)

[20] Coombes, S.: Neural fields. Scholarpedia **1**(6), 1373 (2006)

[21] Coombes, S., beim Graben, P., Potthast, R., Wright, J.: Neural fields: theory and applications. Springer (2014)

[22] Dakos, V., Carpenter, S.R., Brock, W.A., Ellison, A.M., Guttal, V., Ives, A.R., Kefi, S., Livina, V., Seekell, D.A., van Nes, E.H., et al.: Methods for detecting early

warnings of critical transitions in time series illustrated using simulated ecological data. PloS One **7**(7), e41010 (2012)

[23] Doane, D.P., Seward, L.E.: Measuring skewness: a forgotten statistic? Journal of statistics education **19**(2) (2011)

[24] Erchova, I.A., Lebedev, M.A., Diamond, M.E.: Somatosensory cortical neuronal population activity across states of anaesthesia. European Journal of Neuroscience **15**(4), 744–752 (2002)

[25] Farquhar, E., Hasler, P.: A bio-physically inspired silicon neuron. IEEE Transactions on Circuits and Systems I: Regular Papers **52**(3), 477–488 (2005)

[26] FitzHugh, R.: Impulses and physiological states in theoretical models of nerve membrane. Biophysical Journal **1**(6), 445–466 (1961)

[27] Friedman, N., Ito, S., Brinkman, B.A.W., Shimono, M., DeVille, R.E.L., Dahmen, K.A., Beggs, J.M., Butler, T.C.: Universal critical dynamics in high resolution neuronal avalanche data. Physical Review Letters **108**(20) (2012), doi: 10.1103/physrevlett.108.208102

[28] Garcia, P.S., Kolesky, S.E., Jenkins, A.: General anesthetic actions on GABAA receptors. Current Neuropharmacology **8**(1), 2 (2010)

[29] Gardiner, C.W.: Handbook of stochastic methods, vol. 3. Springer Berlin, 3rd edn. (2004)

[30] Grau Moya, J.: Integration of the information in complex neural networks with noise (2011)

[31] Groeneveld, R.A., Meeden, G.: Measuring skewness and kurtosis. Journal of the Royal Statistical Society: Series D (The Statistician) **33**(4), 391–399 (1984)

[32] Hahn, G., Petermann, T., Havenith, M.N., Yu, S., Singer, W., Plenz, D., Nikolić, D.: Neuronal avalanches in spontaneous activity in vivo. Journal of Neurophysiology **104**(6), 3312–3322 (2010)

[33] Harris, T.E.: The theory of branching processes. Courier Corporation (2002)

[34] Heneghan, C., McDarby, G.: Establishing the relation between detrended fluctuation analysis and power spectral density analysis for stochastic processes. Physical Review E **62**(5), 6103 (2000)

[35] Hesse, J., Gross, T.: Self-organized criticality as a fundamental property of neural systems. Frontiers in Systems Neuroscience **8**, 166 (2014)

[36] Hodgkin, A.L.: The local electric changes associated with repetitive action in a non-medullated axon. The Journal of Physiology **107**(2), 165–181 (1948)

[37] Hodgkin, A.L., Huxley, A.F.: Propagation of electrical signals along giant nerve fibres. Proceedings of the Royal Society of London. Series B, Biological Sciences pp. 177–183 (1952)

[38] Hutt, A., Sleigh, J., Steyn-Ross, D.A., Steyn-Ross, M.L.: General anaesthesia. Scholarpedia **8**(8), 30485 (2013), doi:10.4249/scholarpedia.30485, revision #135739

[39] Indiveri, G., Chicca, E., Douglas, R.: A VLSI array of low-power spiking neurons and bistable synapses with spike-timing dependent plasticity. IEEE Transactions on Neural Networks **17**(1), 211–221 (2006)

[40] Ivanova, K., Ausloos, M.: Application of the detrended fluctuation analysis (DFA) method for describing cloud breaking. Physica A: Statistical Mechanics and its Applications **274**(1-2), 349–354 (1999)

[41] Izhikevich, E.M.: Resonate-and-fire neurons. Neural Networks **14**(6-7), 883–894 (2001)

[42] Izhikevich, E.M.: Dynamical systems in neuroscience. MIT press (2007)

[43] Izus, G., Deza, R., Wio, H.: Exact nonequilibrium potential for the Fitzhugh-Nagumo model in the excitable and bistable regimes. Physical Review E **58**(1), 93 (1998)

[44] Kantelhardt, J.W., Koscielny-Bunde, E., Rego, H.H., Havlin, S., Bunde, A.: Detecting long-range correlations with detrended fluctuation analysis. Physica A: Statistical Mechanics and its Applications **295**(3-4), 441–454 (2001)

[45] Keener, J., Sneyd, J.: Mathematical physiology: I: Cellular physiology. Springer Science & Business Media (2010)

[46] Kestin, J.: A course in statistical thermodynamics. Elsevier (1971)

[47] Kim, S.J., C Manyam, S., J Warren, D., A Normann, R.: Electrophysiological mapping of cat primary auditory cortex with multielectrode arrays. Annals of Biomedical Engineering **34**, 300–9 (2006), doi:10.1007/s10439-005-9037-9

[48] Klaus, A., Yu, S., Plenz, D.: Statistical analyses support power law distributions found in neuronal avalanches. PloS One **6**(5), e19779 (2011)

[49] Kuizenga, K., Wierda, J., Kalkman, C.: Biphasic EEG changes in relation to loss of consciousness during induction with thiopental, propofol, etomidate, midazolam or sevoflurane. British Journal of Anaesthesia **86**(3), 354–360 (2001)

[50] Kuznetsov, Y.A.: Elements of applied bifurcation theory, vol. 112. Springer Science & Business Media (2013)

[51] Liang, P., Wu, S., Gu, F.: Neural information processing in different brain areas. In: An Introduction to Neural Information Processing, pp. 233–292, Springer (2016)

[52] Liley, D.T., Cadusch, P.J., Wright, J.J.: A continuum theory of electro-cortical activity. Neurocomputing **26**, 795–800 (1999)

[53] Liu, Y., Cizeau, P., Meyer, M., Peng, C.K., Stanley, H.E.: Correlations in economic time series. Physica A: Statistical Mechanics and its Applications **245**(3-4), 437–440 (1997)

[54] Mahowald, M., Douglas, R.: A silicon neuron. Nature **354**(6354), 515 (1991)

[55] Malamud, B.D., Morein, G., Turcotte, D.L.: Forest fires: an example of self-organized critical behavior. Science **281**(5384), 1840–1842 (1998)

[56] Mandl, F.: Statistical Physics. Edmundsbury Press, 2 edn. (1988)

[57] Márton, L., Brassai, S., Bakó, L., Losonczi, L.: Detrended fluctuation analysis of EEG signals. Procedia Technology **12**, 125–132 (2014)

[58] Meisel, C., Klaus, A., Kuehn, C., Plenz, D.: Critical slowing down governs the transition to neuron spiking. PLoS Computational Biology **11**(2), e1004097 (2015)

[59] Moors, J.J.A.: The meaning of kurtosis: Darlington reexamined. The American Statistician **40**(4), 283–284 (1986)

[60] Movahed, M.S., Jafari, G., Ghasemi, F., Rahvar, S., Tabar, M.R.R.: Multifractal detrended fluctuation analysis of sunspot time series. Journal of Statistical Mechanics: Theory and Experiment **2006**(02), P02003 (2006)

[61] Nagumo, J., Arimoto, S., Yoshizawa, S.: An active pulse transmission line simulating nerve axon. Proceedings of the IRE **50**(10), 2061–2070 (1962)

[62] Negahbani, E., Steyn-Ross, D.A., Steyn-Ross, M.L., Wilson, M.T., Sleigh, J.W.: Noise-induced precursors of state transitions in the stochastic Wilson–Cowan model. The Journal of Mathematical Neuroscience **5**(1), 9 (2015)

[63] Newman, M.E.: Power laws, Pareto distributions and Zipf's law. Contemporary Physics **46**(5), 323–351 (2005)

[64] Palva, J.M., Zhigalov, A., Hirvonen, J., Korhonen, O., Linkenkaer-Hansen, K., Palva, S.: Neuronal long-range temporal correlations and avalanche dynamics are correlated with behavioral scaling laws. Proceedings of the National Academy of Sciences **110**(9), 3585–3590 (2013)

[65] Peng, C.K., Buldyrev, S.V., Havlin, S., Simons, M., Stanley, H.E., Goldberger, A.L.: Mosaic organization of DNA nucleotides. Physical Review E **49**(2), 1685 (1994)

[66] Peng, C.K., Havlin, S., Stanley, H.E., Goldberger, A.L.: Quantification of scaling exponents and crossover phenomena in nonstationary heartbeat time series. Chaos: An Interdisciplinary Journal of Nonlinear Science **5**(1), 82–87 (1995)

[67] Penzel, T., Kantelhardt, J.W., Grote, L., Peter, J.H., Bunde, A.: Comparison of detrended fluctuation analysis and spectral analysis for heart rate variability in sleep and sleep apnea. IEEE Transactions on Biomedical Engineering **50**(10), 1143–1151 (2003)

[68] Petermann, T., Thiagarajan, T.C., Lebedev, M.A., Nicolelis, M.A., Chialvo, D.R., Plenz, D.: Spontaneous cortical activity in awake monkeys composed of neuronal avalanches. Proceedings of the National Academy of Sciences **106**(37), 15921–15926 (2009)

[69] Plenz, D., Thiagarajan, T.C.: The organizing principles of neuronal avalanches: cell assemblies in the cortex? Trends in Neurosciences **30**(3), 101–110 (2007), doi: 10.1016/j.tins.2007.01.005

[70] Priesemann, V., Valderrama, M., Wibral, M., Le Van Quyen, M.: Neuronal avalanches differ from wakefulness to deep sleep–evidence from intracranial depth recordings in humans. PLoS Computational Biology **9**(3), e1002985 (2013)

[71] Priesemann, V., Wibral, M., Valderrama, M., Pröpper, R., Le Van Quyen, M., Geisel, T., Triesch, J., Nikolić, D., Munk, M.H.: Spike avalanches in vivo suggest a driven, slightly subcritical brain state. Frontiers in Systems Neuroscience **8**, 108 (2014)

[72] Rennie, C.J., Wright, J.J., Robinson, P.A.: Mechanisms of cortical electrical activity and emergence of gamma rhythm. Journal of Theoretical Biology **205**(1), 17–35 (2000)

[73] Ribeiro, T.L., Copelli, M., Caixeta, F., Belchior, H., Chialvo, D.R., Nicolelis, M.A., Ribeiro, S.: Spike avalanches exhibit universal dynamics across the sleep-wake cycle.

PloS One **5**(11), e14129 (2010)

[74] Rinzel, J., Ermentrout, G.B.: Methods in neuronal modeling. Koch C., Segev I (1989)

[75] Rizvi, S.A.R., Dewandaru, G., Bacha, O.I., Masih, M.: An analysis of stock market efficiency: Developed vs Islamic stock markets using MF-DFA. Physica A: Statistical Mechanics and its Applications **407**, 86–99 (2014)

[76] Robinson, P.: Interpretation of scaling properties of electroencephalographic fluctuations via spectral analysis and underlying physiology. Physical Review E **67**(3), 032902 (2003)

[77] Robinson, P.A., Rennie, C.J., Wright, J.J.: Propagation and stability of waves of electrical activity in the cerebral cortex. Physical Review E **56**(1), 826 (1997)

[78] San-juan, D., Chiappa, K.H., Cole, A.J.: Propofol and the electroencephalogram. Clinical Neurophysiology **121**(7), 998–1006 (2010)

[79] Scheffer, M., Bascompte, J., Brock, W.A., Brovkin, V., Carpenter, S.R., Dakos, V., Held, H., Van Nes, E.H., Rietkerk, M., Sugihara, G.: Early-warning signals for critical transitions. Nature **461**(7260), 53 (2009)

[80] Sethna, J.P., Dahmen, K.A., Myers, C.R.: Crackling noise. Nature **410**(6825), 242–250 (2001)

[81] Shew, W.L., Yang, H., Petermann, T., Roy, R., Plenz, D.: Neuronal avalanches imply maximum dynamic range in cortical networks at criticality. Journal of Neuroscience **29**(49), 15595–15600 (2009), doi:10.1523/jneurosci.3864-09.2009

[82] Sleigh, J.W., Vizuete, J.A., Voss, L., Steyn-Ross, D.A., Steyn-Ross, M.L., Marcuccilli, C.J., Hudetz, A.G.: The electrocortical effects of enflurane: experiment and theory. Anesthesia and Analgesia **109**(4), 1253 (2009)

[83] Stewart, C.V., Plenz, D.: Inverted-u profile of dopamine–NMDA-mediated spontaneous avalanche recurrence in superficial layers of rat prefrontal cortex. Journal of Neuroscience **26**(31), 8148–8159 (2006)

[84] Stewart, C.V., Plenz, D.: Homeostasis of neuronal avalanches during postnatal cortex development in vitro. Journal of Neuroscience Methods **169**(2), 405–416 (2008)

[85] Steyn-Ross, D.A.: Modelling the anaestheto-dynamic phase transition of the cerebral cortex. Ph.D. thesis, University of Waikato (2002)

[86] Steyn-Ross, D.A., Steyn-Ross, M.L.: Modeling phase transitions in the brain. Springer (2010)

[87] Steyn-Ross, D.A., Steyn-Ross, M.L., Wilson, M.T., Sleigh, J.W.: White-noise susceptibility and critical slowing in neurons near spiking threshold. Physical Review E **74**(5), 051920 (2006)

[88] Steyn-Ross, M.L., Steyn-Ross, D.A., Sleigh, J.W., Whiting, D.R.: Theoretical predictions for spatial covariance of the electroencephalographic signal during the anesthetic-induced phase transition: Increased correlation length and emergence of spatial self-organization. Physical Review E **68**(2) (2003), doi:10.1103/physreve.68.021902

[89] Steyn-Ross, M.L., Steyn-Ross, D.A., Sleigh, J.W.: Modelling general anaesthesia as a first-order phase transition in the cortex. Progress in Biophysics and Molecular Biology **85**(2-3), 369–385 (2004)

[90] Steyn-Ross, M.L., Steyn-Ross, D.A., Sleigh, J.W.: Interacting Turing–Hopf instabilities drive symmetry-breaking transitions in a mean-field model of the cortex: a mechanism for the slow oscillation. Physical Review X **3**(2), 021005 (2013)

[91] Steyn-Ross, M.L., Steyn-Ross, D.A., Sleigh, J.W., Liley, D.: Theoretical electroencephalogram stationary spectrum for a white-noise-driven cortex: evidence for a general anesthetic-induced phase transition. Physical Review E **60**(6), 7299 (1999)

[92] Steyn-Ross, M.L., Steyn-Ross, D.A., Sleigh, J.W., Wilcocks, L.C.: Toward a theory of the general-anesthetic-induced phase transition of the cerebral cortex. I. A thermodynamics analogy. Physical Review E **64**(1), 011917 (2001)

[93] Steyn-Ross, M.L., Steyn-Ross, D.A., Sleigh, J.W.: Gap junctions modulate seizures in a mean-field model of general anesthesia for the cortex. Cognitive Neurodynamics **6**(3), 215–225 (2012)

[94] Steyn-Ross, M.L., Steyn-Ross, D.A., Wilson, M.T., Sleigh, J.W.: Gap junctions mediate large-scale Turing structures in a mean-field cortex driven by subcortical noise. Physical Review E **76**(1), 011916 (2007)

[95] Tateno, T., Harsch, A., Robinson, H.: Threshold firing frequency–current relationships of neurons in rat somatosensory cortex: type 1 and type 2 dynamics. Journal of Neurophysiology **92**(4), 2283–2294 (2004)

[96] Touboul, J., Destexhe, A.: Can power-law scaling and neuronal avalanches arise from stochastic dynamics? PloS one **5**(2), e8982 (2010)

[97] Voss, L., Sleigh, J.: Monitoring consciousness: the current status of EEG-based depth of anaesthesia monitors. Best Practice & Research Clinical Anaesthesiology **21**(3), 313–325 (2007)

[98] Wang, K.: Analysis of pattern dynamics for a nonlinear model of the human cortex via bifurcation theories. Ph.D. thesis, University of Waikato (2014)

[99] Wang, R., Dearing, J.A., Langdon, P.G., Zhang, E., Yang, X., Dakos, V., Scheffer, M.: Flickering gives early warning signals of a critical transition to a eutrophic lake state. Nature **492**(7429), 419 (2012)

[100] Westfall, P.H.: Kurtosis as peakedness, 1905-2014. RIP. The American Statistician **68**(3), 191–195 (2014)

[101] Wijekoon, J.H., Dudek, P.: A CMOS circuit implementation of a spiking neuron with bursting and adaptation on a biological timescale. In: Biomedical Circuits and Systems Conference, 2009. BioCAS 2009. IEEE, pp. 193–196, IEEE (2009)

[102] Wilson, H.R.: Spikes, decisions, and actions: the dynamical foundations of neurosciences (1999)

[103] Wilson, H.R., Cowan, J.D.: Excitatory and inhibitory interactions in localized populations of model neurons. Biophysical Journal **12**(1), 1–24 (1972)

[104] Wilson, M.T., Steyn-Ross, M.L., Steyn-Ross, D.A., Sleigh, J.W.: Predictions and simulations of cortical dynamics during natural sleep using a continuum approach. Physical Review E **72**(5), 051910 (2005)

[105] Wilting, J., Priesemann, V.: Inferring collective dynamical states from widely unobserved systems. Nature communications **9**(1), 1–7 (2018)

[106] Xia, J., Shang, P., Wang, J.: Estimation of local scale exponents for heartbeat time series based on DFA. Nonlinear Dynamics **74**(4), 1183–1190 (2013)

[107] Zou, Q., Bornat, Y., Tomas, J., Renaud, S., Destexhe, A.: Real-time simulations of networks of Hodgkin–Huxley neurons using analog circuits. Neurocomputing **69**(10-12), 1137–1140 (2006)